University of Alberta

Surface modification of group 14 nanocrystals

by

Joel Alexander Kelly

A thesis submitted to the Faculty of Graduate Studies and Research
in partial fulfillment of the requirements for the degree of

Doctor of Philosophy

Department of Chemistry

© Joel Alexander Kelly
Spring, 2012
Edmonton, Alberta

Abstract

Group 14 semiconductor nanocrystals exhibit size-dependent optoelectronic properties through the influence of quantum size effects, notably intense photoluminescence (PL). A crucial step toward the realization of their technological potential is the development of effective methods to control the surface chemistry of freestanding nanocrystals. This thesis describes five investigations with this central goal in mind, based on silicon (Si) and silicon-germanium alloy (Si_xGe_{1-x}) nanocrystals obtained from hydrogen silsesquioxane (HSQ).

These composite materials were etched using hydrofluoric acid (HF), to yield freestanding hydride-terminated nanocrystals that undergo a hydrosilylation reaction with terminal olefins, with thermal or near-UV initiation. This reaction produced well-dispersed nanocrystals with increased stability against oxidation, which degrades their PL.

The use of near-UV initiation was studied in detail, based on its compatibility with a wide range of olefins and the observation of unique reactivity unseen for hydrosilylation of molecular species. This reactivity of Si nanocrystals was size-dependent, consistent with an exciton-mediated mechanism previously proposed. This observation was explored through separation of a mixture of sizes based on their hydrosilylation reactivity.

Exciton-mediated reactivity was also observed in the HF etching of oxide-embedded Si nanocrystal composites. The PL from these materials could be conveniently controlled by irradiating the etching solution, presenting a strategy for

controlling the nanocrystal size and polydispersity; however, defect-containing nanocrystals were suggested to be inactive in this etching pathway.

The origin of luminescence from Si nanocrystals functionalized using near-UV hydrosilylation was demonstrated to arise from quantum confinement effects using X-ray absorption spectroscopy. These results confirm that the alkyl grafting does not appreciably alter the emission pathway. Oxidation caused by ambient exposure reduced the ensemble PL quantum yield and shift the emission maximum.

The morphology of nanocrystals obtained from the co-reaction of HSQ and GeI_2 solubilized with trialkylphosphines was evaluated spectroscopically and microscopically to be a heterogeneous mixture of Si- and Ge-rich nanocrystals. The trialkylphosphine used to facilitate GeI_2 co-precipitation influences nanocrystal nucleation and growth processes. Indirect evidence was presented for the involvement of Ge in the emission pathway.

Acknowledgements

When I walked into Jon's office in the old Chemistry building five years ago, looking for a summer job, I had no idea I had some of the best years of my life ahead. Nor did I know how much I would come to love science— being able to design an proper experiment that could reproducibly determine how some small part of the universe works. Nor did I realize how hard that could actually be. I can't imagine the impossibility of a Ph.D. without the support from my friends, family, collaborators and colleagues.

Jon, I will always be so proud of the work we did together. Your unconditional support, sympathy and enthusiasm kept me going throughout ups and downs. You have always been first and foremost a good friend to your students. You have assembled a group of great people around you, and I'm so excited to see where the next chapter of research takes you.

Past and present members of the Veinot group, you have contributed to this thesis in countless ways. I will always cherish your seemingly-endless patience, no-nonsense editing abilities, availability and relentless enthusiasm for team fitness and brainflexing, penchant for high fives, and tolerance of my coffee/food/music snobbery (even if Tim Horton's coffee and Robbie Williams are still *gross*). Defending was a snap after having to answer to all of you during many practice talks and group meetings.

I especially want to acknowledge Eric Henderson, José Rodriguez, Melanie Johnson/Hoffman and Sarah Regli. I couldn't have asked for a better role model as a scientist than Dr. Eric J. Henderson. Your scientific creativity, determination,

attention to detail and handlebar-mustache-growing ability continue to inspire and amaze me. You are a great researcher, an even better friend, and an okay user of MS Paint. I'll be the first in line to apply for a position at Hendercorp faster than the sonic boom of the eagle's cry.

José, our friendly competition to finish our degrees has motivated me more than I'd like to admit. Trying to match your level of dedication and hard work has pushed me to keep reading the literature, reproduce that experiment one last time, and get the next draft to Jon's desk sooner rather than later. Our time spent together working on our theses in our little office over the last year has been some of the most rewarding time throughout my degree. Ciao ciao, take care.

Melly and Sarah, you guys have picked up the work we started and haven't looked back since. You are both hard working, diligent, seriously talented ladies. It's been amazing to see you two truly come into your own as scientists. The paths ahead that you have each created are both so exciting! I leave the lab knowing it is in the best hands it could possibly be.

I've had the privilege of working with so many awesome mentors, collaborators and supporters. I wouldn't be where I am today if not for the tireless efforts of Dr. Grace Strom and Dr. Peter Mahaffy, who mentored the clumsiest undergraduate researcher the King's University College has ever seen. Mike Fleischauer, resident SAXS master, exudes savvy and patience in all of our interactions alongside an enviable mastery of *gnuplot*. His epic beard is entirely a bonus. Every chemist needs a few good physicist friends when the going gets quantized, and I am so lucky mine were Marco Taucer and Kyle Manchee. Likewise,

Table of Contents

Chapter 6: Structure and Optical Properties of Silicon-Germanium Nanocrystals

List of Figures

List of Schemes

List of Symbols, Nomenclature and Abbreviations

arb.	Arbitrary units
CB	Conduction band
CCD	Charge-coupled device
CLS	Canadian Light Source
DOS	Density of states
E	Energy
EDS	Energy dispersive X-ray spectroscopy
E_g	Bandgap
EXAFS	Extended X-ray absorption fine structure
ϕ	Fluorescence quantum yield
FFT	Fast Fourier transform
FLY	Fluorescence yield
FTIR	Fourier transform infrared spectroscopy
FWHM	Full-width at half maximum
G	Gravitational Force
η	Refractive index
HAADF	High-angle annular dark field electron microscopy
HOMO	Highest occupied molecular orbital
HRTEM	High resolution transmission electron microscopy
HSQ	Hydrogen silsesquioxane
I	Intensity
IPFY	Inverted partial fluorescence yield

IR	Infrared
k_b	Boltzmann constant
λ	Wavelength
LED	light emitting diode
LPDOS	Local partial density of states
LUMO	Lowest unoccupied molecular orbital
MIBK	Methyl isobutyl ketone
MO	Molecular orbital
n	Number
NCs	Nanocrystals
NEXAFS	Near-edge X-ray absorption fine structure
P	Form factor
PGM	Planar Grating Monochromator
PL	Photoluminescence
PLE	Photoluminescence excitation
PLY	Photoluminescence yield
q	Scattering wavevector
QY	Quantum yield
R	Radius
ρ	radius
RoHS	Restriction of Hazardous Substances Directive
rpm	Rotations per minute
SAED	Selected area electron diffraction

SAXS	Small-angle X-ray scattering
SGM	Spherical Grating Monochromator
Si-NCs	Silicon nanocrystals
Si_xGe_{1-x}-NCs	Silicon germanium alloy nanocrystals
TBP	Tributylphosphine
TEM	Transmission electron microscopy
TEY	Total electron yield
TOP	Trioctylphosphine
UV	Ultraviolet
UV-vis	Ultraviolet-visible (spectroscopy)
VB	Valence band
XANES	X-ray absorption near-edge spectroscopy
XAS	X-ray absorption spectroscopy
XEOL	X-ray excited optical luminescence
XRD	X-ray powder diffraction
ΔE	Energy difference (E_2-E_1, where E_2>E_1)
σ	Standard deviation

Chapter 1:

Introduction

1.1 Introduction

When the electronic motion in a material is restricted in one or more dimensions to the nanometer scale, the material's functional properties can be dramatically altered. Over the past 30 years, this phenomenon have been a driving force for tremendous development across the fields of chemistry, physics, biology and engineering toward the synthesis, characterization and application of nanomaterials (being composed of hundreds to thousands of atoms).[1, 2] The influence of quantum effects on certain nanomaterials has led to unexpected, size-dependent and technologically interesting properties.

An example of this development is the range of unique optoelectronic properties exhibited by graphene, a single-atom-thick layer of sp^2-hybridized carbon arranged in a two-dimensional hexagonal lattice. Although monolayers of graphite have been studied since 1947,[3] pioneering work by Drs. Andre Geim and Konstantin Novoselov (quickly followed by many other groups) demonstrated that the confinement of charge carriers within its planar structure gives rise to fascinating phenomena, such as very high intrinsic mobility, Dirac-like electronic excitations, and the observation of the quantum Hall effect at room temperature.[4] The discovery of these properies has sparked a "gold rush" of potential technologies where graphene is viewed as a next generation material suitable for use in transistors, spintronics and sensing, among many others.[5] In recognition of their significant contributions to this nascent field, Geim and Novoselov shared the 2011 Nobel Prize for Physics, only 7 years after their initial report.[6]

In many cases, the fascinating properties of nanomaterials can be understood by considering the progression from atomic and molecular species up to macroscopic bulk solids. As will be discussed throughout this thesis, a classic example of this is the emergence of size-dependent optoelectronic properties, notably intense photoluminescence (PL), from semiconductor nanocrystals (NCs), also known as quantum dots. Their unique combination of properties has drawn significant interest for a wide range of applications, including optoelectronics,[7, 8] biological imaging,[9, 10] and photovoltaics.[11, 12]

An archetypal example of semiconductor NCs exhibiting size-dependent PL is the family of II-VI NCs (*e.g.*, CdSe, ZnS and HgS). In 1983, Dr. Louis Brus and his group reported an aqueous synthesis for CdS-NCs exhibiting size-dependent light absorption,[13] an "accidental observation" as he would later describe it.[14] This initial report sparked worldwide interest into the development of wet chemical methods to prepare these materials with controlled size and narrow polydispersity, enabling detailed characterization of their optoelectronic properties through the influence of size effects, generally referred to as quantum confinement.[15]

Currently there are over 1300 consumer products containing nanomaterials,[16] and many more are expected in the near future; worldwide funding of nanomaterials-related research rose to \$18.2 billion in 2008, and \$3.1 trillion worth of nanomaterials-related manufactured goods are expected by 2015.[17] Semiconductor NCs have been incorporated into a number of products currently available in the marketplace, including light emitting diodes (LEDs) in lighting and display technologies, biomedical diagnostics, and flash memory devices.[18]

Although the II-VI family of semiconductor NCs have drawn much research interest for their impressive optical properties, concerns have been raised regarding the toxicity of some of their constituent heavy metal elements (notably Cd and Hg).[19, 20] In many regions of the world, governments have restricted the sale of manufactured goods containing these heavy metals to minimize risk of environmental and societal exposure. Notably, the Restriction of Hazardous Substances Directive (RoHS), enacted by the European Union in 2003, limits the use of Cd in electronic goods to 100 ppm of any separable component; for example, an LED containing a thin film of CdSe-NCs as the emissive layer would be prohibited even if the overall amount of Cd in the device was below the acceptable threshold.[21] Other countries have since followed suit, using the RoHS as a model for their own legislation.[22] This movement away from heavy metal-containing materials is a major impetus for the study and application of environmentally benign semiconductor NCs that can match the impressive quantum-confined properties of II-VI NCs.

The family of group 14 semiconductors (*i.e.*, Si, Ge, Sn, SiC and Si_xGe_{1-x} alloys) holds much promise in this regard. PL from group 14 nanostructured materials was first observed in porous Si by Dr. Leigh Canham in 1990.[23] Although bulk group 14 materials exhibit extremely low PL quantum yields, many reports have noted a remarkable increase in PL efficiency through the influence of quantum confinement effects, with PL spanning the visible and near-IR spectral regions.[24] As well, owing to silicon's role as the workhorse material of the microelectronics industry, group 14 NCs might allow facile epitaxial incorporation into integrated circuits using existing microfabrication techniques.[25]

Many reports thus far have suggested group 14 nanomaterials, notably Si and SiC, exhibit minimal toxicity.[26] For example, Si has been studied as an attractive biomaterial for human *in vivo* applications because it biodegrades into orthosilicic acid ($Si(OH)_4$), which is naturally occurring in numerous tissues and can be easily excreted from the body through urine.[27]

For these reasons, group 14 NCs have attracted considerable attention within the luminescent semiconductor nanostructures research community. Figure 1-1 shows the number of scientific publications per year on semiconductor NCs in comparison to group 14 NCs and their related porous materials.
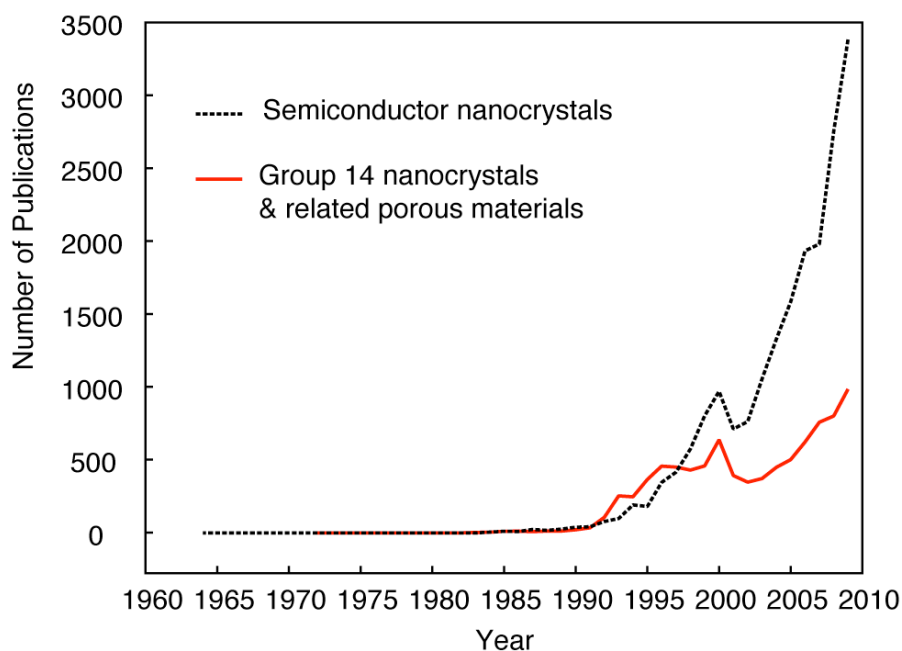
Figure 1-1: Interest in semiconductor NCs in comparison to group 14 NCs and related porous materials, in terms of research publications per year to 2009. Data derived from Scopus (accessed May 22, 2011).

Understanding the size-dependent properties of semiconductor NCs is facilitated by an appreciation of the common features that they share between molecular species (*e.g.*, quasidiscrete, size-dependent energy levels) and bulk materials (*e.g.*, broadband absorption, crystalline faceting).[28] Therefore, before we consider the impact of quantum confinement on group 14 semiconductors, it is instructive to first discuss the underlying factors contributing to the similarities and differences of molecules, nanomaterials and bulk materials, starting from the atomic level.

1.2 The electronic structure of group 14 semiconductors

In molecular orbital (MO) theory, Group 14 elements have a half-filled valence shell (*i.e.*, ns^2np^2, n = 2, 3, 4 and 5 for C, Si, Ge and Sn), and are therefore capable of forming four bonding MOs. As Si, Ge and Sn have much larger radii than C, they form much weaker π bonds, preferring to form σ bonds.[29] Therefore, in the solid state, Si, Ge and α-Sn favor the diamond crystal structure (with exclusively tetrahedral σ bonding) while C forms both diamond and planar graphite (with both σ and π bonding).

The driving force for the formation of MOs between two neighboring atoms comes from the stabilization of a bonding MO (resulting from the favourable increase in electron density between both nuclei), alongside the destabilization of an antibonding MO (resulting from the unfavorable decrease in electron density between both nuclei).[30] This stabilization is proportional to the amount of orbital overlap, which depends on the atomic size, orbital symmetry and orbital diffuseness. In an extended solid, interaction between neighboring atoms is further stabilized or destabilized through secondary bonding or antibonding interactions with other orbitals from the surrounding lattice. These interactions produce an ensemble of MOs nearly continuous in energy, referred to collectively as a band (Figure 1-2).

For both molecular and bulk species, their bandgap is defined as a non-zero gap in energy between the frontier occupied and unoccupied states. In molecular terminology, this is the difference in energy between the highest-occupied MO (HOMO) and lowest-unoccupied MO (LUMO). The bandgap of bulk materials

(*i.e.*, semiconductors and insulators) corresponds to the difference in energy between their valence (occupied) and conduction (unoccupied) bands.

The bandgap is of fundamental relevance for understanding the optoelectronic properties of a given material. It corresponds to the lowest energy of light absorption. According to the Pauli exclusion principle, electrons cannot move between filled states in the valence band but must be energetically promoted above the bandgap to unoccupied states for conduction to occur. Although most molecular species have a non-zero bandgap, bulk metals have a negligible difference between occupied and unoccupied states and thus present a tiny energetic barrier for electron promotion. Metals exhibit very low resistivity as electrons are only loosely bound to nuclei (on the order of 10^{-8} $\Omega \bullet m$). Conversely, bulk semiconductor and insulators exhibit intermediate-to-high resistivity resulting from their non-zero bandgap (from *ca.* 10^{-9} $\Omega \bullet m$ to 10^2 $\Omega \bullet m$ for semiconductors and beyond for insulators).[31] By convention, semiconductors are classified apart from insulators as materials having a bandgap equal to or less than *ca.* 4 eV.

The bandgap of bulk semiconductors is determined by two factors: bond strength and the degree of secondary interactions. Increasing atomic size results in poorer orbital overlap and reduced energy stabilization for bonding interactions. Orbital diffuseness also increases, leading to a higher degree of secondary interactions and so increasing the width of the band (*i.e.*, the energy range of near-continuous states). Together, these factors contribute to a decreasing bandgap moving down the group. For example, diamond C has a wide bandgap with narrow valence and conduction bands stemming from strong orbital overlap and reduced secondary

interactions, whereas α-Sn has a very small bandgap with wide valence and conduction bands arising from reduced orbital overlap and increased secondary interactions. Table 1-1 shows the correlation between atomic size, molecular bond strength, lattice constant and bulk bandgap.
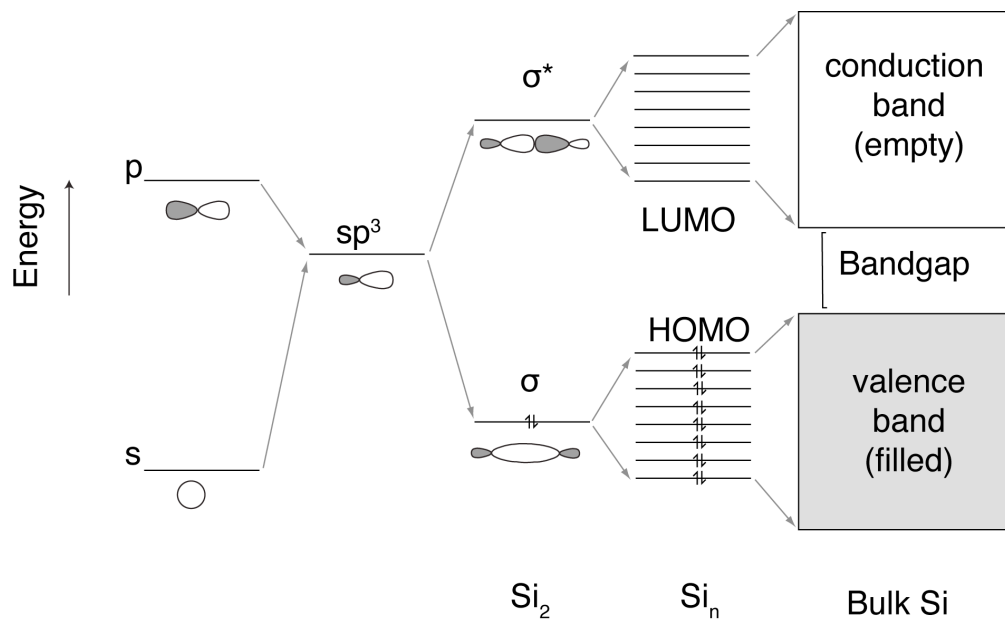
Figure 1-2: Molecular orbital model for the band structure of bulk semiconductors.

Adapted from reference 15.

Table 1-1: Group 14 periodic trends.

	Covalent radius (pm)[a]	Bond dissociation energy (kJ mol^{-1})[b]	Lattice constant (Å)[c]	Bandgap (eV)[d]
Carbon (diamond, C)	77	346	3.57	5.5
Silicon (Si)	118	222	5.43	1.1
Germanium (Ge)	122	188	5.66	0.7
Tin (α-Sn)	140	146	6.49	< 0.1

[a] Half of the distance between bonded nuclei.[32]
[b] Determined from heats of atomization.[30]
[c] Determined by X-ray diffraction.[30]
[d] Measured at 300 K. [30]

1.2.1 Band structures

As its name implies, MO theory was developed primarily to describe the bonding for molecular species. For crystalline solids, it is necessary to employ band structure diagrams to more fully describe the complexity of electronic interactions extending in three dimensions.

In an extended crystalline material, the arrangement of atoms is defined by a periodic lattice with a characteristic spacing between repeat units (a lattice constant). The translational symmetry of the lattice is well described using the terminology of reciprocal space. Reciprocal space is also referred to as momentum space or k-space since these terms originate from the de Broglie equations relating a particle's momentum and wave-like properties. Although the reasons for this transformation may appear initially non-obvious, it greatly facilitates the depiction of electronic band in the solid state.

For a simplified case, consider a series of atomic orbitals (with wavefunctions labeled χ_n, n = 0, 1, 2, *etc.*) arranged in an infinite linear chain defined by spacing *a*. These orbitals combine to form a band continuous in energy. It can be shown that solutions to the Schrödinger equation for this chain, known as Bloch functions, can be written as:[33]
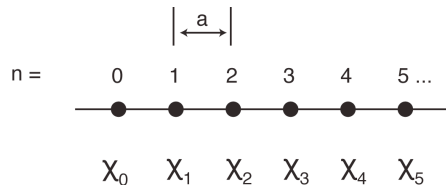
$$\psi_k = \sum_n e^{ikna} \chi_n$$

<div align="right">(1-1)</div>

where k is an index for the irreducible representations of the system. The k-value

helps determine if an interaction will be bonding or antibonding. For example,

consider two contrasting k values, at $k = 0$ and $k = \pi/a$ for a chain of s-orbitals:

$$k = 0 \qquad \psi_0 = \sum_n \chi_n = \chi_0 + \chi_1 + \chi_2 + \chi_3 + \chi_4 + \chi_5 + \cdots$$

$$k = \frac{\pi}{a} \qquad \psi_{\frac{\pi}{a}} = \sum_n e^{i\pi n} \chi_n = \chi_0 - \chi_1 + \chi_2 - \chi_3 + \chi_4 - \chi_5 + \cdots \qquad (1\text{-}2)$$

At $k = 0$, the orbitals are all in phase with each other and thus form a low

energy bonding interaction. Conversely, at $k = \pi/a$, all orbitals are out of phase with

their neighbors and so form a high energy antibonding interaction. The band formed

will therefore "run" up in energy from $k = 0$ to $k = \pi/a$. In general, the number of k

values is equal to the number of translations available within the material (for a

macroscopic crystal, this is very, very large). However, outside the range of $|k|$ values

of 0 *to* π/a, solutions repeat themselves. This range of unique k values is termed the

first Brillouin zone and is the region depicted in band structure diagrams.

In three dimensions, k values become k vectors, but the principle remains the

same. A band structure diagram is constructed by considering the energy of each

Bloch function as a function of k. To simplify the depiction, the band structure

diagram focuses on certain k vectors of high symmetry and special interest (*e.g.*, the Γ

point at k = (0,0,0)). The degree of orbital overlap and topology of interaction

determines the magnitude and direction of change in band energy as a function of k

(*e.g.*, *s* or *p* orbitals with σ- or π-interactions).

Band structures are a very useful tool in understanding the optoelectronic properties of group 14 materials. In comparison to other compound semiconductors(*e.g.*, CdSe or GaAs) used in LEDs, bulk group 14 semiconductors have indirect bandgaps, resulting in very low PL quantum efficiencies; bulk Si has a PL quantum yield of *ca.* 10^{-5} % at room temperature.[34] Figure 1-3 shows a simplified comparison of the band structures of Si and zinc blende CdSe, which are indirect and direct bandgap semiconductors, respectively.[28] Although both materials exhibit similar diamond-type symmetry, the lowest energy transition for CdSe occurs vertically at the Γ point whereas for Si the transition occurs from the Γ-point to the region marked * near the X ($k = (1,0,0)\pi/a$) point. In Si, the top of the valence band and bottom of the conduction band lie in different regions of k-space. Recall, k is related to momentum; in accordance with the principles of conservation of momentum, a transition between these states is dipole-forbidden. Participation of a phonon (a lattice vibration) must compensate for this change in momentum. This three-body transition has a much lower probability of than that of the direct transition (*e.g.*, for CdSe), approximately a factor of 1000.[28]
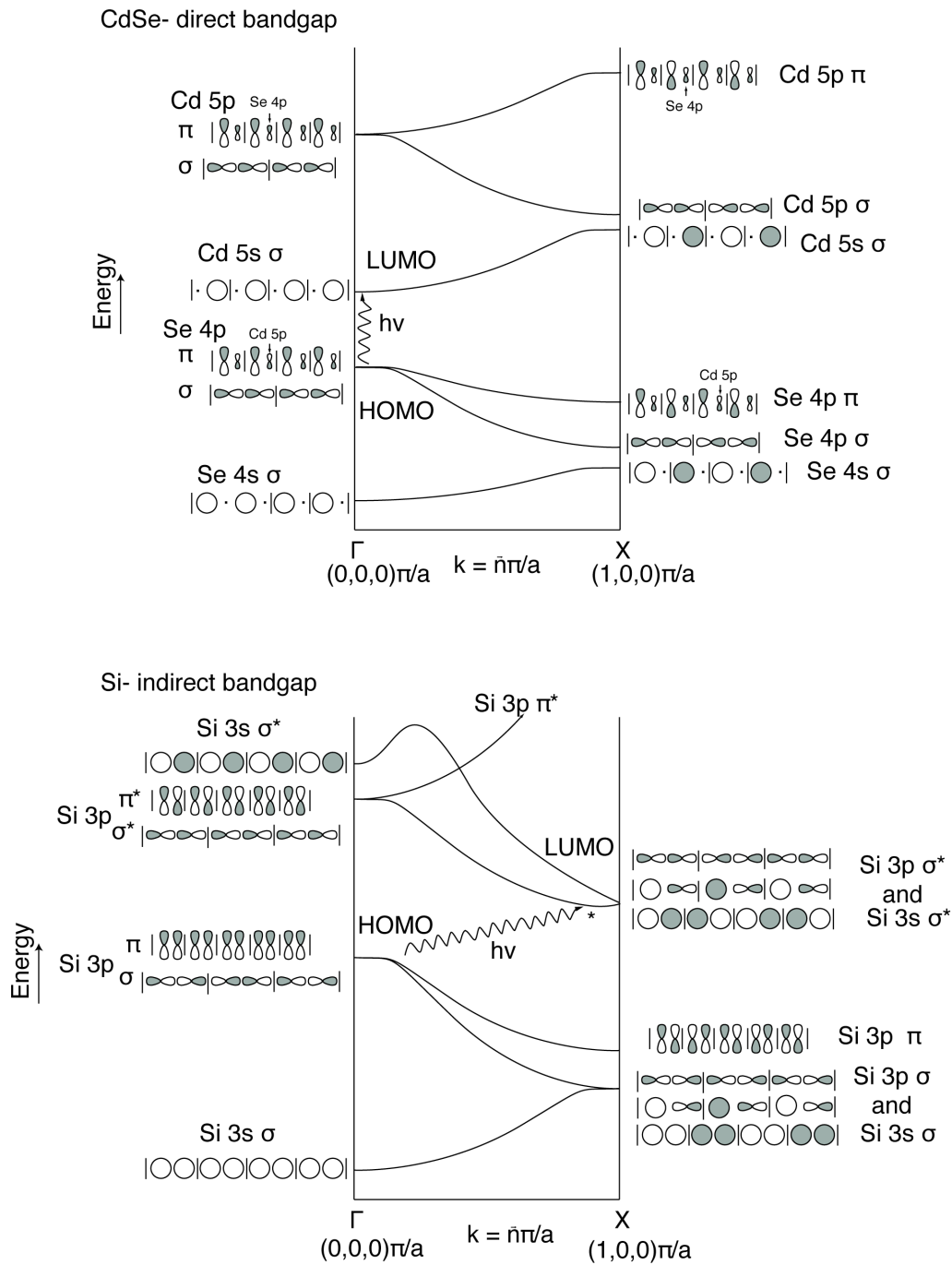
Figure 1-3: A comparison of band structures of CdSe (direct bandgap, top) and Si (indirect bandgap, bottom) in the Γ to X regions of k-space, with a simplified depiction of the associated bonding interactions. Figure adapted from reference 28.

The indirect bandgap exhibited by group 14 semiconductors has several important implications. First, the low transition probability results in very long (~μs to ms) excited state lifetimes, during which the excited charge carriers can migrate over very long distances, inviting nonradiative pathways to dominate relaxation (*e.g.*, Auger or defect-mediated recombination).[35] Second, the absorption probability is also very low; absorption cross-sections of indirect bandgap materials are 100 times lower than their direct bandgap cousins. Finally, in a direct bandgap semiconductor, the transitions are fundamentally electronic, with weak sidebands arising from vibrational coupling. Only a small number of transitions are strongly allowed, resulting in an absorption spectrum exhibiting information-rich structure. In an indirect bandgap semiconductor, all electronic transitions are weakly allowed through vibrational (phonon) coupling, resulting in a congested, featureless absorption spectrum (Figure 1-4).
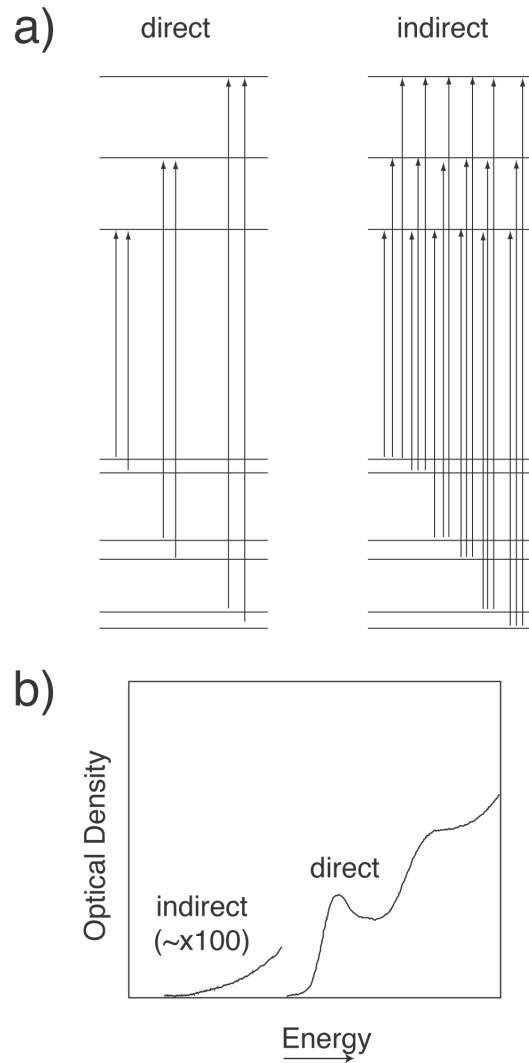
Figure 1-4: a) Comparison of transitions in direct and indirect semiconductors, showing a small number of strongly allowed transitions for the direct case, and a large number of weakly allowed transitions for the indirect case. b) Resulting qualitative absorption spectra, with the indirect semiconductor exhibiting featureless absorption with a much lower absorption cross-section than the direct semiconductor. Figure adapted from reference 28.

A plot of density of states (DOS) as a function of energy depicts the distribution of electrons across bands, analogous to MO diagrams (a DOS diagram is shown pictorially in Figure 1-5). In the DOS, the energy level separating occupied and unoccupied states (at absolute zero when no thermal energy is available for electron movement) is termed the Fermi level. For metals, the Fermi level occurs in the middle of a band, with a negligible energy barrier for electrons to access unoccupied conductive states. For semiconductors and insulators the Fermi level lies between the filled valence and empty conduction states (*i.e.*, in the bandgap).

The DOS of bands is not uniform throughout their entire width; rather, it is densest in the centre of the band. For nanomaterials, their reduced size (and thus reduced number of orbitals available to participate in delocalized bonding) leads to a "thinning" of the DOS. As a function of decreasing size, when the difference between energy levels within the bands is greater than the thermal energy available for intraband charge carrier promotion (*i.e.*, k_bT, approximately 26 meV at 300 K), the energy levels of the material will become quasidiscrete.[28]

Because the DOS is sparsest at band edges, DOS thinning in semiconducting nanomaterials narrows the bands, leading to a strong modulation in bandgap as a function of size. Conversely, metallic nanostructures, whose Fermi level lies at the centre of the band (where thinning is of minimal impact), exhibit bulk-like optoelectronic properties, even down to very small sizes.
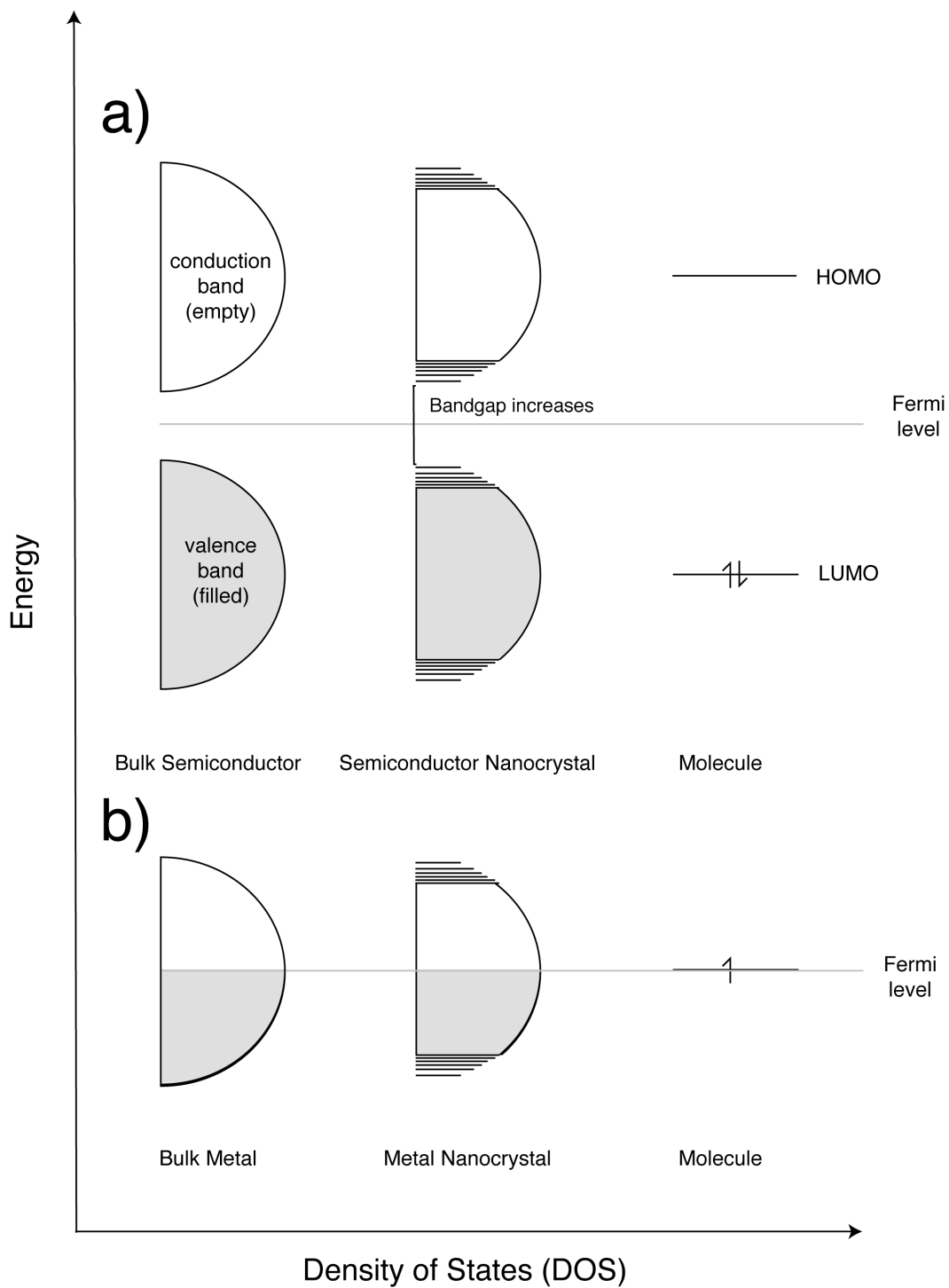
Figure 1-5: Simplified schematic of a Density of States (DOS) versus energy diagram as a function of size in the bulk, nanocrystalline and molecular limit for semiconductors (a) and metals (b). Adapted from reference 28.

1.2.2 Dominant factors contributing towards intense PL from group 14 nanostructures

Having established the basis for key differences between group 14 nanocrystals and other nanomaterials, let us now summarize the dominant factors of quantum confinement suggested to produce the dramatic increase in PL quantum yield efficiency for these materials:

1. *Bandgap widening*: As discussed above, when a reduction in size to the nanoscale leads to an increase in spacing between energy levels near the Fermi level beyond k_bT, semiconductors will undergo bandgap widening, thus leading to a blue shifting in their PL with decreasing size.

2. *Increased exciton binding energy*: When an electron is promoted from the valence band to the conduction band, it leaves behind a vacant state with positive charge, referred to as a hole (analogous to a bubble of air in an otherwise full glass of water).[36] The electron and hole pair, classified as an exciton, are electrostatically attracted to each other (with a characteristic binding energy on the order of meV) but are prevented from immediate recombination through dielectric screening from the surrounding lattice atoms. This balance of forces leads to a characteristic physical separation between the electron and hole, known as the Bohr exciton radius, with typical distances for inorganic semiconductors ranging from 1-50 nm.[37] For bulk Si, excitons have a binding energy of 14 meV and a Bohr exciton radius of *ca.* 5 nm.[35] Within a nanocrystal smaller than the Bohr exciton radius, the electron and hole become spatially confined and so experience

a greater binding energy. This effect scales approximately inversely with nanocrystal diameter.[37] The increased binding energy increases the probability of exciton recombination, leading to a corresponding increase in PL quantum yield. For direct bandgap nanocrystals, this is thought to be the dominant factor in the increased quantum yields.

3. *Relaxation of the indirect selection rule:* As described above, the indirect bandgap of group 14 bulk semiconductors severely lowers their PL quantum yields because radiative recombination requires phonon assistance. Nanoparticles consisting of only a few unit cells might lack the translational symmetry that give rise to the selection rules governing the indirect bandgap. It has been suggested group 14 NCs could exhibit direct bandgap PL (*e.g.*, with a much faster radiative rate). Such an observation would be of enormous technological significance, as group 14 nanostructures could be easily incorporated as the emissive material into existing Si-based microelectronics. Although some research on extremely small Si-NCs (less than *ca.* 1 nm) has suggested the emergence of direct bandgap behaviour,[38] the majority of reports of nanostructured Si PL in the near-IR and visible spectral regions have shown millisecond to microsecond PL lifetimes, characteristic of an indirect bandgap.[39] This suggests that vestiges of translational symmetry persist in nanocrystals down to very small sizes, and the selection rule still holds for radiative recombination.

4. *Removal of nonradiative pathways:* In bulk Si, the long excited state lifetimes arising from the indirect bandgap and relatively low exciton binding energy mean the electron and hole are easily separated and travel macroscopic distances before recombination occurs. As a result, the probability of each charge carrier encountering a nonradiative trap (*e.g.*, defects at grain boundaries or other charge carriers resulting in Auger recombination) is high. Confinement of the exciton within a nanocrystal greatly suppresses these pathways as the volume over which the carriers can move is correspondingly reduced. Therefore, it has been suggested that the dramatic increase in PL quantum yield does not originate from an enhanced exciton binding energy or relaxation of the selection rule, but rather a consequence of the barriers to carrier mobility suppressing nonradiative recombination.[35] Furthermore, the very high number of surface atoms within a nanocrystal and their increased probability over core atoms to contain electronically active defects (*vide infra*) implies that the effective passivation of indirect bandgap group 14 NCs must be a primary goal for the realization of high PL quantum yields.

1.3 Surface chemistry of group 14 materials

The surfaces of nanomaterials necessarily play a fundamental role in the realization of their size-dependent properties. The fraction of surface atoms has been estimated for a spherical nanoparticle (containing *ca.* 100- 10,000 atoms) to increase from less than 10% for a 20 nm particle up to *ca.* 50% for a 3 nm particle.[40] These surface atoms are often highly reactive through coordinative unsaturation.[41] In semiconductor NCs, strained or unsaturated surface atoms can represent electronically active defects which can impede the movement of charge carriers, resulting in a decrease in the radiative quantum yield (through competitive non-radiative pathways) and a red shift of the PL away from the quantum-confined bandgap emission.[42] Thus, effective surface passivation is a foremost consideration for the fundamental study and technological application of their size-dependent optoelectronic properties.

Freestanding nanocrystals requiring colloidal dispersibility must also be stabilized against sedimentation and agglomeration through the formation of attractive intermolecular interactions (*e.g.*, electrostatic or van der Waals forces) with surrounding solvent molecules. Stabilization is frequently accomplished through the use of sterically bulky organic surface ligands to confer solubility in organic solvents. However, the large size of these ligands, which helps colloidally stabilize the particle, also constrains their ability to fully passivate the densely packed surface atoms (*vide infra*). As well, in many envisioned applications of group 14 nanostructures, their surface chemistry must also be amenable toward derivatization to attach further functionalities (*e.g.*, biomolecules for sensing or labeling[43]).

Understanding the arrangement of atoms at the nanoparticle surface is the first step in developing a successful strategy for the realization of freestanding, well-passivated NCs with superior colloidal stability and amenability toward further derivatization. In classic nucleation theory, nanoparticle nucleation and growth are governed by a balance between increasing the nanoparticle volume (thermodynamically favorable) and increasing the nanoparticle surface area (thermodynamically unfavorable).[44] A pseudospherical morphology is often observed because this minimizes the particle surface area (and by extension number of reactive, unsaturated surface atoms). Conversely, when nanoparticle growth occurs under conditions sufficient for crystallization (*e.g.,* high temperatures enhancing atomic mobility for crystalline rearrangement), the resulting nanocrystals form faceted surfaces corresponding to their crystallographic planes with the densest packing of atoms.[45] This also minimizes surface energy by minimizing surface tension.

Figure 1-6 shows a depiction of a diamond-type crystal cleaved along its commonly encountered low-index crystal faces (labeled with their Miller indices). Within the "normal" (111) plane (*i.e.*, assuming no rearrangement of surface atoms has taken place), each surface atom has three σ-bonds to atoms in the second layer, with one bond perpendicular to the surface. The (100) and (110) planes contain surface atoms with two σ-bonds to atoms in the second layer, presenting two bonds away from the surface in tetrahedral geometry.[46]
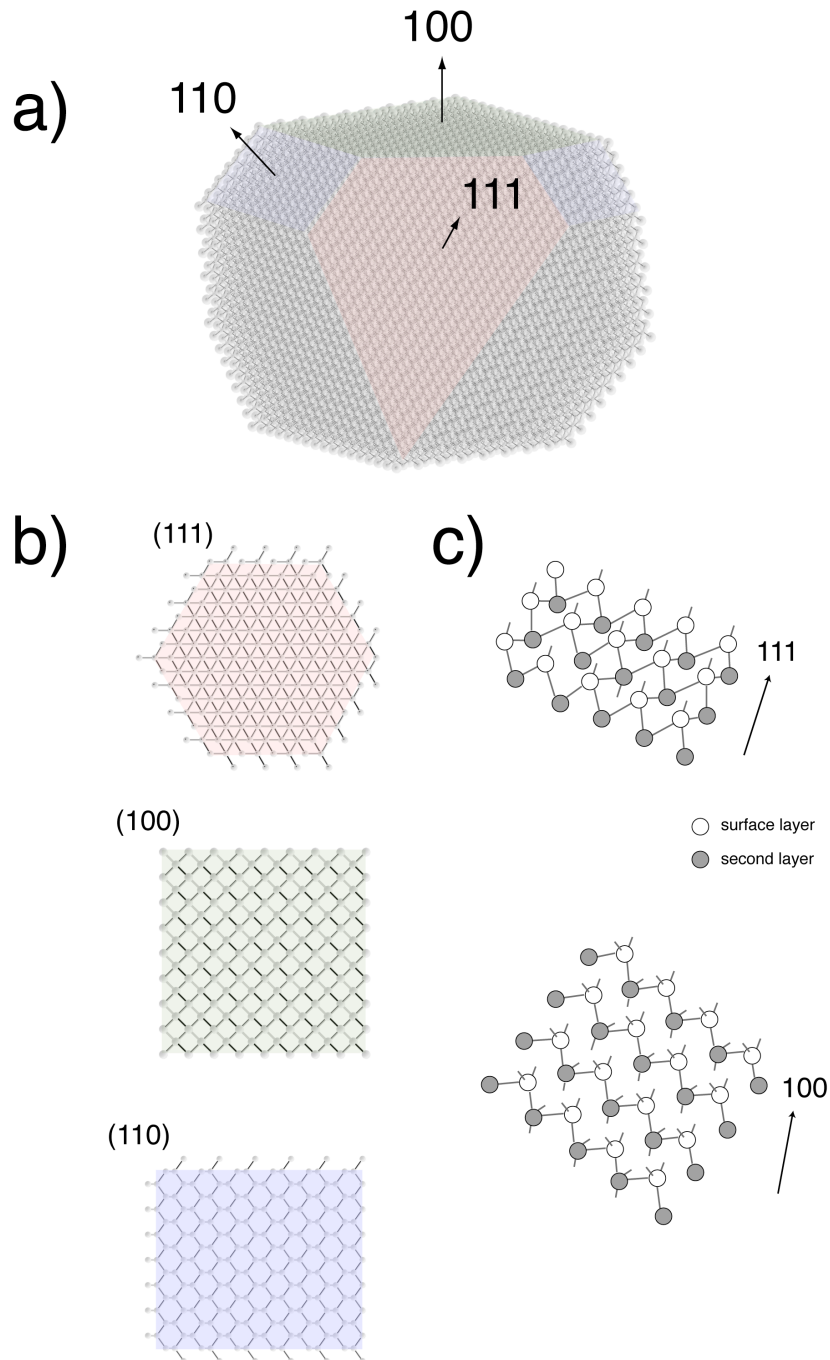
Figure 1-6: a) A Diamond-structured crystal cleaved along the (111) (red), (100) (green) and (110) (blue) planes. b) Top view of each plane. c) Oblique view of the (111) and (100) planes showing their different bonding motifs.

Of the bulk group 14 elements, Si has by far the best understood surface chemistry, owing to its critical importance in the microelectronics industry. Passivation of surface species that might hinder charge carrier mobility (*e.g.*, dangling bonds) is of the utmost importance in the fabrication of high quality integrated circuits, and is frequently carried out *via* etching and oxidation processing to yield an insulating oxide surface layer.[47]

Si oxide species are readily etched in aqueous hydrofluoric acid (HF) solutions to form gaseous and water-soluble silicon fluoride species with overall stoichiometry of:

$$SiO_2 + 6HF_{(aq)} \rightarrow H_2SiF_{6\ (aq)} + 2\ H_2O$$

$$SiO_2 + 4HF_{(aq)} \rightarrow SiF_{4\ (g)} + 2\ H_2O$$
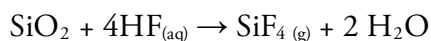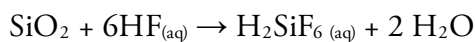
The driving force for this reaction is the formation of very strong Si-F bonds (582 kJ mol^{-1}).[48] However, owing to the high polarity of this bond (*i.e.*, $^{\delta+}$Si-F$^{\delta-}$), Si-F surface species are kinetically very labile, as the formation of one Si-F bond invites further nucleophilic attack from fluoride species, liberating H_2SiF_6 and SiF_4. Therefore, Si surfaces exposed by HF etching of oxides are hydride-terminated. Si (111) surfaces are dominated by monohydride (Si-H) species, whereas dihydride species (Si-H$_2$) are typically encountered for Si (100) and (110) surfaces resulting from their bonding motifs discussed above in Figure 1-6c.

Further etching of the Si surface after oxide removal is generally accomplished through the addition of an oxidizing agent and subsequent facile

removal of the resulting oxide species. For example, the overall reaction for etching with nitric acid (HNO_3) is:

$$Si + HNO_{3\ (aq)} + 6HF_{(aq)} \rightarrow H_2SiF_{6\ (aq)} + HNO_{2\ (aq)} + H_{2\ (g)} + H_2O$$

Oxidation-mediated etching of the Si surface can also occur by hydroxide (OH^-) ions. However, under alkaline conditions, this etching process can be anisotropic, resulting in the preferential formation of (111) facets. As (111) surface atoms have three bonds to other Si atoms that do not polarize the surface atoms towards further nucleophilic attack, these planes are slower to react than other facets (*e.g.*, the (100) plane with two Si-Si bonds). Similarly, etching (111) surfaces using buffered HF solutions produces atomically flat monohydride surfaces with remarkably low defect densities (about 1 electronically active defect per 40,000,000 surface atoms).[49] Conversely, etching (100) surfaces under the same conditions leads to "roughening" of the surface as (111)-like facets are developed, resulting in a complex mixture of hydride species.[50]

Hydride termination is metastable under ambient conditions, oxidizing to give a *ca.* 3 nm thick oxide layer riddled with electronically active defects.[51] It is unsuited for use as a robust passivation method for microelectronic devices. Instead, deliberate thermal growth of a thin layer of amorphous SiO_2 on Si surfaces can provide excellent chemical stability and low defect density, greatly enabling the use of Si over other semiconductors in integrated circuits. Although Ge exhibits favorable electronic properties that attracted much interest during the early years of

semiconductor electronics,[52] the Ge-GeO$_2$ interface is plagued by roughness, high concentration of defects, and chemical instability.[53, 54]

Thermal oxidation of bulk Si surfaces is typically carried out by heating at 700-1200°C in the presence of water vapor or molecular oxygen. This process is limited by the diffusivity of Si through SiO$_2$, and therefore occurs at the Si/SiO$_2$ interface (importantly, away from any impurities at the substrate surface). The amount of Si consumed is about 44% of the final oxide thickness. Through careful control of processing conditions, thermal oxidation achieves the rigorous levels of perfection demanded for transistors and other electronic devices (*i.e.*, less than about 1 defect in 5000 atoms for a 15 nm thick oxide layer).[47]

However, Si oxide passivation has some drawbacks that limit its applicability for certain uses. For example, its insulating nature impedes direct electronic communication between the Si substrate and surface species (*e.g.*, as required for a Si-based photoelectrode for water splitting).[55, 56] Although further derivatization of the oxide interface (as demanded by certain applications of group 14 nanostructures) is achievable through hydrolysis and condensation of chloro- and alkoxysilanes (*i.e.*, RSiCl$_3$ and RSi(OR')$_3$, R and R'= alkyl), the resulting Si-O bonds are susceptible to hydrolysis, especially under basic conditions or elevated temperatures.[43] For luminescent Si nanostructures, oxidation has been correlated with changes to the desired optoelectronic properties, including a significant reduction in PL quantum yield.[57-59] As well, melting point suppression of Si nanostructures limits the processing temperature at which thermal oxidation might be carried out.[60]

Therefore, surface chemists have explored a variety of alternate passivation methods for group 14 surfaces, both bulk and nanostructured.

In particular, exploration of the wide variety of organometallic reactions developed for molecular silane and germane species has proven fruitful.[61] Overall, the key differences between Si surfaces and molecular silanes are thought to be the large steric encumbrance of the lattice-locked atoms, and the availability of delocalized low-energy orbitals which can stabilize reactive intermediates.[62, 63] As will be discussed throughout this thesis, these considerations can substantially influence the reaction pathway and resulting surface coverage, and in some cases lead to the observation of unique reactivity.

Passivation methods centered on the formation of a Si-C surface bond have drawn considerable attention because Si-C bonds are thermodynamically and kinetically stable, (with a bond strength of 369 kJ mol^{-1} and a relatively small difference in electronegativity, 1.9 for Si versus 2.55 for C on the Pauling scale).[64] Hydrosilylation of hydride-terminated surfaces (reacting with the unsaturated bond of an alkene or alkyne) is the best-studied Si-C formation process, drawing from decades of study on molecular substrates.

The first report of hydrosilylation of a bulk Si (111) surface using terminal alkenes by Chidsey *et al.* utilized a diacyl peroxide radical initiator,[65] on the basis of the radical mechanism proposed for hydrosilylation of *tris*(trimethylsilyl)silane by Chatgilialoglu and coworkers.[66] This initial observation sparked much interest in hydrosilylation of Si surfaces, and was quickly followed by reports that demonstrated monolayer formation using a variety of methods to initiate reaction.[61]

Hydrosilylation has also been demonstrated as an effective functionalization method for porous Si,[61] freestanding Si-NCs[67] and Si nanowires.[68] The reaction can be initiated catalytically (*e.g.*, with transition metal complexes widely utilized for reaction of molecular silanes, or using Lewis acids), or spontaneously under photochemical and thermal conditions.[43] These reactions carried out in the absence of any chemical initiators are of particular interest, because they minimize post-reaction processing and purification, and avoid by-products or impurities that might hinder effective passivation. For example, the use of Wilkinson's catalyst (RhCl(PPh)$_3$, a well-known molecular hydrosilylation catalyst) to catalyze hydrosilylation on porous Si surfaces has been observed to lead to PL quenching and deposition of a metallic film,[69] likely through a galvanic displacement process.[70]

Hydrosilylation with ω-substituted olefins (*e.g.*, undecylenic acid) produces well-ordered monolayers, presenting the possibility for further surface derivitization (*e.g.*, coupling the resulting carboxylic acid surface groups to amines through carbodiimide coupling).[43] However, it is worth noting that several functional groups can compete with the unsaturated olefin bond for addition to the Si surface, resulting in disrupted packing and poorer passivation. For instance, aldehydes can also undergo hydrosilylation chemistry, resulting in a Si-OC surface bond.[71, 72]

Reports of Si-C passivation through hydrosilylation have demonstrated the robust nature of the resulting surfaces under a variety of harmful conditions which rapidly degrade hydride-terminated surfaces, including immersion in acidic and basic aqueous solutions, boiling aerated chloroform, concentrated HF solutions and steam

treatment.[61] Conversely, Si-OC tethered species (formed using hydrosilylation with aldehydes) are susceptible towards HF attack.[71]

Other methods to introduce alkyl and aryl surface species through the formation of Si-C bonds include electrochemical grafting of diazonium salts or alkynes, or through derivatization of a reactive halogenated surface.[43] Notably, Lewis' group has investigated Si-C bond formation on bulk Si surfaces through methylation *via* a two-step chlorination/alkylation process.[73] Photoconductivity measurements of these surfaces have demonstrated that the modification procedure introduces extremely few defects, as low as about 1 for every 1,000,000 surface atoms, and is very stable, maintaining this high degree of electronic passivation over months of operation under ambient conditions. This stability is attributed to the high degree of surface coverage afforded by the methylation, as the minimal steric footprint of a methyl group (*i.e.*, a van der Waals radius of 2.5 Å versus 3.8 Å separation between adjacent Si(111) surface atoms) facilitates well-ordered, near-complete monolayer formation. In comparison, estimation of the surface coverage of alkyl monolayers on bulk Si surfaces prepared by hydrosilylation is lower, ranging from *ca.* 30-50% because of the increased steric bulk of the alkyl chains (*i.e.*, ethyl or larger, with a methylene van der Waals radius of 4.5Å). Photoconductivity measurements of a Si(111) surface functionalized with 1-hexene by Lewis acid catalysis estimated the initial number of defects at approximately 1 for every 13,000 surface atoms.[74] However, this value increased to 1 for every 4,300 surface atoms after 24 h of exposure to ambient conditions, consistent with a lower degree of surface coverage because of steric considerations. It is important to note methylation

does not allow any further derivatization of the surface and likely unable to colloidially stabilize freestanding nanostructures against aggregation. Depending on the desired application, the favorable ordered packing of longer alkyl chains within monolayers might provide adequate protection against oxidation to compensate for a lower degree of surface coverage.[75]

Efforts towards the modification of other group 14 surfaces have largely followed the example set for Si. Hydrogermylation on hydride-terminated Ge surfaces has been carried out using Lewis acid catalysis, thermal or photochemical initiation, lending increased stability to the modified Ge surfaces.[76] Interestingly, Ge-H_x species were observed to exhibit increased kinetic lability than the corresponding Si-H_x analogues, stemming from the increased diffuseness of Ge $4sp^3$ bonding orbitals. Reports on the surface modification of Si_xGe_{1-x} systems have remained sparse; the vast majority of reports are on porous or oxide-embedded nanostructures (*vide infra*),[77] and rely on the as-prepared hydride- and oxide-termination. Freestanding Si_xGe_{1-x} NCs have been functionalized through a thermal hydrosilylation/hydrogermylation.[78]

1.4 Preparation of group 14 NCs

When considering the substantial breadth of synthetic approaches reported for group 14 NCs, it is important to take into account their differences in morphology, composition, polydispersity, surface chemistry, *etc.* in evaluating their size-dependent optoelectronic properties, chemical reactivity, or toxicity effects. Although porous Si has played an enormous role in helping establish many fundamental size-dependent properties of nanostructured Si, its use as a synthetic route to luminescent Si-NCs since been largely superseded by other methods offering improvements in polydispersity, scale and the desired optoelectronic properties.

Solution-based colloidal syntheses, extremely effective for scalable production of highly crystalline, near-monodisperse, II-VI, IV-VI and III-V NCs,[79, 80] have been explored for Si- and Ge-NCs, starting with the solvothermal reductions developed by Heath *et al.*[81, 82] Other methods building upon this work have explored other precursors and reducing methods, yielding improvements in yield, size control, shape and surface chemistry.[67] However, reports of group 14 NC solution methods demonstrating PL spanning the visible and near-IR spectral regions have remained relatively rare in the literature.[83-85] This has been attributed to the high crystallization temperatures associated with the directional covalent bonds in these materials.[86, 87]

Gas phase methods hold noteworthy potential, first being investigated with studies of aerosol pyrolysis of disilane by Brus' group.[35, 39, 88] More recently, laser[89] and non-thermal plasma pyrolysis of silane and germane,[90] by the groups of Swihart and Kortshagen have demonstrated large-scale production of size-controlled NCs

with very attractive PL properties, including silicon nanocrystals with ensemble quantum yields of 60%, the highest reported to date.[91]

1.4.1 Oxide-embedded group 14 NCs

Considerable attention has also been given to oxide-embedded group 14 NCs, the family of materials to which the materials studied in the present thesis belong. These have attracted attention in particular for their potential in photonics[25, 92] and non-volatile memory applications.[93, 94] These materials are often prepared through the thermal processing of non-stoichiometric oxides with empirical compositions of MO_x ($0 \leq x \leq 2$) where M is a group 14 element. MO_x precursors are generally prepared by physical methods including ion implantation, evaporation, chemical vapor deposition, molecular beam epitaxy and cosputtering. Oxide-embedded Si-NCs,[95-98] Ge-NCs[99-101] and $Si_{1-x}Ge_x$ alloy NCs[102-106] have been prepared in this manner. Owing to their relative thermodynamic instability, thermal processing causes these intermediate oxides to undergo disproportionation into elemental and fully oxidized species, providing a source for elemental group 14 atoms for NC nucleation and growth. The average diameter of the NCs can be controlled through changes to the composition (x) and processing temperature.[107]

The versatility of this approach for oxide-embedded group 14 NCs can be extended through the use of sol-gel derived polymers with MO_x composition.[108] The sol-gel chemistry of group 14 elements has been extensively studied.[109] At its foundation, it is based on hydrolysis and condensation reactions of $R_nM(OR')_{4-n}$ and R_nMCl_{4-n} species to give polymers with R_xMO_{2-x} stoichiometry (*e.g.*, silicates,

polysiloxanes and silsesquioxanes). Through judicious choice of the reaction conditions, including the pH at which the reactions are performed (*i.e.*, acid- or base-catalysis), the amount of solvent, use of additives such as surfactants, temperature, and drying process, sol-gel chemistry can yield a range of morphologies, including fibers and monoliths, aero- and xerogels, porous materials, thin films or colloidal spherical particles. Through straightforward compositional tailoring, sol-gel polymers with $RMO_{1.5}$ stoichiometry (*e.g.*, $HSiO_{1.5}$) can be prepared, and under analogous thermal processing to the physical methods described above, yield oxide-embedded group 14 NCs with controlled size. SiO_2-embedded Si-NCs, SiC-NCs, Si_xGe-NCs, and GeO_2-embedded Ge-NCs have been prepared in this manner.[108, 110]

For the purposes of this thesis, the thermal processing of hydrogen silsesquioxane (HSQ, structure shown in Figure 1-7) can be used to prepare large quantities (*i.e.*, grams per batch) of Si- and Si_xGe_{1-x}-NCs with promising optoelectronic properties. HSQ, an oligomeric silsesquioxane, has received substantial attention for its use as a spin-on dielectric in the microelectronics industry. Thermal curing of HSQ in an oxidizing atmosphere has been thoroughly investigated, noting collapse of the molecular cage structure, releasing SiH_4, and can be tailored to produce high purity quartz.[111]

As shown in Figure 1-7, heating HSQ at temperatures ranging from 900-1400°C gives broad, diamond-type Si X-ray powder diffraction (XRD) reflections, growing sharper and more intense as the temperature increases.[112] Scherrer analysis of the diffraction peaks in samples processed at 1100-1400°C suggested an increase

in NC size from *ca.* 4 to 14 nm. The oxide composites exhibit PL that red shifts with increasing processing temperature from *ca.* 700 to 925 nm.[113]
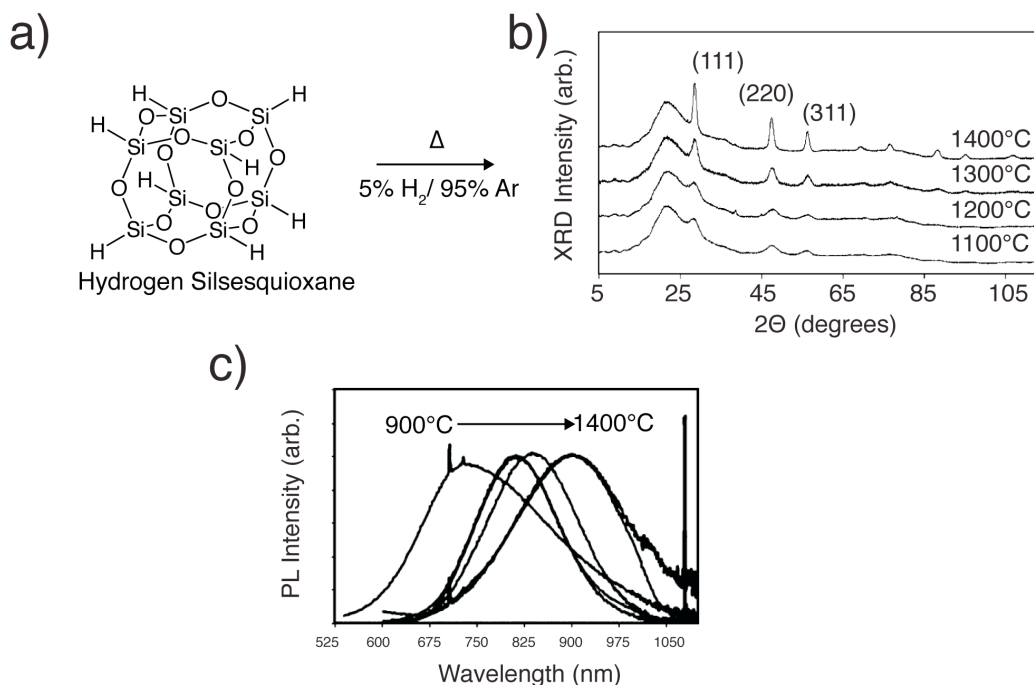
Figure 1-7: a) The cage structure of hydrogen silsesquioxane (HSQ). b) XRD patterns of HSQ processed from 1100-1400°C under 5% H_2/ 95% Ar. The characteristic diamond-type reflections are noted. C) PL spectra of oxide-embedded Si-NCs derived from HSQ processed from 900-1400°C (λ_{ex} = 325 nm). Adapted from reference 110.

1.4.2 Liberation of freestanding group 14 NCs

Much of the work described in this thesis is centered around the properties of freestanding NCs. The scalability of HSQ makes it well-suited for this purpose, as etching of the oxide matrix can be achieved through the use of hydrofluoric acid (HF) etching, yielding hydride-terminated Si-NCs[112] isolated by extraction with a

hydrophobic solvent. As shown in Figure 1-8, these Si-NCs exhibit PL in the visible region of the electromagnetic spectrum, blue shifting from red to green with etching time, consistent with a reduction in NC size influencing the PL through quantum confinement effects described above.
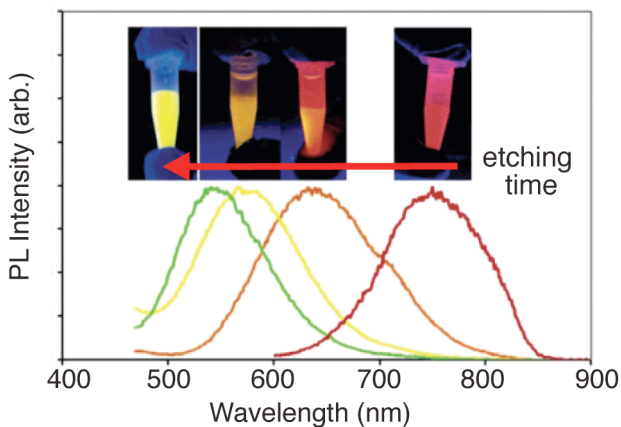
Figure 1-8: PL spectra of freestanding hydride-terminated Si-NCs obtained through HF etching of HSQ-derived oxide composite (λ_{ex} = 325 nm). Adapted from reference 110.

1.4.3 Synthesis of Si$_x$Ge$_{1-x}$-NCs

Compositional modification of group 14 NCs has drawn considerable research interest, mainly toward the formation of Si$_x$Ge$_{1-x}$ alloy NCs. Silicon and germanium form a continuous solid solution throughout the entire compositional range, and thus the alloy bandgap energy may be tuned by changing the Si:Ge ratio (in the bulk, this ranges from 0.66 eV to 1.1 eV).

Unlike the 1:1 ordered composition observed for crystalline SiC, crystalline Si-Ge mixtures adopt a random statistical alloy. This difference can be understood in

terms of a balance between enthalpy and entropy; unlike Si-Ge bonds, bulk Si-C bonds are stronger than the average of bulk Si-Si and C-C bonds.[114] Furthermore, Si and Ge have similar atomic radii, whereas Si and C do not (Table 1-1), and so macroscopic strain that might be induced *via* the formation of Si-Si and Ge-Ge species is minimized. Therefore, although it is enthalpically favorable for crystalline Si to form regular SiC_4 and CSi_4 tetrahedra, entropic considerations favor the formation of a Si_xGe_{1-x} solid state solution.

Preparation of Si_xGe_{1-x} alloy nanostructures has followed closely behind that of Si nanostructures. Reports of porous Si_xGe_{1-x} prepared by anodic etching of thin films (formed at the desired composition by chemical vapor deposition) have shown efficient room temperature PL.[77] Physical methods including evaporation, magnetron co-sputtering and molecular beam epitaxy followed by high temperature annealing have been used in the preparation of thin films of oxide-embedded Si_xGe_{1-x} NCs. Non-thermal plasma pyrolysis of mixtures of silane and germane gases has also received attention in the preparation of freestanding Si_xGe_{1-x} NCs.[78]

1.5 Synchrotron radiation and its use in X-ray absorption spectroscopy (XAS)

When charged particles are accelerated in a circular orbit to relativistic energies (close to the speed of light), they emit electromagnetic radiation at a tangent to their orbit. Because the discovery of this phenomenon was made at a synchrotron (a cyclic accelerator that uses synchronized electric and magnetic fields to accelerate and circulate particles) by researchers at General Electric laboratories in 1947,[115] this is known as synchrotron radiation. Although originally thought to be a nuisance for the purposes of high-energy particle physics, synchrotron radiation has unique properties that make it an ideal light source for many areas of research because of its intrinsic brilliance (photons/second/area) over conventional sources (10^4 to 10^{12} times depending on the desired wavelength), tunable nature (ranging in energy from a few meV to hundreds of thousands of eV), high degree of collimation, coherent polarization, and pulsed structure (arising from the nature of the accelerating electric field).[116] Synchrotron radiation has proven useful for a diverse range of scientific experiments. For instance, it has spurred considerable advances in the field of protein crystallography through significant gains in diffraction intensity, such that virtually all publications rely on synchrotron radiation.[117]

The maximum energy of the emitted radiation depends on the energy of the accelerated particles. For an electron, this can be expressed as

$$\Delta E = 88.5 \frac{E^4}{\rho} \qquad (1\text{-}3)$$

where ΔE is the range of energies in keV, E is the energy of electrons in GeV and ρ is the radius of orbit in m.[116] Modern synchrotrons operate at energies on the order of

2-8 GeV; the Canadian Light Source (CLS) synchrotron operates at 2.9 GeV with a storage ring radius of 27 m, giving an energy range of *ca.* 232 keV.

1.5.1 X-ray absorption spectroscopy (XAS)

X-ray absorption spectroscopy (XAS) greatly benefits from the use of synchrotron radiation and its history closely follows the development of modern synchrotron facilities to today, where it is a versatile and powerful tool for characterizing the local and extended chemical environment in a wide variety of samples. XAS encompasses several related techniques, namely near-edge X-ray absorption fine structure (NEXAFS, also referred to as X-ray absorption near-edge spectroscopy, XANES, depending on the X-ray energies examined) and extended X-ray absorption fine structure (EXAFS).[118] The versatility of XAS lies in its elemental selectivity, high sensitivity through the use of synchrotron radiation, and wide tolerance of samples (*e.g.*, amorphous solids, gases and solutions).

During the XAS experiment, X-rays are tuned in energy to the threshold of exciting a core electron for a particular element into a unoccupied (bonding) or continuum state. X-ray absorption can be recorded either through measuring the transmission of X-rays through the sample (analogous to UV-vis spectroscopy, following the Beer-Lambert law), or by the various relaxation pathways available to the excited atom (*e.g.*, X-ray fluorescence, visible luminescence or Auger, secondary or photo-electron emission), as a function of incident X-ray energy.[118] The excitation follows dipole selection rules, *i.e.*, $\Delta l = \pm 1$ (*e.g.*, Si 2p $\rightarrow$ Si 3s and 3d).

NEXAFS/XANES experiments study X-ray energies close to the absorption threshold (*i.e.*, transitions from core states to bonding orbitals just above the Fermi level). The energy of these transitions are sensitive to the absorbing atom's oxidation state, coordination environment as well as the local partial density of unoccupied states (LPDOS). The sharp increase in absorption cross-section at the threshold is called an "edge". As the incident X-ray energy increases (past the region typically studied in NEXAFS into EXAFS territory), core electrons are ejected from the atom as photoelectrons. These photoelectrons can undergo backscattering from neighboring atoms. The wave-like interaction of outgoing and backscattered photoelectrons produces a pattern of constructive and destructive interference characteristic of the local environment (*e.g.*, interatomic distances, coordination number and next nearest neighbor). The XAS experiment is depicted schematically in Figure 1-9.
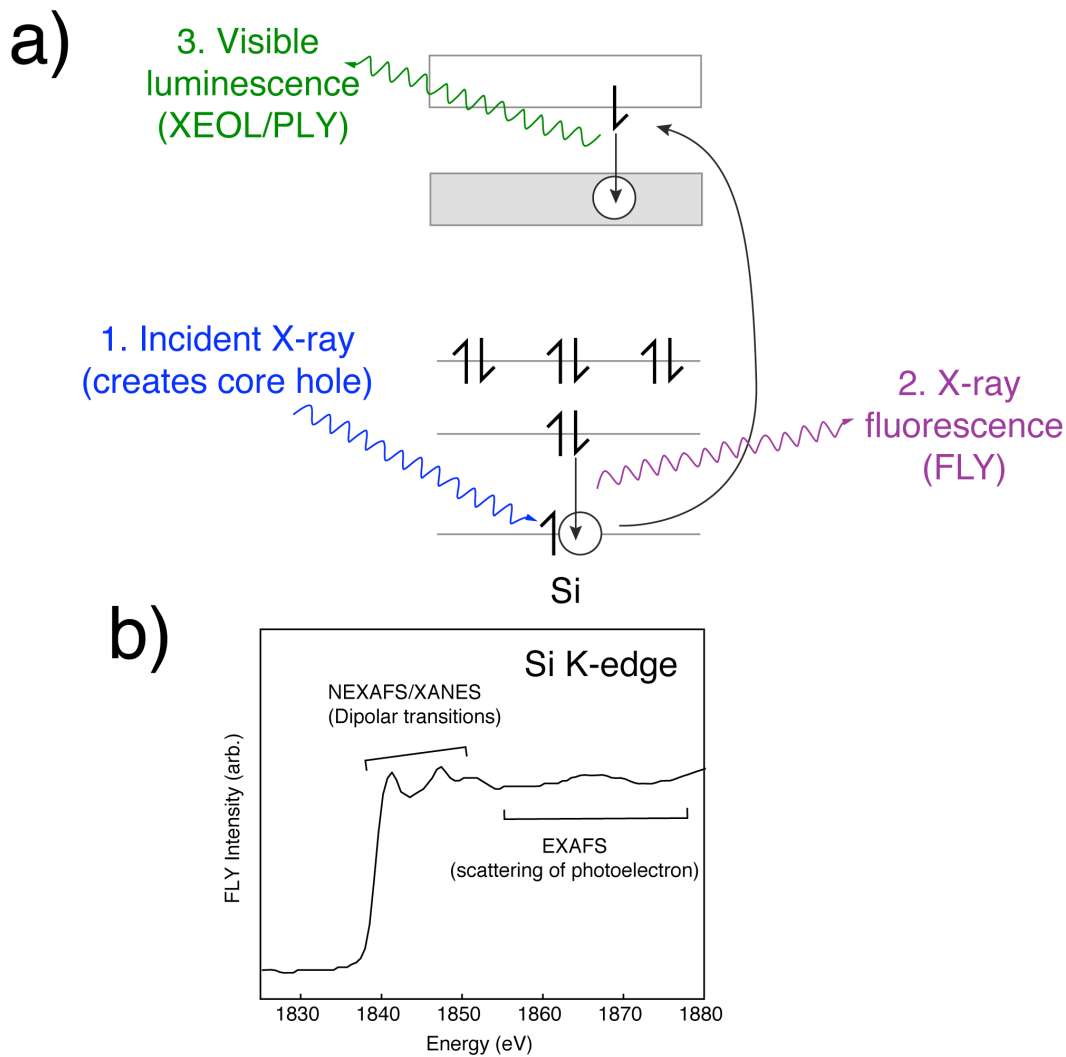
Figure 1-9: a) Depiction of the XAS experiment: Excitation by an incident X-ray (step 1, blue trace) creates a core hole, rapidly filled by electrons from outer shells, relaxing via X-ray fluorescence (FLY, step 2, purple trace) or Auger electron emission (not pictured). Relaxation eventually leads to the formation of a valence hole, which can stimulate visible luminescence (XEOL/PLY, step 3, green trace). b) Resulting FLY XAS spectra, illustrating the NEXAFS/XANES and EXAFS regions.

The absorption edge for a given element's core shell can range in energy from soft ($\sim <2$ keV) to hard ($\sim >2$ keV) X-rays, increasing with atomic number Z and decreasing with principal quantum number n. Because soft X-rays are strongly attenuated in air, the XAS experiments performed in this thesis were carried out under vacuum. As well, although hard X-ray XAS is typically recorded using straightforward transmittance measurements, soft X-ray fluorescence yield (FLY) and total electron yield (TEY) detectors are employed to overcome the limited penetration depth of soft X-rays. These detection methods also impart surface sensitivity to XAS because the escape depth of electron is very shallow, increasing as a function of energy (as low as a few nm for Auger electron emission under 100 eV excitation).

1.5.2 X-ray excited optical luminescence (XEOL)

XAS is also a valuable characterization technique for the study of luminescent materials. X-ray excitation in these samples will cause emission as the excited state core hole will rapidly relax through X-ray fluorescence and electron emission processes until it recombines with the excited electron at a transition in the visible region of the electromagnetic spectrum. By integrating the intensity of visible luminescence as a function of X-ray incident energy, the oxidation state and coordination number of the emissive species can be determined. This experiment is referred to as X-ray excited optical luminescence (XEOL), or PL yield (PLY). This experiment is analogous to acquiring an excitation spectrum in fluorescence spectroscopy, with the added benefit of chemical specificity owing to the use of X-

rays rather than visible photons as an excitation source. Visible photons have a greater escape depth than X-rays or electrons, and therefore XEOL is considered a bulk-sensitive technique.

The utility of XEOL in characterizing nanostructured Si was first demonstrated by Sham's group in the study of porous Si.[119] As mentioned above, after Canham reported visible luminescence from porous Si, several competing theories on the origin of luminescence quickly arose. In particular, it was proposed the observed PL might arise from siloxene, a molecular species ($Si_6O_3H_6$) that might form during anodization. By comparing the TEY and PLY spectra of porous Si with crystalline Si and siloxene, it was conclusively demonstrated the origin of porous Si luminescence was different from that of siloxene.

There are several caveats in interpreting XAS and XEOL spectra. First, as soft X-rays are strongly attenuated, FLY detection can be hampered by reabsorption of the fluorescent X-rays, limiting quantitative interpretation. Self-absorption can sometimes be avoided through preparation of a "thin" sample (with thickness less than 3 times the X-ray attenuation length), although for soft X-rays this is usually impractical.[118] Conversely, TEY detection (measured through the current needed to maintain a neutral sample) is often unsuitable for study of insulating materials because of charging effects but is less susceptible to self-absorption. Ongoing development in XAS detection through the use of inverted partial fluorescence yield (IPFY) may hold promise to avoid these issues.[120]

For PLY detection, relaxation of the excited core hole occurs on a much faster timescale than luminescence, during which the excited state can migrate from

the absorbing species to any luminescent species, potentially resulting in a loss of site-specificity.[121] As well, PLY spectra can sometimes be distorted through "edge-inversion" effects, arising through competition for X-ray absorption between luminescent and non-luminescent species, where an increase in absorption cross-section of the non-luminescent species decreases the effective absorption cross-section from the luminescent species, resulting in a decrease in PLY intensity unrelated to chemical environment.

1.6 Thesis Outline

This thesis investigates the optoelectronic properties of Si and Si_xGe_{1-x} NCs derived from the thermal processing of HSQ. In many anticipated applications of group 14 NCs, the surface chemistry of these materials must be tailored for colloidal dispersibility in different solvents (*e.g.*, aqueous media for biological sensing applications), as well as effective electronic passivation, particularly with regards to resilience against oxidation (leading to a significant shift and/or loss of quantum confined properties). Throughout the thesis, the use of hydrosilylation to accomplish these goals will be critically evaluated in light of both the wide range of applications currently being studied for these materials and their fundamental properties.

Chapter 2 presents the use of near-UV light to initiate hydrosilylation of Si-NCs exhibiting size-dependent PL in the visible spectral region using a range of alkenes and alkynes. The near-UV light used to initiate hydrosilylation corresponds to a region of direct-gap light absorption by Si-NCs, and so effectively stimulates exciton formation. This increased absorption coefficient may be a useful consideration in light of the exciton-mediated mechanism proposed for this process. The Si-NC PL was monitored *in situ* in order to better understand the impact of the changing surface chemistry during the reaction.

In Chapter 3, the use of near-UV hydrosilylation to functionalize larger Si-NCs with PL in the near-IR is evaluated in comparison to thermal initiation. Larger Si-NCs reacted at a slower rate under near-UV conditions using PL and small-angle X-ray scattering, consistent with an exciton-mediated process instead of a radical homolysis based mechanism. A mixture of Si-NC sizes could be partially separated

based on their reactivity towards near-UV hydrosilylation. Interestingly, the size-dependent reactivity was observed in reaction with phenylacetylene, an alkyne previously thought incompatible with the exciton-mediated mechanism proposed for Si-NCs.

Chapter 4 describes an investigation into the HF etching of HSQ-derived oxide-embedded Si-NC composites. By adjusting the pH and HF concentration, the rate of oxide etching could be dramatically enhanced, facilitating the liberation of larger Si-NCs. As well, the etching of Si-NCs under low pH proceeded through an exciton-mediated process rather than an oxidize/etch pathway often used to control the size of Si-NCs. The use of this exciton-mediated process to narrow the Si-NC polydipersity was evaluated using PL and small-angle X-ray scattering. Non-radiative defects were demonstrated to slow the etching of non-luminescent Si-NCs; this could be partially overcome through a two-step etching process.

Chapter 5 presents an XAS study into the origin of PL from Si-NCs functionalized using near-UV hydrosilylation. The emission process was shown to be consistent with quantum confinement effects using XEOL spectroscopy. A discussion on the role of surface species affecting the XEOL results is presented.

In Chapter 6, the use of HSQ along with trialkylphosphine GeI_2 complexes as a precursor system for the formation of Si_xGe_{1-x} NCs is presented. The liberation of freestanding NCs through HF etching allowed their characterization by high-resolution electron microscopy, demonstrating the presence of homogeneously alloyed, Ge-rich Si_xGe_{1-x} NCs alongside a Si-rich population. These alloyed materials exhibited near-IR PL, red shifted from HSQ-prepared samples processed at the same

temperature. Qualitative evidence for the participation of Ge in the emission process was shown. As well, these materials were characterized using Si K- and Ge $L_{3,2}$-edge XAS, showing the trialkylphosphine used to solubilize GeI_2 significantly influences NC growth. XEOL characterization proved inconclusive, likely resulting from self-absorption effects arising out of the heterogeneous nature of these materials.

Finally, a brief discussion outlining important implications from each investigation will be presented, including an outlook on future research directions and possible applications.

1.7 References

1. Rao, C. N. R.; Müller, A.; Cheetham, A. K., Eds.; *Nanomaterials Chemistry: Recent Developments and New Directions;* Wiley-VCH: Weinheim, 2007; pp 403.

2. Cademartiri, L.; Ozin, G. A. *Concepts of Nanochemistry;* Wiley-VCH: Weinheim, **2009**; pp 261.

3. Wallace, P. R. *Phys. Rev.* **1947**, *71*, 622-634.

4. Geim, A. K.; Novoselov, K. S. *Nat. Mater.* **2007**, *6*, 183-191.

5. Geim, A. K. *Science* **2009**, *324*, 1530-1534.

6. The Nobel Prize in Physics 2010; Nobel Foundation, http://nobelprize.org/nobel_prizes/physics/laureates/2010/ (accessed May 22, 2011).

7. Klimov, V. I.; Mikhailovsky, A. A.; Xu, S.; Malko, A.; Hollingsworth, J. A.; Leatherdale, C. A.; Eisler, H. -J.; Bawendi, M. G. *Science* **2000**, *29*0, 314-317.

8. Lee, J.; Sundar, V. C.; Heine, J. R.; Bawendi, M. G.; Jensen, K. F. *Adv. Mater.* **200**0, *12*, 1102-1105.

9. Michalet, X.; Pinaud, F. F.; Bentolila, L. A.; Tsay, J. M.; Doose, S.; Li, J. J.; Sundaresan, G.; Wu, A. M.; Gambhir, S. S.; Weiss, S. *Science* **2005**, *30*7, 538-544.

10. Bruchez Jr., M.; Moronne, M.; Gin, P.; Weiss, S.; Alivisatos, A. P. *Science* **1998**, *28*1, 2013-2016.

11. Greenham, N. C.; Peng, X.; Alivisatos, A. P. *Phys. Rev. B- Condens. Matter* **1996**, *54*, 17628-17637.

12. Nozik, A. J. *Physica E* **2002**, *1*4, 115-120.

13. Rossetti, R.; Nakahara, S.; Brus, L. E. *J. Chem. Phys.* **1983**, *7*9, 1086-1088.

14. "2005 ACS National Award Winners" *Chem. Eng. News* **2005**, *83*, 39.

15. Bawendi, M. G.; Steigerwald, M. L.; Brus, L. E. *Annu. Rev. Phys. Chem.* **1990**, *4*1, 477-496.

16. The Project on Emerging Nanotechnologies- Consumer Products. http://www.nanotechproject.org/inventories/consumer/ (accessed May 22, 2011).

17. Woskie, S. *Wiley Interdisciplinary Reviews: Nanomedicine and Nanobiotechnology* **2010**, 2, 685-692.

18. Oliver, J. "Quantum Dots: Technologies and Global Markets." http://www.reportlinker.com/p0461667/Quantum-Dots-Technologies-and-Global-Markets.html (accessed May 22, 2011).

19. Soo Choi, H.; Liu, W.; Misra, P.; Tanaka, E.; Zimmer, J. P.; Itty Ipe, B.; Bawendi, M. G.; Frangioni, J. V. *Nat. Biotechnol.* **2007**, *25*, 1165-1170.

20. Lewinski, N.; Colvin, V.; Drezek, R. *Small* **2008**, 4, 26-49.

21. Restriction of Hazardous Substances Directive. http://www.rohs.eu (accessed May 22, 2011).

22. California Department of Toxic Substances Control- Restrictions on the use of Certain Hazardous Substances in General Purpose Lights. http://www.dtsc.ca.gov/HazardousWaste/UniversalWaste/RoHs_Lighting.cfm (accessed May 22, 2011).

23. Canham, L. T. *Appl. Phys. Lett.* **1990**, *57*, 1046-1048.

24. Cullis, A. G.; Canham, L. T.; Calcott, P. D. J. *J. Appl. Phys.* **1997**, *82*, 909-965.

25. Lockwood, D. J.; Pavesi, L. *Top. Appl. Phys.* **2004**, *94*, 1-50.

26. Fan, J.; Chu, P. K. *Small* **2010**, 6, 2080-2098.

27. Popplewell, J. F.; King, S. J.; Day, J. P.; Ackrill, P.; Fifield, L. K.; Cresswell, R. G.; di Tada, M. L.; Liu, K. *J. Inorg. Biochem.* **1998**, *69*, 177-180.

28. Alivisatos, A. P. *J. Phys. Chem.* **1996**, *100*, 13226-13239.

29. Power, P.P. *Chem. Commun.* **2003**, 2091-2101..

30. Ellis, A. B. *Teaching general chemistry: a materials science companion;* American Chemical Society: Washington, DC, 1993; pp 554.

31. Grahn, H. T. *Introduction to Semiconductor Physics;* World Scientific: Singapore, 1999; pp 183.

32. Silberberg, M. S. *Chemistry: the molecular nature of matter and change;* McGraw-Hill: Boston, 2009.

33. Hoffmann, R. *Angew. Chem. Int. Ed Engl.* **1987**, *26*, 846-878.

34. Tsybeskov, L. *MRS Bull.* **1998**, *23*, 33-38.

35. Brus, L. E.; Szajowski, P. F.; Wilson, W. L.; Harris, T. D.; Schuppler, S.; Citrin, P. H. *J. Am. Chem. Soc.* **1995**, *117*, 2915-2922.

36. Weller, P. F. *J. Chem. Educ.* **1967**, *44*, 391-393.

37. Scholes, G. D. *ACS Nano* **2008**, 2, 523-537.

38. Kholod, A. N.; Borisenko, V. E.; Saúl, A.; Arnaud d'Avitaya, F.; Fuhr, *Opt. Mater.* **2001**, *17*, 61-63.

39. Wilson, W. L.; Szajowski, P. F.; Brus, L. E. *Science* **1993**, *262*, 1242-1244.

40. Klabunde, K. J.; Stark, J.; Koper, O.; Mohs, C.; Park, D. G.; Decker, S.; Jiang, Y.; Lagadic, I.; Zhang, D. *J. Phys. Chem.* **1996**, *100*, 12142-12153.

41. Katari, J. E. B.; Colvin, V. L.; Alivisatos, A. P. *J. Phys. Chem.* **1994**, *98*, 4109-4117.

42. Koch, F.; Petrova-Koch, V.; Muschik, T. *J. Lumin.* **1993**, *57*, 271-281.

43. Ciampi, S.; Harper, J. B.; Gooding, J. J. *Chem. Soc. Rev.* **2010**, *39*, 2158-2183.

44. Ring, T. A. *Adv. Colloid Interface Sci.* **2001**, *91*, 473-499.

45. Zangwill, A. *Physics at Surfaces;* Cambridge University Press: New York, 1988; pp 454.

46. Haneman, D. *Physical Review* **1961**, *121*, 1093-1100.

47. Campbell, S. A. *The science and engineering of microelectronic fabrication;* Oxford series in electrical and computer engineering; Oxford University Press: New York, 2001; pp 603.

48. Spierings, G. A. C. M. *J. Mater. Sci.* **1993**, *28*, 6261-6273.

49. Yablonovitch, E.; Allara, D. L.; Chang, C. C.; Gmitter, T.; Bright, T. B. *Phys. Rev. Lett.* **1986**, *57*, 249-252.

50. Higashi, G. S.; Chabal, Y. J.; Trucks, G. W.; Raghavachari, K. *Appl. Phys. Lett.* **1990**, *56*, 656-658.

51. Gstrein, F.; Michalak, D. J.; Royea, W. J.; Lewis, N. S. *J. Phys. Chem. B* **2002**, *106*, 2950-2961.

52. Teal, G. K. *IEEE Trans. Electron Devices* **1976**, *ED-23*, 621-639.

53. Tsetseris, L.; Pantelides, S. T. *Microelectronic Engineering* **2011**, *88*, 395-398.

54. Loscutoff, P. W.; Bent, S. F. *Annu. Rev. Phys. Chem.* **2006**, *57*, 467-495.

55. Bansal, A.; Lewis, N. S. *J Phys Chem B* **1998**, *102*, 4058-4060.

56. Gstrein, F.; Michalak, D.J.; Royea, W.J.; Lewis, N.S. *J. Phys. Chem. B* **2002**, *106*, 2950-2961.

57. Ledoux, G.; Guillois, O.; Porterat, D.; Reynaud, C.; Huisken, F.; Kohn, B.; Paillard, V. *Phys. Rev. B Condens. Matter* **2000**, *62*, 15942-15951.

58. Pi, X. D.; Mangolini, L.; Campbell, S. A.; Kortshagen, U *Phys. Rev. B Condens. Matter* **2007**, *75*, 085423.

59. Pereira, R. N.; Rowe, D. J.; Anthony, R. J.; Kortshagen, U. *Phys. Rev. B* **2011**, *83*, 155327.

60. Chao, Y.; Šiller, L.; Krishnamurthy, S.; Coxon, P. R.; Bangert, U.; Gass, M.; Kjeldgaard, L.; Patole, S. N.; Lie, L. H.; O'Farrell, N.; Alsop, T. A.; Houlton, A.; Horrocks, B. R. *Nat. Nanotechnol.* **2007**, 2, 486-489.

61. Buriak, J. M. *Chem. Rev.* **2002**, *102*, 1271-1308.

62. Sailor, M. J.; Lee, E. J. *Adv. Mater.* **1997**, 9, 783-793.

63. Wang, D.; Buriak, J. M. *Langmuir* **2006**, *22*, 6214-6221.

64. Brook, M. A. *Silicon in Organic, Organometallic, and Polymer Chemistry*; John Wiley: New York, 2000, pp 680.

65. Linford, M. R.; Chidsey, C. E. D. *J. Am. Chem. Soc.* **1993**, *115*, 12631-12632.

66. Chatgilialoglu, C.; Timokhin, V. I. *Adv. Organomet. Chem.* **2008**, *57*, 117-181.

67. Veinot, J. G. C. *Chem. Commun.* **2006**, , 4160-4168.

68. Zhang, G. -J.; Chua, J. H.; Chee, R. -E.; Agarwal, A.; Wong, S. M.; Buddharaju, K. D.; Balasubramanian, N. *Biosens. Bioelectron.* **2008**, *23*, 1701-1707.

69. Marciniec, B.; Gulinski, J. *J. Organomet. Chem.* **1993**, *446*, 15-23.

70. Aizawa, M.; Buriak, J. M. *Chem. Mater.* **2007**, *19*, 5090-5101.

71. Boukherroub, R.; Morin, S.; Sharpe, P.; Wayner, D. D. M. *Langmuir* **2000**, *16*, 7429-7434.

72. Effenberger, F.; Götz, G.; Bidlingmaier, B.; Wezstein, M *Angew. Chem. Int. Ed Engl.* **1998**, *37*, 2462-2464.

73. Lewis, N. S. *Inorg. Chem.* **2005**, *44*, 6900-6911.

74. Webb, L. J.; Lewis, N. S. *J. Phys. Chem. B* **2003**, *107*, 5404-5412.

75. Sieval, A. B.; Vleeming, V.; Zuilhof, H.; Sudhölter, E. J. R. *Langmuir* **1999**, *15*, 8288-8291.

76. Choi, K.; Buriak, J. M. *Langmuir* **2000**, *16*, 7737-7741.

77. Cullis, A. G.; Canham, L. T.; Calcott, P. D. J. *J. Appl. Phys.* **1997**, *82*, 909-965.

78. Pi, X. D.; Kortshagen, U. *Nanotechnology* **2009**, *20*.

79. Yin, Y.; Alivisatos, A. P. *Nature* **2005**, *437*, 664-670.

80. Cademartiri, L.; Ozin, G. A. *Philos. Trans. R. Soc. London, Ser. A* **2010**, *368*, 4229-4248.

81. Heath, J. R.; Shiang, J. J.; Alivisatos, A. P. *J. Chem. Phys.* **1994**, *101*, 1607-1615.

82. Heath, J. R. *Science* **1992**, *258*, 1131.

83. Ruddy, D. A.; Johnson, J. C.; Smith, E. R.; Neale, N. R. *ACS Nano* **2010**, 4, 7459-7466.

84. Codoluto, S. C.; Baumgardner, W. J.; Hanrath, T. *Cryst. Eng. Comm.* **2010**, *12*, 2903-2909.

85. Lee, D. C.; Pietryga, J. M.; Robel, I.; Werder, D. J.; Schaller, R. D.; Klimov, V. I. *J. Am. Chem. Soc.* **2009**, *131*, 3436-3437.

86. Gerion, D.; Zaitseva, N.; Saw, C.; Casula, M. F.; Fakra, S.; Van Buuren, T.; Galli, G. *Nano Lett.* **2004**, 4, 597-602.

87. Buhro, W. E.; Hickman, K. M.; Trentler, T. J. *Adv. Mater.* **1996**, 8, 685-688.

88. Littau, K. A.; Szajowski, P. J.; Muller, A. J.; Kortan, A. R.; Brus, L. E. *J. Phys. Chem.* **1993**, *97*, 1224-1230.

89. Li, X.; He, Y.; Talukdar, S. S.; Swihart, M. T. *Langmuir* **2003**, *19*, 8490-8496.

90. Kortshagen, U.; Anthony, R.; Gresback, R.; Holman, Z.; Ligman, R.; Liu, C. -Y.; Mangolini, L.; Campbell, S. A. *Pure Appl. Chem.* **2008**, *80*, 1901-1908.

91. Jurbergs, D.; Rogojina, E.; Mangolini, L.; Kortshagen, U. *Appl. Phys. Lett.* **2006**, *88*.

92. Pavesi, L. *Proc. SPIE Int. Soc. Opt. Eng.* **2003**, *4997*, 206-220.

93. Tiwari, S.; Rana, F.; Hanafi, H.; Hartstein, A.; Crabbé, E. F.; Chan, K. *Appl. Phys. Lett.* **1996**, *68*, 1377-1379.

94. Lombardo, S.; Corso, D.; Crupi, I.; Gerardi, C.; Ammendola, G.; Melanotte, M.; De Salvo, B.; Perniola, L. *Microelectron. Eng.* **2004**, *72*, 411-414.

95. Meldrum, A.; Hryciw, A.; MacDonald, A. N.; Blois, C.; Marsh, K.; Wang, J.; Li, Q. *J. Vac. Sci. Technol., A* **2006**, *24*, 713-717.

96. Kahler, U.; Hofmeister, H. *Opt. Mater.* **2001**, *17*, 83-86.

97. Meldrum, A.; Haglund Jr., R. F.; Boatner, L. A.; White, C. W. *Adv. Mater.* **2001**, *13*, 1431-1444.

98. Shimizu-Iwayama, T.; Ohshima, M.; Niimi, T.; Nakao, S.; Saitoh, K.; Fujita, T.; Itoh, N. *J. Phys. Condens. Matter* **1993**, 5, L375-L380.

99. Gorokhov, E. B.; Volodin, V. A.; Marin, D. V.; Orekhov, D. A.; Cherkov, A. G.; Gutakovskiĭ, A. K.; Shvets, V. A.; Borisov, A. G.; Efremov, M. D. *Semiconductors* **2005**, *39*, 1168-1175.

100. Sharp, I. D.; Xu, Q.; Liao, C. Y.; Yi, D. O.; Beeman, J. W.; Liliental-Weber, Z.; Yu, K. M.; Zakharov, D. N.; Ager III, J. W.; Chrzan, D. C.; Haller, E. E. *J. Appl. Phys.* **2005**, *97*, 1-4.

101. Takeoka, S.; Fujii, M.; Hayashi, S.; Yamamoto, K. *Phys. Rev. B Condens. Matter* **1998**, *58*, 7921-7925.

102. Takeoka, S.; Toshikiyo, K.; Fujii, M.; Hayashi, S.; Yamamoto, K. *Phys. Rev. B Condens. Matter* **2000**, *61*, 15988-15992.

103. Yang, Y. M.; Wu, X. L.; Siu, G. G.; Huang, G. S.; Shen, J. C.; Hu, D. S. *J. Appl. Phys.* **2004**, *96*, 5239-5242.

104. Palfinger, G.; Bitnar, B.; Sigg, H.; Müller, E.; Stutz, S.; Grützmacher, D. *Physica E* **2003**, *16*, 481-488.

105. Tang, Y. S.; Cai, S.; Jin, G.; Duan, J.; Wang, K. L.; Soyez, H. M.; Dunn, B. S. *Appl. Phys. Lett.* **1997**, *71*, 2448-2450.

106. Hwang, C. -W.; Ryu, M. -K.; Kim, K. -B.; Lee, S. -C.; Kim, C. -S. *J. Appl. Phys.* **1995**, *77*, 3042-3047.

107. Wang, J.; Wang, X. F.; Li, Q.; Hryciw, A.; Meldrum, A. *Philos. Mag.*. **2007**, *87*, 11-27.

108. Henderson, E. J. Ph.D. thesis. Group 14 Semiconductor Nanocrystals, University of Alberta, Canada, 2009.

109. Schubert, U.; Hüsing, N. *Synthesis of Inorganic Materials;* Wiley-VCH.: Weinheim, 2005.

110. Kelly, J. A.; Henderson, E. J.; Veinot, J. G. C. *Chem. Commun.* **2010**, *46*, 8704-8718.

111. Albrecht, M. G.; Blanchette, C. *J. Electrochem. Soc.* **1998**, *145*, 4019-4025.

112. Hessel, C. M.; Henderson, E. J.; Veinot, J. G. C. *Chem. Mater.* **2006**, *18*, 6139-6146.

113. Hessel, C. M.; Summers, M. A.; Meldrum, A.; Malac, M.; Veinot, J. G. C. *Adv. Mater.* **2007**, *19*, 3513-3516.

114. Mélinon, P.; Masenelli, B.; Tournus, F.; Perez, A. *Nat. Mater.* **2007**, *6*, 479-490.

115. Elder, F. R.; Gurewitsch, A. M.; Langmuir, R. V.; Pollock, H. C. *Phys. Rev.* **1947**, *71*, 829-830.

116. Sham, T. K.; Rivers, M. L. *Rev. Mineral. Geochem.* **2002**, *49*.

117. Hendrickson, W. A. *Trends Biochem. Sci.* **2000**, *25*, 637-643.

118. Sham, T. K.; Coulthard, I.; Naftel, S. J. *Multicore, multichannel detection (MCMD) X-ray absorption fine structure studies of thin films;* Sham, T. K., Ed.; Chemical Applications of Synchrotron Radiation, Part II: X-ray Applications; World Scientific: Singapore, 2002; Vol. 1, pp 1154-1212.

119. Sham, T. K.; Jiang, D. T.; Coulthard, I.; Lorimer, J. W.; Feng, X. H.; Tan, K. H.; Frigo, S. P.; Rosenberg, R. A.; Houghton, D. C.; Bryskiewicz, B. *Nature* **1993**, *363*, 331-334.

120. Achkar, A. J.; Regier, T. Z.; Wadati, H.; Kim, Y. -J.; Zhang, H.; Hawthorn, D. G. *Phys. Rev. B* **2011**, *83*, 081106.

121. Rogalev, A.; Goulon, J. *X-ray Excited Optical Luminescence Spectroscopies;* Chemical Applications of Synchrotron Radiations Part II; World Scientific: Singapore, 2002; Vol. 2, pp 707-760.

Chapter 2:

Near-UV Hydrosilylation

of Silicon Nanocrystals[*]

2.1 Introduction

Nanostructured silicon exhibits fascinating size-dependent electronic and optical properties. Efficient photoluminescence (PL) in the visible and near-IR spectral regions has generated tremendous interest in the synthesis and characterization of these materials for a range of applications.[1-3] In particular, concerns regarding the cytotoxicity of compound semiconductor NCs (*e.g.*, CdSe, GaAs) for *in vivo* fluorescent labeling and sensing [4, 5] may be addressed through the use of freestanding silicon nanocrystals (Si-NCs). Although toxicity studies have indicated that several factors beyond the NC core can contribute significantly to cytotoxic effects (*e.g.*, surface charge[6] or hydrodynamic radius[4]), several studies have suggested that nanostructured Si can be biologically compatible.[1, 7-11]

Hessel *et al.* have developed a synthetic method for Si-NCs embedded in SiO_2, from the thermal processing of hydrogen silsesquioxane (HSQ) under reducing atmosphere.[12, 13] This synthesis is scalable to multigram quantities of composite material with relatively narrow size distribution and a well-defined oxide interface. These Si-NCs exhibit size-dependent PL shifts consistent with quantum confinement effects, with emission maxima spanning the visible and near-IR spectral region. The origin of luminescence in these materials was recently studied using X-ray excited optical luminescence (XEOL), showing evidence for quantum confinement effects influencing the PL.[14]

A key step in the development of applications utilizing freestanding Si-NC is tailoring of surface groups to render the NCs dispersible in the desired medium and to protect the surface against oxidation. This goal is commonly achieved through

realization of a chemically active surface (*e.g.*, Si-Br, Si-Cl, Si-OH, Si-H) that allows for further modification.[15] These chemically active nanostructured Si surfaces rapidly oxidize under ambient conditions, resulting in undesirable changes to their solution dispersibility and the PL properties. Oxidation under ambient conditions impacts the desired electronic and optical properties of Si-NCs, even at low levels. For example, Wolkin and coworkers proposed that the formation of a silanone (Si=O) surface defect on an otherwise hydride-terminated surface leads to localized midgap states, leading to a red shift in the PL of Si-NCs below *ca.* 3 nm.[16] As well, Eyre and coworkers predicted that other oxide species such as silanol (Si-OH) and bridging oxide (Si-O-Si) groups can affect Si-NC PL, leading to red or blue shifts with strong dependence on the surface species and degree of oxidation.[17]

Of the methods reported for surface modification, hydrofluoric acid (HF) etching to realize surface hydride species and subsequent hydrosilylation with alkenes and alkynes offers several advantages for tailoring the NC surface.[15, 18-20] HF etching of Si-NCs prepared from HSQ removes the oxide matrix and reduces the NC size, shifting the PL emission maxima to higher energy, from the near IR to the visible spectral regions.[12] Hydrosilylation can be carried out under extremely mild conditions, with minimal reaction byproducts and toleration of a range of functional groups. The Si-C surface bonds formed are both thermodynamically and kinetically robust, limiting oxidative surface degradation under a variety of damaging conditions;[15, 19, 21, 22] for freestanding Si-NCs, hydrosilylation helps stabilize the PL under conditions where hydride-terminated NCs are rapidly oxidized.[23, 24] Importantly, for many applications such as *in vivo* labeling which require highly

luminescent, water-soluble Si-NCs, hydrosilylation produces colloidal Si-NCs in aqueous environments, either by way of covalent attachment of a polar species (*e.g.*, carboxylic acid, [2, 25, 26] amine[3, 6, 23, 27], alcohol[28] and polyethylene glycol[29]) on the distal end of the alkene or through the use of a dispersing agent such as a phospholipid micelle,[7, 30] polymer,[31, 32] or cosolvent.[33]

Many reports of surface modification of Si-NCs have indicated a shift in the optical properties of Si-NCs (*i.e.*, emission maxima and high quantum yield) during the modification procedures. Both blue and red shifts have been reported depending on the starting NC diameter and method of functionalization.[34] In particular, reports on the origin of blue PL from Si-NCs have differed depending on the synthetic technique and functionalization procedure used. For example, the groups of Swihart and Kortshagen have shown that oxidative treatment of orange-emitting alkyl-capped Si-NCs can "shut off" the orange emission with the concurrent appearance of a new emission centered in the blue.[20, 35] Conversely, the groups of Kauzlarich, Zuilhof and Tilley have demonstrated solution-phase syntheses of Si-NCs with subsequent Pt-catalyzed hydrosilylation that give blue PL.[3, 31, 36]

Many reports of red- to green-emitting Si-NCs have shown an indirect bandgap with characteristic long (μs to ms) radiative lifetimes, suggesting that the electronic structure of nanostructured Si is intimately related to its parent bulk properties. Brus suggested that the dominant factor that gives rise to efficient PL from Si-NCs is the removal of efficient nonradiative relaxation mechanisms such as Auger and deep trap processes, rather than a transition to a pseudodirect bandgap.[37]

Yet, some reports of blue-emitting Si-NCs have shown fast (ns) radiative lifetimes.[3, 20, 36]

The reported differences in the optical response of Si-NCs functionalized by hydrosilylation could arise through a wide range of variables, including the methods used to prepare and purify the Si-NCs (*e.g.*, starting NC diameter, inherent size distribution, byproduct impurities), differences in the reaction conditions utilized (*e.g.*, thermal, photochemical or metal-catalyzed reaction), or differences in post-functionalization treatment. Critical evaluation of the impact of hydrosilylation on the electronic and optical properties is thus challenging.

Photochemically initiated hydrosilylation merits unique consideration for photoluminescent Si materials. Photochemical and thermal hydrosilylation of bulk surfaces has been generally regarded to follow a free-radical mechanism *via* homolytic cleavage of a hydride bond (requiring *ca.* 3.5 eV).[19, 38] However, Stewart and Buriak proposed a secondary mechanism specific to nanostructured, photoluminescent Si that operates *via* the absorption of white light to form excitons (*i.e.*, below the energy required for hydride cleavage).[39, 40] This "white light" method occurs under extremely mild conditions and is compatible with a range of alkene substrates. The main stipulation for this proposed mechanism is that the nanostructure remains photoluminescent during the reaction, to facilitate a long-lived exciton that can drive the irreversible Si-C formation process. Although radical quenching species were observed to have no impact on the functionalization, energy- and charge-transfer species that quenched the PL resulted in a low degree of surface coverage. Low

surface coverage was noted in particular for alkenes and alkynes that quench nanostructured Si PL, such as phenylacetylene and vinylferrocene.

Furthermore, recent controversy has emerged over the mechanism of photochemical hydrosilylation on Si surfaces, in particular the initiation step. New mechanisms have been proposed, including exciton-mediated [41, 42] and photoemission[43] processes for bulk Si surfaces. These mechanisms hint that there may be a complex relationship between the wavelength of irradiation, the alkene or alkyne species attached, as well as quantum size effects in determining the mechanism of hydrosilylation.

Here, the investigation into the impact of near-UV photochemical hydrosilylation on the optical and electronic properties of Si-NCs is reported. The near-UV irradiating wavelength (365 nm) was chosen to study photochemical hydrosilylation for several reasons. First, these reactions can be carried out using commercially available UV-LEDs, which offer relatively high power and low heat output, and may present a "gentler" method for surface modification in comparison to other light sources (*e.g.*, a Hg bulb for deep-UV light). As well, some alkene and alkyne substrates of interest absorb strongly at deep-UV wavelengths, leading to undesired decomposition and polymerization byproducts. Conversely, some substrates are expected to quench hydrosilylation *via* the proposed exciton-mediated mechanism; a near-UV source might be able to initiate functionalization through both the free-radical and exciton-mediated mechanism, giving a wider range of accessible alkene and alkynes. Near-UV light can also efficiently stimulate PL in these materials, because Si-NCs can absorb this spectral range by means of a direct-

gap transition, giving a significantly larger absorption coefficient than phonon-mediated indirect absorption at energies closer to the Si-NC bandgap.[37, 44] This facilitates collection of the PL produced during the reaction, and allows assessment of the impact of the changing surface chemistry on the optical properties. Finally, the use of a precursor that yields freestanding Si-NCs with narrow size distribution and well-defined hydride surface chemistry aids evaluation of the impact of quantum size effects on the possible mechanisms and reactivity of hydrosilylation with near UV initiation.

The influence of near UV initiated hydrosilylation with straight-chain alkenes was investigated because of their popularity in protecting the Si-NC surface from ambient oxidation and its detrimental effects on the PL. The reaction of Si-NC surfaces with conjugated alkynes with varied electron demand was also studied to better understand the interaction between the surface of Si-NCs and PL-quenching species. This interaction may be useful as a model for the interface between Si-NCs and species such as organic semiconductors. The materials were characterized by PL, UV-vis absorption and Fourier-transform infrared (FTIR) spectroscopies, dynamic light scattering (DLS), thermogravimetric analysis (TGA), high-resolution transmission electron microscopy (HRTEM), selected electron area diffraction (SAED) and energy dispersive X-ray spectroscopy (EDS).

2.2. Materials and methods

2.2.1 Materials

HSQ (Dow Corning, trade name FOx-17, sold as a solution in methyl isobutyl ketone and toluene), 49% hydrofluoric acid (HF, J.T. Baker, electronics grade), and 95% ethanol (Sigma-Aldrich) were used as received. High-purity water (18.2 MΩ/cm) was obtained from a Barnstead Nanopure Diamond purification system. Reagent grade toluene and methanol were obtained from Sigma Aldrich. All alkenes and alkynes (styrene, 1-hexene, phenylacetylene, 4-ethnylanisole, 1-ethynyl-3-fluorobenzene, 3-ethynylthiophene) were purchased from Sigma Aldrich as the highest purity available (95% or greater) and were purified immediately before use by passing over neutral alumina to remove hydroperoxide impurities formed by reaction with ambient oxygen.[45]

For quantum yield measurements, 9,10-diphenylanthracence, coumarin 1 and rhodamine 590 dissolved in spectrophotometric-grade cyclohexane, ethanol and toluene were obtained from Sigma Aldrich as the highest grade available.

2.2.2 Synthesis and etching of Si-NCs

Oxide-embedded Si-NC composites were prepared as previously described.[12] In brief, solvent was removed from a solution of HSQ under vacuum to yield a white solid. Heating at 18°C/min to 1100°C in a Lindberg Blue furnace and annealing for 1 h under a flowing 5% H_2/95% Ar atmosphere yielded a glassy brown product. Previous X-ray diffraction and TEM characterization are in agreement with the formation of *ca.* 3 nm diamond structured Si-NCs encapsulated in an silica matrix.

To produce freestanding hydride-terminated Si-NCs, the oxide composite was etched using solutions of HF adapted from a previously described method.[12] To 1 g of composite (ground using a wrist-action shaker and glass beads for 15 h) in a Teflon beaker equipped with a stir bar was added 30 mL of a 1:1:1 solution of HF/ethanol/ water. After 1 h of stirring, the dispersion changed color from brown to yellow, and gave Si-NCs with initial red PL (*ca.* 700 nm, referred to as "red" Si-NCs in the text). Etching for 2 h gave Si-NCs with initial green/yellow PL (*ca.* 580-600 nm, referred to as "green" Si-NCs in the text). Liberated hydride-terminated Si-NCs were extracted with two 25 mL aliquots of toluene.

2.2.3 Functionalization

Immediately after etching, the organic extracts were combined and added to a Schlenk flask equipped with a quartz insert, a stir bar and 32.5 mmol freshly purified alkene/alkyne. The flask was placed on a Schlenk line under an argon atmosphere and degassed by three freeze-pump-thaw cycles.

Hydrosilylation functionalization was initiated using a near-UV LED light source. The light source consisted of two 365 nm LEDs (Nichia, model NCSU033A) operated at 4.5 V, mounted at 180° to each other on a water-cooled bracket. The measured light intensity 2 cm away from the source was 16.6 mW cm^{-2}. A photograph of the light source and Schlenk flask is shown in Figure 2-1. After the flask was completely wrapped in aluminum foil, irradiation commenced for 15 h. The Si-NC emission was monitored during functionalization as described below.
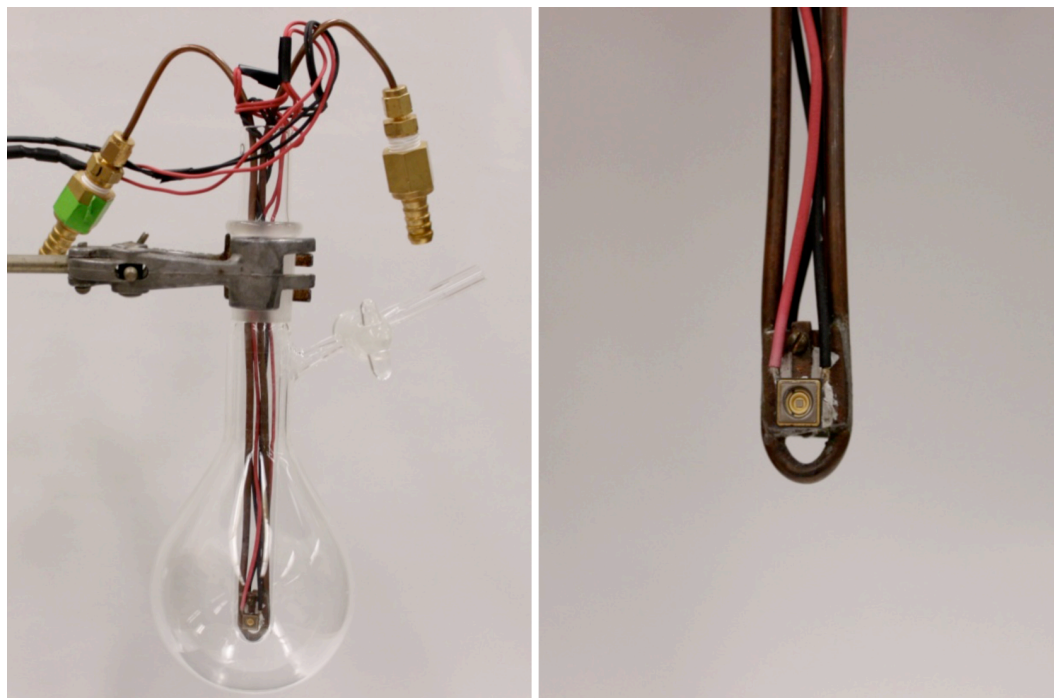
Figure 2-1: Photochemical reactor utilizing 365 nm LEDs.

2.2.4 Si-NC purification

Following functionalization, the Si-NCs were transferred into test tubes and centrifuged at 3,000 rpm to remove any aggregated or unreacted material. The supernatant was filtered through a 250 nm PTFE filter and transferred to a round bottom flask equipped with a stir bar. Excess solvent and alkene/alkyne was removed under vacuum on a Schlenk line. The sample was redispersed in a minimum of toluene and purified through three cycles of solvent/anti-solvent purification. To accomplish this, the dispersion was transferred into centrifuge tubes and precipitated via the addition of methanol followed by 20 min centrifugation in a high speed centrifuge at 25,850 G (17,000 rpm). The supernatant was decanted and the redispersion, precipitation, centrifugation and decanting steps were repeated twice.

Following the final cycle of purification, the functionalized Si-NCs could be redispersed in hydrophobic organic solvents (*e.g.,* chloroform or toluene) as desired.

2.2.5 Material characterization and instrumentation

In order to minimize the effect of ambient oxidation, samples were freshly prepared for each characterization technique where possible.

2.2.5.1 Fourier Transform Infrared Spectroscopy (FTIR)

FTIR spectra were collected using a Nicolet Magna 750 IR spectrometer on drop-cast films.

2.2.5.2 High-resolution Transmission Electron Microscopy (HRTEM), Selected Area Electron Diffraction (SAED) and Energy Dispersive X-ray Spectroscopy (EDS)

HRTEM was performed at the Brockhouse Institute for Materials Research (BIMR) at McMaster University using a Titan3 G2 60-300 TEM operating at 300 kV. SAED and EDS were performed using a JEOL-2010 field-emission electron microscope operating at 200 kV. Prior to analysis, samples of functionalized Si-NCs were purified through two additional solvent/antisolvent cycles and resuspended in chloroform to fully remove any organic species that might have hindered analysis through electron-beam induced decomposition. Samples were dropcoated from a dilute chloroform dispersion onto a carbon-coated copper grid.

2.2.5.3 Thermogravimetric Analysis (TGA)

TGA was performed using a Perkin-Elmer Pyris 1 TGA. Samples were dropcoated from a concentrated toluene dispersion into a Pt pan and evaporated under a N_2 stream while heating at 40°C until no further weight loss was observed and a dried mass greater than 1 mg was obtained. The pan was then heated under N_2 from 40 to 900°C at a rate of 10°C/min.

2.2.5.4 Dynamic Light Scattering (DLS)

DLS measurements were performed using a Malvern Zetasizer Nano S series dynamic light scatterer using a 632 nm laser. Dilute samples in toluene were equilibrated to 25°C and refiltered through a 0.45 μm PTFE syringe filter prior to analysis. Samples sets (of 10) were scanned three times. Intensity scans were converted to volume distributions using the Zetasizer software.

2.2.5.5 *In situ* photoluminescence spectroscopy

During the functionalization, the Si-NC PL was collected at 3 min intervals through an optical fibre connected to an Ocean Optics USB2000 spectrometer. The spectrometer's spectral response was normalized using a blackbody radiator.

2.2.5.6 Quantum yield determination

The PL quantum yield of red styrene-functionalized silicon nanocrystals was determined through the relative approach[46] using the relationship:

$$\Phi_{Si} = \Phi_{ST}\left(\frac{Grad_{Si}}{Grad_{ST}}\right)\left(\frac{\eta^2{}_{Si}}{\eta^2{}_{ST}}\right)$$

where the subscripts *Si* and *ST* denote the Si-NC sample and standard reference respectively, Φ is the fluorescent quantum yield, *Grad* the gradient from a plot of integrated fluorescence intensity versus absorbance over a range of absorbances from $0 - 0.1$ at the exciting wavelength, and η the refractive index of the solvent. The absorbances were kept very low and a range of concentrations were examined to avoid any self-absorption or other non-linear effects. The standards used were 9,10-diphenylanthracence in cyclohexane (λ_{ex} = 354 nm, λ_{em} = 400- 500 nm, Φ = 0.90, η = 1.4262), coumarin 1 in ethanol (λ_{ex} = 373 nm, λ_{em} = 400-600 nm, Φ = 0.73, η = 1.3614) and rhodamine 590 in ethanol (λ_{ex} = 524, λ_{em} = 525-600 nm, Φ = 0.95, η = 1.3614).[47] The relative quantum yields of the standards were compared and found to match their literature counterparts ± 10%. Fluorescence spectra of the Si-NC samples were acquired with excitation at 354, 373 and 450 nm in toluene (η = 1.4969); the quantum yield of the Si-NCs stayed within 15% regardless of exciting wavelength. Absorbance and photoluminescence spectra of the sample in a quartz cuvette were collected using a Cary 400 UV/vis spectrometer and a Cary Eclipse fluorescence spectrophotometer.

2.3 Results and discussion

2.3.1 Near-UV hydrosilylation with model alkenes/alkynes

A common goal in functionalization of silicon nanostructures is protection of PL under ambient conditions. As mentioned above, hydrosilylation with straight-chain alkenes imparts stability to Si-NC surfaces; however, some authors have observed shifts in the optical response during the functionalization process. Near-UV hydrosilylation was studied using the model molecules 1-hexene, styrene and 1-hexyne and compared to a control sample where hydride-terminated Si-NCs were irradiated by the light source in toluene in the absence of any alkene/alkyne.

Figures 2-2 and 2-3 shows representative HRTEM of red Si-NCs functionalized with 1-hexene, with a mean size 2.3 ± 0.6 nm and green Si-NCs functionalized with 1-hexene with a mean size 2.0 ± 0.5 nm. Lattice parameters and selected area electron diffraction were consistent with crystalline Si. EDS indicated the presence of Si, C and O.
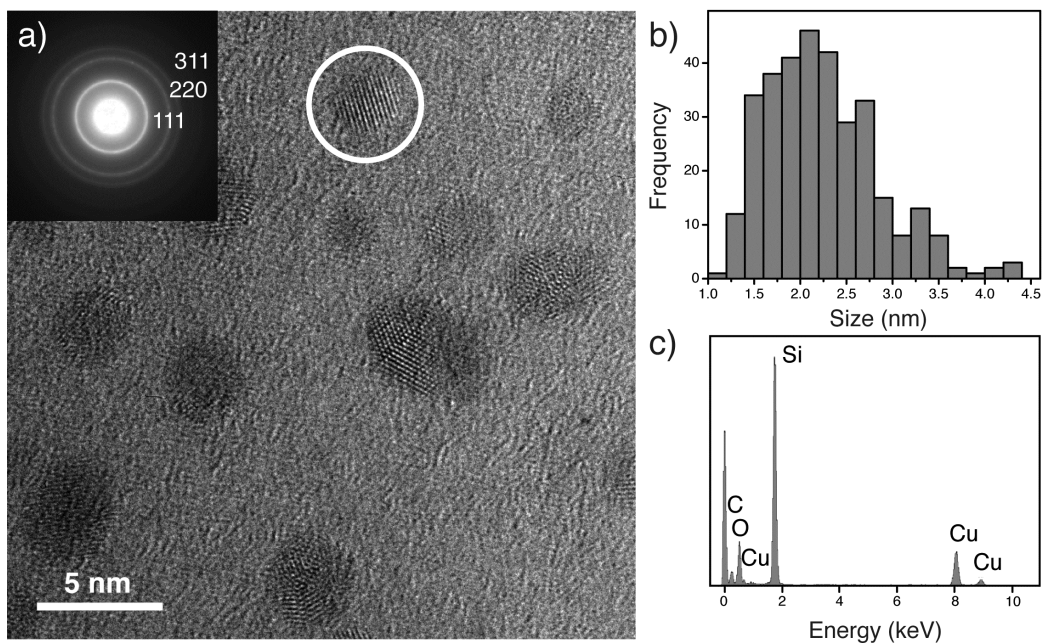
Figure 2-2: a) HRTEM (inset: SAED), b) size distribution information (2.3 +/- 0.6 nm, n = 328) and c) EDS of Si-NCs functionalized with 1-hexene (etched for 1 h, initially red emitting). The lattice fringes of the circled nanocrystal had a d-spacing of 1.9Å, matching the (220) plane of crystalline Si.
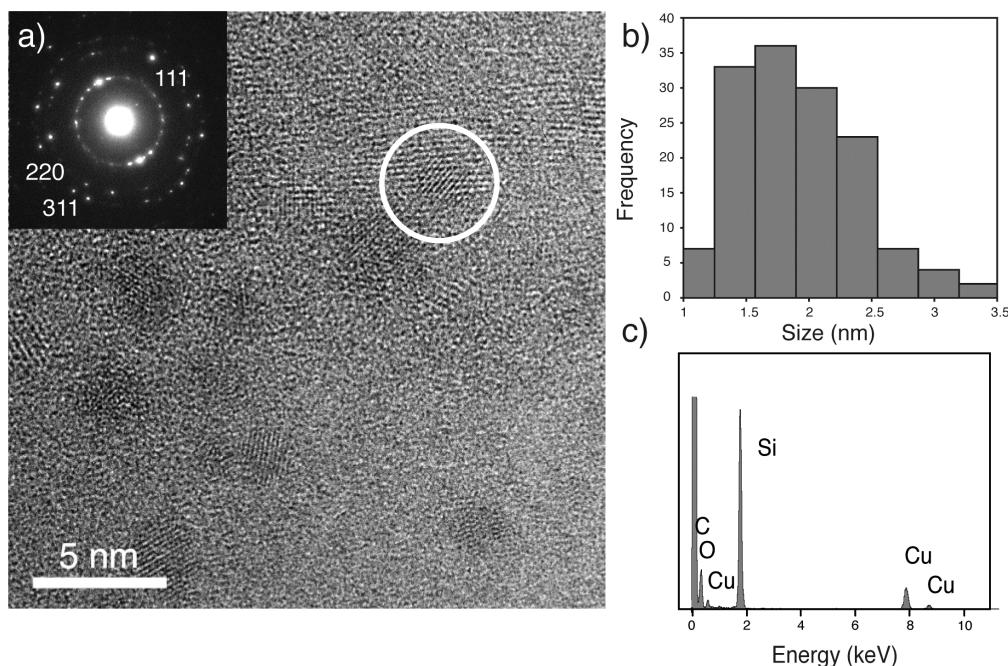
Figure 2-3: a) HRTEM (inset: SAED), b) size distribution information (2.0 ± 0.5 nm, n = 142) and c) EDS of Si-NCs functionalized with 1-hexene (etched for 2 h, initially green emitting). The circled NC had lattice fringes of 1.6Å matching the 311 plane of crystalline Si.

Absorption, PL and PL excitation (PLE) spectra of red Si-NCs after functionalization with styrene are shown in Figure 2-4. The Si-NCs exhibit continuous and relatively featureless absorption, characteristic of an indirect bandgap. Extrapolation to the x-axis gives an approximate bandgap of 2.6 eV. The PLE spectrum shows a broad feature centered at approximately 4 eV. These features can be related to the calculated absorption spectrum of bulk Si, which has an indirect region from 1.1 to 3.4 eV and direct-gap absorption from 3.4 to 4.4 eV.[37, 48] Absorption studies of other nanostructured Si materials show similar spectra to those presented here, and suggest that the direct-gap transition broadens and slightly red

shifts at the nanoscale.[37, 44, 48] The size dependence of this direct-gap transition has also been investigated in detail using PL with time-correlated photon counting (TCPC) detection.[49] Thus, a rationalization for the choice of a near UV exciting wavelength for photochemical hydrosilylation can be inferred. In the exciton-mediated mechanism proposed by Stewart and Buriak, the functionalization process is driven by surface-localized excitons created through photoabsorption. The correlation of direct-gap absorption with a significant increase in intensity in the PLE spectrum implies that this absorption route leads to more efficient exciton formation over indirect-gap absorption, which requires a phonon. Therefore, more excitons are created which can facilitate Si-C bond formation.
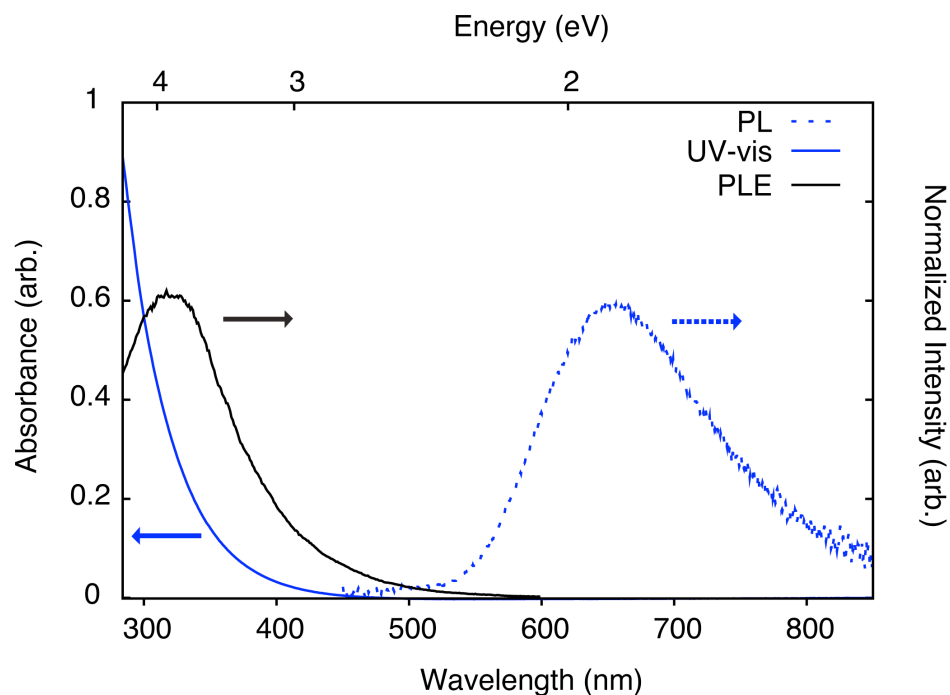
Figure 2-4: Absorption (blue solid line), PLE (black solid line, monitoring at 640 nm) and PL (blue dashed line, λ_{ex} = 365 nm) of styrene-functionalized red Si-NCs after hydrosilylation in toluene.

FTIR spectroscopy was used to qualitatively study the degree of Si-C bond formation, shown in Figure 2-5. This bond formation process is most evident in the formation of a Si-C=C stretch at 1600 cm^{-1} in Si-NCs functionalized with 1-hexyne. This stretch is characteristic of a silyl-bonded alkene, being red shifted by *ca.* 40 cm^{-1} in comparison to aliphatic alkenes;[39] furthermore, the absence of sp C-H and C≡C stretches at *ca.* 3300 and 2120 cm^{-1} is consistent with no starting material remaining.

Immediately following HF etching, the hydride-terminated Si-NCs exhibit SiH$_x$ (x = 1-3) stretching bands at *ca.* 2100 cm^{-1} and scissoring bands at *ca.* 910 cm^{-1} with little or no evidence of oxide in the 1100 and 3400 cm^{-1} spectral regions. Upon

functionalization, a broad SiH$_x$ stretching band is typically observed at reduced intensity in qualitative comparison to other features, consistent with other reports that coverage of nanostructured Si surfaces by hydrosilylation is limited by steric interactions between surface bonded moieties.[19] Partial oxidation of SiH$_x$ surfaces has been observed to shift the hydride stretching band to higher energy, with a characteristic stretch at 2250 cm^{-1} for O$_3$Si-H species indicating high levels of surface oxidation. Conversely, formation of Si-C bonds has been predicted to shift the C-SiH stretching frequency to lower energy.[50] The broad feature centered at 2100 cm^{-1} in the present samples is consistent with Si-C bond formation without the formation of the heavily oxidized O$_3$Si-H species. Surface oxidation is observed in functionalized samples through the formation of Si-O-Si and Si-OH bands at *ca.* 1100 and 3400 cm^{-1}, respectively. One disadvantage of using aqueous HF etching to control NC size is the difficulty in eliminating any trace water from the reaction mixture; photochemical oxidation of the Si surface *via* water-related radical species is one possible source of this oxidation.[51] Furthermore, while efforts were made to minimize exposure of the functionalized surfaces after reaction where possible, the propensity of surface hydride species to oxidize under ambient conditions makes it challenging to fully rule out the impact of ambient exposure on the oxide-related features in the FTIR spectra.

FTIR spectra of the alkene-functionalized Si-NCs exhibit alkyl stretching features at *ca.* 2900 cm^{-1} (CH$_2$ and CH$_3$ ν stretching) and *ca.* 1460 and 1380 cm^{-1} (CH δ deformation) consistent with alkyl species grafted during hydrosilylation. Styrene functionalized Si-NCs also show aromatic C-H stretching bands at *ca.* 3070-

3010 cm^{-1} and combination and overtone bands at 2000-1650 cm^{-1}. An FTIR spectrum of the control Si-NC sample also shows prominent alkyl stretching, which could arise from physisorbed organic species. Thus, quantitative integration of these signals in comparison to the Si-H features would give an artificially high degree of surface coverage. The Si-C ν stretching band, which would directly confirm surface hydrosilylation, is obscured in the fingerprint region.[50, 52] However, qualitative comparison of the hydride to alkyl stretching regions show the styrene and 1-hexene functionalized samples have reduced hydride intensity, consistent with a higher degree of surface coverage.
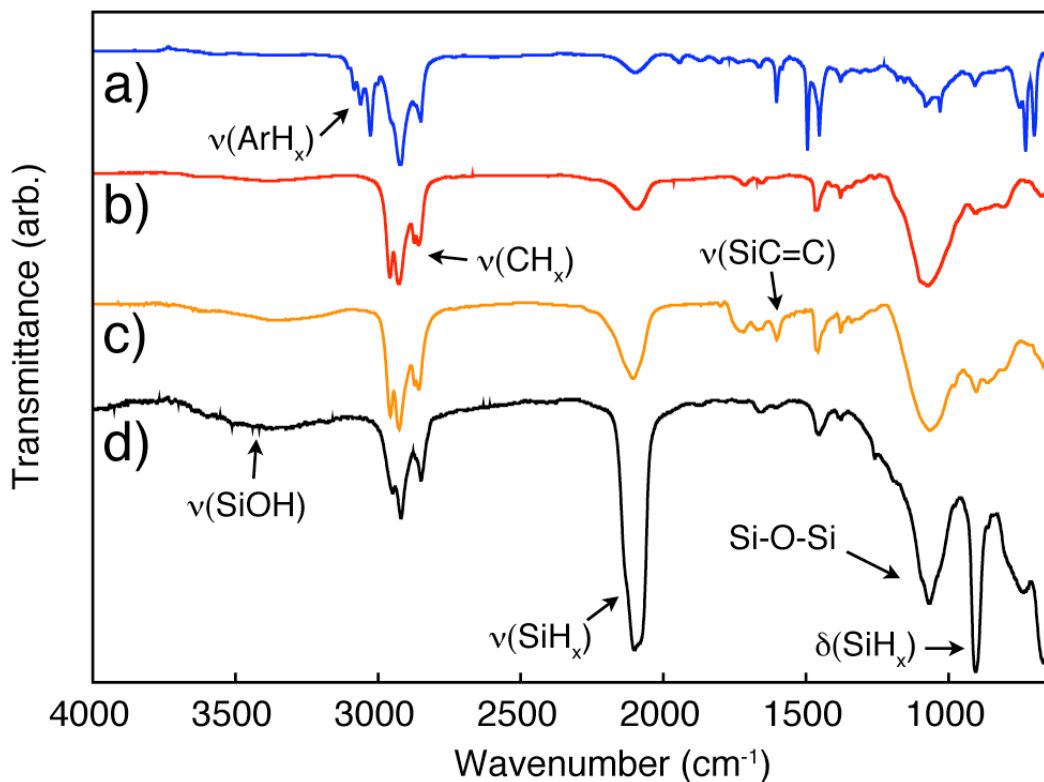
Figure 2-5: FTIR spectra of red Si-NCs functionalized with a) styrene, b) 1-hexene and c) 1-hexyne. A control sample irradiated in the absence of any alkene/alkyne (d) is also shown. Spectra are normalized to the alkyl stretching band at *ca.* 2950 cm^{-1}.

Functionalization with near-UV hydrosilylation was also qualitatively evaluated based on the quality of dispersions (photo shown in Figure 2-6). Functionalization yielded Si-NCs that gave clear dispersions that could easily pass through a 0.45 μm filter. DLS measurements of functionalized Si-NCs in toluene gave hydrodynamic radii in the range of 8-15 nm, shown in Figure 2-7. The control (hydride-terminated) Si-NCs gave a cloudy dispersion that precipitated out of dispersion within minutes; DLS showed agglomerates around 100 nm. These results are consistent with the replacement of surface hydrides with alkyl/alkenyl groups,

increasing particle-solvent affinity and decreasing particle agglomeration. Reports of hydrodynamic radii of other functionalized NCs with 2-3 nm diameters in toluene are in a similar range to the present observations;[53] this is dependent on the NC core, surface capping agent and concentration effects.
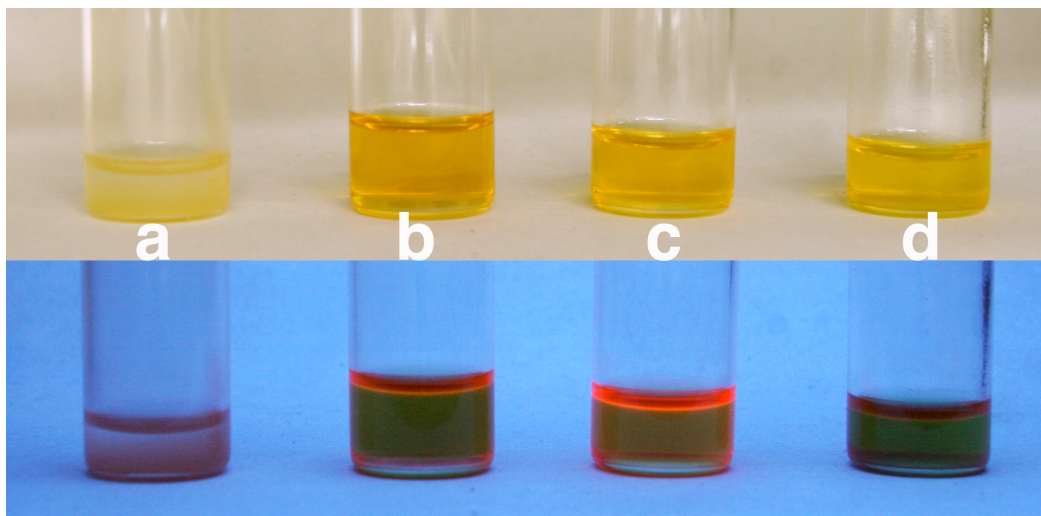
Figure 2-6: Toluene dispersions of Si-NCs under ambient (top) and UV irradiation (bottom): functionalization with a) control sample (no alkene present), b) styrene, c) 1-hexene and d) phenylacetylene.
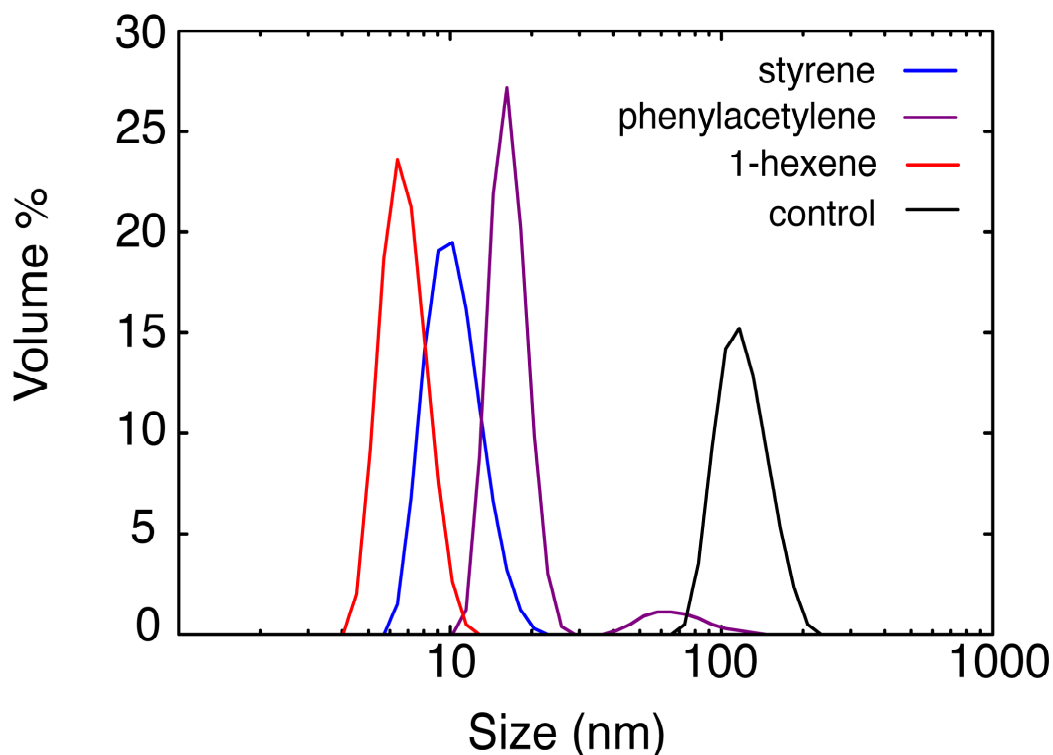
Figure 2-7: Dynamic light scattering (DLS) measurements of Si-NCs (initially red emitting) in toluene.

TGA was used to qualitatively evaluate surface coverage of red Si-NCs, shown in Figure 2-8. TGA has some advantages over other methods such as integration of FTIR band intensities[39] for freestanding systems where reproducible integration of IR bands are challenging.[18]

TGA of red-emitting Si-NCs functionalized with styrene and 1-hexene showed weight losses of *ca.* 70 and 55%, respectively; taking into account the molecular weight of the alkenes, this could suggest similar degrees of surface coverage. These results are very close to reported weight losses for deep-UV hydrosilylation of Si-NCs with these alkenes.[18] TGA of green functionalized Si-NCs

with these alkenes gave similar weight losses. In comparison, TGA of 1-hexyne-functionalized Si-NCs showed a reduced weight loss of 30%. As will be discussed below, functionalization with conjugated alkynes that quench the Si-NC PL also translates to a reduced weight loss, in the range of 20-25%.

These observations can be explained in the context of the free-radical and exciton-mediated mechanisms proposed for photochemical hydrosilylation on nanostructured Si surfaces. If the exciton-mediated pathway is dominant at the exciting wavelength of 365 nm (possibly through direct-gap absorption increasing the cross-section for exciton formation), reaction with alkenes or alkynes that preserve the PL (correlated with an increased exciton lifetime) should lead to a higher degree of surface coverage and hence greater TGA weight loss. Quenching substrates would reduce the availability of excitons to react at the surface. Alternatively, they might only react by the free-radical route. A lower degree of surface coverage for these species is also supported qualitatively by the relative intensity of Si-H features in the FTIR spectra of functionalized samples (*vide supra*). Surface alkenyl groups formed by reaction with 1-hexyne or phenylacetylene have been observed in the literature to partially or fully quench Si-NC PL, also consistent with PL data during reaction described below. However, a complicating factor in interpreting these TGA results is the potential for partial decomposition of surface alkenyl groups during heating, which may limit the overall weight loss and skew the observed trend. A recent study of alkyl-capped Ge-NCs has shown the alkyl groups decompose during heating, forming carbonaceous residues.[54]
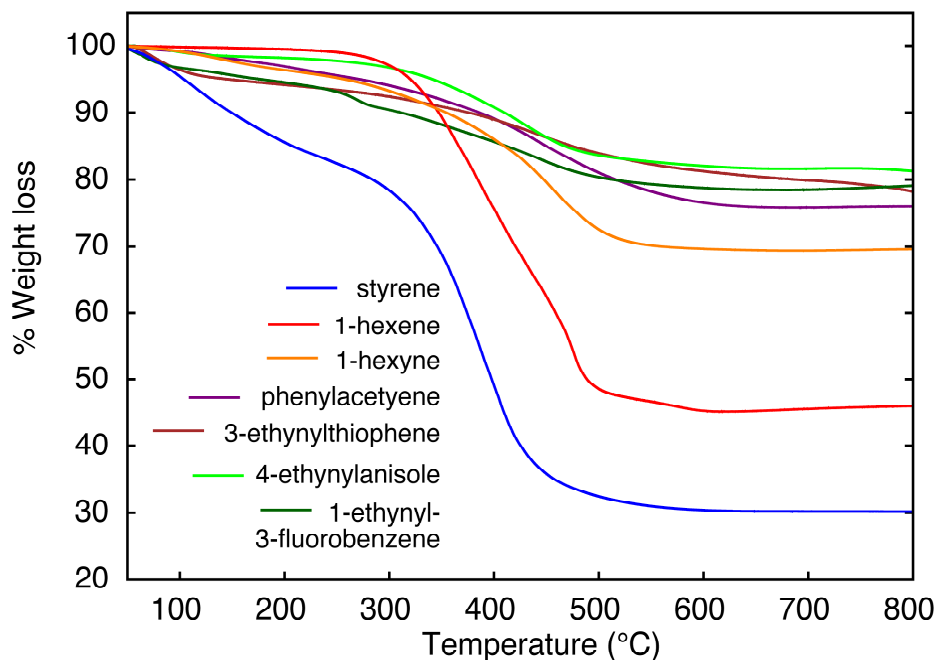
Figure 2-8: Thermogravimetric analysis (TGA) weight loss curves of silicon nanocrystals (initially red-emitting) functionalized with alkenes and alkynes.

Since near-UV light can initiate exciton formation through direct gap absorption (and thus enable the hydrosilylation process to occur by the exciton mediated pathway), it can also efficiently stimulate PL in these materials. This increase in intensity enables observation of the PL as the surface chemistry changes during the reaction, making *in situ* comparisons of emission maxima and intensity possible. Direct measurement also eliminates any ambient oxidation during post-reaction analysis that might complicate comparisons. Figure 2-9 shows *in situ* PL measurements made throughout the functionalization of Si-NCs. Initially red-emitting samples functionalized with styrene, 1-hexene and 1-hexyne exhibit at first a decrease in PL intensity, followed by a blue shift of *ca.* 40 nm and increase in intensity. The rate at which these changes occur is dependent on the alkene used.

Functionalization with styrene and 1-hexene resulted in an increase to *ca.* 160-180% of the original PL intensity whereas reaction with 1-hexyne gave approximately 95% of the original intensity. In comparison, the control sample (which was irradiated in the absence of any alkene/alkyne) did not show any shift in the PL maxima, and a decrease in intensity to *ca.* 75% of the original PL. The QY of the styrene-functionalized red Si-NCs was found to be 4.6 ± 0.7% , comparable to similar Si-NCs functionalized by deep-UV hydrosilylation.[35] While this QY is lower than some of the highest reports in the literature,[55] one possible way to increase this would be extended annealing under H_2/Ar of the Si-NC/SiO$_2$ composites before etching, which reduces nonradiative defects in these materials.[13]
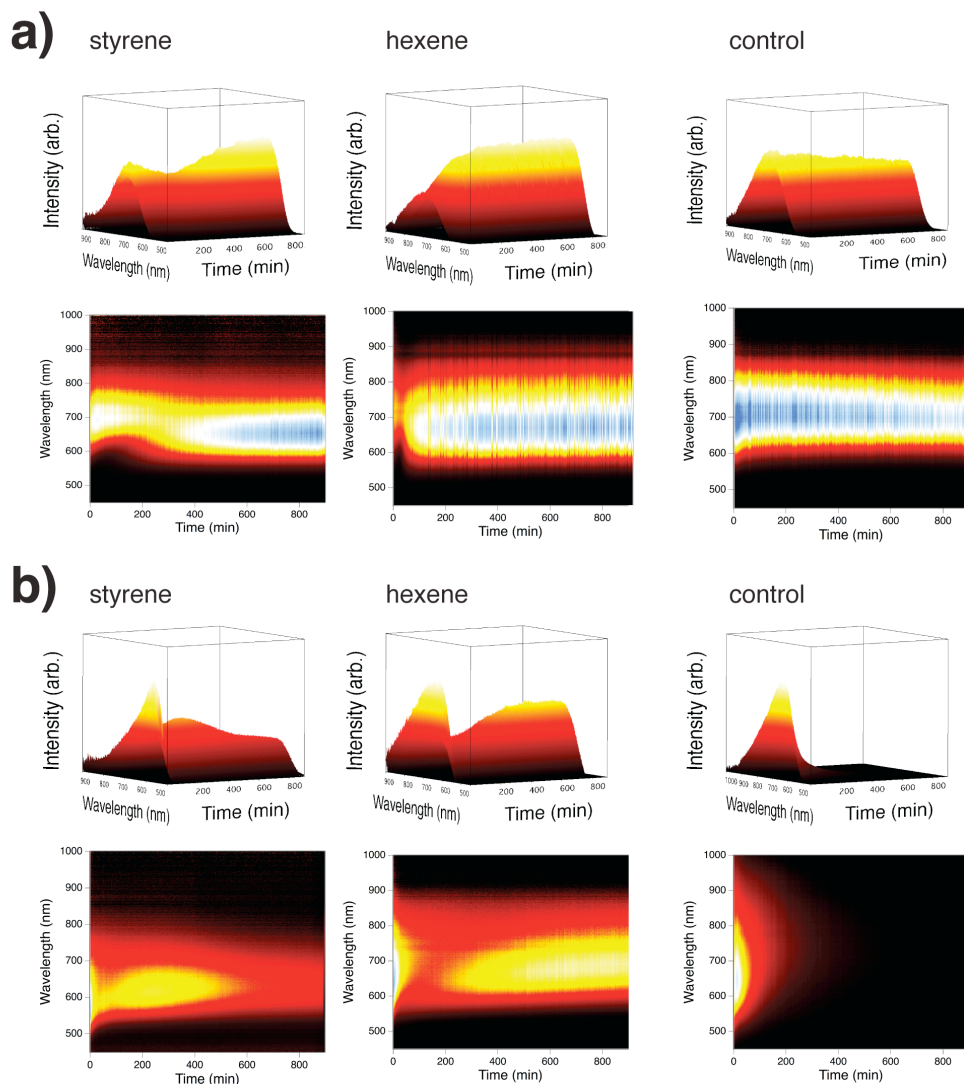
Figure 2-9: *In situ* PL measurements of a) red and b) green Si-NCs during reaction with styrene and 1-hexene, in comparison to control samples. Oblique (top) and top-down (bottom) views of the spectra are shown.

Functionalization of green Si-NCs showed a decrease in intensity during the reaction; reaction with styrene reduced the intensity to *ca.* 35%, whereas 1-hexene reduced it to *ca.* 70%. This loss in intensity was accompanied by a red shift of *ca.* 40-

60 nm. The green control sample showed rapid, near-complete PL quenching. Although FTIR spectra and TGA of the functionalized green samples did not suggest appreciable differences in surface coverage between the styrene and 1-hexene functionalized samples, the lower PL intensity observed for the styrene sample may result from poorer packing of the alkyl surface groups through greater solvent interactions, resulting in a surface more susceptible to oxidation during reaction.[56]

The observed changes in intensity for these samples are a product of the intrinsic quantum yield and scattering of the dispersion as it changes from cloudy to clear. As the surface chemistry changes during the functionalization, it could introduce a transient reaction intermediate (such as surface radicals or cations produced as part of the free radical or exciton-mediated hydrosilylation mechanisms) or oxide-related surface states that could quench or trap NC excited states. Furthermore, as aggregates of nonfunctionalized Si-NCs disperse into the solvent, more light reaches the spectrometer, resulting in an apparent increase in PL intensity.

Similar PL shifts have been observed for other nanostructured Si materials, and have been generally attributed to the influence of surface oxidation. The model of silanone defects proposed by Wolkin *et al.* has three size regimes relevant to the trapping of Si-NC excited states by metastable silanone (Si=O) species, formed during the oxidation of the Si surface; this species is thought to trap electrons or both electrons and holes depending on the size of the NC. These traps result in band to mid-gap state or entirely "trapped exciton" transitions respectively, and hence a resulting red shift.[16] This model is in agreement with our observations of PL from

functionalized green Si-NCs; as the Si-NC size decreases as a result of HF etching, the conduction and valence band states "open up," allowing the mid-gap state formed by oxidation during the near-UV irradiation to alter the luminescence. The rapid decrease of PL from the control PL sample, and overall decrease in intensity of the functionalized green samples suggests that oxidation also introduces nonradiative trap states, consistent with other reports showing a decrease in QY as a result of oxidation.[55]

However, this does not fully explain the blue shift observed for the styrene and 1-hexene functionalized red Si-NCs. Pi *et al.* observed a blue shift of *ca.* 30 nm for Si-NCs with a mixture of Si-H, Si-C, Si-F and Si-CF$_x$ surface species, and attributed it to a quantum-confined related blue shift thought to arise from oxidation reducing the Si-NC diameter.[20, 57] However this does not appear to be the case in the present system, as PL from the control sample irradiated without alkene, which also showed signs of surface oxidation, did not shift appreciably, suggesting the red Si-NCs lie outside the size regime where silanone defects could affect the PL. Similar observations of this blue shift has been made by Gupta *et al.* for deep-UV hydrosilylation,[34] but an explanation was not proposed.

One possible explanation for this behavior could be the involvement of surface states other than the oxide-related ones extensively studied in the literature. The "smart confinement" model of Si-NC luminescence first suggested that strained surface and/or dangling bonds (*e.g.*, Si=Si dimers) could form trapping midgap states, resulting in a red shift away from a purely band-mediated transition.[58, 59] It has also been suggested that dangling bonds formed as a result of surface reconstruction can

quench the Si-NC PL through the formation of deep mid-gap states. Recently, the role of shallow-trapping mid-gap states formed by a sub-oxide surface species was demonstrated in the PL of oxide-embedded Si-NCs by high-field magneto-PL.[60] Although it is a considerable challenge to conclusively determine the structure of the (possibly metastable) surface species responsible for this behaviour (analogous to the highly reactive Si=Si dimer first proposed), the concept of a shallow-trap with as-of-yet unknown structure present in the hydride-terminated Si-NCs could explain the blue shift in PL observed. If trapping states were formed by surface reconstruction of the hydride-terminated Si-NCs during HF etching, this could result in a surface-mediated transition red shifted from the purely quantum confined bandgap. Evidence for strained surface bonding is qualitatively consistent with the inhomogeneously broadened $Si-H_x$ stretching region of these NCs, with linewidths significantly larger than that of hydride-terminated bulk Si.[58] However the formation of (111) and (100) facets during etching might also broaden this region.[61] Changing the surface chemistry to Si-C species during hydrosilylation could alter the structure of these traps or alleviate surface strain from participating in, or quenching the emission process, and remove their influence on the PL. This removal of surface traps would cause a blue shift and increase in quantum yield; qualitatively this is consistent with the present observations.

2.3.2 Near-UV hydrosilylation with conjugated alkynes

In addition to preservation of the Si-NC PL and tailoring particle dispersibility in a range of solvents, functionalization by hydrosilylation may also be of interest for the synthesis and study of hybrid organic/inorganic composite materials where the optical and electronic properties (*e.g.,* charge separation and carrier mobility) are tunable based on the interaction of the Si-NCs and host polymer matrix at the NC surface. One family of model organic semiconductors that has received attention is π-conjugated species tethered to the Si surface with covalent alkyl/alkenyl linkages via hydrosilylation. For example, hydrosilylation of bulk Si with phenylacetylene, creating a surface styrenyl group, has been suggested as a route to well-defined organic/inorganic junctions,[38] and has been noted to enhance interfacial conductivity over bare hydride-terminated surfaces.[62, 63] Other conjugated species such as thiophenes have been studied, for example in the preparation of covalently-tethered polythiophenes.[64, 65] In contrast, hydrosilylation of nanostructured Si surfaces with π-conjugated aromatics has not been as fully investigated for their resulting optical and electronic properties. As noted above, in the proposed exciton mechanism for photochemical hydrosilylation, conjugated alkynes did not react appreciably under white light irradiation. Their low surface coverage was attributed to the ability of these species to effectively trap excitons required for nucleophilic attack from the alkyne, the first step required in the mechanism, supported by low levels of surface group incorporation (<1% based on FTIR integration) and a significant reduction in PL intensity.

The present 365 nm source corresponds to a region of direct-gap Si-NC absorption, which might dramatically enhance the rate of exciton formation. Alternatively, the light source is at the threshold of energy required for homolytic cleavage of surface hydrides indentified in the free-radical mechanism. Figure 2-10 shows *in situ* PL of Si-NCs reacted with alkynes phenylacetylene, 4-ethynylanisole, 1-ethynyl-3-fluorobenzene, and 3-ethynylthiophene. These were chosen on the basis of their electron withdrawing/donating ability (based on the functional group's Hammet equation constant) while being cognizant of any competing side reactions with functional groups (*e.g.*, amines[66] or bromine groups[67]). The PL decays over the course of the experiment at a rate dependent on the alkyne used; the greater the electron-donating character of the substituent, the faster the rate of PL decay. For example, functionalization with 3-ethynylthiophene gave near complete PL quenching, whereas 1-ethynyl-3-fluorobenzene reduced the Si-NC PL to *ca.* 38% of the original intensity over the course of the reaction. The remaining PL intensity comes from unfunctionalized hydride-terminated NCs, which are separated from the reaction mixture during workup as they quickly precipitate out of dispersion during the first centrifugation; FTIR of this precipitate (not shown) gave predominately Si–H and Si–O–Si features at *ca.* 2100 and 1100 cm^{-1}, respectively, with very small amounts of alkyl features.
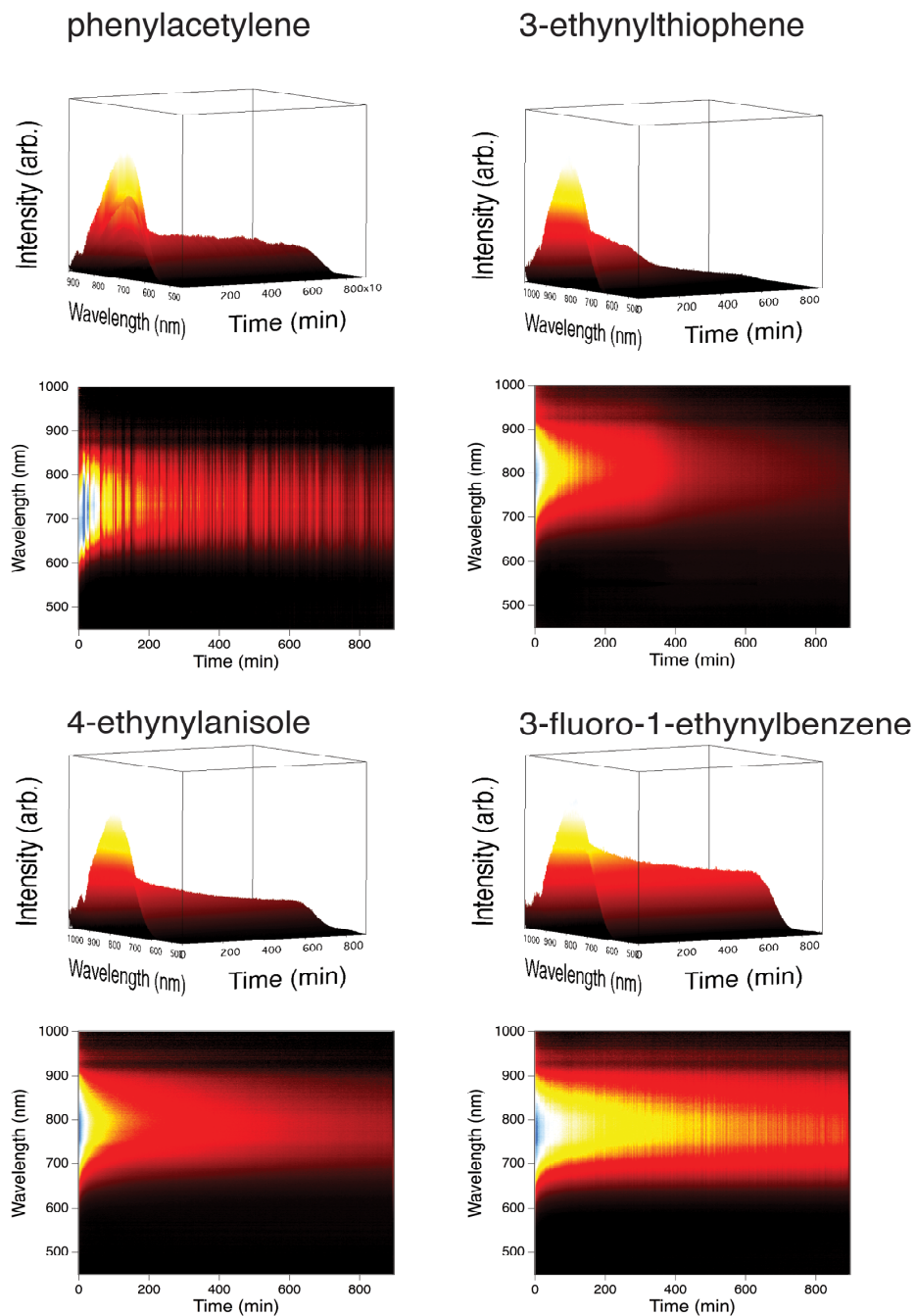
Figure 2-10: *In situ* PL measurements of red Si-NCs during reaction with a) phenylacetylene, b) 3-ethynylthiophene, c) 4-ethynylanisole and d) 1-ethynyl-3-fluorobenzene. Oblique (top) and top-down (bottom) views of the spectra are shown.

This trend in reactivity was also supported qualitatively by FTIR of the Si-NCs after purification, shown in Figure 2-11. Si-NCs functionalized with alkynes of greater electron-withdrawing character show an increase in the intensity of hydride- and oxide-related bands compared to alkyl stretching features, implying a lower degree of incorporation of the alkenyl surface groups, with the fluorine-substituted alkyne exhibiting the lowest degree of surface coverage. In the exciton-mediated mechanism, alkynes with greater nucleophilic character are expected to be more reactive toward attack of a surface-localized hole. Alternatively, in the free radical mechanism, greater electron density in the alkyne would attract attack from electrophilic surface radicals, and therefore would lead to a faster rate of reaction, higher degree of surface coverage, and hence faster rate of PL quenching. A similar trend was noted in the deep UV hydrosilylation of Si-NCs with alkenes.[18] It is noted that in the photoemission mechanism for hydrosilylation of bulk surfaces with deep UV light proposed by Wang *et al.* the rate of reaction and therefore degree of surface coverage depended on the affinity of the alkene to accept a photoelectron from the bulk Si surface.[43] The observed trend of electron-donating groups increasing the rate of reaction in the present system seems to contradict this observation; this may suggest the photoemission mechanism does not hold for these alkyne substrates and on nanostructured Si surfaces. It is important to emphasize the challenge in comparing hydrosilylation reactivity between systems with different alkenes (and purity), initiating wavelength, and different quantum size effects (*i.e.*, bulk surface *versus* nanostructured). Other recent reports of hydrosilylation have also suggested factors intrinsic to the experimental design may influence reactivity,

including the observations of self-assembly in the dark at room temperature,[68] and reaction catalyzed by surface groups on the glassware commonly used to carry out these reactions.[69] Further study is required in this area to better understand hydrosilylation of Si-NCs and optimize surface coverage.
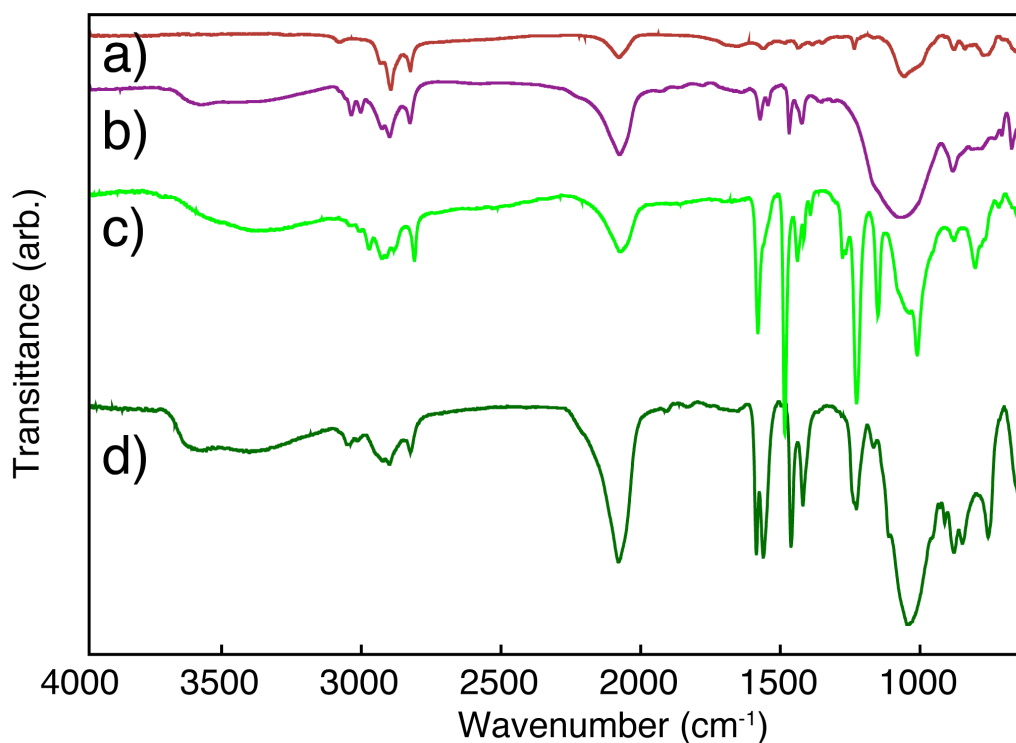
Figure 2-11: FTIR spectra of silicon nanocrystals (initially red emitting) functionalized with a) 3-ethynylthiophene, b) phenylacetylene, c) 4-ethynylanisole and d) 1-ethynyl-3-fluorobenzene. Spectra are normalized to the alkyl stretching band at *ca.* 2950 cm^{-1}.

Quenching of nanostructured Si PL has been reported for other conjugated species, both physisorbed[66] and covalently bonded.[39, 70] However, the mechanism of

quenching has remained unclear. In the present system, all of the alkynes gave functionalized Si-NCs with no PL detectable to the naked eye following particle purification, suggesting the differences observed in the *in situ* PL measurements arises from differences in hydrosilylation reactivity. This quenching could arise from the formation of a deep trap in the Si-NC bandgap, as changing the electron demand of the surface group did not turn on the Si-NC PL. Further experimental and computational studies to understand this quenching are ongoing.

2.4 Conclusions

The photochemical hydrosilylation of silicon nanocrystals (Si-NCs) with alkene and alkynes using a near-UV light source was investigated. The impact of the changing surface chemistry on the photoluminescence (PL) and the relevant mechanism of hydrosilylation were demonstrated to be dependent on the NC size and structure of the alkene/alkyne. For Si-NCs with initial green/yellow (580-600 nm) PL reacted with model alkenes styrene and 1-hexene, a red shift and decrease in PL intensity was observed, consistent with the formation of midgap oxide-related states. Hydrosilylation of Si-NCs with initial red (680-700 nm) PL gave an increase in intensity, possibly related to the production of well-dispersed particles with less scattering or an increase in the intrinsic quantum yield, as well as a blue shift. A qualitative model based on the formation of Si-C surface species was proposed to account for the shift. Hydrosilylation with conjugated alkynes was demonstrated to quench the Si-NC PL at a rate dependent on the nucleophilicity of the alkyne. These results were rationalized in the context of the free-radical and exciton-

mediated mechanisms postulated for hydrosilylation of nanostructured Si surfaces. These model alkynes may be interesting in the integration of Si-NCs into hybrid composite materials with tunable optical and electronic properties.

2.5 References

1. Park, J. –H.; Gu, L.; von Maltzahn, G.; Ruoslahti, E.; Bhatia, S. N.; Sailor, M. J. *Nat. Mater.* **2009**, *8*, 331-336.

2. Li, Z. F.; Ruckenstein, E. *Nano Lett.* **2004**, *4*, 1463-1467.

3. Warner, J. H.; Hoshino, A.; Yamamoto, K.; Tilley, R. D. *Angew. Chem. Int. Ed.* **2005**, *44*, 4550-4554.

4. Soo Choi, H.; Liu, W.; Misra, P.; Tanaka, E.; Zimmer, J. P.; Itty Ipe, B.; Bawendi, M. G.; Frangioni, J. V. *Nat. Biotechnol.* **2007**, *25*, 1165-1170.

5. Lewinski, N.; Colvin, V.; Drezek, R. *Small* **2008**, *4*, 26-49.

6. Ruizendaal, L.; Bhattacharjee, S.; Pournazari, K.; Rosso-Vasic, M.; De Haan, L. H. J.; Alink, G. M.; Marcelis, A. T. M.; Zuilhof, H. *Nanotoxicology* **2009**, *3*, 339-347.

7. Erogbogbo, F.; Yong, K. -T.; Roy, I.; Xu, G. X.; Prasad, P. N.; Swihart, M. T. *ACS Nano* **2008**, *2*, 873-878.

8. Alsharif, N. H.; Berger, C. E. M.; Varanasi, S. S.; Chao, Y.; Horrocks, B. R.; Datta, H. K. *Small* **2009**, *5*, 221-228.

9. Bayliss, S. C.; Heald, R.; Fletcher, D. I.; Buckberry, L. D. *Adv. Mater.* **1999**, *11*, 318-321.

10. Nagesha, D. K.; Whitehead, M. A.; Coffer, J. L. *Adv. Mater.* **2005**, *17*, 921-924.

11. Low, S. P.; Voelcker, N. H.; Canham, L. T.; Williams, K. A. *Biomaterials* **2009**, *30*, 2873-2880.

12. Hessel, C. M.; Henderson, E. J.; Veinot, J. G. C. *Chem. Mater.* **2006**, *18*, 6139-6146.

13. Hessel, C. M.; Henderson, E. J.; Veinot, J. G. C. *J. Phys. Chem. C* **2007**, *111*, 6956-6961.

14. Hessel, C. M.; Henderson, E. J.; Kelly, J. A.; Cavell, R. G.; Sham, T. K.; Veinot, J. G. C. *J. Phys. Chem. C* **2008**, *112*, 14247-14254.

15. Veinot, J. G. C. *Chem. Commun.* **2006**, , 4160-4168.

16. Wolkin, M. V.; Jorne, J.; Fauchet, P. M.; Allan, G.; Delerue, C. *Phys. Rev. Lett.* **1999**, *82*, 197-200.

17. Eyre, R. J.; Goss, J. P.; Briddon, P. R. *Phys. Rev. B Condens. Matter* **2008**, *77*.

18. Hua, F.; Swihart, M. T.; Ruckenstein, E. *Langmuir* **2005**, *21*, 6054-6062.

19. Buriak, J. M. *Chem. Rev.* **2002**, *102*, 1271-1308.

20. Pi, X. D.; Liptak, R. W.; Deneen Nowak, J.; Wells, N. P.; Carter, C. B.; Campbell, S. A.; Kortshagen, U. *Nanotechnology* **2008**, *19*.

21. Ciampi, S.; Harper, J. B.; Gooding, J. J. *Chem. Soc. Rev.* **2010**, *39*, 2158-2183.

22. Chatgilialoglu, C.; Timokhin, V. I. *Adv. Organomet. Chem.* **2008**, *57*, 117-181.

23. Rosso-Vasic, M.; Spruijt, E.; Popović, Z.; Overgaag, K.; Van Lagen, B.; Grandidier, B.; Vanmaekelbergh, D.; Domínguez-Gutiérrez, D.; De Cola, L.; Zuilhof, H. *J. Mater. Chem.* **2009**, *19*, 5926-5933.

24. Li, X.; He, Y.; Swihart, M. T. *Langmuir* **2004**, *20*, 4720-4727.

25. Rogozhina, E. V.; Eckhoff, D. A.; Gratton, E.; Braun, P. V. *J. Mater. Chem.* **2006**, *16*, 1421-1430.

26. Sato, S.; Swihart, M. T. *Chem. Mater.* **2006**, *18*, 4083-4088.

27. Rosso-Vasic, M.; DeCola, L.; Zuilhof, H. *J. Phys. Chem. C* **2009**, *113*, 2235-2240.

28. Shiohara, A.; Hanada, S.; Prabakar, S.; Fujioka, K.; Lim, T. H.; Yamamoto, K.; Northcote, P. T.; Tilley, R. D. *J. Am. Chem. Soc.* **2010**, *132*, 248-253.

29. Sudeep, P. K.; Page, Z.; Emrick, T. *Chem. Commun.* **2008**, , 6126-6127.

30. Goller, B.; Polisski, S.; Wiggers, H.; Kovalev, D. *Appl. Phys. Lett.* **2010**, *96*.

31. Zhang, X.; Neiner, D.; Wang, S.; Louie, A. Y.; Kauzlarich, S. M. *Nanotechnology* **2007**, *18*.

32. Hessel, C. M.; Rasch, M. R.; Hueso, J. L.; Goodfellow, B. W.; Akhavan, V. A.; Puvanakrishnan, P.; Tunnel, J. W.; Korgel, B. A. *Small* **2010**, *6*, 2026-2034.

33. Dickinson, F. M.; Alsop, T. A.; Al-Sharif, N.; Berger, C. E. M.; Datta, H. K.; Siller, L.; Chao, Y.; Tuite, E. M.; Houlton, A.; Horrocks, B. R. *Analyst* **2008**, *133*, 1573-1580.

34. Gupta, A.; Swihart, M. T.; Wiggers, H. *Adv. Funct. Mater.* **2009**, *19*, 696-703.

35. Hua, F.; Erogbogbo, F.; Swihart, M. T.; Ruckenstein, E. *Langmuir* **2006**, *22*, 4363-4370.

36. Rosso-Vasic, M.; Spruijt, E.; Van Lagen, B.; De Cola, L.; Zuilhof, H. *Small* **2008**, *4*, 1835-1841.

37. Brus, L. E.; Szajowski, P. F.; Wilson, W. L.; Harris, T. D.; Schuppler, S.; Citrin, P. H. *J. Am. Chem. Soc.* **1995**, *117*, 2915-2922.

38. Cicero, R. L.; Linford, M. R.; Chidsey, C. E. D. *Langmuir* **2000**, *16*, 5688-5695.

39. Stewart, M. P.; Buriak, J. M. *Journal of the American Chemical Society* **2001**, *123*, 7821-7830.

40. Reboredo, F. A.; Schwegler, E.; Galli, G. *J. Am. Chem. Soc.* **2003**, *125*, 15243-15249.

41. Sun, Q. -Y.; De Smet, L. C. P. M.; Van Lagen, B.; Giesbers, M.; Thüne, P. C.; Van Engelenburg, J.; De Wolf, F. A.; Zuilhof, H.; Sudhölter, E. J. R. *J. Am. Chem. Soc.* **2005**, *127*, 2514-2523.

42. De Smet, L. C. P. M.; Pukin, A. V.; Sun, Q. -.; Eves, B. J.; Lopinski, G. P.; Visser, G. M.; Zuilhof, H.; Sudhölter, E. J. R. *Appl. Surf. Sci.* **2005**, *252*, 24-30.

43. Wang, X.; Ruther, R. E.; Streifer, J. A.; Hamers, R. J. *J. Am. Chem. Soc.* **2010**, *132*, 4048-4049.

44. Holmes, J. D.; Ziegler, K. J.; Doty, R. C.; Pell, L. E.; Johnston, K. P.; Korgel, B. A. *J. Am. Chem. Soc.* **2001**, *123*, 3743-3748.

45. Jackson, H. L.; McCormack, W. B.; Rondestvedt, C. S.; Smeltz, K. C.; Viele, I. E. *J. Chem. Educ.* **1970**, *47*, A175-A188.

46. Rhys Williams, A. T.; Winfield, S. A.; Miller, J. N. *Analyst* **1983**, *108*, 1067-1071.

47. Scaiano, J. C. In *Handbook of Organic Photochemistry;* CRC Press: London, 1989.

48. Ben-Chorin, M.; Averboukh, B.; Kovalev, D.; Polisski, G.; Koch, F. *Phys. Rev. Lett.* **1996**, *77*, 763-766.

49. De Boer, W. D. A. M.; Timmerman, D.; Dohnalová, K.; Yassievich, I. N.; Zhang, H.; Buma, W. J.; Gregorkiewicz, T. *Nat. Nanotechnol.* **2010**, *5*, 878-884.

50. Bateman, J. E.; Eagling, R. D.; Horrocks, B. R.; Houlton, A. *J. Phys. Chem. B* **2000**, *104*, 5557-5565.

51. Bahruji, H.; Bowker, M.; Davies, P. R. *Int. J. Hydrogen Energy* **2009**, *34*, 8504-8510.

52. Canaria, C. A.; Lees, I. N.; Wun, A. W.; Miskelly, G. M.; Sailor, M. J. *Inorg. Chem. Commun.* **2002**, *5*, 560-564.

53. Pons, T.; Uyeda, H. T.; Medintz, I. L.; Mattoussi, H. *J. Phys. Chem. B* **2006**, *110*, 20308-20316.

54. And, Z. C. H.; Kortshagen, U. R. *Langmuir* **2009**, *25*, 11883-11889.

55. Jurbergs, D.; Rogojina, E.; Mangolini, L.; Kortshagen, U. *Appl. Phys. Lett.* **2006**, *88*.

56. Sieval, A. B.; Vleeming, V.; Zuilhof, H.; Sudhölter, E. J. R. *Langmuir* **1999**, *15*, 8288-8291.

57. Ledoux, G.; Guillois, O.; Porterat, D.; Reynaud, C.; Huisken, F.; Kohn, B.; Paillard, V. *Phys. Rev. B Condens. Matter* **2000**, *62*, 15942-15951.

58. Koch, F.; Petrova-Koch, V.; Muschik, T. *J. Lumin.* **1993**, *57*, 271-281.

59. Nayfeh, M. H.; Rigakis, N.; Yamani, Z. *Phys. Rev. B Condens. Matter* **1997**, *56*, 2079-2084.

60. Godefroo, S.; Hayne, M.; Jivanescu, M.; Stesmans, A.; Zacharias, M.; Lebedev, O. I.; Van Tendeloo, G.; Moshchalkov, V. V. *Nat. Nanotechnol.* **2008**, *3*, 174-178.

61. Higashi, G. S.; Chabal, Y. J.; Trucks, G. W.; Raghavachari, K. *Appl. Phys. Lett.* **1990**, *56*, 656-658.

62. Hiremath, R. K.; Mulimani, B. G.; Rabinal, M. K.; Khazi, I. M. *J. Phys. Condens. Matter* **2007**, *19*.

63. Saito, N.; Hayashi, K.; Sugimura, H.; Takai, O. *Langmuir* **2003**, *19*, 10632-10634.

64. Fabre, B.; Lopinski, G. P.; Wayner, D. D. M. *J. Phys. Chem. B* **2003**, *107*, 14326-14335.

65. Sathyapalan, A.; Ng, S. C.; Lohani, A.; Ong, T. T.; Chen, H.; Zhang, S.; Lam, Y. M.; Mhaisalkar, S. G. *Thin Solid Films* **2008**, *516*, 5645-5648.

66. Song, J. H.; Sailor, M. J. *J. Am. Chem. Soc.* **1997**, *119*, 7381-7385.

67. Wang, D.; Buriak, J. M. *Langmuir* **2006**, *22*, 6214-6221.

68. Scheres, L.; Arafat, A.; Zuilhof, H. *Langmuir* **2007**, *23*, 8343-8346.

69. Mischki, T. K.; Lopinski, G. P.; Wayner, D. D. M. *Langmuir* **2009**, *25*, 5626-5630.

70. Song, J. H.; Sailor, M. J. *J. Am. Chem. Soc.* **1998**, *120*, 2376-2381.

Chapter 3:

Size-Dependent

Reactivity in

Hydrosilylation of

Silicon Nanocrystals[*]

3.1 Introduction

Interest in the chemical modification of hydride-terminated silicon surfaces has grown rapidly since the first report of hydrosilylation of a bulk Si surface by Lindford and Chidsey.[1] Functionalization of bulk and nanostructured surfaces is a critical step in many envisioned applications where control over the chemical, physical, and electronic properties of the Si surface is required. Among the various methods used to functionalize Si surfaces, hydrosilylation produces high quality, densely packed organic monolayers under relatively mild reaction conditions and provides excellent stability against oxidation.[2-6]

Despite the growing number of publications on surface hydrosilylation, uncertainty regarding the mechanism responsible has remained. The first reports of hydrosilylation with bulk surfaces utilized a peroxide initiator (*i.e.,* ROOR');[1] subsequently, reports of hydrosilylation in the absence of a chemical initiator under photochemical[7, 8] or thermal conditions[9, 10] have been made. Scanning tunneling microscopy (STM) studies of bulk surfaces suggested a radical propagation mechanism,[11, 12] analogous to the free radical process proposed for *tris*(trimethylsilyl)silane by Chatgilialogu and coworkers.[13]

The pathway through which this reaction is initiated has been an ongoing issue of debate; direct Si-H homolysis under thermal or photochemical energy has been suggested in some cases, although this is not fully consistent with reports of hydrosilylation under conditions insufficient for direct cleavage of surface hydrides. Several alternate theories have been proposed, including initiation from trace molecular oxygen,[14] alkyl radicals produced by photolysis[15] or thermal olefin

decomposition,[16] and the involvement of excitons (*vide infra*). Non-radical mechanisms under certain conditions have also been proposed, including deep-UV photoemission,[17] fluoride-assisted nucleophilic attack (from residual F^- from hydrofluoric acid etching)[18] and concerted addition under thermal conditions.[19]

Exciton-mediated mechanisms for hydrosilylation have received substantial attention for reactions performed under very mild reaction conditions, using visible light (*i.e.*, far below the threshold for direct hydride homolysis) as an initiator,[20, 21] or even for formation of self-assembled monolayers in the dark at room temperature.[22, 23] Stewart and Buriak proposed a non-radical exciton-mediated mechanism relevant for nanostructured Si, involving nucleophilic attack from the olefin at a surface-localized hole.[20] Subsequently, Zuilhof and coworkers observed monolayer formation on bulk surfaces by visible light.[21] On the basis of a dopant dependence and STM measurements demonstrating island growth,[24] they proposed a radical mechanism whereby delocalized holes susceptible to nucleophilic attack from the incoming olefin initiate radical propagation (analogous to the free radical mechanisms originally proposed). The involvement of delocalized excited states in these reactions is fascinating, for it has no obvious molecular counterpart; for example, while the molecular silylium ion (R_3Si^+) exhibits transient stability,[25] these mechanisms invoke such species as long-lived intermediates on the basis of enhanced back-bonding from surrounding lattice Si atoms. The exciton-based nanoscale and bulk mechanisms are compared to the free radical mechanism in Scheme 3-1.
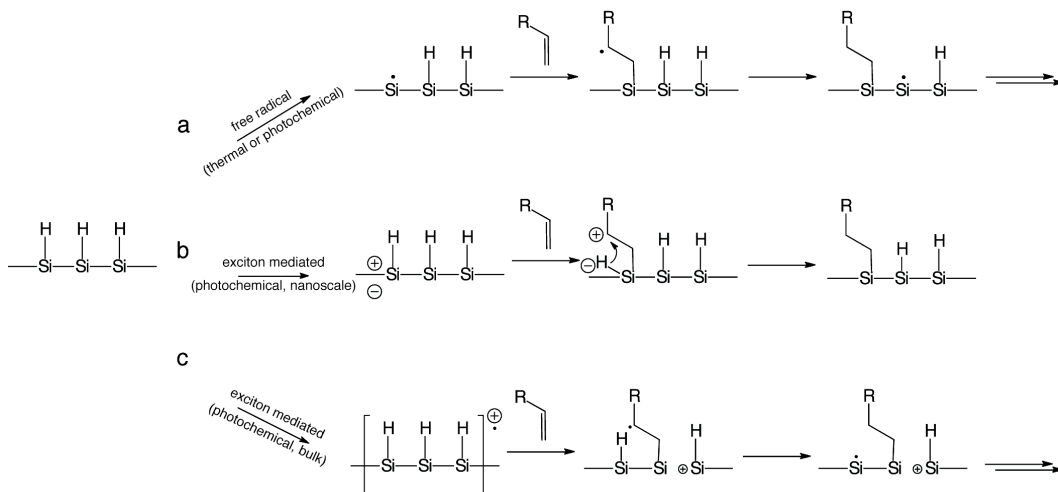
Scheme 3-1: Depiction of the proposed a) free radical mechanism under thermal and photochemical conditions (involving direct hydride homolysis),[7, 9, 10] b) exciton-mediated mechanism for nanoscale Si under photochemical conditions[20] and c) exciton-mediated mechanism for bulk Si under photochemical conditions.[21]

Theoretical studies of visible light initiated hydrosilylation reactions have also given evidence for the involvement of excitons. Using model Si clusters reacting with ethene, Reboredo *et al.* calculated energy barriers for the reaction with the cluster in the ground (singlet) and excited (triplet) state at the DFT level of theory (following path B in Scheme 3-1, reaction energy diagram depicted in Figure 3-1).[26] The excited state reaction was predicted to involve a metastable intermediate state, lowering the activation energy for Si-C bond formation. A rationale was proposed to account for differences in reactivity based on size; as a localized midgap state, the energy of the intermediate state was found to be independent of cluster size. However, the energy of the cluster in the exicted state was predicted to depend upon size, decreasing with larger size (as expected for quantum confinement effects). Thus,

smaller Si nanostructures were predicted to be more reactive in this mechanism. Subsequently, Kanai and Selloni investigated the exciton-mediated mechanism on bulk surfaces (path C in Scheme 3-1),[27] suggesting that radical chain propagation from a neighboring surface hydride may have a lower activation barrier than abstraction from the Si-C bound surface atom, in keeping with the experimental results of Zuilhof and coworkers.
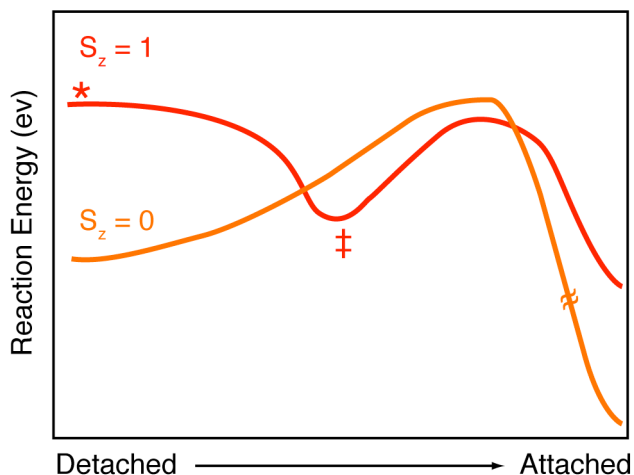
Figure 3-1: Schematic potential energy diagram of a hydrosilylation reaction computed using a model alkene and Si cluster.[26] The reaction pathway for the cluster in the ground singlet state (S_z = 0, orange trace, *i.e.,* the free radical mechanism) and the excited triplet state (S_z = 1, red trace, *i.e.*, the nanoscale exciton-mediated mechanism). The energy of the reaction coordinates in the exciton-mediated mechanism denoted * and ‡ are discussed in the text. Scheme adapted from reference 26.

For nanostructured Si (including silicon nanocrystals, Si-NCs) exhibiting intense size-dependent photoluminescence (PL) through the influence of quantum confinement effects,[28] the chief goals of functionalization through hydrosilylation are to protect the surface against oxidation (which has been implicated in shifting/quenching Si-NC PL)[29, 30] and ensure colloidal dispersity in a range of solvents (especially biological/aqueous conditions, as Si-NCs have garnered much interest as biocompatible quantum dots for *in vivo* imaging).[31-35] Yet, depending on their desired application, further requirements (*e.g.*, incorporation of a ω-substituted

bioactive moiety) may complicate the choice of reaction conditions used to modify Si-NC surfaces. For example, a recent interest in the functionalization of compound II-VI and III-V semiconductor NCs (*e.g.*, CdSe, GaAs) has been the development of surface ligands that do not hinder thin-film conductivity (either through a post-reaction treatment to remove the insulating alkyl chains from the as-synthesized materials,[36, 37] or through use of novel inorganic ligands[38]) for devices utilizing their quantum confined optical and electronic properties. The use of shorter alkyl chains is incompatible with the reported temperature requirements of thermal hydrosilylation (*ca.* 120-200°C), and some olefins can decompose under deep-UV irradiation.[39] Furthermore, several functional groups compete for addition to hydride-terminated Si surfaces (*e.g.*, amines,[40] halides[41] and nitro moieties[42]). It is therefore important to understand the mechanistic considerations that might limit reactivity for a given Si-NC size, alkene or alkyne, and method of initiation desired.

Chapter 2 presented an investigation into the use of near-UV light to initiate hydrosilylation using Si-NCs with PL in the visible region (*e.g.*, sizes of *ca.* 1.5-3 nm).[30] The irradiating wavelength of 365 nm was chosen because it corresponds to a region of direct-gap light absorption, which might enhance the rate of reaction in the exciton-mediated mechanisms (*i.e.*, paths B or C in Scheme 3-1). Si-NCs were prepared through the thermal decomposition of hydrogen silsesquioxane (HSQ).[43, 44] This synthesis yields size-controlled Si-NCs with a relatively narrow polydispersity, making it well suited for a fundamental investigation into size-dependent reactivity.

Here, small-angle X-ray scattering (SAXS), photoluminescence (PL) and Fourier transform infrared (FTIR) spectroscopy have been employed to

experimentally investigate the reactivity of Si-NCs as a function of size in near-UV hydrosilylation. The size ranges selected (*ca.* 2-3 nm Si-NCs with PL centered at *ca.* 700 nm, referred to as "small" NCs in the text and *ca.* 5-7 nm Si-NCs with PL centered at *ca.* 950 nm, referred to as "large" NCs in the text) were chosen because these populations are near the Bohr radius of Si of *ca.* 5 nm, the threshold where quantum size effects that might impact the hydrosilylation are expected to arise.[28] The present results demonstrate that "large" Si-NCs react at a slower rate than "small" Si-NCs under near-UV hydrosilylation, allowing a mixture of the two populations to be partially size-selected based on their reactivity. This difference in reactivity is suggested to arise through the impact of quantum confinement effects on the exciton-mediated mechanisms,[20] and is consistent with the theoretical predictions made by Reboredo *et al* (*vide supra*).[26]

3.2. Materials and methods

3.2.1 Materials

HSQ (Dow Corning, trade name FOx-17, sold as a solution in methyl isobutyl ketone and toluene), 49% hydrofluoric acid (HF, J.T. Baker, electronics grade), and 95% ethanol (Sigma-Aldrich) were used as received. High-purity water (18.2 MΩ•cm) was obtained from a Barnstead Nanopure Diamond purification system. All other reagents were purchased from Sigma Aldrich as the highest purity available (95% or greater) and unless specified were used as received. Phenylacetylene and 1-dodecene were purified immediately before use by passing over neutral activated alumina to remove peroxide impurities.[45]

3.2.2 Synthesis and etching of Si-NCs

Oxide-embedded Si-NC composites were prepared from HSQ as previously described.[43] Previous X-ray diffraction study has shown the formation of *ca.* 4 nm and 6 nm Si-NCs encapsulated in an silica matrix by processing at 1100°C and 1200°C, respectively.[46]

To produce freestanding hydride-terminated Si-NCs of different sizes, two different etching procedures were employed. To obtain Si-NCs with PL centered at *ca.* 650 nm, referred to as "small" Si-NCs (shown by previous electron microscopy to be *ca.* 2-3 nm),[30] a previously described etching procedure was used.[43] In brief, to 1 g of mechanically ground composite (previously processed at 1100°C) in a Teflon beaker equipped with a stir bar was added 30 mL of a 1:1:1 solution of HF/ ethanol/ water. After 1 h of stirring, the dispersion changed color from brown to yellow.

To obtain Si-NCs with PL centered at *ca.* 950 nm, referred to as "large" Si-NCs (*ca.* 5-6 nm as shown below), 1 g of mechanically ground composite processed at 1200°C was added to a Teflon beaker equipped with a stir bar along with 0.5 mL concentrated HCl and 15 mL HF (see Chapter 4 for a detailed explanation of the differences between these etching recipes). After 5 min of stirring, 7.5 mL of ethanol was added and the mixture stirred for an additional 5 min, yielding a cloudy brown dispersion.

Hydride-terminated Si-NCs were extracted from both etch mixtures using 2 aliquots of 15 mL of toluene.

3.2.3 Size-dependent photochemical functionalization

Following extraction, 12.5 mL of the "small" and "large" extracts were transferred to centrifuge tubes along with a "combined" sample containing 12.5 mL of a 10:1 ratio by volume of the "small": "large" toluene dispersions. Assuming the initial number of Si-NCs per gram is approximately constant for 1100-1200°C-processed composites (reasonable given the dominant mechanism for Si-NC formation and growth is the diffusion of Si suboxide species through the matrix, rather than Ostwald ripening[46]), this should yield similar Si-NC concentrations for the "small" and "large" extracts.

After centrifugation at 3,000 rpm, the toluene was decanted and the precipitated hydride-terminated NCs redispersed into the desired alkene mixture (25 mL neat 1-dodecene or 25 mL toluene and 4 mL phenylacetylene). The mixtures were transferred into Schlenk flasks equipped with stir bars and quartz inserts for

photochemical reaction under an argon atmosphere. The reaction mixtures were subjected to three freeze-pump-thaw cycles, and photochemical hydrosilylation was carried out using a 365 nm light source for 15 h as previously described.[30]

3.2.4 Si-NC purification

Following photochemical functionalization, the reaction mixtures were transferred into centrifuge tubes and spun at 3,000 rpm to precipitate any unreacted NCs. These precipitated NCs were washed three times with hexane, and could be reacted using a secondary thermal hydrosilylation, described below. The supernatant from each reaction was filtered through a 250 nm PTFE syringe filter into a 50 mL centrifuge tube. Dodecene-functionalized NCs were purified by precipitation by the addition of 37.5 mL of a 3:1 ethanol/methanol mixture and centrifugation (20 min at 25,900 G), chosen because of the insolubility of dodecene in methanol. Three additional purification cycles by centrifugation were performed using toluene and methanol as the solvent/anti-solvent.

To purify phenylacetylene-functionalized NCs, the majority of the toluene and phenylacetylene reaction mixture after filtration was removed under vacuum on a Schlenk line. The remaining concentrated mixture was subjected to three purification by centrifugation cycles using toluene and methanol as the solvent/anti-solvent as described above.

3.2.5 Thermal hydrosilylation

Hydride-terminated Si-NCs (either freshly HF etched or separated after photochemical functionalization) were dispersed in 25 mL 1-dodecene and

106

transferred to a Schlenk flask equipped with a stirbar under an argon atmosphere. The reaction mixture was degassed by three cycles of evacuation and purging with argon, after which the flask was placed in a silicon oil bath and heated at 190°C for 15 h. The reaction mixture typically turned from turbid to transparent in the first 3 h of heating. Purification was carried out as described above.

3.2.6 Material Characterization and Instrumentation

3.2.6.1 Fourier Transform Infrared Spectroscopy (FTIR)

FTIR spectra were collected using a Nicolet Magna 750 IR spectrometer on drop-cast films.

3.2.6.2 Photoluminescence Spectroscopy

Photoluminescence spectra of dilute toluene Si-NC dispersions under excitation from the 325 nm line of a He/Cd laser were collected using a fiber optic connected to an Ocean Optics USB2000 spectrometer. The spectrometer spectral response was normalized using a blackbody radiator.

3.2.6.3 Small Angle X-ray Scattering (SAXS)

SAXS was performed on dilute dispersion of silicon nanocrystals in toluene sealed in a boron-rich silicate capillary (Charles Supper, 2 mm outer diameter, 80 mm length, 10 μm wall thickness). Measurements were performed using a Bruker NanoStar with a rotating copper anode X-ray generator (λ = 1.54 Å) operating at 5.5 kW. The scattered photons were collected on a 2D multiwire gas-filled detector

(Bruker Histar.) and the scattering angle was calibrated using a silver behenate ($CH_3(CH_2)_{20}COOAg$) standard. Radial integrations of scattering intensity were performed using Bruker GADDS software. Experimental data were corrected for background scattering.

3.2.6.3.1 SAXS theory and fitting

The scattering intensity ($I(q)$) of a dilute dispersion of scatterers is given by equation 3-1:[31, 47]

$$I(q) \propto \int_{0}^{\infty} N(R)P(qR)R^6 dR \qquad (3\text{-}1)$$

where $P(qR)$ is the form factor; for a dispersion of solid homogeneous spheres this is described by equation 3-2:

$$P(qR) = 9\left(\frac{\sin(qR) - qR\cos(qR)}{(qR)^3}\right)^2 \qquad (3\text{-}2)$$

where q is the scattering wave vector, related to the scattering angle and X-ray wavelength by equation 3-3:

$$q = \frac{4\pi}{\lambda}\sin(\frac{\theta}{2}) \qquad (3\text{-}3)$$

The number fraction of scatterers of radius R, $N(R)$, was assumed to follow a Gaussian distribution, given by equation 3-4:

$$N(R) = \frac{1}{\sigma\sqrt{(2\pi)}} e^{\frac{-(R-\bar{R})^2}{2\sigma^2}} \qquad (3\text{-}4)$$

where $\bar{R}$ is the mean nanocrystal radius and σ is the standard deviation.

Least squares fitting using the parameters $\overline{R}$ and σ was carried out using the Irena package for Igor Pro.[48] An additional constant was included to account for residual background signal, typically 1% of the sample scattering intensity. "Combined" samples were fit using the parameters $\overline{R}$ and σ obtained for each separate population and allowing the volume fraction of each population to vary.

3.3 Results and Discussion

A natural extension of the investigation in Chapter 2 of near-UV hydrosilylation using Si-NCs with PL in the visible region is the functionalization of larger Si-NCs with PL in the near IR (*e.g.*, 700-1100 nm). This spectral region is of particular interest for application in biological imaging, as it occurs in the therapeutic window where light maximally penetrates tissue.[49] Si-NCs with PL in this spectral region have been successfully employed as *in vivo* luminescent tags with properties rivaling direct bandgap quantum dots.[35]

Initial attempts to functionalize larger Si-NCs (with PL centered at *ca.* 950 nm) with near-UV light were unsuccessful, yielding unreacted hydride-terminated Si-NCs as shown by FTIR spectroscopy in Figure 3-1; these Si-NCs exhibited poor dispersability. Attempts to perform near-UV hydrosilylation with other larger sizes of Si-NCs that exhibit near-IR PL gave similar results. After 15 h of reaction, the FTIR spectrum is dominated by well-defined $Si-H_x$ stretching at *ca.* 2100 cm^{-1} and scissoring at *ca.* 910 and 820 cm^{-1}. A small amount of oxidation is evidenced by Si-O-Si stretching at *ca.* 1100 cm^{-1}. Alkyl ν stretching at *ca.* 2900 cm^{-1} and δ deformation bands at *ca.* 1460 and 1380 cm^{-1} (attributed to residual hexane in the drop cast film analyzed, or possibly to a small degree of hydrosilylation) is also observed. In comparison, the equivalent photochemical reaction of "small" Si-NCs, or thermal hydrosilylation of "large" Si-NCs at 190° C, resulted in a substantial decrease in $Si-H_x$ vibrations (accompanied with a broadening/red shift of the $Si-H_x$ stretching vibrations), relative to the alkyl features. Correspondingly, the reaction

mixtures turned from cloudy to clear as the Si-NCs became colloidally dispersed in neat 1-dodecene.
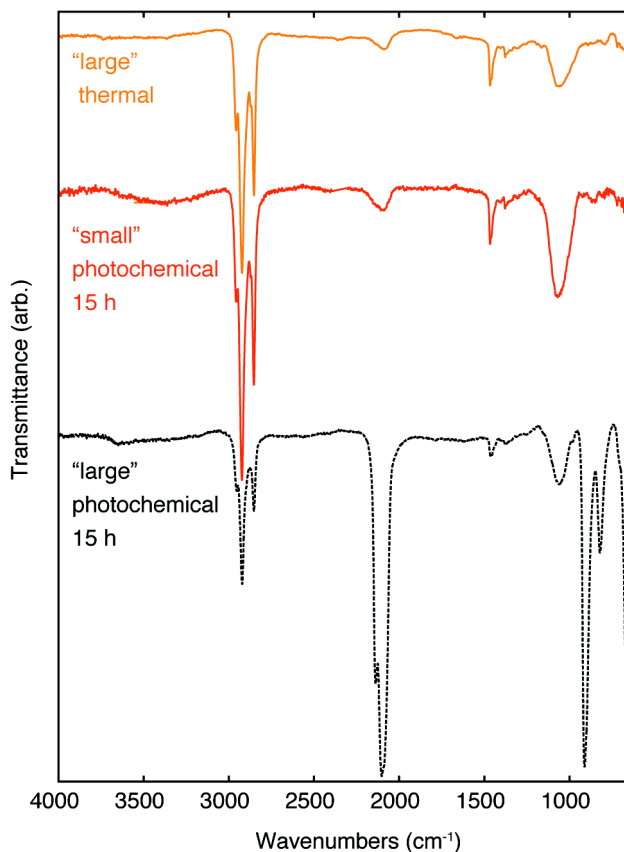
Figure 3-2: FTIR spectra of the "large" and "small" Si-NCs after thermal and photochemical reaction (orange and red traces) in comparison to the large Si-NCs after photochemical reaction (dashed black trace).

To better understand this difference in reactivity of various sizes of Si-NCs, photochemical hydrosilylation was attempted on a 10:1 "combined" mixture by mass of "small":"large" Si-NCs. The size of the "large" sample (6.3 ± 1.0 nm as shown by

SAXS below) was chosen as it straddles the Bohr radius of Si (*ca.* 5 nm), below which quantum confinement effects are expected to arise.[28]

Attempts to functionalize 1:1 and 5:1 "small":"large" mixtures proved unsuccessful, resulting in hydride-terminated Si-NCs as indicated by FTIR (not shown). Two possible explanations could account for this observation. First, despite difficulties associated with quantitative study of Si-NC absorption cross-sections arising from their indirect bandgap and relatively broad size distributions, Beard *et al.* have observed a substantial size dependence in the absorption cross-section of freestanding Si-NCs similar to the present samples.[50] These observations suggest that absorption of near-UV light during the reaction is dominated by the "large" population, slowing the rate of functionalization of the "small" population. Second, efficient energy transfer from the "small" to "large" population could also hinder reactivity, especially if the NCs are aggregated in close proximity.[51]

Figure 3-3 shows PL of Si-NC samples after photochemical and/or thermal hydrosilylation with 1-dodecene. The "small" Si-NC sample exhibits PL centered at *ca.* 675 nm after photochemical reaction, in good agreement with previous *in situ* PL measurements;[30] the "large" Si-NC sample exhibits PL centered at *ca.* 950 nm after thermal hydrosilylation. After photochemical reaction, the "combined" sample was separated by centrifugation and filtration, resulting in PL centered at *ca.* 635 nm, blue shifted compared to the small Si-NC sample. The residual precipitate from the photochemical reaction was redispersed in 1-dodecene and thermally functionalized, resulting in collodially-dispersed Si-NCs exhibiting PL with two features centered at *ca.* 700 and 935 nm. Extending the photochemical reaction time and heating the

reaction gently at 40°C to increase the reaction rate (*i.e.*, well below the threshold for thermal Si-H homolysis as discussed above) gave PL with two features centered at *ca.* 700 nm and 900 nm. The characteristic "small" PL was broadened in comparison to the 15 h reaction whereas the "large" PL was blue shifted from the thermal reaction.
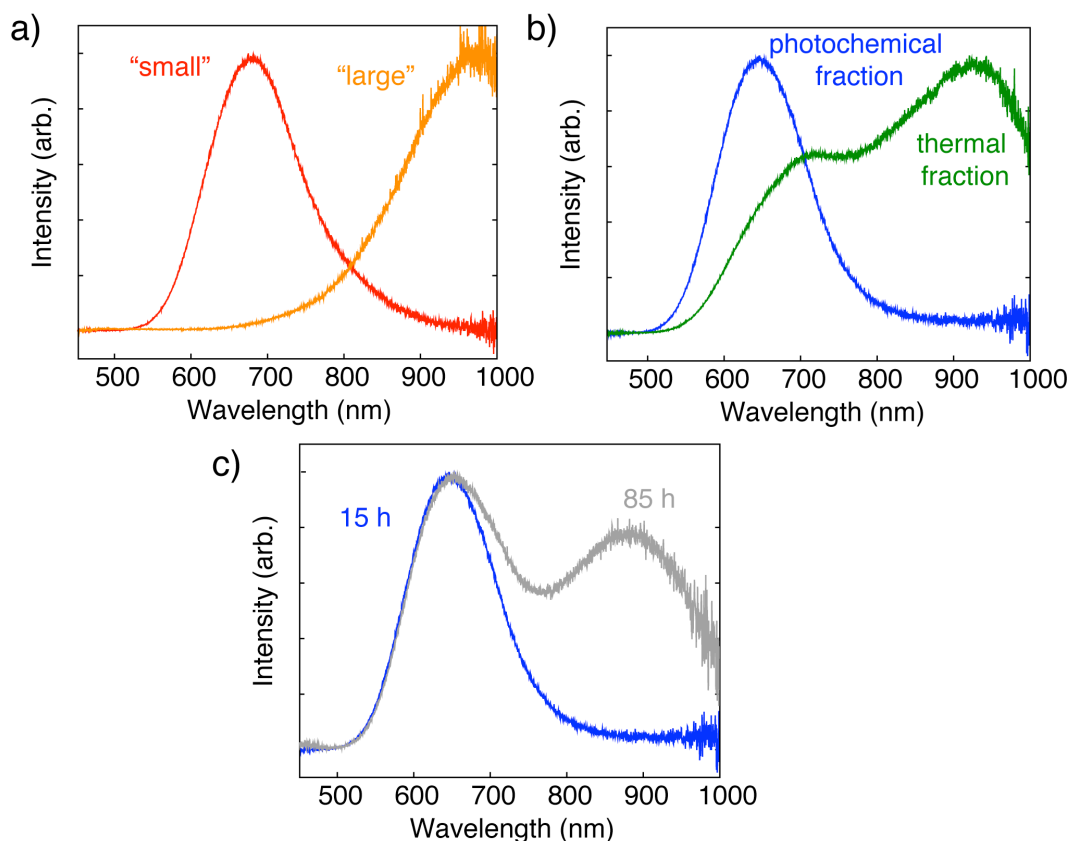
Figure 3-3: PL spectra of a) "small" and "large" Si-NCs functionalized by photochemical and thermal hydrosilylation with 1-dodecene, respectively; b) isolated fractions from sequential photochemical and thermal hydrosilylations with 1-dodecene with the "combined" Si-NC sample; c) photochemical fractions of the "combined" Si-NC sample after 15 and 85 h.

It is important to note that PL only probes the luminescent fraction of these samples, which are expected to contain a subpopulation of defect-ridden non-luminescent Si-NCs.[52] As well, PL spectroscopy could be affected by energy transfer processes that further hinder quantitative interpretation of the observed size-dependent reactivity. To better understand the size-dependent reactivity suggested

by the PL results, the Si-NC samples were also characterized using SAXS, shown for the "small" and "large" Si-NCs in Figure 3. Compared to other techniques (*e.g.*, atomic force microscopy or transmission electron microscopy, TEM), SAXS is a useful tool for rapid, quantitative determination of size and dispersity of nanomaterials, particularly for elements such as Si with low electron density contrast with carbon which can make TEM measurements very challenging.[31, 53-56] Fitting the SAXS data in Figure 3-3 to a spherical particle model with a Gaussian distribution gave average nanocrystal diameters of 2.9 ± 0.6 and 6.3 ± 1.0 nm for the "small" and "large" samples, respectively, in good agreement with previous high resolution TEM[30] and X-ray diffraction analysis.[46]
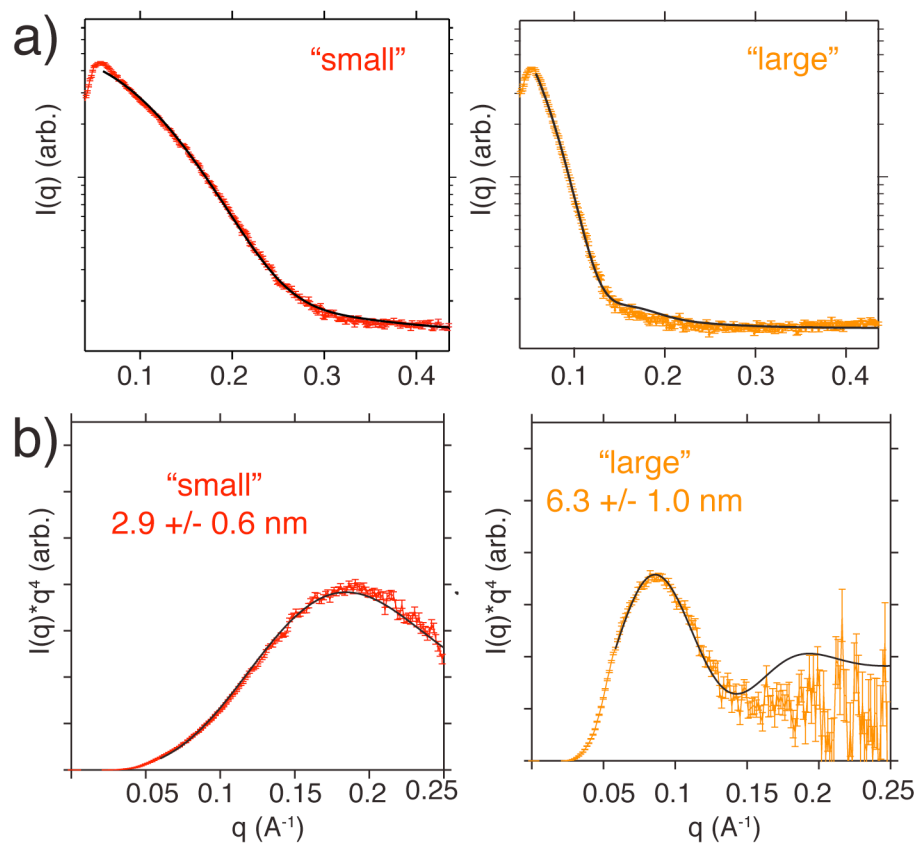
Figure 3-4: SAXS of "small" and "large" Si-NCs functionalized by photochemical and thermal hydrosilylation with 1-dodecene respectively: plotted as a) $I(q)$ vs. q and b) as a Porod plot with $I(q)*q^4$ vs q. Fitting the data to Equation 3.1 (solid black line, residual shown in b as a dashed grey line) gave average nanocrystal diameters of 2.9 ± 0.6 and 6.3 ± 1.0 nm for the "small" and "thermal" samples, respectively.

The validity of the SAXS fitting approach for determining the relative concentrations of each population was verified by comparing results of mixtures of the "small" and "large" samples in known ratios (*i.e.*, 1:2, 1:1, 10:1 and 25:1 "small": "large" mixtures, Figure 3-5). Fitting the SAXS data of the "combined" samples using the "small" and "large" populations revealed the relative volume fraction of each size

in the aliquot of well-functionalized particles isolated after each functionalization (Figure 3-6). As mentioned above, the 10:1 mixture in the initial hydride-terminated reaction mixture contains approximately equal volume fractions of each population. After photochemical functionalization, the relative volume fraction of the "small" population was found to be 70%. The subsequent thermal hydrosilylation gave a "small" volume fraction of 24%. Increasing the photochemical reaction time from 15 h to 85 h decreased the "small" volume fraction to 33%. However, it should be noted these fits assume the mean size of each population does not shift appreciably between the "combined" samples.

Although the blue shifted, slightly narrowed PL from the "combined" sample after 15 h of photochemical reaction is consistent with a shift in NC size, attempts to fit these data by allowing the size of each population to vary were unsuccessful. This lack of convergence may result from the challenge of allowing too many parameters to vary during the fitting, or from the role of surface states in shifting the PL rather than solely size effects.[57]
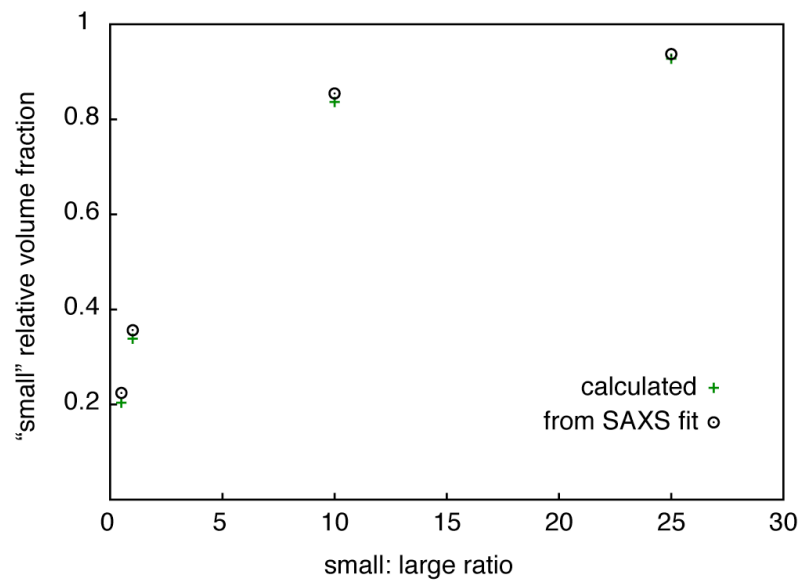
Figure 3-5: Calibration curve of relative volume fraction, obtained from fitting SAXS data of mixtures of small/large Si-NCs in known ratio.
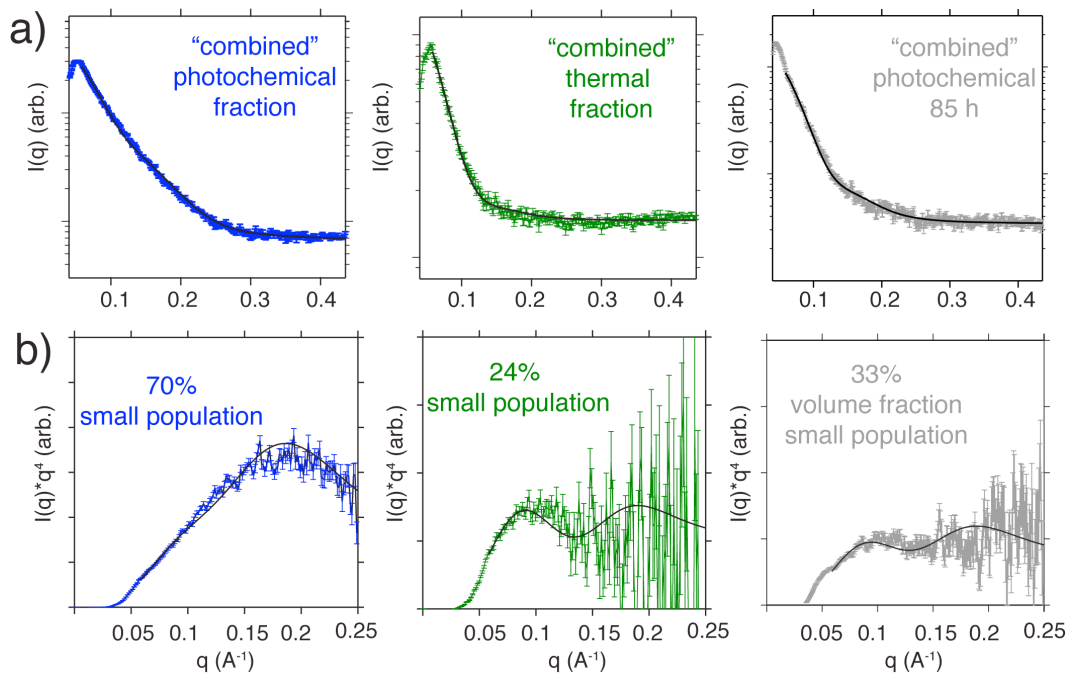
Figure 3-6: SAXS of fractions isolated from the "combined" samples after photochemical, thermal and extended photochemical hydrosilylation. plotted as a) *I(q)* vs. *q* and b) as a Porod plot with *I(q)*q⁴* vs *q*. The data were fit (solid black line, residual shown in b as a dashed grey line) to a linear combination of the populations obtained from SAXS of the "small" and "large" samples shown in Figure 3-4.

Although the SAXS data suggest a significant volume of large Si-NCs in the 15 h photochemical aliquot, seemingly at odds with the PL results which show no PL from the large fraction, it is feasible this could occur through a small number of the "large" Si-NCs reacting through an alternate free radical (non-size dependent) pathway somewhat analogous to the decomposition-initiated pathway in thermal hydrosilylation observed by Mischki *et al.*[16] Recall that PL only probes the luminescent fraction, which are expected to be well-passivated and defect-free; it is reasonable that a fraction of non-luminescent Si-NCs might contain a surface radical

defect that could initiate this process. As well, it is important to note the total number of Si-NCs in the "combined" samples is always dominated by the "small" fraction, and thus relatively few events occurring within the "large" fraction could conceivably skew the SAXS results owing to their larger volume per particle. The considerable difference in NC volume, the higher probability of the large NCs to contain volume defects,[58-60] and an extended chain length for the propagation reaction after relatively few initiation events[14] could all influence the increased volume fraction of the large population in the SAXS results.

The influence of size on the rate of the hydrosilylation of nanostructured Si surfaces using other initiation methods has been reported qualitatively. Hua *et al.* noted that deep-UV hydrosilylation of Si-NCs exhibits a size dependence, on the basis of the length of irradiation required for the dispersion to change from cloudy to clear.[61] This was attributed to the smaller NCs requiring a lower degree of alkyl grafting to produce stable colloidal dispersions. Although this is an important consideration (along with the other factors mentioned above) for the present results, it cannot account for the size-dependent reactivity observed, because similar degrees of alkyl and hydride FTIR stretching features would be expected for the small and large 15 h photochemical samples.

This observed size-dependent reactivity is consistent with the calculations of Reboredo *et al.*,[26] who predicted that exciton-mediated hydrosilylation involves a metastable transition state forming a localized midgap state (not size-dependent). The formation of this transition state was predicted to be energetically favorable if the initial energy of the (photoexcited and thus size-dependent) reactants were high

enough. These predictions are consistent with the present observation that the large population requires longer irradiation times to produce colloidal, luminescent NCs.

In Stewart and Buriak's original report of exciton-mediated hydrosilylation, the reactivity was proposed to be limited to nanoscale Si on the basis of limited reactivity observed with nonluminescent porous Si samples.[20] However, only luminescent samples with PL centered at *ca.* 600-640 nm were investigated. The subsequent reports by Zuilhof and coworkers suggesting that an exciton-mediated process initiated by visible light on bulk surfaces appears to conflict with Buriak's conclusion upon first inspection.[22-24] It is important to note (particularly for nanostructured Si surfaces) that although Si surfaces are known to share many common properties (*e.g.*, low toxicity and possible biodegradation pathways),[32, 33, 35, 62-65] they can exhibit substantial differences in surface chemistry, impurities, homogeneity, quantum size effects, *etc.* that could drastically influence the rate of hydrosilylation, and so a direct comparison between porous Si and the present freestanding Si-NCs may not be straightforward.

In the present system near-UV hydrosilylation with phenylacetylene was demonstrated to produce colloidal, non-luminescent Si-NC dispersions. Phenylacetylene was previously observed to be unreactive in visible light hydrosilylation with porous Si by Stewart and Buriak. Observations of low surface coverage was originally attributed this difference to the 365 nm light source having sufficient energy to directly initiate hydride homolysis (*i.e.*, following path A in Scheme 3-1).[30] In this mechanism, no size-dependent reactivity is expected, as the rate limiting step is direct photo-induced cleavage of the surface hydride.[7]

However, fitting SAXS data of a "combined" sample reacted photochemically for 15 h with phenylacetylene showed the same size-dependent reactivity observed with 1-dodecene, with a "small" Si-NC volume fraction of 69% (Figure 3-7). As these styrenyl-capped Si-NCs are non-luminescent, PL spectroscopy could not be used to assess the size-dependence of the reactivity. FTIR of the well-functionalized fraction (Figure 3-8) showed an increase in alkenyl stretching and decrease in hydride stretching features in comparison to non-functionalized NCs. Although the relative intensity of the hydride and oxide features is somewhat increased compared to the dodecyl-functionalized Si-NCs, suggesting a lower degree of surface coverage, this may also be related to the resulting smaller alkenyl group, decreased oscillator strength for alkene CH stretching vibrations compared to alkyl, or packing considerations of the surface styrenyl rings.[66, 67]
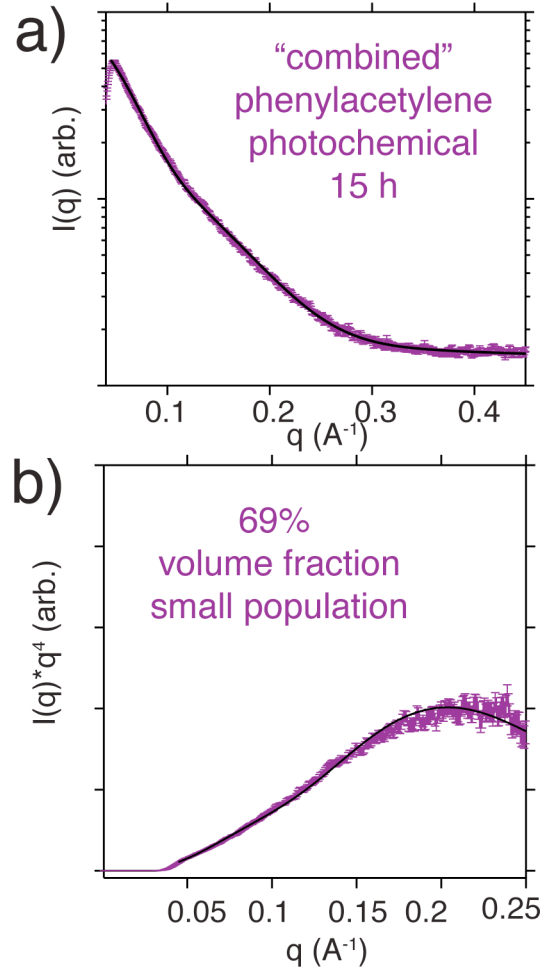
Figure 3-7: SAXS of the well-functionalized fraction isolated from the "combined" sample after photochemical hydrosilylation with phenylacetylene. Plotted as a) $I(q)$ vs. q and b) as a Porod plot with $I(q)*q^4$ vs q. The data were fit (solid black line, residual shown in b as a dashed grey line) to a linear combination of the populations obtained from SAXS of the "small" and "large" samples shown in Figure 3-4.
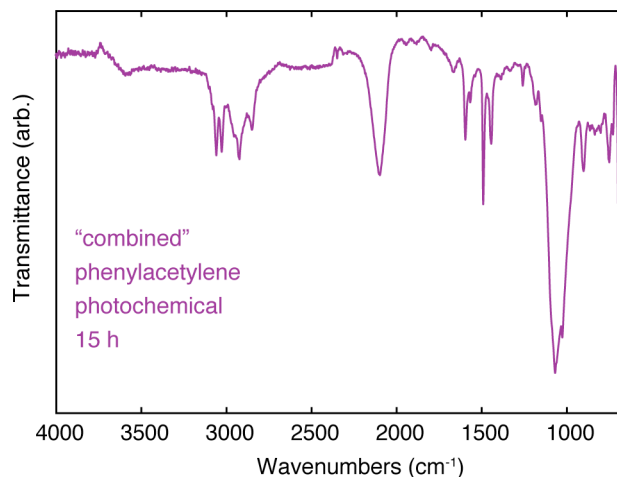
Figure 3-8: FTIR of the combined Si-NC sample photochemically functionalized with phenylacetylene.

The size-dependent reactivity observed with phenylacetylene implies an exciton-mediated mechanism rather than direct homolysis. Reaction with phenylacetylene quenches Si-NC PL, conflicting with the stipulations of Stewart and Buriak's nanoscale exciton-mediated mechanism (Path B, Scheme 3-1). They suggested that a small number of phenylacetylene molecules would react and then trap excitons, preventing further reaction. However, phenylacetylene is expected to be reactive in Zuilhof's exciton-mediated mechanism (Path C, Scheme 3-1) because excitons are only involved in the initial nucleophilic attack, with radical propagation driving subsequent functionalization. Indeed, alkynes have been suggested to be more reactive in this pathway owing to their increased nucleophilicity and ability to stabilize radicals through delocalization over the resulting surface vinyl group.[23] The difference between Stewart and Buriak's results with phenylacetylene and the present observations might arise from different absorption cross-sections at the irradiating

wavelength, as near-UV light corresponds to a direct gap transition. As mentioned above, Kanai and Selloni suggested that the radical propagation in Path C is more favorable than hydride abstraction from the reactive site for bulk Si.[27] However, the intermediate and transition states for both paths involve highly localized electronic distortions, whereas the Si-NC electronic states are delocalized over the entire nanocrystal (and thus are sensitive to size). The same considerations for size-dependent reactivity predicted by Reboredo *et al.*[26] for Path B are therefore expected to hold for Path C, in keeping with the present observations.

3.4 Conclusions

In summary, the influence of size on the reactivity of Si-NCs in near-UV hydrosilylation was demonstrated using PL, FTIR and SAXS. These results are in keeping with the size-dependent reactivity predicted by theoretical studies of exciton-mediated mechanisms, with larger NCs reacting at a slower rate through the influence of quantum size effects. Size-dependent reactivity was observed in hydrosilylation with both 1-dodecene and phenylacetylene, suggesting the exciton mechanisms may be dominant in near-UV initiation in either radical and non-radical hydrosilylation rather than direct hydride homolysis. Mechanistic considerations in the functionalization of Si-NCs by hydrosilylation could be important for selecting a set of reaction conditions for a desired Si-NC size and olefin to be grafted.

3.5 References

1. Linford, M. R.; Chidsey, C. E. D. *J. Am. Chem. Soc.* **1993**, *115*, 12631-12632.

2. Buriak, J. M. *Chem. Rev.* **2002**, *102*, 1271-1308.

3. Veinot, J. G. C. *Chem. Commun.* **2006**, , 4160-4168.

4. Ciampi, S.; Harper, J. B.; Gooding, J. J. *Chem. Soc. Rev.* **2010**, *39*, 2158-2183.

5. Rosso-Vasic, M.; Spruijt, E.; Popović, Z.; Overgaag, K.; Van Lagen, B.; Grandidier, B.; Vanmaekelbergh, D.; Domínguez-Gutiérrez, D.; De Cola, L.; Zuilhof, H. *J. Mater. Chem.* **2009**, *19*, 5926-5933.

6. Li, X.; He, Y.; Swihart, M. T. *Langmuir* **2004**, *20*, 4720-4727.

7. Cicero, R. L.; Linford, M. R.; Chidsey, C. E. D. *Langmuir* **2000**, *16*, 5688-5695.

8. Effenberger, F.; Götz, G.; Bidlingmaier, B.; Wezstein, M. *Angew. Chem. Int. Ed.* **1998**, *37*, 2462-2464.

9. Boukherroub, R.; Morin, S.; Bensebaa, F.; Wayner, D. D. M. *Langmuir* **1999**, *15*, 3831-3835.

10. Linford, M. R.; Fenter, P.; Eisenberger, P. M.; Chidsey, C. E. D. *J. Am. Chem. Soc.* **1995**, *117*, 3145-3155.

11. Cicero, R. L.; Chidsey, C. E. D.; Lopinski, G. P.; Wayner, D. D. M.; Wolkow, R. A. *Langmuir* **2002**, *18*, 305-307.

12. Loplnski, G. P.; Wayner, D. D. M.; Wolkow, R. A. *Nature* **2000**, *406*, 48-51.

13. Chatgilialoglu, C.; Timokhin, V. I. *Adv. Organomet. Chem.* **2008**, *57*, 117-181.

14. Woods, M.; Carlsson, S.; Hong, Q.; Patole, S. N.; Lie, L. H.; Houlton, A.; Horrocks, B. R. *J. Phys. Chem. B* **2005**, *109*, 24035-24045.

15. Eves, B. J.; Lopinski, G. P. *Langmuir* **2006**, *22*, 3180-3185.

16. Mischki, T. K.; Lopinski, G. P.; Wayner, D. D. M. *Langmuir* **2009**, *25*, 5626-5630.

17. Wang, X.; Ruther, R. E.; Streifer, J. A.; Hamers, R. J. *J. Am. Chem. Soc.* **2010**, *132*, 4048-4049.

18. Boukherroub, R.; Morin, S.; Wayner, D. D. M.; Bensebaa, F.; Sproule, G. I.; Baribeau, J. -M.; Lockwood, D. J. *Chem. Mater.* **2001**, *13*, 2002-2011.

19. Coletti, C.; Marrone, A.; Giorgi, G.; Sgamellotti, A.; Cerofolini, G.; Re, N. *Langmuir* **2006**, *22*, 9949-9956.

20. Stewart, M. P.; Buriak, J. M. *J. Am. Chem. Soc.* **2001**, *123*, 7821-7830.

21. Sun, Q. -Y.; De Smet, L. C. P. M.; Van Lagen, B.; Giesbers, M.; Thüne, P. C.; Van Engelenburg, J.; De Wolf, F. A.; Zuilhof, H.; Sudhölter, E. J. R. *J. Am. Chem. Soc.* **2005**, *127*, 2514-2523.

22. Scheres, L.; Arafat, A.; Zuilhof, H. *Langmuir* **2007**, *23*, 8343-8346.

23. Scheres, L.; Giesbers, M.; Zuilhof, H. *Langmuir* **2010**, *26*, 10924-10929.

24. Eves, B. J.; Sun, Q. -.; Lopinski, G. P.; Zuilhof, H. *J. Am. Chem. Soc.* **2004**, *126*, 14318-14319.

25. Reed, C. A. *Acc. Chem. Res.* **1998**, *31*, 325-332.

26. Reboredo, F. A.; Schwegler, E.; Galli, G. *J. Am. Chem. Soc.* **2003**, *125*, 15243-15249.

27. Kanai, Y.; Selloni, A. *J. Am. Chem. Soc.* **2006**, *128*, 3892-3893.

28. Cullis, A. G.; Canham, L. T.; Calcott, P. D. J. *J. Appl. Phys.* **1997**, *82*, 909-965.

29. Wolkin, M. V.; Jorne, J.; Fauchet, P. M.; Allan, G.; Delerue, C. *Phys. Rev. Lett.* **1999**, *82*, 197-200.

30. Kelly, J. A.; Veinot, J. G. C. *ACS Nano* **2010**, *4*, 4645-4656.

31. Hessel, C. M.; Rasch, M. R.; Hueso, J. L.; Goodfellow, B. W.; Akhavan, V. A.; Puvanakrishnan, P.; Tunnel, J. W.; Korgel, B. A. *Small* **2010**, *6*, 2026-2034.

32. Erogbogbo, F.; Yong, K. -.; Roy, I.; Xu, G. X.; Prasad, P. N.; Swihart, M. T. *ACS Nano* **2008**, *2*, 873-878.

33. Park, J. -H.; Gu, L.; von Maltzahn, G.; Ruoslahti, E.; Bhatia, S. N.; Sailor, M. J. *Nature Materials* **2009**, *8*, 331-336.

34. Erogbogbo, F.; Yong, K. -T.; Hu, R.; Law, W. -.; Ding, H.; Chang, C. -.; Prasad, P. N.; Swihart, M. T. *ACS Nano* **2010**, *4*, 5131-5138.

35. Erogbogbo, F.; Yong, K.; Roy, I.; Hu, R.; Law, W.; Zhao, W.; Ding, H.; Wu, F.; Kumar, R.; Swihart, M. T.; Prasad, P. N. *ACS Nano* **2011**, *5*, 413-423.

36. Law, M.; Luther, J. M.; Song, Q.; Hughes, B. K.; Perkins, C. L.; Nozik, A. J. *J. Am. Chem. Soc.* **2008**, *130*, 5974-5985.

37. Talapin, D. V.; Murray, C. B. *Science* **2005**, *310*, 86-89.

38. Kovalenko, M. V.; Scheele, M.; Talapinl, D. V. *Science* **2009**, *324*, 1417-1420.

39. Cornelisse, J. *Chem. Rev.* **1993**, *93*, 615-669.

40. Song, J. H.; Sailor, M. J. *J. Am. Chem. Soc.* **1997**, *119*, 7381-7385.

41. Wang, D.; Buriak, J. M. *Langmuir* **2006**, *22*, 6214-6221.

42. Content, S.; Trogler, W. C.; Sailor, M. J. *Chem. Eur. J.* **2000**, *6*, 2205-2213.

43. Hessel, C. M.; Henderson, E. J.; Veinot, J. G. C. *Chem. Mater.* **2006**, *18*, 6139-6146.

44. Kelly, J. A.; Henderson, E. J.; Veinot, J. G. C. *Chem. Commun.* **2010**, *46*, 8704-8718.

45. Jackson, H. L.; McCormack, W. B.; Rondestvedt, C. S.; Smeltz, K. C.; Viele, I. E. *J. Chem. Educ.* **1970**, *47*, A175-A188.

46. Hessel, C. M.; Henderson, E. J.; Veinot, J. G. C. *J. Phys. Chem. C* **2007**, *111*, 6956-6961.

47. Glatter, O; Kratky, O., Eds.; *Small-angle X-ray Scattering* Academic Press: New York, 1982.

48. Ilavsky, J.; Jemian, P. R. *J. Appl. Cryst.* **2009**, *42*, 347-353.

49. Weissleder, R. *Nat. Biotechnol.* **2001**, *19*, 316-317.

50. Beard, M. C.; Knutsen, K. P.; Yu, P.; Luther, J. M.; Song, Q.; Metzger, W. K.; Ellingson, R. J.; Nozik, A. J. *Nano Lett.* **2007**, *7*, 2506-2512.

51. Lockwood, R.; Hryciw, A.; Meldrum, A. *Appl. Phys. Lett.* **2006**, *89*.

52. Wilson, W. L.; Szajowski, P. F.; Brus, L. E. *Science* **1993**, *262*, 1242-1244.

53. Choi, J.; Tung, S. -.; Wang, N. S.; Reipa, V. *Nanotechnology* **2008**, *19*.

54. Matsumoto, T.; Suzuki, J. -.; Ohnuma, M.; Kanemitsu, Y.; Masumoto, Y. *Phys. Rev. B Condens. Matter* **2001**, *63*, 1953221-1953225.

55. Gracin, D.; Bernstorff, S.; Dubcek, P.; Gajovic, A.; Juraic, K. *J. Appl. Cryst.* **2007**, *40*, s373-s376.

56. Bernstorff, S.; Dubček, P.; Kovačević, I.; Radić, N.; Pivac, B. *Thin Solid Films* **2007**, *515*, 5637-5640.

57. Kelly, J. A.; Henderson, E. J.; Clark, R. J.; Hessel, C. M.; Cavell, R. G.; Veinot, J. G. C. *J. Phys. Chem. C* **2010**, *114*, 22519-22525.

58. Cheylan, S.; Elliman, R. G. *Nucl. Instrum. Methods Phys. Res., Sect. B* **2001**, 175-177, 422-425.

59. Cheylan, S.; Elliman, R. G. *Appl. Phys. Lett.* **2001**, *78*, 1912-1914.

60. Cheylan, S.; Elliman, R. G. *Appl. Phys. Lett.* **2001**, *78*, 1225-1227.

61. Hua, F.; Swihart, M. T.; Ruckenstein, E. *Langmuir* **2005**, *21*, 6054-6062.

62. Alsharif, N. H.; Berger, C. E. M.; Varanasi, S. S.; Chao, Y.; Horrocks, B. R.; Datta, H. K. *Small* **2009**, *5*, 221-228.

63. Bayliss, S. C.; Heald, R.; Fletcher, D. I.; Buckberry, L. D. *Adv. Mater.* **1999**, *11*, 318-321.

64. Nagesha, D. K.; Whitehead, M. A.; Coffer, J. L. *Adv. Mater.* **2005**, *17*, 921-924.

65. Low, S. P.; Voelcker, N. H.; Canham, L. T.; Williams, K. A. *Biomaterials* **2009**, *30*, 2873-2880.

66. Bateman, J. E.; Eagling, R. D.; Horrocks, B. R.; Houlton, A. *J. Phys. Chem. B* **2000**, *104*, 5557-5565.

67. Sieval, A. B.; Vleeming, V.; Zuilhof, H.; Sudholter, E. J. R. *Langmuir* **1999**, *15*, 8288-8291.

Chapter 4:

Hydrofluoric Acid

Etching of

Silicon Nanocrystals[*]

4.1 Introduction

Chief among synthetic considerations for nanomaterials is precise control over their size and polydispersity. Prime examples of this are the successful wet chemical syntheses for compound semiconductor nanocrystals (NCs, e.g., CdSe, CdS) first investigated by Brus.[1] Polydispersities (σ) of 4-6% are now routine,[2, 3] enabling study of the unique optoelectronic phenomena exhibited by these materials (e.g., size dependent absorption and emission of light,[4] multiple exciton generation[5]) as well as increasing their potential in numerous applications (e.g., narrow photoluminescence, PL, for multiplexed biological imaging[6, 7] and self-assembed nanoparticle superlattices[8]).

By comparison, polydispersities of silicon and other group 14 NCs have remained substantially broader, with typical standard deviations around 15-25% which is a dominant factor for inhomogeneous broadening of the PL bandwidths.[9] This can be attributed in part to the higher temperatures needed to crystallize these materials,[10] which presents a challenge for exploiting the "focusing" phase credited with the narrow size distributions for compound semiconductor wet chemical methods.[11] The biocompatibility of Si-NCs may enable their use in areas where concerns over leaching of Cd^{2+} or other toxic ions may limit the development of some compound semiconductor NCs.[12-17] Thus, a successful strategy to narrow the polydispersity of Si-NCs to produce well-defined optical properties might have considerable fundamental and technological significance.

Beginning with the discovery of intense PL from the prototypical Si nanostructure porous Si,[18] hydrofluoric acid (HF) etching is a popular "top-down"

approach for the size control of Si nanomaterials. Owing to the very strong, highly polarized Si-F bond, HF rapidly etches away Si oxides, leaving hydrophobic, hydride-terminated Si surface. Because of this reactivity towards Si oxides, HF etching is frequently employed to control the size of Si nanostructures in a oxidize/etch process. For example, Swihart's group has employed HF/HNO_3 etching to control the size dispersity and optical properties of freestanding Si-NCs derived laser pyrolysis of silane.[19, 20] Similarly, Reipa *et al.* investigated etching of Si-NCs derived from porous Si with HF/HNO_3, noting the etching rate could be influenced by irradiating the reaction mixture with near-UV light.[21] This was proposed to occur through photocatalyzed oxidation. Similar observations have also been reported for etching of Ge-NCs.[22]

The mechanism of the oxidize/etch process is well understood (Scheme 4-1A). Oxidation of Si surfaces leads to the formation of silanol (Si-OH) and bridging oxides (Si-O-Si); the etching mechanism of SiO_2 and other oxides proceeds similarly through the presence of these species. Owing to the large difference in electronegativity between Si and O (1.9 versus 3.4 on the Pauling scale), polar oxide bonds deplete Si of electron density, and invites nucleophilic attack from HF to form a Si-F bond. Under acidic conditions, the O species can be protonated, making it a better leaving group. Once one Si-F bond has been formed, the Si atom is further depleted of electron density (F has an electronegativity of 4.0 on the Pauling scale), and rapidly attracts further nucleophilic attack from additional HF species. Gaseous SiF_4 is quickly liberated, leaving behind a hydride-terminated surface as the kinetic product.

In addition to the use of a tandem oxidize/etch pathway for top-down size control, HF etching of hydride-terminated bulk and nanostructured Si can be directly initiated by exciton-mediated hole capture at the surface, arising either from absorption of light or under anodic electrochemical conditions (Scheme 4-1B).[23, 24] This etching process is very similar to the oxidize/etch pathway but importantly does not require an electronegative atom bonded to Si to initiate the etching process. In this case, the localization of a hole in a silicon atom is what polarizes the bond and drives nucleophilic attack. As will be discussed in more detail below, this exciton-mediated pathway is responsible for the formation of luminescent porous Si through the influence of quantum size effects.

a) oxidize/etch pathway
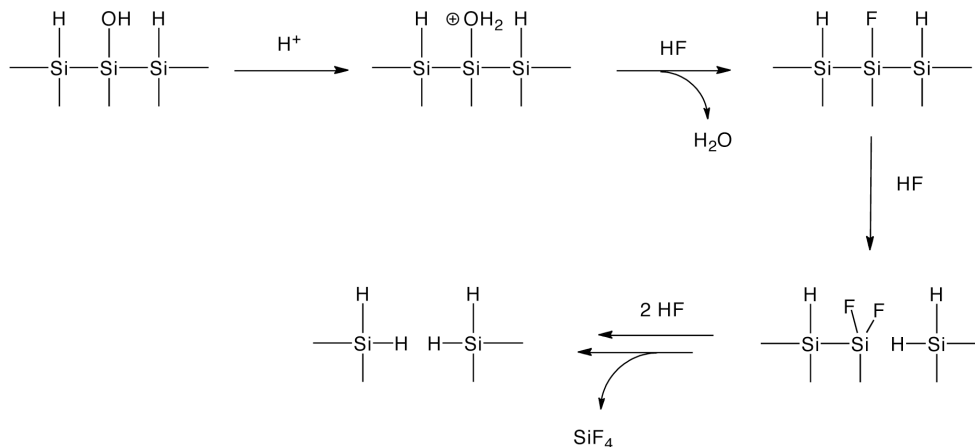
b) exciton-mediated pathway
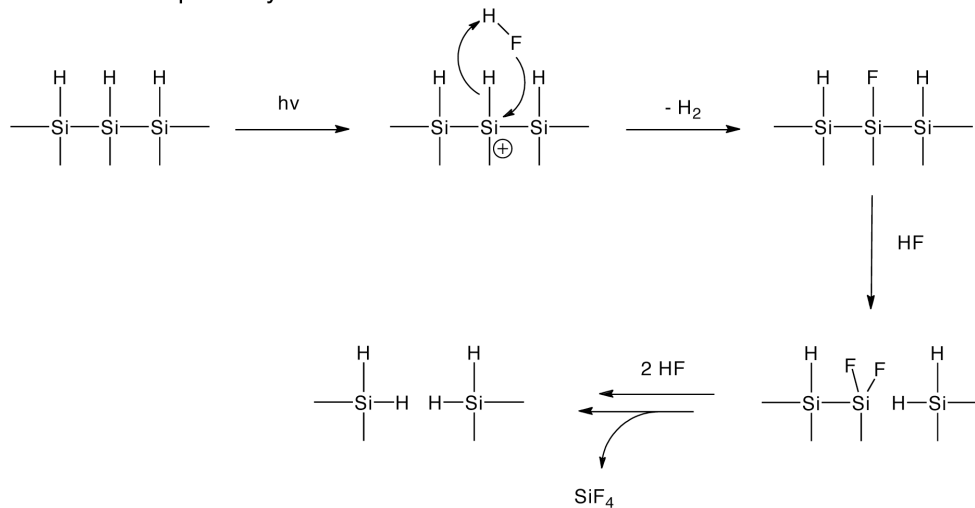
Scheme 4-1: a) HF etching mechanism starting from a surface silanol (Si-OH). b) Light-assisted HF etching mechanism of a surface hydride (Si-H).

Reported etch rates of nanostructured Si vary substantially depending on reagent concentrations, pH, composition, morphology and other factors. For example, the etching of oxide-embedded Si-NC composites derived from HSQ using a HF/water/ethanol mixture yields freestanding NCs with emission spanning the

visible spectral region (referred to as the "water" etching method throughout the present text).[25] Compared to other etching procedures employing HNO_3 (*vide supra*), the etch rate is much slower, requiring *ca.* 1 h to fully remove all SiO_2, during which the NC diameter is reduced from *ca.* 4 to 2-3 nm.[26] The grain size of the ground composite powder and the stirring speed markedly impacts the etch rate, with larger grains slowing the rate and broadening the resulting PL. Grinding the composite using a wrist-action shaker resulted in a mean grain size of *ca.* 200 nm, and a more homogeneous etch rate. Although annealing HSQ at higher temperatures yields larger Si-NCs (up to *ca.* 14 nm at 1400°C),[27] initial attempts to utilize this etching recipe on larger Si-NC composites were unsuccessful, with significant amounts of SiO_2 remaining after extended etching.

Here, a modified etching procedure of oxide-embedded Si-NC composites is described (referred to as the "acid" etching method throughout the present text), using a much higher HF concentration (49%) and lowering the pH through the addition of HCl. The advantages of this modified procedure are two-fold:

1) As noted by Spierings,[28] the etch rate of amorphous SiO_2 is greatly enhanced at higher HF concentrations because of the formation of polymeric $H_nF_{n+1}^-$ ions, which are more reactive toward Si-O bonds. Lowering the pH also increases the SiO_2 etching rate through the catalytic role of H_3O^+ by protonating oxide species. Significantly increasing the SiO_2 etch rate eliminates the dependence of the Si-NC etch rate on the composite grain size, and allows the complete removal of the oxide before noticibly shifting the Si-NC size. This new etching procedure facilitates the liberation of larger Si-NCs.

135

2) Owing to the increased stability of Si hydride species in acidic media,[29] the oxidize/etch pathway is limited. Instead, here it is shown Si-NC etching proceeds through the exciton-mediated pathway. In the formation of porous Si, etching by this pathway has been identified as a key factor in the production of nanoscale, luminescent structures through the influence of quantum confinement effects.[24] As the nanostructures are etched below 5 nm (the exciton Bohr radius),[30] their bandgap begins to widen, lowering the energy of holes in the valence band. As holes "bubble up" to the highest electronic state available, preferential etching of non-quantum-confined crystallites occurs.

Quantum confinement effects analogously affect light absorption in Si-NCs, presenting an interesting strategy for size selection based on photochemical, exciton-mediated etching. By irradiating the reaction mixture during HF etching at high HF concentration and low pH, larger Si-NCs with bandgaps equal or lower in energy than the irradiating wavelength would be anticipated to be preferentially etched, leading to a narrowing of sample polydispersity.

To test this hypothesis, the influence of irradiating wavelength on the resulting Si-NC PL, size and polydispersity have been investigated under the "acid" etching conditions. The results suggest this approach can yield improvements in Si-NC polydispersity under certain conditions.

4.2 Materials and methods

4.2.1 Materials

HSQ (Dow Corning, trade name FOx-17, sold as a solution in methyl isobutyl ketone and toluene), 49% hydrofluoric acid (HF, J.T. Baker, electronics grade), and anhydrous ethanol (Sigma-Aldrich) were used as received. High-purity water (18.2 MΩ/cm) was obtained from a Barnstead Nanopure Diamond purification system. All other reagents were purchased from Sigma Aldrich as the highest purity available (95% or greater). 1-Dodecene was purified before use by passing over neutral activated alumina to remove peroxide impurities.[31]

4.2.2 Synthesis of oxide-embedded Si-NCs

Oxide-embedded Si-NC composites were prepared from HSQ as previously described by thermal processing under 5% H_2/95% Ar for 1 h.[25] Previous X-ray diffraction characterization has shown heating at temperatures ranging from 1100°C to 1400°C yields Si-NCs from *ca.* 4 nm up to 14 nm.[27] The glassy brown solids were ground in a mortar and pestle into a free flowing powder.

4.2.3 Hydrofluoric acid (HF) etching

Etching of oxide-embedded Si-NC composites by two different methods were compared. In the previously described "water" etch,[25] 100 mg of mechanically ground composite was added to a polypropylene beaker equipped with a stir bar along with 3 mL of a 1:1:1 mixture of 49% HF, water and anhydrous ethanol. The mixture was stirred, and 100 μL aliquots were extracted with a small volume of

toluene for PL spectroscopy. Alternatively, the etching mixture was extracted with two 15 mL aliquots of toluene for thermal hydrosilylation (*vide infra*).

In a modified "acid" etching procedure, 100 mg of the oxide-embedded Si-NC composite, 75 μL concentrated HCl and 3 mL 49% HF was added sequentially to a polypropylene beaker equipped with a stir bar. The reaction mixture was stirred for 5 min, during which vigorous bubbling was observed. 1.5 mL of ethanol was then added, and the mixture was stirred for a controlled period of time, either in the dark, under ambient laboratory lighting, or under illumination from a light source of controlled wavelength and power. Several light sources were employed yielding similar trends in etching behaviour: a Xenon light source equipped with a monochromator, whose output had been calibrated using an Ocean Optics USB2000+ spectrometer (full-width at half maximum of *ca.* 28 nm, power of 2.75± 0.25 mW measured incident to the etching solution); the 568 nm line of a variable wavelength Ar^+/Kr^+ laser (40 mW); and a 660 nm laser diode (186 mW). 100 μL aliquots were extracted with a small volume of toluene for PL spectroscopy every 2 h and extracted with 2 mL toluene. After completion of the etch, hydride-terminated Si-NCs for thermal hydrosilylation were isolated by extraction with two 15 mL aliquots of toluene.

4.2.4 Thermal hydrosilylation

The toluene extracts were transferred into centrifuge tubes and centrifuged at 3,000 rpm. The toluene was decanted, and the precipitated Si-NCs were redispersed in 10 mL freshly purified 1-dodecene and transferred to a Schlenk flask equipped

with a stir bar under an argon atmosphere. The reaction mixture was degassed by three cycles of evacuation and purging with argon and placed in a silicon oil bath heated at 190°C for 15 h. The reaction mixture typically turned from turbid to transparent in the first 3 h of heating.

4.2.5 Si-NC purification

Following photochemical functionalization, the reaction mixtures were transferred into centrifuge tubes and spun at 3,000 rpm to precipitate any unreacted NCs. The supernatant from each reaction was filtered through a 250 nm PTFE syringe filter into a 50 mL centrifuge tube and precipitated by the addition of 37.5 mL of a 3:1 ethanol/methanol mixture and centrifugation (25,900 G) because of the insolubility of 1-dodecene in methanol. Three additional purification by centrifugation cycles were performed using toluene and methanol as the solvent/antisolvent (procedure described in detail in Chapter 2).

4.2.6 Materials characterization and instrumentation

4.2.6.1 Photoluminescence (PL) spectroscopy

Photoluminescence (PL) spectra were acquired on dilute toluene dispersions excited with the 325 nm line of a He/Cd laser. Luminescence between 350 and 1100 nm was detected using an Ocean Optics USB2000+ spectrometer whose spectral response was calibrated with a blackbody radiator.

4.2.6.2 Fourier Transform Infrared Spectroscopy (FTIR)

FTIR spectra were collected using a Nicolet Magna 750 IR spectrometer on drop-cast films. Owing to the low volatility of toluene, freshly etched samples were instead extracted with hexane for analysis.

4.2.6.3 Small-Angle X-ray Scattering (SAXS)

SAXS was performed on dilute dispersion of silicon nanocrystals in toluene sealed in a boron-rich silicate capillary (Charles Supper, 2 mm outer diameter, 80 mm length, 10 μm wall thickness). Measurements were performed using a Bruker NanoStar with a rotating copper anode X-ray generator (λ = 1.54 Å) operating at 5.5 kW. The scattered photons were collected on a 2D multiwire gas-filled detector (Bruker HiStar.) and the scattering angle was calibrated using a silver behenate ($CH_3(CH_2)_{20}COOAg$) standard. Radial integrations of scattering intensity were performed using Bruker GADDS software. Experimental data was corrected for background scattering. Data were fit to a spherical particle model with a Gaussian size distribution, described in detail in Chapter 3.

4.2.6.4 Transmission Electron Microscopy (TEM)

High resolution TEM was performed using a Titan[3] G2 60-300 TEM operating at 300 kV. Selected area electron diffraction (SAED) and energy dispersive X-ray spectroscopy (EDS) were acquired with a FEI Titan 80-300 operated at 300 kV and equipped with a spherical aberration corrector of the imaging lens. Prior to analysis, functionalized samples were purified through two additional solvent/antisolvent cycles and resuspended in chloroform to fully remove any organic

species that might have hindered analysis through electron-beam induced decomposition. Samples were dropcoated from a dilute chloroform dispersion onto a carbon-coated copper grid.

4.3 Results and discussion

4.3.1 Comparison between etching procedures

The "water" and "acid" etching recipes were compared in the etching of oxide-embedded Si-NC composites processed at 1100°C and 1400°C. As previously reported, etching 1100°C-processed composite using the "water" recipe yields freestanding, hydride-terminated Si-NCs *ca.* 2-3 nm in diameter. After 2.5 h etching of 1400°C-processed composite using the "water" recipe, an intense Si-O-Si stretching band at *ca.* 1000-1100 cm^{-1} is still observed by FTIR spectroscopy (Figure 4-1). As well, in the Si-H$_x$ stretching region (*ca.* 2100 cm^{-1}), a distinct three-part structure is observed, with distinct features corresponding to Si-H$_3$, Si-H$_2$ and Si-H species at *ca.* 2140, 2100 and 2087 cm^{-1}. In comparison, after 5 min of etching 1400°C composite using the "acid" recipe, little or no Si-O-Si stretching can be observed, with the spectrum dominated by Si-H$_x$ stretching (with a relative increase in the Si-H$_2$ component) and scissoring vibrations at *ca.* 2100 and 910 cm^{-1} respectively. Alkyl stretching and bending vibrations are observed for the "water" etched sample, attributed to residual hexanes in the drop-cast film.
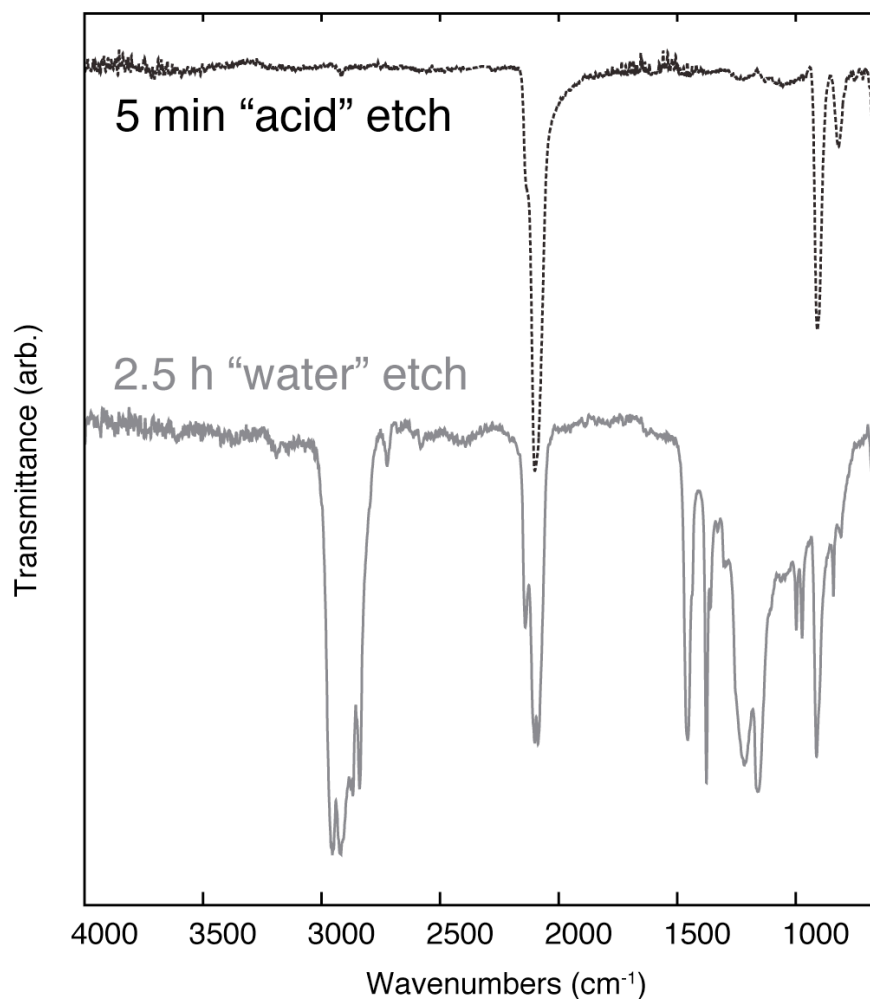
Figure 4-1: Comparison of FTIR spectra of hydride-terminated Si-NCs from 1400°C-processed composite etched using the "acid" (top, dotted black trace) and "water" (bottom, solid grey trace) recipes.

As noted above, the rate of etching in the "water" recipe (as measured by the Si-NC PL shift) is appreciably influenced by the stirring rate of the reaction mixture. This observation implies the reaction is limited by diffusion of the etching species onto the surface of the composite, as stirring changes the diffusion boundary layer thickness.[32] However, the etching rate of amorphous silica is known to be insensitive

143

to agitation rate,[32] suggesting the rate of etching in the "water" recipe is limited through the influence of the hydrophobic hydride-terminated Si-NC surfaces formed during etching. A possible explanation for the influence of the hydride terminated Si-NCs is depicted in Scheme 4-2. In the "water" etch, SiO_2 is etched away from the composite until the hydride surface of the embedded Si-NCs are revealed. Etching of the SiO_2 is then slowed because of the unfavorable interaction between the highly polarized HF molecules and the hydrophobic surface. Despite the residual oxide observed by FTIR, the partially etched 1400°C-composite is still hydrophobic enough to be extracted into toluene, consistent with the formation of hydride species at the surface of the composite.

Si-NC surface oxidation (*e.g.*, through photo-induced oxidation in the presence of water or oxygen[33]) facilitates HF etching through the oxidize/etch pathway, reducing their diameter and allowing more HF to attack the residual oxide matrix. This observation is consistent with the blue shift in PL observed for "water" etching of the 1100°-composite. Etching of the 1400°C composite is thus expected to be slower through the increased hydrophobic surface area revealed during etching. Gradual oxidation of the exposed Si-NC hydride surface leads to surface "roughening", consistent with the observation of increased $Si-H_3$ and Si-H species through the formation of thermodynamically-favoured (111) facets (similar to the roughening of Si 100 bulk surfaces etched with dilute HF[34]).

It has been noted that the HF etching of amorphous silica can proceed preferentially at flaws or "microcracks" in the surface.[28] This behavior could explain the vastly increased rate of Si-NC liberation for the "acid" recipe, as the very fast

etching of SiO_2 (through the impact of increased HF concentration and lowered pH) could dissolve the connective oxide matrix before the hydrophobic Si-NC surfaces begin to impede the etching rate.
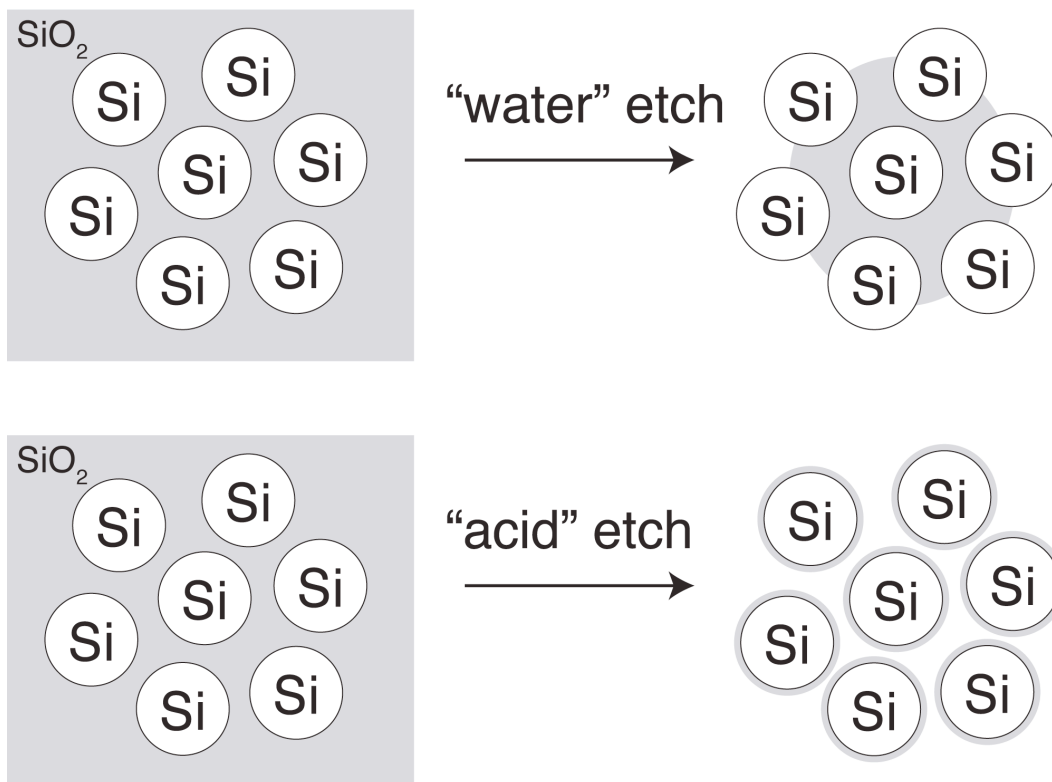
Scheme 4-2: Depiction of the possible influence of the hydride-terminated Si-NC surfaces on the "water" and "acid" etching recipes.

The use of the "acid" etching procedure is interesting for the liberation of Si-NCs larger than previously studied. After "acid" etching, hydride-terminated Si-NCs from composites processed from 1100° to 1400°C were readily functionalized through thermal hydrosilylation with 1-dodecene at 190°C, resulting in colloidally-dispersed Si-NCs. These Si-NCs exhibit lattice fringes expected for crystalline Si, as shown by HRTEM analysis (Figure 4-2).
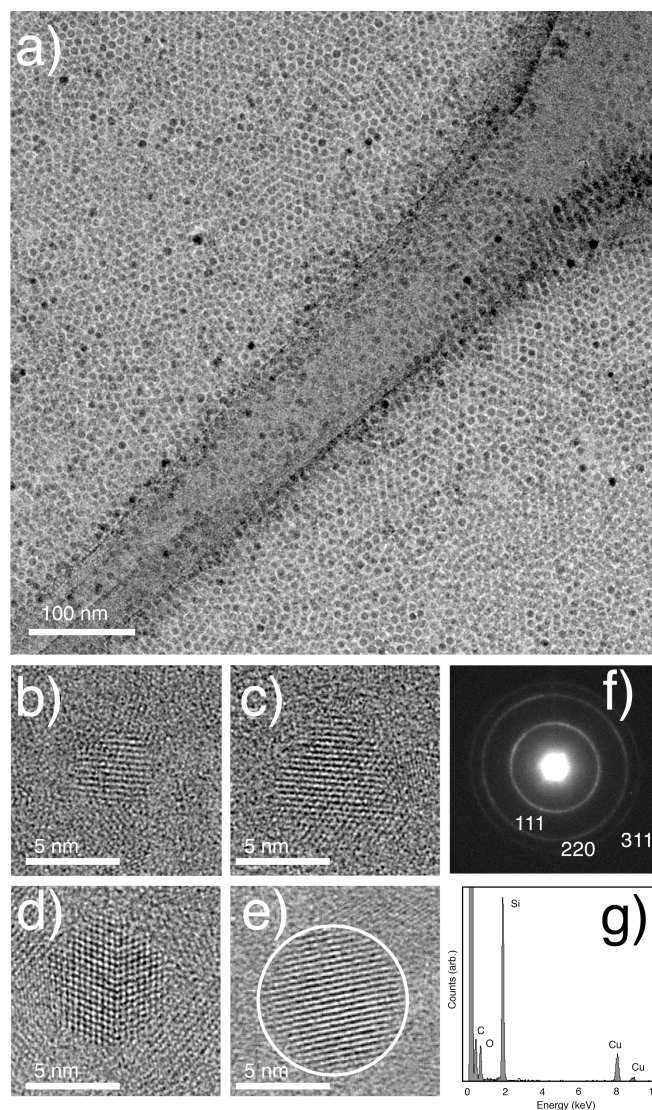
Figure 4-2: a) Low-resolution TEM of 1400°C-processed Si-NCs liberated using the "acid" etch and functionalized via thermal hydrosilylation. b-e) High-resolution TEMs of freestanding Si-NCs processed from 1100-1400°C showing lattice fringes characteristic of crystalline Si. The circled particle in e) had a lattice spacing of 3.1Å consistent with the Si 111 plane. f) SAED pattern of 1400°C-processed Si-NCs exhibiting the (111), (220) and (311) planes of diamond type Si. g) EDS spectrum of 1100°C-processed Si-NCs showing the presence of Si, C and O. The Cu signal arises from the grid.

4.3.2 Wavelength dependent photo-assisted HF etching

HF etching of Si nanostructures often employs a strong oxidizing agent such as HNO_3 for size control through the oxize/etch pathway described above. However, this pathway is also active in the "water" etching recipe previously described for this system,[25] through oxidation of the surface by water.[33] Initial attempts to control Si-NC size by irradiating the "water" etching mixture through an exciton-mediated strategy proved unsuccessful, as the Si-NC PL blue shifted even in the dark, suggesting photo-induced exciton formation did not substantially influence the etching rate. However, lowering the pH by addition of a strong acid provides a convenient way to "trap" any water as H_3O^+, an electrophile incapable of oxidizing the NC surface. The addition of HCl to the etching mixture to lower the pH substantially reduces the rate of oxidation, and allows the influence of exciton-mediated etching to be observed.

Figure 4-1 shows the PL maxima of hydride-terminated Si-NCs during "acid" etching as a function of irradiating wavelength. The PL from Si-NCs etched in the dark did not shift appreciably from *ca.* 800 nm, even after 10 h of etching. By comparison, using the "water" etch recipe in the dark resulted in a PL blue-shift of *ca.* 100 nm after 3 h; after etching for 4 h the NC PL was undetectable suggesting complete Si-NC dissolution. These observations are consistent with the "water" etch proceeding through the oxidize/etch pathway stemming from a higher concentration of water available to oxidize the Si-NCs.

Irradiating the "acid" etching mixture blue shifted the PL as a function of the irradiating wavelength. After 10 h etching with 700 nm light using a Xenon light

source (FWHM of *ca.* 28 nm), a PL maximum of *ca.* 700 nm was achieved; using 600 nm light for 10 h gave an emission maximum of *ca.* 585 nm. For both the 600 nm and ambient light etches, an unexpected red shift of *ca.* 25 nm was observed after 4 h etching. This shift may arise from the formation of oxidation-related mid-gap states before PL spectra could be collected (typically within 2 minutes after extraction). Wolkin *et al.* have suggested Si-NCs with bandgaps greater than *ca.* 2 eV become susceptible to the formation of silanone (Si=O) related traps, red shifting the PL.[35]

The PL FWHM of the Si-NCs during etches narrowed, qualitatively consistent with a decrease in Si-NC polydispersity. Si-NCs etched in the dark had a PL FWHM of *ca.* 200 nm (*ca.* 0.8 eV*)*, in comparison to as low as *ca.* 90 nm for 700 nm and 600 nm photoetched samples (*ca.* 0.5 and 0. 6 eV respectively).
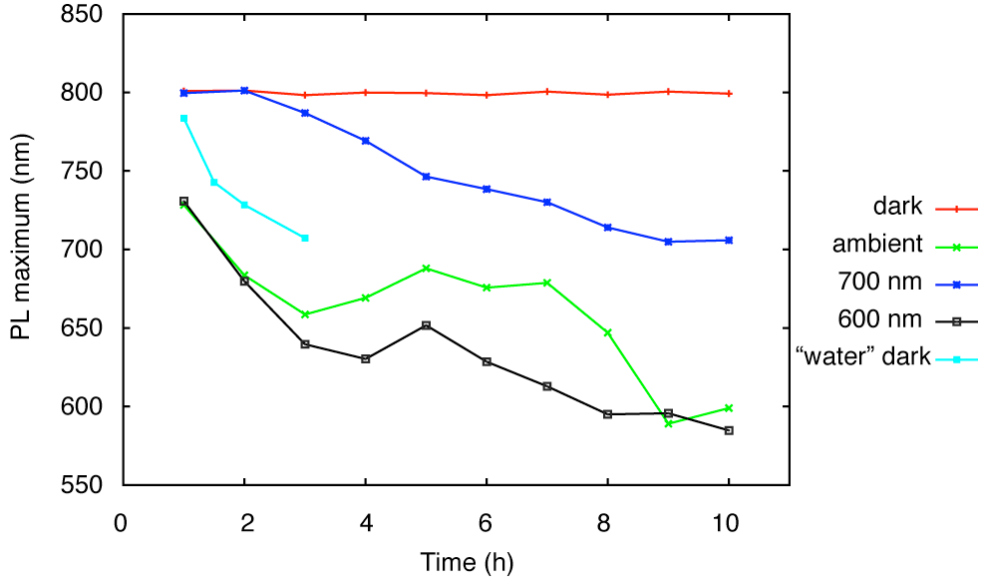
Figure 4-3: PL maxima of hydride-terminated Si-NCs "acid" etched under monochromatic irradiation from a Xenon light source. A "water" etched sample etched in the dark is shown for comparison.

PL FWHM is a common measure to evaluate Si-NC polydispersity.[21, 36] Based on the assumption that quantum confinement effects dominate the observed PL, the Si-NC size and polydispersity are often approximated from the PL maxima and FWHM (in eV) using the reduced mass model:

$$E(R) = \sqrt{E_g{}^2 + \frac{4.8 eV^2 nm^2}{R^2}} \qquad (4\text{-}1)$$

where E_g is the bandgap of bulk silicon in eV (1.1 eV), E(R) is the Si-NC bandgap, and R the radius of the nanocrystal. However, it is important to note PL of hydride-terminated Si-NCs can be influenced by surface traps (notably through the impact of oxidation, *vide supra*),[35] and necessarily only yields information on the luminescent fraction of Si-NCs within the entire sample. Determination of Si-NC sizes by

150

electron microscopy is challenging, owing to the small sizes (*ca.* 2-3 nm for Si-NC with visible PL) and low electron density for Si over C. Therefore, to determine if the observed wavelength dependence of the PL was truly arising through a shift in the Si-NC size (as expected by quantum confinement effects), a series of samples was etched using the "acid" recipe for 6 h under dark, ambient and 568 nm laser illumination, and subsequently functionalized by thermal hydrosilylation with 1-dodecene. Etching with laser illumination produced a narrower PL than with the Xenon source, likely because of superior monochromacity and higher power of the light source. PL after extraction and functionalization, shown in Figure 4-4, was compared with size and polydispersity obtained using SAXS, shown in Figure 4-5.

During etching, the PL shifted with irradiating wavelength, in keeping with the trend observed in Figure 4-1. PL maxima (and FWHM) of 577 nm (FWHM 94 nm, 0.4 eV), 695 nm (FWHM 196 nm, 0.5 eV) and 893 (FWHM 209 nm, 0.4 eV) were observed for the laser-assisted, ambient and dark samples, respectively. These PL results correspond to Si-NC sizes of 2.4 ± 0.5 nm, 3.1 ± 1.3 nm and 5.2 ± 3.3 nm using the effective mass approximation.

However, after functionalization, PL from all samples shifted substantially to the near-IR, with the laser-assisted and ambient sample PL red shifting to maxima of 740 nm (FWHM 200 nm, 0.4 eV). The dark sample PL blue shifted to 815 nm (FWHM 215 nm, 0.4 eV). Notably, the red shift of *ca.* 160 nm exhibited by the laser-assisted sample is significantly larger than the shifts in PL we observed for near-UV photochemical hydrosilylation of Si-NCs.[26] These red shifted PL correspond to Si-NC sizes of 3.6 ± 1.9, 3.4 ± 1.9 and 4.1 ± 3.3 nm for the laser-assisted, ambient

and dark samples, respectively. It is unlikely the hydrosilylation temperatures would increase the Si-NC size in such a manner owing to the high temperatures necessary to promote crystal growth (*vide infra*).

Fitting SAXS data of the functionalized samples to a spherical particle model with a Gaussian distribution gave average nanocrystal diameters of 4.0 ± 1.4 nm, 3.8 ± 1.5 nm and 5.0 ± 1.2 nm for the laser-assisted, ambient and dark samples. The differences between the PL and SAXS size estimations are summarized in Table 4-1. It is interesting to note the SAXS and PL data for the functionalized samples are in agreement with the liberation of significantly larger, more polydisperse Si-NCs compared to the samples studied previously with similar PL emission maxima, prepared by the "water" etching procedure (*e.g.*, 2.3 ± 0.6 nm, from HRTEM analysis, 2.9 ± 0.6 nm from SAXS analysis).[26]

Table 4-1: Difference in size estimates for "acid" etched samples using the PL effective mass approximation and SAXS

Sample	Effective mass approximation (before hydrosilylation)	Size estimated by SAXS (after hydrosilylation)
Dark	5.2 ± 3.3 nm	5.0 ± 1.2 nm
568 nm laser assisted	2.4 ± 0.5 nm	4.0 ± 1.4 nm
Ambient	3.1 ± 1.3 nm	3.8 ± 1.5 nm
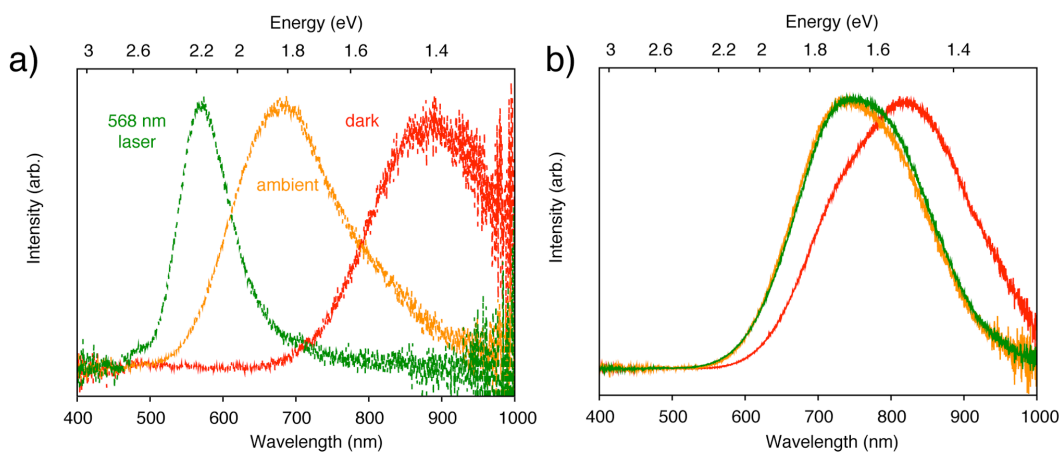
Figure 4-4: a) PL spectra of hydride-terminated Si-NCs prepared by HF etching in the dark (red trace), ambient light (orange trace) and with 568 nm laser irradiation (green trace). b) Corresponding PL spectra after thermal hydrosilylation with 1-dodecene.
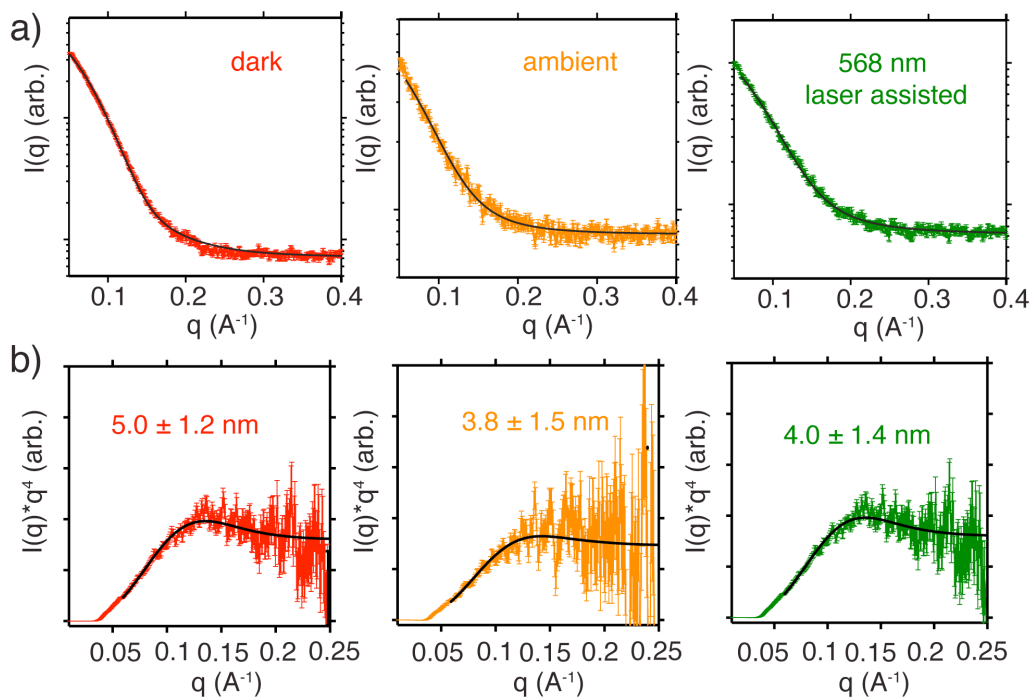
Figure 4-5: SAXS of functionalized Si-NCs prepared by etching under dark, ambient and 568 nm laser irradiation: plotted as a) *I(q) vs. q* and b) as a Porod plot as *I(q)*q⁴ vs. q*. Fitting parameters are summarized in the text.

153

The wavelength-dependent PL shifts exhibited by hydride-terminated Si-NCs during photochemical "acid" etching are suggestive of an exciton-mediated etching mechanism through the etching described above. However, this appears to contradict with the dramatic shift in PL maxima observed after functionalization, and the broad size distributions obtained using SAXS. To explain this discrepancy, it is first important to note that for an exciton to participate in the HF etching, its lifetime must be long enough for the hole to localize at the surface and undergo nucleophilic attack. Si-NCs rendered nonluminescent through the incorporation of a trapping defect (*e.g.*, volume[37-39] or dislocation defects[40]) would thus be inactive in this etching pathway as the exciton would recombine non-radiatively before inducing attack from HF. The presence of defect-containing nonluminescent Si-NCs within an ensemble population has been identified as a major factor in their relatively low quantum yields to date (*e.g.*, for a sample a with 5% quantum yield, 5% of the Si-NCs are defect-free and emissive, with 95% defect-ridden and non-luminescent).[41] Thus, it is likely these samples contain a population of dark Si-NCs (invisible to PL characterization of the hydride-terminated Si-NCs) that are not etched and hence skew the size distributions obtained from SAXS. Attempts to fit the SAXS data to a bimodal distribution were unsuccessful, likely resulting from substantial overlap in size between dark and bright populations preventing the least-squares fitting process from converging.

The presence of a population of dark Si-NCs that are not "acid" etched is also consistent with the anomalous PL red shift observed. Two possible explanations can account for this behaviour. First, if a surface defect is responsible for the loss of

emission, the change in surface chemistry initiated by thermal hydrosilylation might remove these defects, activating these dark NCs. Second, annealing of similarly prepared Si-NCs at similar temperatures to the conditions of thermal hydrosilylation used here is known to reduce the concentration of dangling bond defects (notably, passivating both surface- and core-associated defects).[42] Annealing of core defects during thermal functionalization could also explain the observed red shift.

A modified two-step etching procedure was studied in an attempt to activate the nonluminescent population toward the wavelength-dependent etching process. First, 100 mg of 1100°C-processed oxide composite was etched for 30 minutes using the "water" recipe. During this etch, the oxide matrix is removed, and the Si-NC ensemble size reduced. Etching Si-NCs with dilute HF solutions is known to reduce the number of dangling-bond defects, as confirmed by electron paramagnetic resonance spectroscopy.[42, 43] This would increase the number of bright NCs available to participate in the exciton-mediated pathway. Subsequently, 20 mL of 49% HF and 1.3 mL HCl were added as an excess volume to increase the HF concentration and acidify the reaction mixture. The reaction mixture was then irradiated using a high-powered 660 nm laser diode to switch over to the exciton-mediated pathway.

After 2 h, the 2-step etching process yielded hydride-terminated Si-NCs with PL centered at *ca.* 637 nm (FWHM 91 nm, 0.3 eV, Figure 4-6). By comparison, after 2 h of etching using the "acid" recipe under 660 nm illumination, or etching using the "water" recipe under ambient illumination gave hydride-terminated Si-NCs with PL centered at *ca.* 620 nm (FWHM 92 nm, 0.3 eV) and 612 nm (FWHM 152 nm, 0.5 eV) respectively.

Thermal hydrosilylation with 1-dodecene after the 2-step etch yielded Si-NCs with PL centered at *ca.* 625 nm (FWHM 128 nm, 0.4 eV), a blue shift of 27 nm. The "water" and "acid" etched samples exhibited PL centered at *ca.* 675 nm (FWHM 149 nm, 0.4 eV) and 713 nm (FWHM 159 nm, 0.4 eV).

SAXS characterization of these samples (Figure 4-7), fitting to a spherical particle model with a Gaussian distribution, yielded diameters of 2.6 ± 0.7 nm for the 2-step etched sample, 1.6 ± 0.8 nm for the "water" etched sample, and 3.0 ± 1.9 nm for the "acid" etched sample.
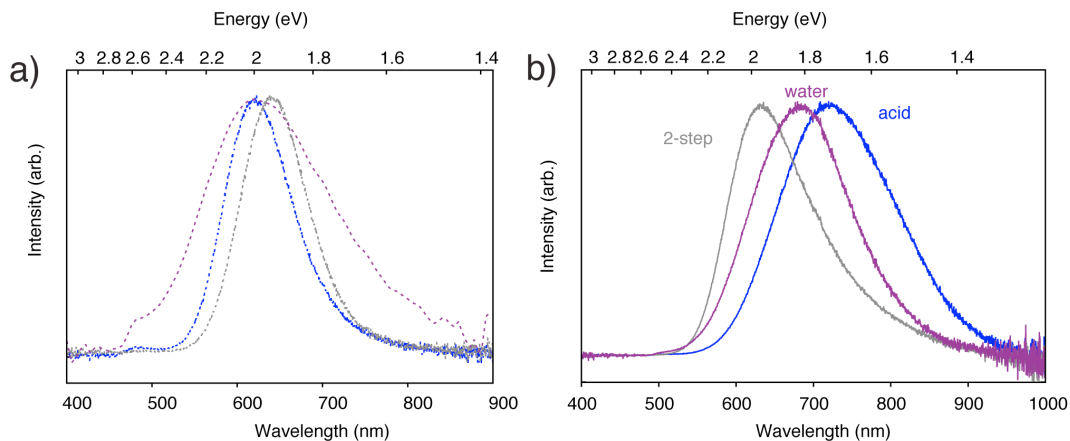
Figure 4-6: a) PL spectra of hydride-terminated Si-NCs prepared using the 2-step HF recipe (grey trace), "acid" recipe (blue trace) and "water" recipes (purple trace) after 2 h of etching. b) Corresponding PL spectra after thermal hydrosilylation.
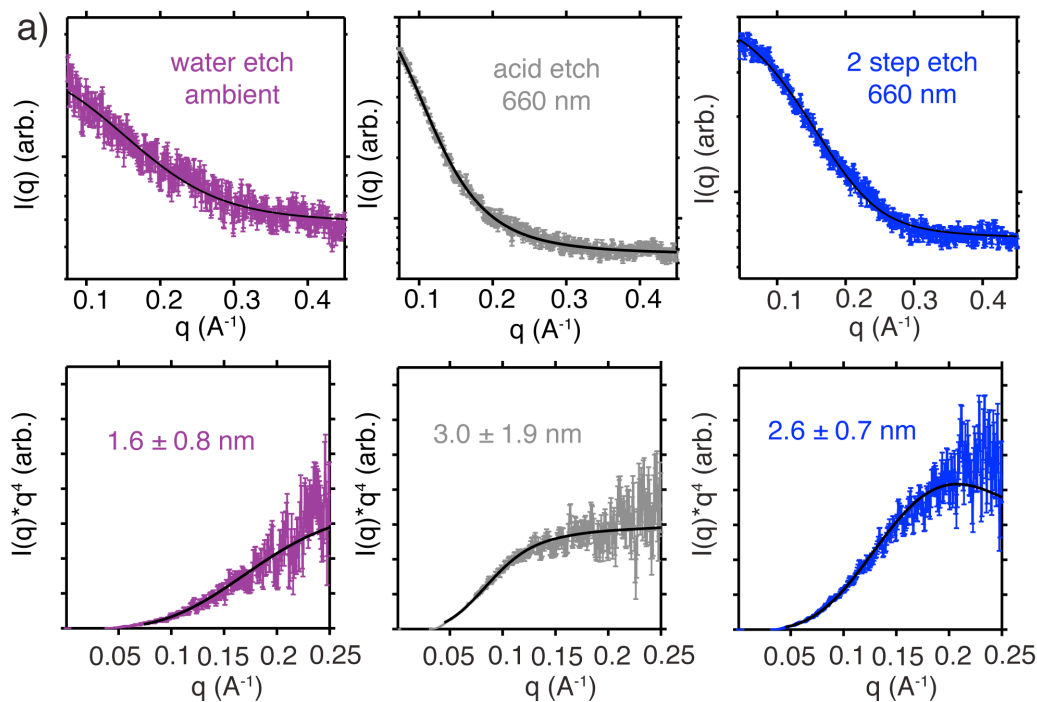
Figure 4-7: SAXS of functionalized Si-NCs prepared using the 2-step HF recipe (grey trace), "acid" recipe (blue trace) and "water" recipes (purple trace) after 2 h of etching. Plotted as a) *I(q) vs. q* and b) as a Porod plot as *I(q)*q⁴ vs. q*. Fitting parameters are summarized in the text.

By employing a 2-step etching process to first remove non-radiative defects, then activate the exciton-mediated (wavelength dependent) etching pathway by addition of excess HF and HCl, the Si-NC polydispersity after 2 h of etching was improved from over σ = 50% for the "water" and "acid" etches to σ = 27%. Correspondingly, instead of the significant PL red shift observed for the "acid" etched NCs, the PL of the 2-step etched Si-NCs blue shifted by only 12 nm (*ca.* 625 nm). Given the similar PL maxima and polydispersity to Si-NCs we have previously studied,[26] it is reasonable this blue shift is in accordance with the "smart confinement" model previously proposed.

However, this improvement is still wider than the applications-enabling narrow polydispersity of wet chemical methods for compound semiconductor NCs. As well, it is close to the polydispersity observed for Si-NCs etched in the "water" recipe for 1 h we previously reported.[26]

Extinction coefficients of Si-NCs have been demonstrated to increase as a function of NC size.[44] Choi *et al.* suggested that this factor is responsible for a narrow polydispersity in their oxide/etching approach.[21] As larger Si-NCs absorb more light, they would be expected to be oxidized (and thus etched) at a faster rate. This hypothesis may explain the relatively narrow polydispersity observed in Chapter 2 for the 1 h "water" etched samples under ambient lighting.

Conversely, this may present an obstacle for the strategy of size control through the exciton-mediated pathway. Non-luminescent NCs unreactive towards etching would remain larger and thus compete for light absorption, slowing the etching of the bright population. Ideally, an exciton-mediated etching strategy would

function best in a sample containing little or no defects, so the majority of the sample would etch at the same rate. In the present system, this could be achieved through the etching of composites prepared through extended annealing under hydrogen atmosphere.[27]

4.4 Conclusions

Through changing the HF concentration and pH, the HF etching rate of oxide-embedded Si-NC composites can be greatly increased, rapidly liberating hydride-terminated Si-NCs within minutes. Furthermore, the HF etching pathway of hydride-terminated Si-NCs can be controlled from a oxide/etch to an exciton-mediated pathway. Exploiting this change through photochemical etching yields Si-NCs whose PL shifts and narrows as a function of irradiating wavelength, as expected from quantum confinement effects. However, after thermal hydrosilylation, a significant PL red shift and broad size distribution (determined by SAXS) was observed. To account for this, a model of dark Si-NCs unreactive in the exciton-mediated etching pathway was proposed. This hypothesis was tested through the development of a 2-step etching process, which improved the resulting Si-NC polydispersity.

Although significant improvements in Si-NC polydispersity through HF etching have yet to be realized for use in practical applications, this investigation has revealed several observations that merit general consideration for size control through HF etching of Si nanostructures:

1) Although a narrow PL FWHM is a primary motivating factor for lowering Si-NC polydispersity, PL alone cannot suffice for characterizing the size distribution

during the etching process. The best FWHM of 90 nm (0.3 eV) observed in this study for "acid" etched samples compares favorably to some of the narrowest reported to date (*i.e.*, FWHM of *ca.* 0.4 eV).[21] However, the true polydispersity revealed by SAXS is consistent with the presence of dark NCs limiting the etching process. Although absorption measurements can also provide valuable information in this regard, the small quantities of material used in this study and relatively broad size distributions made estimate of the absorption onset challenging.

2) The significant red shift observed during hydrosilylation is consistent with the activation of dark Si-NCs upon hydrosilylation, in contrast to the blue shift observed for Si-NCs with similar PL maxima in Chapter 2. This reversal in behaviour is attributed to the difference in polydispersity between these samples, caused by presence of dark NCs. Caution must thus be taken in comparing the impact of surface functionalization and other post-synthetic steps between synthetic methods stemming from their inherent differences in polydispersity.

4.5 References

1. Rossetti, R.; Nakahara, S.; Brus, L. E. *J. Chem. Phys.* **1983**, *79*, 1086-1088.

2. Cademartiri, L.; Ozin, G. A. *Philos. Trans. R. Soc. London, Ser. A* **2010**, *368*, 4229-4248.

3. Yin, Y.; Alivisatos, A. P. *Nature* **2005**, *437*, 664-670.

4. Cademartiri, L.; Montanari, E.; Calestani, G.; Migliori, A.; Guagliardi, A.; Ozin, G. A. *J. Am. Chem. Soc.* **2006**, *128*, 10337-10346.

5. Ellingson, R. J.; Beard, M. C.; Johnson, J. C.; Yu, P.; Micic, O. I.; Nozik, A. J.; Shabaev, A.; Efros, A. L. *Nano Lett.* **2005**, *5*, 865-871.

6. Yong, K. -T.; Roy, I.; Swihart, M. T.; Prasad, P. N. *J. Mater. Chem.* **2009**, *19*, 4655-4672.

7. Michalet, X.; Pinaud, F. F.; Bentolila, L. A.; Tsay, J. M.; Doose, S.; Li, J. J.; Sundaresan, G.; Wu, A. M.; Gambhir, S. S.; Weiss, S. *Science* **2005**, *307*, 538-544.

8. Shevchenko, E. V.; Talapin, D. V.; Murray, C. B.; O'Brien, S. *J. Am. Chem. Soc.* **2006**, *128*, 3620-3637.

9. Kelly, J. A.; Henderson, E. J.; Veinot, J. G. C. *Chem. Commun.* **2010**, *46*, 8704-8718.

10. Buhro, W. E.; Hickman, K. M.; Trentler, T. J. *Adv. Mater.* **1996**, *8*, 685-688.

11. Peng, X.; Wickham, J.; Alivisatos, A. P. *J. Am. Chem. Soc.* **1998**, *120*, 5343-5344.

12. Park, J. –H.; Gu, L.; von Maltzahn, G.; Ruoslahti, E.; Bhatia, S. N.; Sailor, M. J. *Nat. Mater.* **2009**, *8*, 331-336.

13. Erogbogbo, F.; Yong, K. -T.; Roy, I.; Xu, G. X.; Prasad, P. N.; Swihart, M. T. *ACS Nano* **2008**, *2*, 873-878.

14. Alsharif, N. H.; Berger, C. E. M.; Varanasi, S. S.; Chao, Y.; Horrocks, B. R.; Datta, H. K. *Small* **2009**, *5*, 221-228.

15. Bayliss, S. C.; Heald, R.; Fletcher, D. I.; Buckberry, L. D. *Adv. Mater.* **1999**, *11*, 318-321.

16. Nagesha, D. K.; Whitehead, M. A.; Coffer, J. L. *Adv. Mater.* **2005**, *17*, 921-924.

17. Low, S. P.; Voelcker, N. H.; Canham, L. T.; Williams, K. A. *Biomaterials* **2009**, *30*, 2873-2880.

18. Canham, L. T. *Appl. Phys. Lett.* **1990**, *57*, 1046-1048.

19. Li, X.; He, Y.; Swihart, M. T. *Langmuir* **2004**, *20*, 4720-4727.

20. Hua, F.; Swihart, M. T.; Ruckenstein, E. *Langmuir* **2005**, *21*, 6054-6062.

21. Choi, J.; Wang, N. S.; Reipa, V. *Langmuir* **2007**, *23*, 3388-3394.

22. Sato, S.; Ikeda, T.; Hamada, K.; Kimura, K. *Solid State Commun.* **2009**, *149*, 862-865.

23. Kolasinski, K. W. *PCCP* **2003**, *5*, 1270-1278.

24. Lehmann, V.; Gösele, U. *Appl. Phys. Lett.* **1991**, *58*, 856-858.

25. Hessel, C. M.; Henderson, E. J.; Veinot, J. G. C. *Chem. Mater.*

26. Kelly, J. A.; Veinot, J. G. C. *ACS Nano* **2010**, *4*, 4645-4656.

27. Hessel, C. M.; Henderson, E. J.; Veinot, J. G. C. *J. Phys. Chem. C* **2007**, *111*, 6956-6961.

28. Spierings, G. A. C. M. *J. Mater. Sci.* **1993**, *28*, 6261-6273.

29. Pauthe, M.; Phalippou, J.; Corriu, R.; Leclercq, D.; Vioux, A. *J. Non Cryst. Solids* **1989**, *113*, 21-30.

30. Cullis, A. G.; Canham, L. T.; Calcott, P. D. J. *J. Appl. Phys.* **1997**, *82*, 909-965.

31. Jackson, H. L.; McCormack, W. B.; Rondestvedt, C. S.; Smeltz, K. C.; Viele, I. E. *J. Chem. Educ.* **1970**, *47*, A175-A188.

32. Liang, D. A.; Readey, D. W. *J. Am Chem. Soc.* **1987**, *70*, 570-577.

33. Bahruji, H.; Bowker, M.; Davies, P. R. *Int. J. Hydrogen Energy* **2009**, *34*, 8504-8510.

34. Buriak, J. M. *Chem. Rev.* **2002**, *102*, 1271-1308.

35. Wolkin, M. V.; Jorne, J.; Fauchet, P. M.; Allan, G.; Delerue, C. *Phys. Rev. Lett.* **1999**, *82*, 197-200.

36. Meldrum, A.; Bianucci, P.; Marsiglio, F. *Opt. Express* **2010**, *18*, 10230-10246.

37. Cheylan, S.; Elliman, R. G. *Nucl. Instrum. Methods Phys. Res., Sect. B*

2001, *175-177*, 422-425.

38. Cheylan, S.; Elliman, R. G. *Appl. Phys. Lett.* **2001**, *78*, 1912-1914.

39. Cheylan, S.; Elliman, R. G. *Appl. Phys. Lett.* **2001**, *78*, 1225-1227.

40. Wang, Y. Q.; Li, T.; Liang, W. S.; Duan, X. F.; Ross, G. G. *Nanotechnology* **2009**, *20*.

41. Wilson, W. L.; Szajowski, P. F.; Brus, L. E. *Science* **1993**, *262*, 1242-1244.

42. Niesar, S.; Stegner, A. R.; Pereira, R. N.; Hoeb, M.; Wiggers, H.; Brandt, M. S.; Stutzmann, M. *Appl. Phys. Lett.* **2010**, *96*.

43. Pi, X. D.; Mangolini, L.; Campbell, S. A.; Kortshagen, U. *Phys. Rev. B Condens. Matter* **2007**, *75*.

44. Beard, M. C.; Knutsen, K. P.; Yu, P.; Luther, J. M.; Song, Q.; Metzger, W. K.; Ellingson, R. J.; Nozik, A. J. *Nano Lett.* **2007**, *7*, 2506-2512.

Chapter 5: X-ray Absorption Spectroscopy of Functionalized Silicon Nanocrystals[*]

5.1 Introduction

The discovery of efficient photoluminescence (PL) from silicon nanocrystals (Si-NCs) has spurred great interest toward the fundamental understanding and application of these materials.[1] The natural abundance of Si and its prevalence in the microelectronics industry also make it appealing for many technologies including photovoltaics[2, 3] and biological applications such as fluorescent imaging and drug delivery.[4-6] Luminescent Si is biocompatible and biodegradable,[7-10] making it well-suited for *in vivo* medical diagnostic imaging applications where corresponding II-VI and III-V NCs (*e.g.*, CdSe, GaAs) exhibit marked cytotoxic effects that results from the release of metal cations in oxidative environments.[11, 12]

Several groups have reported recent syntheses of Si-NCs that yield tangible quantities of highly crystalline material of controlled size, with PL spanning the visible and near-IR spectral regions.[13-17] A central goal to many of these reports is the realization of a reactive surface suitable for further modification while maintaining the desired optical properties. One approach that has been extensively studied is hydrofluoric (HF) acid etching which yields hydride surface termination that can be conveniently modified through subsequent hydrosilylation with alkenes or alkynes.[18, 19] While the hydride surface oxidizes under ambient conditions, leading to a decrease in PL quantum yield and shift in emission maximum, many reports have noted the robustness of the resulting Si-C surface against unwanted oxidation.

Although hydrosilylation increases the colloidal stability of freestanding Si-NCs and stabilize PL,[14, 20] thereby facilitating the use of these materials in several proof-of-concept applications, uncertainty remains over the degree to which this

process affects the PL response. Reports of both red- and blue shifted PL arising from hydrosilylation have appeared, depending upon the initial NC size and olefin used. Additionally, some reports have also noted the emergence of a new emission band centered in the blue spectral region (similar in many respects to the so-called "fast" band[21] observed in some reports for porous Si).[22, 23] Comparisons between different synthetic and functionalization approaches is a significant challenge as they bring with them inherent differences in NC size and size dispersity, reaction impurities, or in post-reaction treatment.

Generally, changes to the Si-NC PL resulting from hydrosilylation have been explained in the context of oxide-related species formed during and/or after the reaction. Wolkin *et al.* proposed a model invoking silanone (*i.e.,* Si=O, a metastable species suggested to form during the oxidation of Si surfaces) related mid-gap states, suggesting there is a critical size below which quantum confinement effects open up the conduction and valence bands, allowing surface-localized trap states to influence the PL.[24] It has also been suggested that other oxide-related species might produce a red shift effect.[25-27] Oxidation of Si-NC surfaces has also been implicated in the formation of non-radiative traps (*e.g.*, dangling bonds) that decrease the PL quantum yield.[28]

As discussed in detail in Chapter 2 of this thesis, photochemical hydrosilylation of Si-NCs can be initiated using a near-UV LED light source.[29] The Si-NCs studied were obtained *via* HF etching of oxide-embedded composites prepared by the annealing of hydrogen silsesquioxane (HSQ).[16] This procedure yields hydride-terminated Si-NCs exhibiting size dependent PL throughout the

visible spectrum. Reaction of green-emitting Si-NCs (PL maxima at *ca.* 580 nm) produced a red shift in the PL explainable by the formation of oxide-related midgap states, red-emitting Si-NCs (PL maxima at *ca.* 700 nm) exhibited a blue shift that was hypothesized to occur through the removal of defect surface states, in keeping with the "smart confinement" model.[30, 31]

Near edge X-ray absorption fine structure spectroscopy (NEXAFS) and X-ray excited optical luminescence spectroscopy (XEOL, also referred to as Photoluminescent Yield, PLY) are complementary, information-rich characterization techniques that provide detailed information on the electronic and optical properties of luminescent materials such as Si-NCs. [32-35] Through tuning of an incident X-ray photon from a synchrotron source to the threshold energy required to create a core hole (*i.e.*, a transition to an unoccupied or continuum state) and subsequent observation of secondary processes that follow X-ray absorption (*e.g.*, Auger emission, X-ray fluorescence or visible luminescence), NEXAFS and XEOL give element-specific insight into the chemical species (*e.g.*, oxidation state and coordination environment) that comprise a material. In doing so, the contribution of the various species to the electronic structure and optical properties can be elucidated. X-ray absorption spectroscopy benefits from high photoabsorption cross sections of most core and shallow-core levels of interest, as well as inherently narrow linewidths.[35] The use of a synchrotron source with high flux and monochromaticity affords excellent chemical sensitivity and resolving power.

In the field of Si nanomaterials, NEXAFS and XEOL have been used to characterize the luminescent species in porous Si,[21, 36-42] Si nanowires,[43] Si-NCs

embedded in SiO_2,[44, 45] alkylated Si-NCs derived from porous Si,[46-48] Si-NCs derived from thermal vaporization of Si[49] and Si-CdSe heterostructures,[50] among others. In particular, NEXAFS and XEOL have been extensively utilized to understand the origin of luminescence of porous Si, the prototypical Si luminescent nanostructure. At the time of its discovery, several competing theories suggested the observed emission arose from various species including siloxenes, defects, amorphous Si or surface hydrides.[51] NEXAFS and XEOL have shown that the widely observed "slow" band for freshly prepared porous Si (with an orange/red PL maximum) arises from absorption by elemental Si;[36] the emissive species has a disordered structure closely related to crystalline Si;[40] the electronic and optical properties exhibit a size-dependence in accordance with quantum size effects;[41, 42] and the "slow" and "fast" bands originate from different species (*e.g.*, elemental core and oxidized surface regions of the porous layer, respectively).[21] These reports have played an important role in establishing the quantum confinement model as the dominant mechanism of luminescence from hydride-terminated porous Si.

In comparison, NEXAFS and XEOL results of other Si nanostructures have demonstrated that surface species present in Si nanostructures play an active role in the luminescence. Daldosso and coworkers observed oxide-embedded Si-NCs prepared by plasma-enhanced chemical vapor deposition (PECVD) to contain a graded layer of amorphous Si and strained SiO_2 *ca.* 1 nm thick at the NC surface.[44] Selective X-ray excitation of these species enhanced the observed XEOL signal, suggesting that these surface species participate in the absorption and emission processes; this was complemented by detailed computational investigations.

Similarly, Zimina and coworkers examined oxide-embedded Si-NC superlattices and found NEXAFS evidence for a graded suboxide shell at the NC surface.[52] This structure was suggested to influence the electronic properties of these materials, particularly in the conduction band. The origin of PL in these materials was later studied using magneto-PL, showing the participation of defects in the suboxide interface in the PL.[53]

The optical and electronic properties of oxide-embedded and freestanding hydride-terminated Si-NCs derived from HSQ have been studied using Si *K*-edge NEXAFS and XEOL.[45] This investigation demonstrated that the hydride surface immediately after etching is oxide free at the sensitivity level of Si *K*-edge NEXAFS and XEOL, and the emission is consistent with quantum confinement effects. Given the observed shifts in PL induced by functionalization and the important role of surface species identified for Si nanostructures, it is important to better understand the impact of the hydrosilylation process on Si-NC PL. Here, an investigation of the impact of photochemical hydrosilylation on the optical and electronic properties of freestanding Si-NCs is presented. These results show the origin of PL of these alkylated Si-NCs to be consistent with quantum confinement effects, and highlights the critical influence surface oxidation has over the emission. The materials studied were characterized using Si $L_{3,2}$-edge NEXAFS, Si *K*-edge NEXAFS and XEOL, and Fourier transform infrared (FTIR) spectroscopy.

5.2. Materials and methods

5.2.1 Materials

All chemicals were purchased from Sigma Aldrich as reagent grade with the exception of HSQ (Dow Corning, FOx-17) and 49% hydrofluoric acid (HF, J.T. Baker, electronics grade), and were used as received. High-purity water (18.2 MΩ/cm) was obtained from a Barnstead Nanopure Diamond purification system. Toluene and methanol were dried by distillation over sodium/benzophenone and magnesium turnings, respectively. Styrene and 1-hexene were purified immediately before use by passing over neutral alumina to remove inhibitor and/or peroxide impurities.[54]

5.2.2 Photochemical hydrosilylation

Functionalized Si-NCs were prepared from HSQ by methods previously described.[16, 29] In brief, oxide-embedded Si-NCs were prepared by the thermal processing of HSQ to 1100°C for 1 h under a 5% H_2/ 95% Ar atmosphere. Freestanding hydride-terminated Si-NCs were liberated from the oxide composite through etching with an ethanolic HF solution for 1 h, giving hydrophobic Si-NCs that were isolated by extraction with 50 mL toluene. The initially cloudy yellow Si-NC dispersion had red PL (maximum at *ca.* 720 nm). Previous transmission electron microscopy analysis has shown this procedure produces *ca.* 2.3 ± 0.6 nm diameter Si-NCs.[29] Following three freeze-pump-thaw cycles of the reaction Schlenk flask to remove dissolved oxygen, photochemical reaction was carried out by a near-UV LED light source (365 nm) for 15 h, giving a clear yellow colloidal dispersion for the

samples reacted with styrene and 1-hexene. A sample of hydride-terminated Si-NCs in toluene without any alkene was also reacted as a control sample, giving a cloudy dispersion.

In order to minimize the impact of any ambient exposure to the XAS characterization, all purification, storage, transportation and sample preparation steps were conducted under inert atmosphere using dry solvents. Following functionalization, solvent and unreacted alkene were removed under vacuum on a Schlenk line. Three cycles of solvent/anti-solvent washing and centrifugation were carried out using toluene and methanol. The purified Si-NCs were transferred to an Ar-filled glovebox (1 ppm O_2, 0.6 ppm H_2O) and kept until transportation for analysis.

5.2.3 X-ray Absorption Spectroscopy

NEXAFS and XEOL experiments were performed at the Canadian Light Source in Saskatoon, Saskatchewan. Si $L_{3,2}$-edge NEXAFS spectra were collected on the Variable Line Spacing Planar Grating Monochromator beamline (PGM, 11ID-2), which has a photon flux at the Si $L_{3,2}$-edge (90-125 eV) of $ca.$ 10^{12} photons/s /100 mA and a resolving power of 10,000 $E/\Delta E$.[55] Si K-edge NEXAFS and XEOL were collected on the Spherical Grating Monochromator (SGM, 11ID-1) beamline, which has a photon flux at the Si K-edge (1810-1910 eV) of $ca.$ 10^{11} photons/s/100 mA and a resolving power of $ca.$ 5000 $E/\Delta E$.[56] Spectra were normalized to the incident beam intensity (I_o) by measuring the current emitted by a nickel mesh located after the last focusing mirror. X-ray fluorescent yield (FLY) was measured

using a micro-channel plate detector positioned 45° from the sample. Total electron yield (TEY) was measured at the Si *K*-edge by normalizing the drained sample current to the incident photon flux. XEOL spectra were collected during NEXAFS scans through a lens coupled to an Ocean Optics USB4000 spectrometer. PLY spectra were generated by integrating the XEOL signal over the visible region at each X-ray energy and corrected for sample damage effects using Igor Pro. To subtract the sample-damage induced decay from the PLY signal, uncorrected data in the pre-edge region were fit to a decaying exponential of the form:

$$I(E) = Ae^{\frac{-(E-1825)}{\tau}} \qquad \text{(5-1)}$$

where *I* denotes the integrated PLY intensity, *E* the exciting X-ray energy in electron volts, *A* the initial intensity and τ an empirical decay constant. As the PL decay was dependent on the step size, data were fit only over the region where a 0.1 eV step sized was used (*ca.* 1825 -1860 eV).The values A and τ were chosen merely as empirical parameters to describe the decay, and varied over the sample because of thickness inhomogenieties. Therefore representative scans of these data were chosen rather than averages for statistical purposes.

Separate samples were prepared for experiments on each beamline. The reproducibility of the functionalization process was confirmed for each sample before transportation to the CLS through PL spectroscopy of toluene dispersions using a Cary Eclipse fluorescence spectrophotometer and FTIR spectroscopy on drop cast films using a Nicolet Magna 750 IR spectrometer, and found to match previously published results.[29] Immediately prior to XAS analysis, the colloidal dispersions were

drop-coated onto aluminum discs under a sheath of flowing argon, and quickly transferred under inert atmosphere and reduced temperature to the beamline endstation to limit ambient oxidation. All analyses were performed under high-vacuum (10^{-8} Torr). NEXAFS spectra were collected using 100 μm entrance and exit slits. To minimize effects of X-ray induced sample damage on the luminescence, Si K-edge NEXAFS and XEOL measurements were made on samples cooled to *ca.* 80K using a liquid nitrogen crysostat. Scans were averaged and calibrated to a powdered silicon standard by setting the first derivative maximum of the $Si^{(0)}$ $L_{3,2}$-edge absorption to 99.42 eV[57] and the $Si^{(0)}$ K-edge absorption to 1839 eV.[58] NEXAFS spectra were calibrated and normalized using Athena.[58]

5.3. Results and discussion

5.3.1 Si $L_{3,2}$-edge NEXAFS

At X-ray energies near to the Si $L_{3,2}$-edge, excitation occurs from the Si $2p$ shell to unoccupied states of s and d character.[35] The energy at which these transitions occur is sensitive to the oxidation state and the local partial density of states (LPDOS) of the absorbing species. Figure 5-1 shows Si $L_{3,2}$-edge FLY NEXAFS of functionalized Si-NCs prepared by photochemical hydrosilylation; for comparison, spectra of oxide-embedded Si-NCs and bulk Si and SiO_2 standards are also shown. The Si-NC samples show two sets of doublet features, assigned to the elemental Si core at *ca.* 99.5 eV and oxide and alkyl surface species at *ca.* 105.6 eV. The higher energy broad absorptions at *ca.* 108 and 115 eV are attributed to "inner-well" resonances in oxide species.[48, 59]
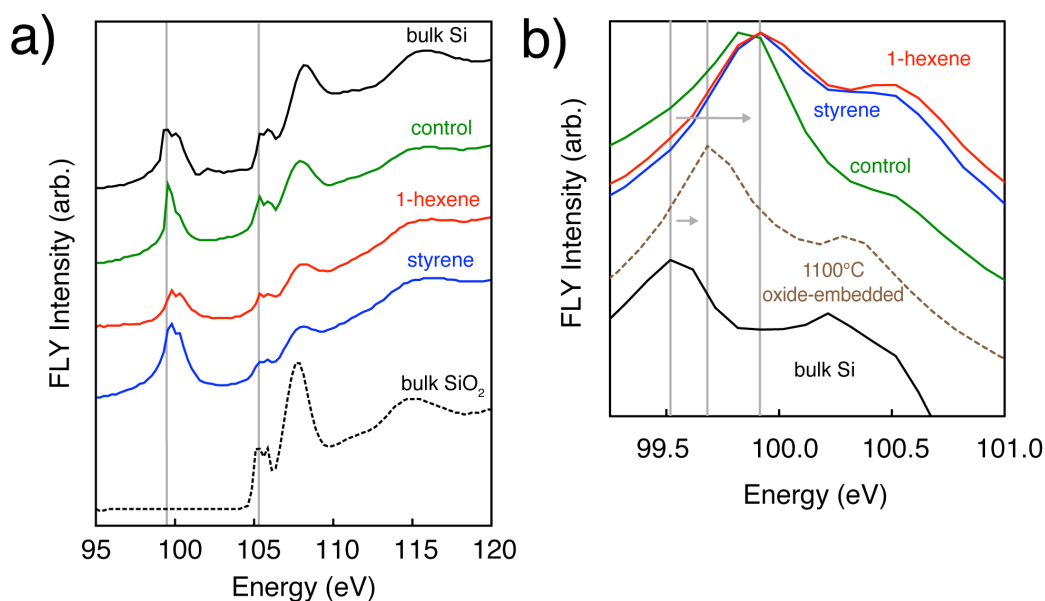
Figure 5-1: a) Si $L_{3,2}$-edge FLY NEXAFS spectra of Si-NCs functionalized with styrene (blue trace), 1-hexene (red trace) and a control sample prepared in the absence of alkene (green trace). Spectra of elemental Si and SiO₂ standards are shown for reference. Absorption maxima for Si and SiO₂, at 99.6 and 105.6 eV respectively are noted with grey vertical lines. Spectra have been shifted vertically for clarity. b) Expanded Si$^{(0)}$ region, showing a shift in this band to higher energies with smaller Si-NC size. Functionalized samples are shown in color. Bulk Si (black trace) and oxide-embedded Si-NCs processed at 1100°C (dotted brown trace) are show for comparison.

FLY detection was chosen at the Si $L_{3,2}$-edge as it does not suffer from charging effects sometimes encountered by electron yield techniques. For these nanostructured materials, whose features are smaller than the depth probed by electron yield techniques, it has been previously shown that FLY data (generally regarded as a bulk-sensitive technique, with an escape depth of *ca.* 10^2 nm at the Si

L$_3$-edge) provides accurate characterization of the structure and composition of the Si-NC core and surface.[45] It is important to note that self-absorption effects can strongly distort the FLY signal resulting from the very short one-absorption length in this soft X-ray regime.[35] This hinders rigorous quantitative interpretation of the near-edge features; the decline in FLY intensity between *ca.* 101-104 eV is attributed to this effect.

Any oxidation on the surface of the freestanding functionalized Si-NCs is expected to include non-stoichiometric suboxides with intermediate oxidation states (*i.e.*, O_xSiR_{1-x}, $0 < x < 4$, R = C, Si or H) rather than an abrupt SiO_2 interface (*i.e.*, dominated by SiO_2 and O_3Si-Si oxide species). However, the formation of core excitons can shift the energy of these oxide resonances associated with a *2p* core level shift.[59] It has also been suggested that Si *2p* $\rightarrow\sigma^*_{Si-C}$ and Si *2p* $\rightarrow\sigma^*_{Si-O}$ transitions occur at similar energies.[39, 60] In this context, the feature at 105.6 eV is assigned to a mixture of alkyl and oxide species formed on the Si-NC surface during functionalization.

For all samples, the Si$^{(0)}$ doublet at *ca.* 99.5 eV is clearly evident with 0.6 eV separation, suggesting the FLY signal can give insight into the electronic structure despite self-absorption effects. The bulk Si standard also shows two additional sets of overlapping doublet features at *ca.* 99-104 eV, arising from the LPDOS of the conduction band (CB).[43] In comparison, the Si-NC samples show a loss of fine structure in the region of 100-104 eV, though the main doublet at 99.5 eV remains well-defined. Loss of structure has also been observed in NEXAFS studies of other Si nanomaterials, and has been attributed to a loss of long range order within the NC

core, and/or chemical inhomogeneities such as a broad size distribution or surface effects.[41, 43] Size distribution effects have been suggested to contribute to the inhomogeneous broadening of the $Si^{(0)}$ $2p_{1/2}$ and $2p_{3/2}$ spin orbit pair at 99.5 eV, related to the overlap of absorption spectra from differently sized nanostructures.[41, 48] The observed well-defined $Si^{(0)}$ splitting is consistent with the narrow size distribution yielded by this synthetic method.[16, 29]

The oxide-embedded Si-NCs prepared by processing at 1100°C exhibit a blue shift of 0.1 eV in the main doublet at *ca.* 99.5 eV relative to bulk Si. The functionalized Si-NCs exhibit a larger shift of *ca.* 0.3 eV. Similar blue shifts have been reported for $L_{3,2}$-edge NEXAFS and electron energy loss spectroscopy (EELS) of hydride-terminated and oxidized Si nanostructures, including porous Si[41-43, 61] and freestanding Si-NCs.[49, 62, 63] This blue shift has been proposed to arise as a result of quantum confinement effects widening the bandgap and shifting the CB minimum to higher energy. Van Buuren and coworkers estimated this trend to follow the relation E_{gap} = 3ΔCB + 1.1 eV.[49] This relation gives a bandgap estimate of 1.4 eV (885 nm) for the oxide-embedded Si-NCs and 2.0 eV (620 nm) for the present functionalized Si-NCs. This calculation is in good agreement with previous PL and UV-vis characterization, and XEOL results discussed below.[45, 64]

Interestingly, several recent XAS reports of Si-NCs of similar size show a red shift in this feature, against the shift predicted through quantum confinement effects.[48, 52] The authors explained this trend in the context of core exciton formation. Interactions between the core Si $2p$ hole and the valence electron were predicted to lower the energy of the excited state, leading to a red shift that

counteracts the blue shift produced from quantum confinement effects. Core exciton formation was suggested in particular to influence XAS of Si-NCs with radii below *ca.* 1.6 nm, the theoretical radius of a core exciton for bulk Si.[48] The present results do not show a red shift and are instead consistent with the previous reports for hydride-terminated freestanding Si nanostructures. The similar shift in $Si^{(0)}$ resonance energy exhibited by the functionalized and control samples, and the good agreement with previous bandgap estimates suggest the functionalization process does not significantly influence quantum confinement effects in these materials. To explain the opposite shifts observed, it is proposed the formation of core excitons may be critically influenced by surface states; the oxide-embedded Si-NCs studied by Zimina[52] and Daldosso[44] exhibit a graded suboxide interface which actively participates in the luminescence, unlike the oxide-embedded Si-NCs in the present system.[45] The participation of surface species through the formation of mid-gap states or in changes to the dielectric screening of the core exciton may account for these differences, and merits further investigation through the use of soft X-ray emission spectroscopy and resonant inelastic X-ray scattering.

5.3.2 Si *K*-edge NEXAFS and XEOL

Figure 5-2 shows Si *K*-edge FLY and TEY NEXAFS spectra of freestanding Si-NCs with bulk Si and SiO_2 standards shown for reference. Compared to the TEY spectra, the white lines in FLY traces are suppressed, likely as a result of self-absorption effects.[35] Similar to the Si $L_{3,2}$-edge data, two resonances assigned to the elemental core and oxidized surface Si are evident in all samples at 1841 and 1848 eV, respectively. As well, there is a intermediate feature at 1844 eV, most evident in the styrene-functionalized sample previously assigned to suboxides and silanol species formed on nanostructured Si surfaces.[21, 36] In addition, NEXAFS studies of molecular silane species have suggested that Si $1s \rightarrow \sigma^*_{Si-C}$ and Si $1s \rightarrow \sigma^*_{Si-O}$ transitions occur at this energy.[60] The present TEY and FLY NEXAFS spectra are consistent with the mixture of surface alkyl, hydride and oxide species formed during etching and functionalization.
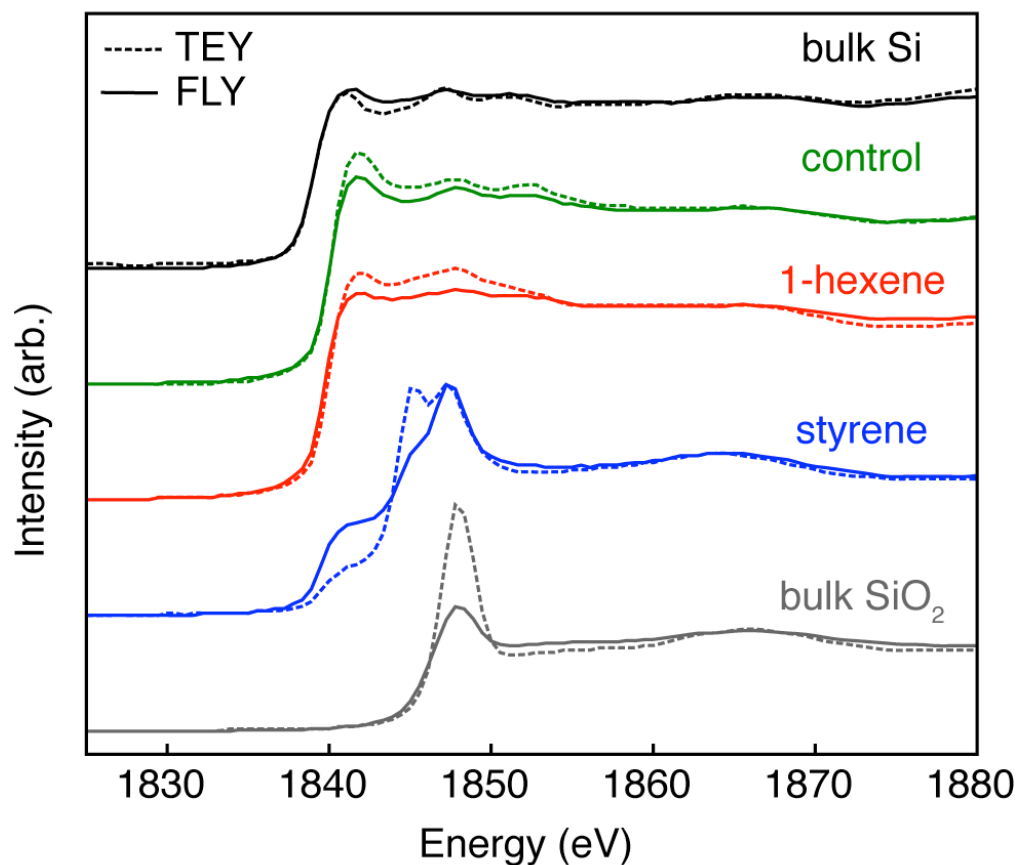
Figure 5-2: Normalized Si *K*-edge FLY (solid lines) and TEY (dashed lines) NEXAFS of Si-NCs functionalized with styrene (blue trace), 1-hexene (red trace) and a control sample prepared in the absence of any alkene/alkyne (green trace). Spectra of elemental Si and SiO₂ standards (black and grey traces respectively) are shown for comparison. Spectra have been shifted vertically for clarity.

An important consideration when comparing XAS results of different Si nanostructures is the homogeneity and thickness of the samples in the context of the different sampling depths of the TEY, FLY and PLY channels monitored; at the Si *K*-edge, accepted sampling depths are *ca.* 60 nm, 200-300 nm and >1000 nm, respectively.[35, 65] For materials with dimensions greater than these sampling depths, a

measure of surface sensitivity is afforded, with TEY probing the surface and FLY and PLY probing the bulk of the sample (although PLY is considered a bulk technique, it is only sensitive to the structure of the luminescent sites and their immediate surroundings). Luminescent porous Si consists of a relatively thick, high internal surface area film within which Si nanostructures reside. The porosity, distribution of luminescent species and surface chemistry varies within the film depending on the sample preparation and handling conditions.[51] TEY, FLY and PLY therefore yield different information regarding the structure of the porous film. In contrast, the present samples contain only freestanding Si-NCs with a relatively narrow size distribution, which are uniformly distributed throughout the sampling depths of all channels monitored. Thus, FLY, TEY and PLY should all be considered "bulk" techniques for these samples.

The PLY signal can also be significantly influenced through so-called "edge-inversion" effects. For a sample containing a distribution of luminescent and non-luminescent species in competition with each other for absorption of X-rays, the PLY signal can become distorted when absorption by the non-luminescent species dominates at X-ray energies above the edge; this leads to a reduction in the PLY signal. This effect has been demonstrated for PLY of hydride-terminated porous Si aged in ambient atmosphere.[21] Whereas the "slow band" red PL exhibited an inverted edge jump, the "fast band" blue PL exhibited a positive edge jump matching a silicon oxide species. Upon rinsing with HF, the blue PL was removed, and the red PL exhibited a positive edge jump matching elemental Si. This observation suggests the red and blue PL originate from the bulk and surface of the film respectively.

Figure 5-3 shows XEOL spectra collected with 1841 eV excitation and UV-excited PL (*i.e.*, 365 nm, 3.4 eV) collected immediately following functionalization. This luminescence is generally similar to the "slow band" red PL widely reported for porous Si. Although XEOL of the control Si-NCs and 1-hexene functionalized Si-NCs are very similar to the UV excited PL (slightly red shifted by 10-20 nm), the styrene-functionalized Si-NCs is substantially blue shifted to a PL maximum of *ca.* 625 nm (shift of *ca.* 75 nm/ 0.2 eV).
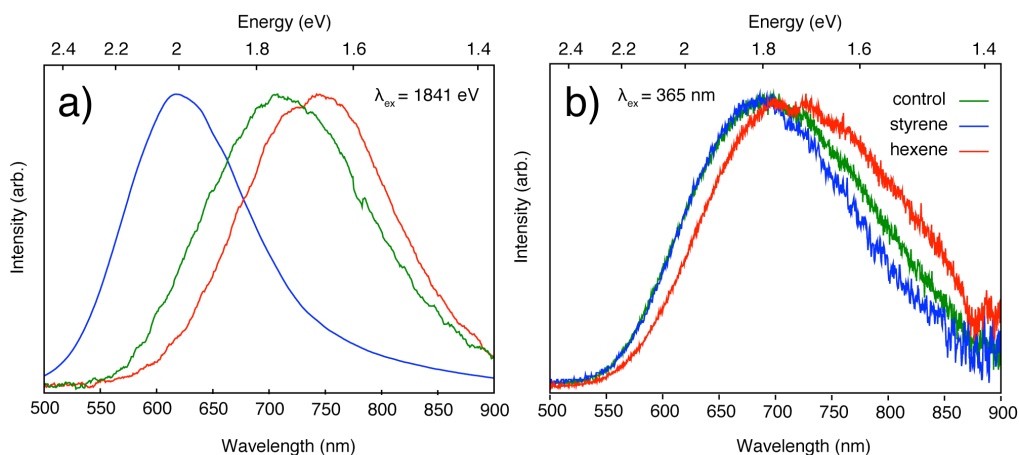
Figure 5-3: a) Normalized XEOL spectra (λ_{ex} = 1841 eV) and b) UV-excited PL spectra (λ_{ex} = 365 nm, 3.4 eV) of 1-hexene and styrene functionalized Si-NCs in comparison to a control sample prepared in the absence of any alkene.

The observed XEOL signal decays irreversibly under X-ray irradiation over the timescale of minutes during the PLY collection (shown with details of the background correction in Figure 5-4). Chao and coworkers have observed oxidation and charging effects induced by soft X-ray exposure during analysis for alkylated Si-NCs derived from porous Si.[47] They found these effects critically depend on the amount of ambient exposure the sample received before analysis. However, in the present investigation, no appreciable damage was observed in subsequent FLY and TEY scans. Rather, it is proposed the observed decay in XEOL may be analogous to the Staebler-Wronski effect in amorphous Si:H photovoltaics whereby irradiation induces the formation of dangling bonds, often described by the hydrogen bond switching model.[66] For the present Si-NCs (composed of hundreds to thousands of Si atoms),[67] electron paramagnetic resonance studies have shown the formation of a surface dangling bond is correlated with loss of luminescence; such a change in the

surface NC structure may not be detectable at the sensitivity of Si *K*-edge NEXAFS.[28] To combat this, samples were cooled to liquid N_2 temperatures (*ca.* 80 K) and a damage correction was performed to the data after collection. Although the XEOL spectra show changes in intensity over the course of the experiment, no appreciable shift was noted upon extended X-ray exposure or change in temperature that might suggest a change in NC size or surface chemistry.
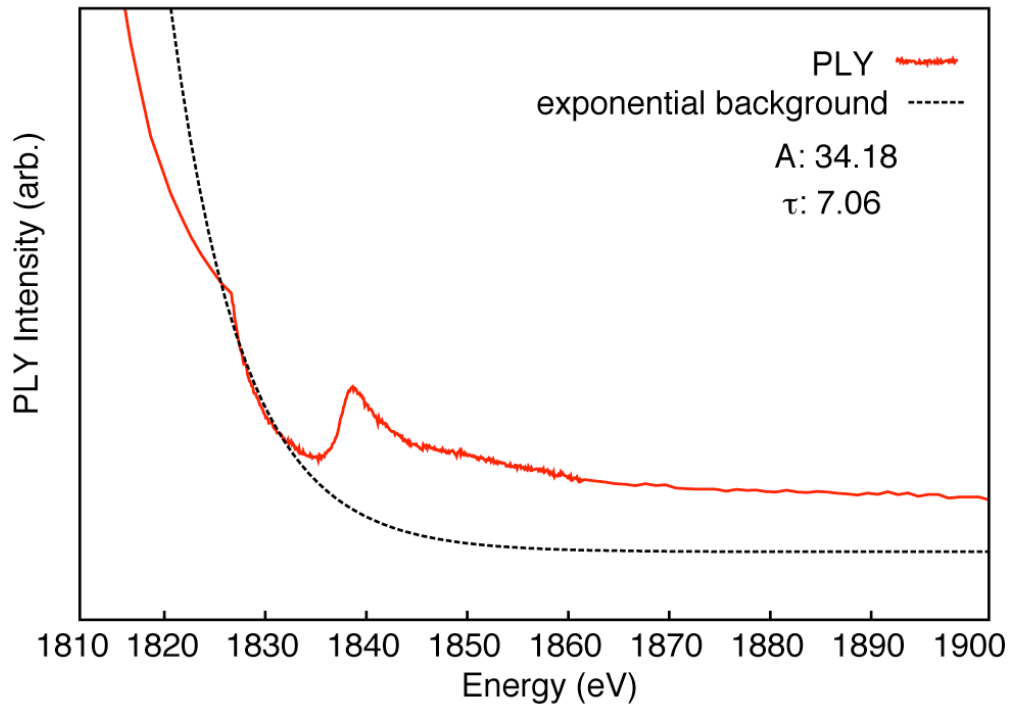
Figure 5-4: Uncorrected PLY NEXAFS of 1-hexene functionalized Si-NCs (red trace) and fitted exponential decay correction (dashed black trace). Parameters of the fit (see section 5.2.3 for details) are listed.

Figure 5-5 shows normalized, background-corrected Si *K*-edge TEY and PLY spectra for functionalized Si-NCs. Each sample shows a positive edge jump at 1841 eV, matching the TEY of elemental Si. This observation confirms absorption by the elemental Si-NC core leads to the observed emission, consistent with the quantum confinement model despite the different surface species identified by TEY and FLY NEXAFS for each sample. The relative intensity of the white line feature at 1841 eV compared to the edge jump varies between samples; this feature is lowest in intensity for the styrene-functionalized Si-NCs which exhibited blue shifted PL. The styrene-functionalized sample shows a small feature at *ca.* 1848 eV that cannot be assigned

unambiguously because of the low signal-to-noise ratio of the sample, possibly through edge-inversion effects (*vide infra*).
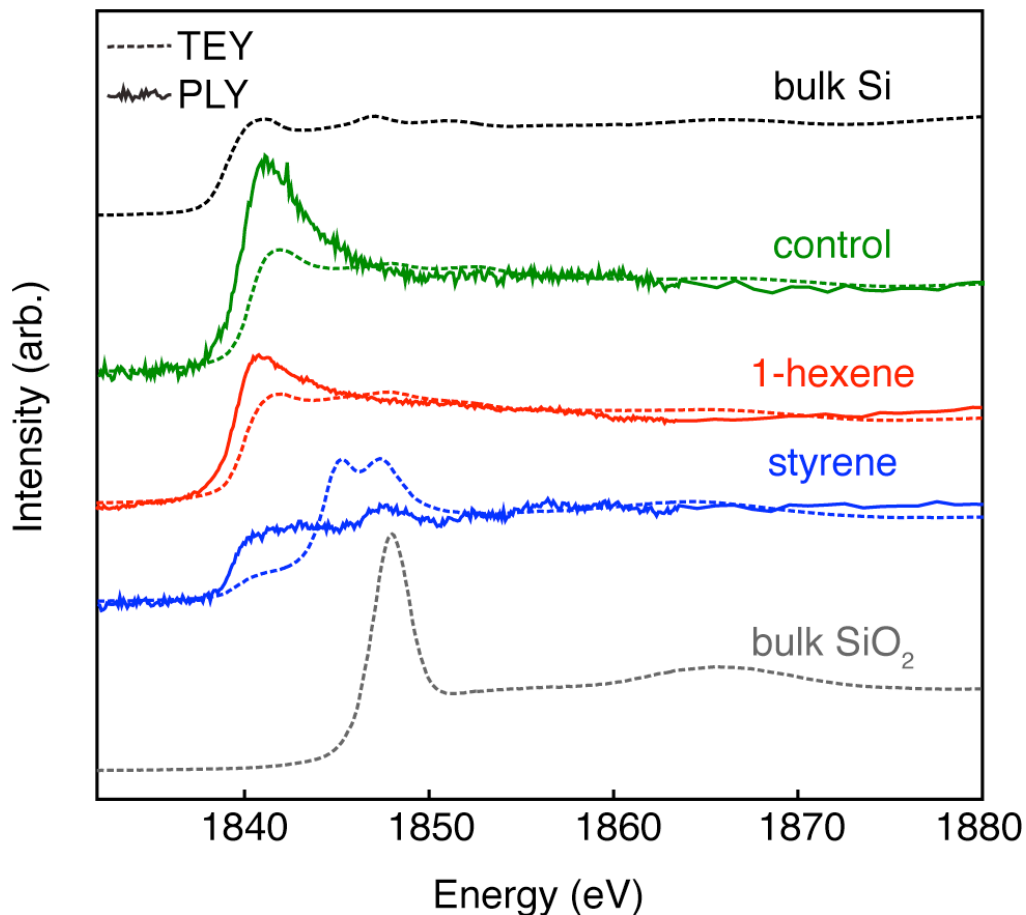
Figure 5-5: Normalized Si *K*-edge TEY (dashed lines) and PLY (solid lines) NEXAFS of Si-NCs functionalized with styrene (blue trace), 1-hexene (red trace) and a control sample prepared in the absence of any alkene/alkyne (green trace). TEY spectra of elemental Si and SiO_2 standards (black and grey traces respectively) are shown for reference. Spectra have been shifted vertically for clarity.

The observed shifts in the Si $L_{3,2}$-edge FLY data and positive edge jump for the Si *K*-edge PLY spectra are consistent with the quantum confinement model, yet

key differences are observed between samples. In particular, the styrene-functionalized Si-NCs show a higher amount of oxidized species, a significantly blue shifted XEOL maximum and suppressed PLY edge jump. In the following discussion, an attempt to rationalize these differences in context of quantum confinement effects and the impact of surface oxidation is presented.

In Chapter 2, it was demonstrated oxidation of the Si-NC surface can occur during functionalization; this was attributed to photoinduced oxidation from trace water remaining from the HF etching procedure.[29] As well, residual hydride species are always observed after reaction resulting from to steric repulsion between adjacent surface groups; the ideal coverage of a Si(111) surface has been estimated to be limited to *ca.* 50%.[18] These species are likely susceptible to oxidation after reaction from exposure to ambient conditions. Although FTIR spectroscopy and thermogravimetric analysis (TGA) suggested similar degrees of surface coverage for hydrosilylation with 1-hexene and styrene, through the use of *in situ* PL measurements during hydrosilylation, functionalization with 1-hexene was observed to result in more intense PL. This difference was explained through the formation of "pin-hole" packing defects in the styrene-functionalized Si-NCs stemming from increased interaction between the surface benzyl groups and the solvent. [68] It is reasonable such defects could render the surface more susceptible toward oxidation, either during reaction or afterward. Furthermore, it has been suggested that oxidation of Si-Si bonds within the NC core may occur preferentially where one Si atom is already oxidized, leading to a progressive sweeping mechanism.[25]

While substantial effort was made towards controlling the exposure of the present samples to ambient conditions before XAS analysis, it is not yet feasible to carry out all steps of the analysis under fully inert conditions. The common approach taken for porous Si of an HF rinse immediately preceding analysis[21] is not practical for freestanding samples, and may further reduce the Si-NC size and in doing so also shift the PL. Thus, it is possible the styrene-functionalized Si-NC sample used for Si *K*-edge analysis may have been exposed to ambient conditions, leading to oxidation during handling (separate samples were freshly prepared for $L_{3,2}$- and *K*-edge analyses). This heightened sensitivity toward oxidation is consistent with the previous report by Chao and coworkers showing ambient exposure of their Si-NC samples could significantly influence soft X-ray characterization.[47]

FTIR spectra of the Si-H region for the styrene-functionalized Si-NCs is shown in Figure 5-6 (full FTIR spectra are shown in Figure 5-7). The hydride-terminated surface immediately following etching exhibits a ν Si-H$_x$ stretching band (x = 1-3) centered at *ca.* 2100 cm^{-1}. After functionalization, this feature broadens asymmetrically and shifts slightly to lower frequency, consistent with the replacement of some SiH$_x$ species with C-Si-H$_x$.[69] However, after XAS analysis, a new feature centered at *ca.* 2250 cm^{-1} is apparent, diagnostic of an O$_3$Si-H species arising from increased oxidation of the NC surface. Other characteristic signs of surface oxidation, including a qualitative increase in the intensity of Si-OH and Si-O-Si features, at *ca.* 3500 and 1100 cm^{-1} respectively, also appear (see Figure 5-7).
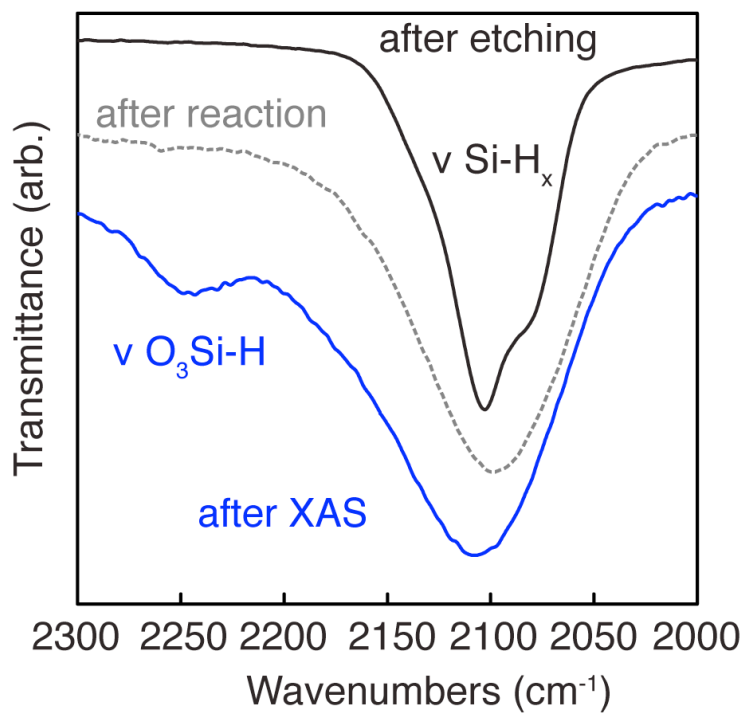
Figure 5-6: FTIR spectra (Si-H$_x$ stretching region) of styrene-functionalized Si-NCs after HF etching, after hydrosilylation and after XAS analysis.
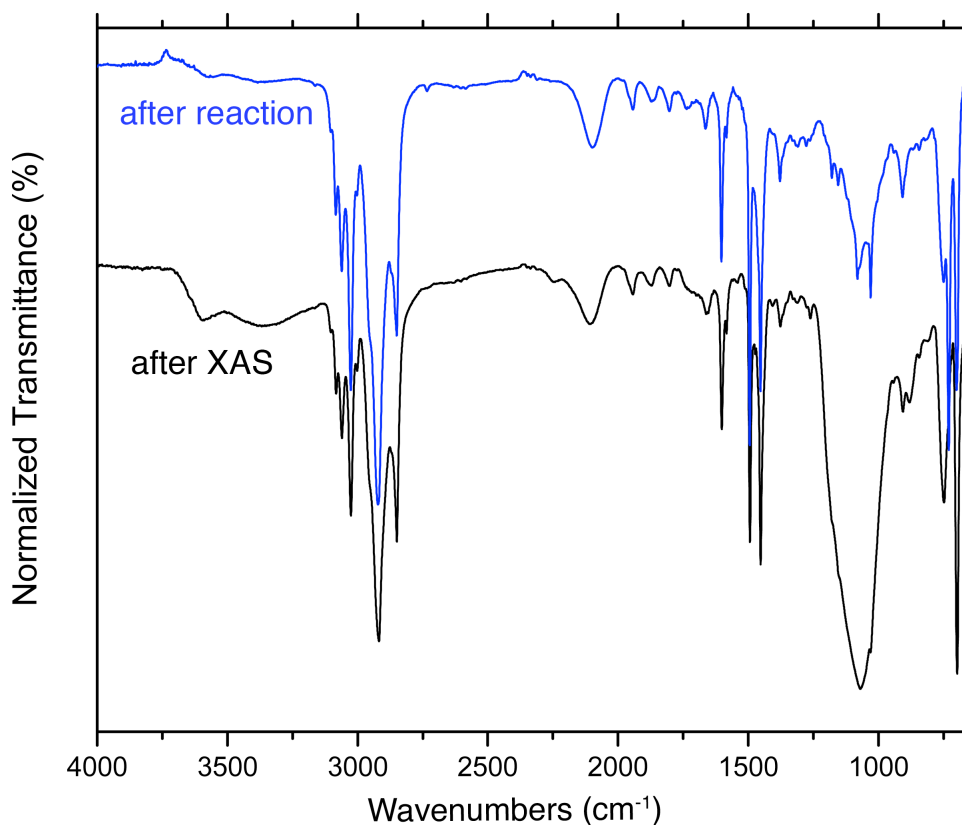
Figure 5-7: FTIR spectra of styrene-functionalized Si-NCs immediately following reaction (blue trace) and after XAS analysis (black trace). Spectra were normalized to the alkyl stretching component at *ca.* 2950 cm⁻¹.

Significant oxidation of Si-NC surfaces has been suggested to induce a blue shift in PL through a net reduction in the diameter of the NC core.[23, 28, 70] This behavior is expected to increase the bandgap until trapping mid-gap states (such as the silanone states proposed by Wolkin)[24] start to influence the optical response. Oxidation has been observed to lead to PL centered at *ca.* 2 eV, consistent with the XEOL spectrum observed here.[20] Oxidation is also expected to lead to the

formation of non-radiative traps, decreasing the PL quantum yield.[28] The reduced intensity of the white line PLY feature therefore could arise from increased competition for X-ray absorption between luminescent and non-luminescent Si-NCs.

While other studies of Si nanostructures have shown oxidation is often correlated with the emergence of a blue PL "fast band",[21-23, 46-48] this is not the case with the present materials. This difference could be related to varying degrees of oxidation through different handling in ambient conditions, or through some intrinsic differences between the NC synthesis and functionalization procedures. For example, Pi and coworkers have shown that different routes to hydride-terminate Si-NC surfaces (*i.e.*, HF etching versus as-prepared from a non-thermal plasma) can yield different reactivity towards oxidation and hence a different shift in optical properties.[28]

Understanding the long-term stability of the Si-NC surface and PL towards oxidation under relevant ambient conditions is of critical importance for the use of these materials in many of their proposed applications. The similarity of the Si *K*-edge FLY and PLY XAS results for the control and 1-hexene functionalized sample suggests the photochemical hydrosilylation process minimally impacts the desired optical properties. However, if the functionalization is unable to prevent oxidation from occurring as observed for the styrene-functionalization, this may limit the utility of photochemical hydrosilylation. A shift of 0.2 eV in the bandgap of the oxidized styrene-functionalized Si-NCs translates to a shift in the CB of 67 meV by the relation proposed by van Buuren and coworkers, [49] a change observable within

the high resolving power of the VLS-PGM. The use of Si $L_{3,2}$-edge XEOL to study the controlled oxidation of functionalized Si-NC surfaces as a function of alkyl species and NC size therefore merits consideration to further understand and control the impact of surface chemistry on Si-NC PL.

5.4. Conclusions

The present chapter outlines a XAS investigation of the optical and electronic properties of freestanding Si-NCs functionalized by photochemical hydrosilylation. Through the use of Si $L_{3,2}$-edge FLY XAS, shifts in the conduction band of these materials attributed to quantum confinement effects were found to be in good agreement with previous reports of other hydride-terminated Si nanostructures. Using Si K-edge FLY, TEY and PLY XAS, it was demonstrated the observed PL originates in absorption by the elemental Si core. Si-NCs functionalized with styrene exhibited changes in their XAS in comparison to samples functionalized with 1-hexene and a control, consistent with oxidation during handling of the styrene sample. Understanding the impact associated with the hydrosilylation process on the origin of luminescence in these materials is important in developing their utility for applications such as biosensing.

5.5 References

1. Canham, L. T. *Appl. Phys. Lett.* **1990**, *57*, 1046-1048.

2. Kortshagen, U. R.; Liu, C. -.; Holman, Z. C. *Nano Letters* **2009**, *9*, 449-452.

3. Liu, C. –Y.; Holman, Z. C.; Kortshagen, U. R. *Adv. Funct. Mater.* **2010**, *20*, 2157-2164.

4. Park, J. –H.; Gu, L.; von Maltzahn, G.; Ruoslahti, E.; Bhatia, S. N.; Sailor, M. J. *Nat Mater* **2009**, *8*, 331-336.

5. Tu, C.; Ma, X.; Pantazis, P.; Kauzlarich, S. M.; Louie, A. Y. *J. Am. Chem. Soc.* **2010**, *132*, 2016-2023.

6. Erogbogbo, F.; Yong, K. -T.; Roy, I.; Xu, G. X.; Prasad, P. N.; Swihart, M. T. *ACS Nano* **2008**, *2*, 873-878.

7. Bayliss, S. C.; Heald, R.; Fletcher, D. I.; Buckberry, L. D. *Adv. Mater.* **1999**, *11*, 318-321.

8. Nagesha, D. K.; Whitehead, M. A.; Coffer, J. L. *Adv. Mater.* **2005**, *17*, 921-924.

9. Ruizendaal, L.; Bhattacharjee, S.; Pournazari, K.; Rosso-Vasic, M.; De Haan, L. H. J.; Alink, G. M.; Marcelis, A. T. M.; Zuilhof, H. *Nanotoxicology* **2009**, *3*, 339-347.

10. Low, S. P.; Voelcker, N. H.; Canham, L. T.; Williams, K. A. *Biomaterials* **2009**, *30*, 2873-2880.

11. Soo Choi, H.; Liu, W.; Misra, P.; Tanaka, E.; Zimmer, J. P.; Itty Ipe, B.; Bawendi, M. G.; Frangioni, J. V. *Nat. Biotechnol.* **2007**, *25*, 1165-1170.

12. Lewinski, N.; Colvin, V.; Drezek, R. *Small* **2008**, *4*, 26-49.

13. Li, X.; He, Y.; Talukdar, S. S.; Swihart, M. T. *Langmuir* **2003**, *19*, 8490-8496.

14. Jurbergs, D.; Rogojina, E.; Mangolini, L.; Kortshagen, U. *Appl. Phys. Lett.* **2006**, *88*.

15. Mangolini, L.; Thimsen, E.; Kortshagen, U. *Nano Lett.* **2005**, *5*, 655-659.

16. Hessel, C. M.; Henderson, E. J.; Veinot, J. G. C. *Chem. Mater.* **2006**, *18*, 6139-6146.

17. Henderson, E. J.; Kelly, J. A.; Veinot, J. G. C. *Chem. Mater.* **2009**, *21*, 5426-5434.

18. Buriak, J. M. *Chem. Rev.* **2002**, *102*, 1271-1308.

19. Veinot, J. G. C. *Chem. Commun.* **2006**, , 4160-4168.

20. Gupta, A.; Swihart, M. T.; Wiggers, H. *Adv. Funct. Mater.* **2009**, *19*, 696-703.

21. Jiang, D. T.; Coulthard, I.; Sham, T. K.; Lorimer, J. W.; Frigo, S. P.; Feng, X. H.; Rosenberg, R. A. *J. Appl. Phys.* **1993**, *74*, 6335-6340.

22. Hua, F.; Erogbogbo, F.; Swihart, M. T.; Ruckenstein, E. *Langmuir* **2006**, *22*, 4363-4370.

23. Pi, X. D.; Liptak, R. W.; Deneen Nowak, J.; Wells, N. P.; Carter, C. B.; Campbell, S. A.; Kortshagen, U. *Nanotechnology* **2008**, *19*.

24. Wolkin, M. V.; Jorne, J.; Fauchet, P. M.; Allan, G.; Delerue, C. *Phys. Rev. Lett.* **1999**, *82*, 197-200.

25. Eyre, R. J.; Goss, J. P.; Briddon, P. R. *Phys. Rev. B Condens. Matter* **2008**, *77*.

26. Vasiliev, I.; Chelikowsky, J. R.; Martin, R. M. *Phys. Rev. B Condens. Matter* **2002**, *65*, 1213021-1213024.

27. Chen, X.; Pi, X.; Yang, D. *J. Phys. Chem. C* **2010**, *114*, 8774-8781.

28. Pi, X. D.; Mangolini, L.; Campbell, S. A.; Kortshagen, U. *Phys. Rev. B Condens. Matter* **2007**, *75*.

29. Kelly, J. A.; Veinot, J. G. C. *ACS Nano* **2010**, *4*, 4645-4656.

30. Koch, F.; Petrova-Koch, V.; Muschik, T. *J. Lumin.* **1993**, *57*, 271-281.

31. Nayfeh, M. H.; Rigakis, N.; Yamani, Z. *Phys. Rev. B Condens. Matter* **1997**, *56*, 2079-2084.

32. Rogalev, A.; Goulon, J. *X-ray Excited Optical Luminescence Spectroscopies;* Chemical Applications of Synchrotron Radiations Part II; World Scientific: Singapore, 2002; Vol. 12 B, pp 707-760.

33. Sham, T. K. *Int. J. Nanotechnol.* **2008**, *5*, 1194-1246.

34. Stöhr, J. *NEXAFS Spectroscopy;* Springer-Verlag: Berlin, 1992.

35. Sham, T. K.; Coulthard, I.; Naftel, S. J. *Multicore, multichannel detection (MCMD) X-ray absorption fine structure studies of thin films;* Sham, T. K., Ed.; Chemical Applications of Synchrotron Radiation, Part II: X-ray Applications; World Scientific: Singapore, 2002; Vol. 1, pp 1154-1212.

36. Sham, T. K.; Jiang, D. T.; Coulthard, I.; Lorimer, J. W.; Feng, X. H.; Tan, K. H.; Frigo, S. P.; Rosenberg, R. A.; Houghton, D. C.; Bryskiewicz, B. *Nature* **1993**, *363*, 331-334.

37. Coulthard, I.; Sham, T. K. *Solid State Commun.* **1999**, *110*, 203-208.

38. Coulthard, I.; Antel Jr., W. J.; Freeland, J. W.; Sham, T. K.; Naftel, S. J.; Zhang, P. *Appl. Phys. Lett.* **2000**, *77*, 498-500.

39. Hu, Y. F.; Boukherroub, R.; Sham, T. K. *J. Electron. Spectrosc. Relat. Phenom.* **2004**, *135*, 143-147.

40. Dalba, G.; Fornasini, P.; Grisenti, R.; Daldosso, N.; Rocca, F. *Appl. Phys. Lett.* **1999**, *74*, 1454-1456.

41. Eisebitt, S.; Lüning, J.; Rubensson, J.; Van Buuren, T.; Patitsas, S. N.; Tiedje, T.; Berger, M.; Arens-Fischer, R.; Frohnhoff, S.; Eberhardt, W. *Solid State Commun.* **1996**, *97*, 549-552.

42. Dalba, G.; Daldosso, N.; Fornasini, P.; Grimaldi, M.; Grisenti, R.; Rocca, F. *Phys. Rev. B Condens. Matter* **2000**, *62*, 9911-9914.

43. Sun, X. -H.; Tang, Y. -H.; Zhang, P.; Naftel, S. J.; Sammynaiken, R.; Sham, T. K.; Peng, H. Y.; Zhang, Y. -F.; Wong, N. B.; Lee, S. T. *J. Appl. Phys.* **2001**, *90*, 6379-6383.

44. Daldosso, N.; Luppi, M.; Ossicini, S.; Degoli, E.; Magri, R.; Dalba, G.; Fornasini, P.; Grisenti, R.; Rocca, F.; Pavesi, L.; Boninelli, S.; Priolo, F.; Spinella, C.; Iacona, F. *Phys. Rev. B Condens. Matter* **2003**, *68*, 853271-853278.

45. Hessel, C. M.; Henderson, E. J.; Kelly, J. A.; Cavell, R. G.; Sham, T. K.; Veinot, J. G. C. *J. Phys. Chem. C* **2008**, *112*, 14247-14254.

46. Chao, Y.; Houlton, A.; Horrocks, B. R.; Hunt, M. R. C.; Poolton, N. R. J.; Yang, J.; Šiller, L. *Appl. Phys. Lett.* **2006**, *88*.

47. Chao, Y.; Krishnamurthy, S.; Montalti, M.; Lie, L. H.; Houlton, A.; Horrocks, B. R.; Kjeldgaard, L.; Dhanak, V. R.; Hunt, M. R. C.; Šiller, L. *J. Appl. Phys.* **2005**, *98*, 1-8.

48. Siller, L.; Krishnamurthy, S.; Kjeldgaard, L.; Horrocks, B. R.; Chao, Y.; Houlton, A.; Chakraborty, A. K.; Hunt, M. R. C. *J. Phys. Condens. Matter* **2009**, *21*, 095005.

49. Van Buuren, T.; Dinh, L. N.; Chase, L. L.; Siekhaus, W. J.; Terminello, L. J. *Phys. Rev. Lett.* **1998**, *80*, 3803-3806.

50. Sun, X. -H.; Sham, T. K.; Rosenberg, R. A.; Shenoy, G. K. *J. Phys. Chem. C* **2007**, *111*, 8475-8482.

51. Cullis, A. G.; Canham, L. T.; Calcott, P. D. J. *J. Appl. Phys.* **1997**, *82*, 909-965.

52. Zimina, A.; Eisebitt, S.; Eberhardt, W.; Heitmann, J.; Zacharias, M. *Appl. Phys. Lett.* **2006**, *88*.

53. Godefroo, S.; Hayne, M.; Jivanescu, M.; Stesmans, A.; Zacharias, M.; Lebedev, O. I.; Van Tendeloo, G.; Moshchalkov, V. V. *Nat. Nanotechnol.* **2008**, *3*, 174-178.

54. Jackson, H. L.; McCormack, W. B.; Rondestvedt, C. S.; Smeltz, K. C.; Viele, I. E. *J. Chem. Educ.* **1970**, *47*, A175-A188.

55. Hu, Y. F.; Zuin, L.; Wright, G.; Igarashi, R.; McKibben, M.; Wilson, T.; Chen, S. Y.; Johnson, T.; Maxwell, D.; Yates, B. W.; Sham, T. K.; Reininger, R. *Rev. Sci. Instrum.* **2007**, *78*.

56. Regier, T.; Krochak, J.; Sham, T. K.; Hu, Y. F.; Thompson, J.; Blyth, R. I. R. *Nucl. Instrum. Methods Phys. Res., Sect. A* **2007**, *582*, 93-95.

57. Bringans, R. D.; Olmstead, M. A.; Uhrberg, R. I. G.; Bachrach, R. Z. *Phys. Rev. B Condens. Matter* **1987**, *36*, 9569-9580.

58. Ravel, B.; Newville, M. *J. Synchrotron Radiat.* **2005**, *12*, 537-541.

59. Bianconi, A. *Surf. Sci.* **1979**, *89*, 41-50.

60. Urquhart, S. G.; Turci, C. C.; Tyliszczak, T.; Brook, M. A.; Hitchcock, A. P. *Organometallics* **1997**, *16*, 2080-2088.

61. Van Buuren, T.; Tiedje, T.; Dahn, J. R.; Way, B. M. *Appl. Phys. Lett.* **1993**, *63*, 2911-2913.

62. Carlisle, J. A.; Germanenko, I. N.; Pithawalla, Y. B.; El-Shall, M. S. *J. Electron Spectrosc. Relat. Phenom.* **2001**, *114-116*, 229-234.

63. Batson, P. E.; Heath, J. R. *Phys. Rev. Lett.* **1993**, *71*, 911-914.

64. Hessel, C. M.; Henderson, E. J.; Veinot, J. G. C. *J. Phys. Chem. C* **2007**, *111*, 6956-6961.

65. Kasrai, M.; Lennard, W. N.; Brunner, R. W.; Bancroft, G. M.; Bardwell, J. A.; Tan, K. H. *Appl. Surf. Sci.* **1996**, *99*, 303-312.

66. Kołodziej, A. *Opto. Electron. Rev.* **2004**, *12*, 21-32.

67. Hua, F.; Swihart, M. T.; Ruckenstein, E. *Langmuir* **2005**, *21*, 6054-6062.

68. Sieval, A. B.; Vleeming, V.; Zuilhof, H.; Sudhölter, E. J. R. *Langmuir* **1999**, *15*, 8288-8291.

69. Bateman, J. E.; Eagling, R. D.; Horrocks, B. R.; Houlton, A. *J. Phys. Chem. B* **2000**, *104*, 5557-5565.

70. Ledoux, G.; Guillois, O.; Porterat, D.; Reynaud, C.; Huisken, F.; Kohn, B.; Paillard, V. *Phys. Rev. B Condens. Matter* **2000**, *62*, 15942-15951.

Chapter 6:

Structure and

Optical Properties

of Silicon-Germanium

Nanocrystals*

6.1 Introduction

As synthetic methods for preparing semiconductor nanocrystals (NCs) have improved to the point where tailoring their optoelectronic properties through precise manipulation of size and polydispersity is now routine, focus has shifted to also include compositional control as an added degree of freedom for increasing the versatility of semiconductor NCs. For example, the incorporation of magnetic dopants raises interesting consequences for the incorporation of these materials into future spintronic devices.[1]

Semiconductor NCs of alloyed composition (*i.e.*, a solid solution of two semiconductors with different bandgaps) are also of considerable research interest, as they offer the possibility of stoichiometric control over the optoelectronic properties while maintaining a constant NC size. For example, although CdSe NCs can be synthesized to emit in the high-energy blue spectral region, their small sizes (< 2 nm) results in a lack of stability; this can be overcome by larger $Zn_xCd_{1-x}Se$-NCs, with highly stable, efficient blue emission.[2] Alloy semiconductor NCs exhibit an increase in bandgap energy with increasing content of the higher energy bandgap semiconductor (*e.g.*, wurtzite ZnSe has a bulk bandgap of 2.8 eV at 300 K in comparison to 1.8 eV for wurtzite CdSe). Alloyed NCs can exhibit unique optoelectronic properties through changes to their structure (*e.g.*, homogeneously alloyed, core-shell or gradient compositions). Graded core-shell alloy $Zn_xCd_{1-x}Se/ZnSe$-NCs have recently been demonstrated immune to the phenomenon of "blinking" where NC emission is intermittently quenched through the presence of charged excited states.[3]

In the family of Group 14 materials, nanostructured Si_xGe_{1-x} has been studied for use in applications including non-volatile memory,[4] thermoelectrics,[5] and high-mobility transistors.[6] Photoluminescence (PL) from Si_xGe_{1-x}-NCs has also drawn significant interest, as it has been proposed that the random distribution of Si and Ge within the alloy may break the translational symmetry that gives rise to the indirect bandgaps in pure Si and Ge, making the transition pseudodirect.[7-9] This might greatly increase the extinction coefficient, radiative rate and quantum yield of Si_xGe_{1-x}-NC PL.

Synthetically, alloy NCs present an interesting challenge through the requirement of an additional precursor whose nucleation and growth reactions must be controlled to produce the desired structure. For a homogeneous alloy, the growth of each constituent material must be similar, and the chemistry of each precursor must allow for facile mixing to prevent the formation of separate unalloyed NCs. For Group 14 alloys, the high annealing temperatures used has also raised concern over the possibility of phase segregation and compositional shifts during cooling.[10] Furthermore, post-synthetic compositional and structural changes resulting from oxidation must also be considered.[11, 12] Evaluating the impact of Si_xGe_{1-x} alloying on the resulting optoelectronic properties is thus challenging. For example, Fuiji *et al.* have demonstrated increasing the Ge content of SiO_2-embedded Si_xGe_{1-x}-NCs results in shorter radiative lifetimes and loss of phonon-coupling in the PL response, consistent with breakdown of translational symmetry.[7, 8] Conversely, Pi and Kortshagen have shown the PL quantum yield from freestanding Si_xGe_{1-x}-NCs (prepared by a non-thermal plasma) decreases with increasing Ge content, and

attributed this to the formation of Ge-related surface defects and a change in composition through oxidation.[11] These factors would also be expected to shorten the radiative lifetime and blur any phonon-coupled vibrational structure through compositional inhomogeneity.

Hydrogen silsesquioxane (HSQ), used through out this thesis as a Si-NC precursor, is adaptable for the synthesis of Si_xGe_{1-x}-NCs through co-reaction with germanium diiodide (GeI_2), as these precursors undergo disproportionation forming elemental Si and Ge at similar temperatures.[13] The low solubility of GeI_2 in non-polar organic solvents can be overcome through the formation of alkyl phosphine GeI_2 adducts, facilitating the homogeneous co-precipitation of each precursor.[14]

Previous investigations have shown annealing mechanically ground mixtures of solid HSQ and GeI_2 yields *ca.* 12 nm $Si_{0.45}Ge_{0.55}$-NCs (with no observable PL) and excess bulk Ge. Conversely, the use of phosphine GeI_2 adducts gives samples with intense near-IR PL, red shifted from pure HSQ annealed under identical conditions (suggestive of Ge alloying impacting the optoelectronic properties). Two nanocrystalline phases were identified by X-ray powder diffraction (XRD), consistent with Si- and Ge-rich particles. The breadth, intensity and position of XRD reflections from both phases were observed to shift through changes to processing temperature, time, atmosphere, precursor stoichiometry, and phosphine alkyl chain length.

Raman spectroscopy of these materials confirmed the formation of a Si_xGe_{1-x} alloy in the GeI_2 phosphine adduct samples through observation of a Si-Ge vibration band at *ca.* 400 cm^{-1}. Although XRD characterization was useful in estimating the

particle size and composition, limited conclusions could be drawn from the available data regarding the NC morphology. Phase segregation during cooling[10] could lead to the formation of core-shell or graded composition NCs (Scheme 6-1a and 6-1b). Conversely, the XRD features could also be consistent with a heterogeneous mixture of Si- and Ge-rich particles (Scheme 6-1c). Thus, the impact of Si_xGe_{1-x} alloying on the observed PL remained unclear.
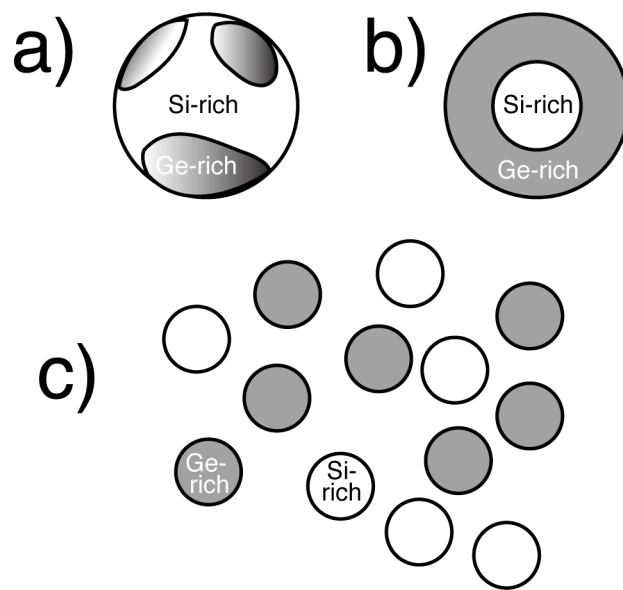
Scheme 6-1: Possible Si_xGe_{1-x}-NC morphologies consistent with previous XRD observations: graded composition (a), core-shell (b) or a heterogeneous mixture of phases (c).

Here, a continuation of the investigation into HSQ and GeI_2: phosphine adducts as precursors for Si_xGe_{1-x}-NCs is presented. First, by adapting the "acid" hydrofluoric acid etching recipe studied in Chapter 4, these oxide composite materials were straightforwardly etched, liberating freestanding NCs which were functionalized through thermal hydrosilylation/hydrogermylation.[15] This has enabled the characterization of these materials by high-resolution transmission electron microscopy (HRTEM) confirming the presence of Ge-rich, homogeneously-alloyed Si_xGe_{1-x}-NCs.

Second, the role of the trialkylphosphine and annealing temperature on the NC nucleation and growth process has been investigated using X-ray absorption

spectroscopy (XAS). As described in detail in Chapter 5, XAS is a powerful, bulk-sensitive technique complementary to previous Raman and XRD characterization of these materials. Notably for Si_xGe_{1-x} materials, the synchrotron beamline utilized in this study can access the Si K- and Ge L_3-edges, allowing concurrent, elemental-selective analysis for both constituent materials. Studying the formation processes in the present system using XAS has allowed greater understanding into the impact of Si_xGe_{1-x}-NC structure and composition on the observed optical properties, characterized by X-ray excited optical luminescence (XEOL), PL spectroscopy, and absolute quantum yield measurements.

6.2 Materials and methods

6.2.1 Materials

All chemicals were purchased from Sigma Aldrich as reagent grade with the exception of HSQ (Dow Corning) and 49% hydrofluoric acid (HF, J.T. Baker, electronics grade), and were used as received. GeI_2 was purified by mixing with benzene and filtering off any iodine or germanium tetraiodide impurities under inert atmosphere. 1-Dodecene was purified immediately before use by passing over neutral alumina to remove peroxide impurities.[16]

6.2.2 Thermal processing of HSQ and GeI_2: phosphine adducts

HSQ was mixed with GeI_2:phosphine adducts and annealed to yield oxide-embedded Si_xGe_{1-x}-NCs as previously described.[14] In brief, GeI_2 (*ca.* 0.4 g) was added to 10 mL of trioctylphosphine (TOP) or tributylphosphine (TBP), forming a bright yellow saturated solution. 3 mL of this solution was mixed with 7 mL of a solution of HSQ in methyl isobutyl ketone (MIBK, 16 wt.%) and stirred for 1 h, forming a deep red color. Next, solvent was removed under vacuum overnight, forming a red powder. Processing at 1000-1100°C in a tube furnace under flowing 5% H_2/ 95% Ar atmosphere yielded a glassy brown product, which was ground with an agate mortar and pestle into a fine powder.

6.2.3 HF etching

Si_xGe_{1-x} oxide composites were etched using a modified procedure from the one described in Chapter 4. To a polypropylene beaker equipped with a stir bar was added 0.3 g of ground composite and 7 mL of 49% HF. The mixture was stirred for 5 min, vigorously producing a gas as the oxide matrix was rapidly etched. Subsequently, 3 mL anhydrous ethanol was added and the mixture was stirred for an additional 2 min to ensure homogeneity. Hydrophobic material was isolated by extraction with two 15 mL aliquots of toluene as a cloudy brown suspension.

6.2.4 Functionalization using thermal hydrosilylation/hydrogermylation

Immediately following etching, the extracted NCs were transferred into glass test tubes and centrifuged at 3,000 rpm to precipitate out the NCs. The toluene was decanted and the NCs redispersed in *ca.* 10 mL of freshly purified 1-dodecene. The mixture was transferred to a Schlenk flask equipped with a stir bar under an argon atmosphere and degassed by three cycles of evacuation and purging with argon. Thermal functionalization was carried out at 190°C for 15 h by heating in a silicone oil bath, resulting in the reaction mixture changing from turbid brown to clear orange/red.

Following functionalization, the reaction mixture was centrifuged at *ca.* 3,000 rpm to remove any unreacted or agglomerated material. The supernatant was filtered through a 250 nm PTFE filter into centrifuge tubes. Purification was carried out by three cycles of precipitation, centrifugation (20 min at 25,900 G) and resuspension using hexane as the solvent and 75% anhydrous ethanol/ 25%

methanol as the antisolvent. The purified samples were redispersed in 10 mL of hexane and kept in a vial until further use.

6.2.5 Optical spectroscopy

Photoluminescence (PL) spectra of oxide-embedded and functionalized samples were collected at room temperature using the 457 nm line of a ArKr ion laser operated with a continuous-wave power of 30 mW. Emission was detected using fiber-optic coupled Ocean Optics USB2000 spectrometer whose spectral response was normalized using a standard black-body radiator. Samples were prepared by drop casting onto silicon wafers.

Absolute PL quantum yields (Φ_{PL}) were measured in a LabSphere integrating sphere, under 600 nm excitation from a Xenon lamp passed through a monochromator (PTI). The emission and excitation spectra were measured with a Si charge-coupled device (CCD) detector. Full details of the experimental setup is available elsewhere.[17] Φ_{PL} of freshly prepared samples in hexane (diluted to an approximate optical transmittance of 95%) were determined by integrating four spectral scans of the sample and of the reference cuvette containing solely hexane through the relation:

$$\Phi_{PL} = \frac{\int I_{sample}(\lambda)d\lambda}{\int E_{ref}(\lambda) - E_{sample}(\lambda)d\lambda} \qquad (6\text{-}1)$$

where E_{ref} is the transmitted intensity of the 600 nm light measured with the reference cuvette, E_{sample} is the transmitted intensity of the 600 nm light with the sample, and I_{sample} is the PL intensity. This approach has been used to verify the

quantum yield reference dyes commonly used for relative quantum yield determination (utilized in Chapter 2). For the TBP-processed sample which exhibited near-IR PL extending beyond the Si CCD detector limit, the obtained Φ_{PL} is considered a lower limit.

6.2.6 Fourier Transform Infrared Spectroscopy (FTIR)

FTIR spectra were collected using a Nicolet Magna 750 IR spectrometer on drop-cast films.

6.2.7 High-resolution Transmission Electron Microscopy (HRTEM), Selected Area Electron Diffraction (SAED) and Energy Dispersive X-ray Spectroscopy (EDS)

HRTEM was performed using a Titan^3 G2 60-300 TEM operating at 300 kV. High Angle Annular Dark Field (HAADF) images and energy dispersive X-ray spectroscopy (EDS) line scans were acquired with a FEI Titan 80-300 operated at 300 kV and equipped with a spherical aberration corrector of the imaging lens. Spectral acquisition and data analysis were carried out using Inca EDXS software (Oxford Instruments).

Prior to analysis, functionalized samples were purified through two additional solvent/antisolvent cycles and resuspended in chloroform to fully remove any organic species that might have hindered analysis through electron-beam induced decomposition. Samples were dropcoated from a dilute chloroform dispersion onto a carbon-coated copper grid.

6.2.8 X-ray Absorption Spectroscopy (XAS)

NEXAFS and XEOL experiments were performed at the Canadian Light Source in Saskatoon, Saskatchewan. Ge $L_{3,2}$-edge and Si K-edge NEXAFS and XEOL were collected on the Spherical Grating Monochromator (SGM, 11ID-1) beamline, which has a photon flux at 1900 eV of *ca.* 10^{11} photons/s/100 mA and a resolving power of *ca.* 5000 E/ΔE.[18] Spectra were normalized to the incident beam intensity (I_o) by measuring the current emitted by a nickel mesh located after the last focusing mirror. X-ray fluorescent yield (FLY) was measured using a micro-channel plate detector positioned 45° from the sample. Total electron yield (TEY) was measured by normalizing the drained sample current to the incident photon flux. XEOL spectra were collected during NEXAFS scans through a lens coupled to an Ocean Optics USB4000 CCD spectrometer. PLY spectra were generated by integrating the XEOL signal over the visible region at each X-ray energy. To minimize effects of X-ray induced sample damage on the luminescence, samples were cooled to *ca.* 80K using a liquid nitrogen cryostat. NEXAFS scans were averaged, calibrated to a powdered bulk standard by setting the first derivative maximum of the $Ge^{(0)}$ L_3-edge absorption to 1217 eV and the $Si^{(0)}$ K-edge absorption to 1839 eV, and normalized using Athena.[19] Powdered samples were mounted as a thin layer on carbon tape. Etched and functionalized samples were drop cast onto aluminum discs. In order to minimize the impact of ambient oxidation, functionalized samples were prepared and purified the day before transportation to the CLS; hydride terminated

samples were freshly etched, drop cast under inert atmosphere and quickly transferred to the endstation.

6.3 Results and discussion

Rendering GeI_2 soluble in HSQ-compatible solvents *via* the formation of trialkylphosphine adducts (*i.e.*, $R_3P:GeI_2$) allows straightforward co-precipitation of HSQ and GeI_2 from solution to form an intimately homogeneous precursor of varied Si:Ge ratios. Following reductive thermal processing, the resulting oxide composites contain Si-rich and Ge-rich NCs rather than excess bulk Ge, and exhibit near-IR PL. The impact of processing temperature, processing time, processing atmosphere, trialkylphosphine chain length, and GeI_2:HSQ stoichiometry on the size and composition of the resulting materials has been previously evaluated. However, XRD and Raman characterization was unable to conclusively determine the morphology of the bimodal nanocrystal populations (*vide supra*) and the contribution (if any) of Ge species in the emission process.

6.3.1 Etching and Functionalization of Si_xGe_{1-x}-NCs

HF etching of oxide composites (prepared by thermal processing of HSQ:GeI_2 phosphine adducts at 1100°C) removes the oxide matrix, facilitating characterization of the resulting freestanding NCs by HRTEM. The liberated particles could be functionalized using 1-dodecene *via* thermal hydrosilylation/hydrogermylation at 190 °C. FTIR spectroscopy (Figure 6-1) of HF-etched TBP-processed particles shows a strong feature centered at *ca.* 2080 cm^{-1} consistent with the formation of $Si-H_x$ and $Ge-H_x$ species.[15] After thermal functionalization, alkyl vibrations at *ca.* 2950 and 1465 cm^{-1} and a broadened $Si-H_x$/$Ge-H_x$ stretching feature centered at 2084 cm^{-1} reduced in intensity is observed,

consistent with the alkyl grafting process. A small degree of oxidation is noted by a Si-O-Si feature at *ca.* 1050 cm^{-1}.
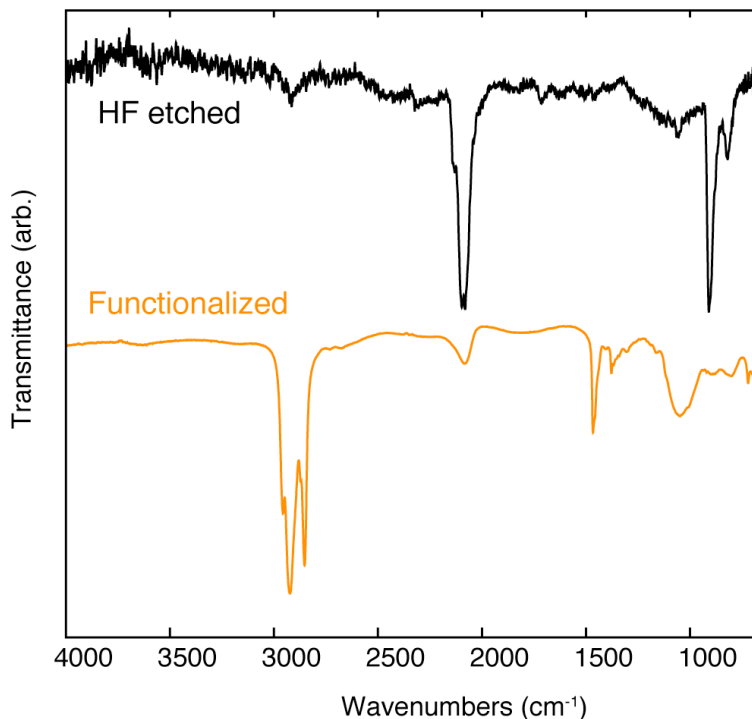
Figure 6-1: FTIR spectra of TBP-processed composite after HF etching (black trace) and thermal functionalization (orange trace).

Figure 6-2 shows a bright field TEM image of TBP 1100°C-processed particles after functionalization. Similar results were observed for TOP-prepared particles. HRTEM lattice fringes matching the diamond-structure d-spacings observed by XRD of the oxide-composites are evident; fast Fourier transformation (FFT) analysis of the HRTEM image showed ensemble characteristic 111 d-spacing ranging from *ca.* 3.3-3.15Å. To determine the elemental distribution within these particles, they were analyzed by HAADF and EDS. In comparison to the bright field image, showing evenly distributed particles, HAADF images highlight a

211

subpopulation of particles with higher Z-contrast suggestive of enriched Ge content. EDS indicated the presence of Si and Ge along with O and C. A Cu signal is observed arising from the grid.

An EDS line scan of a *ca.* 12 nm particle from the high Z-contrast subpopulation indicates the presence of Si and Ge homogeneously distributed through its entirety (Figure 6-3). In comparison, a EDS line scan of a *ca.* 5 nm particle with low Z-contrast shows predominately Si, with low amounts of Ge and O. Thus, these TEM results are consistent with the bimodal motif with separate Ge- and Si-rich populations discussed above (Scheme 6-1c).
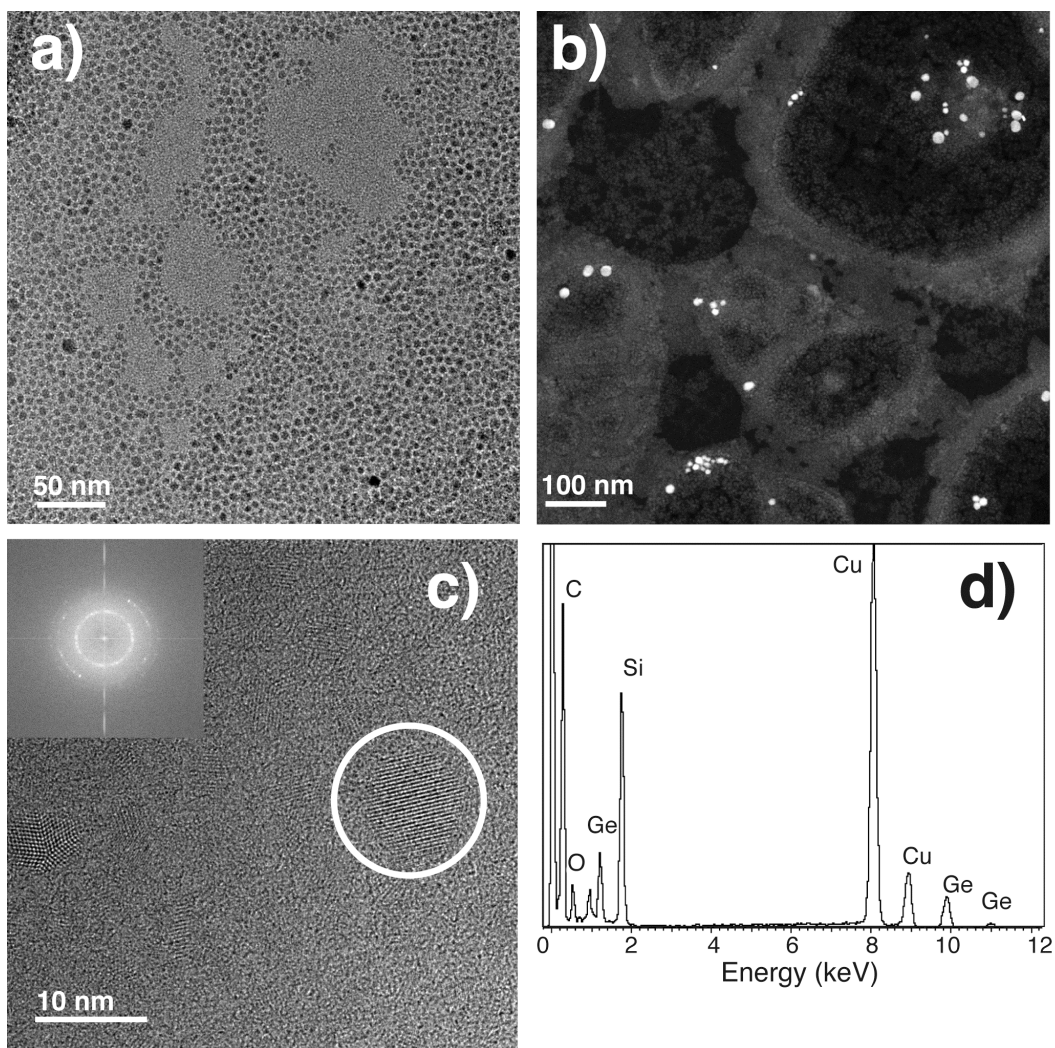
Figure 6-2 a) Bright-field TEM of TBP-processed particles after etching and thermal functionalization. b) HAADF image indicating a subpopulation with higher Z-contrast. c) High-resolution TEM showing nanocrystalline particles. The circled *ca.* 8 nm NC had a lattice spacing of 3.2 Å, corresponding to the 111 plane with approximate $Si_{0.5}Ge_{0.5}$ composition. Inset: FFT of the high-resolution image, showing characteristic diamond-type d-spacing. d) EDS indicating the presence of Si, Ge, C, O and Cu.
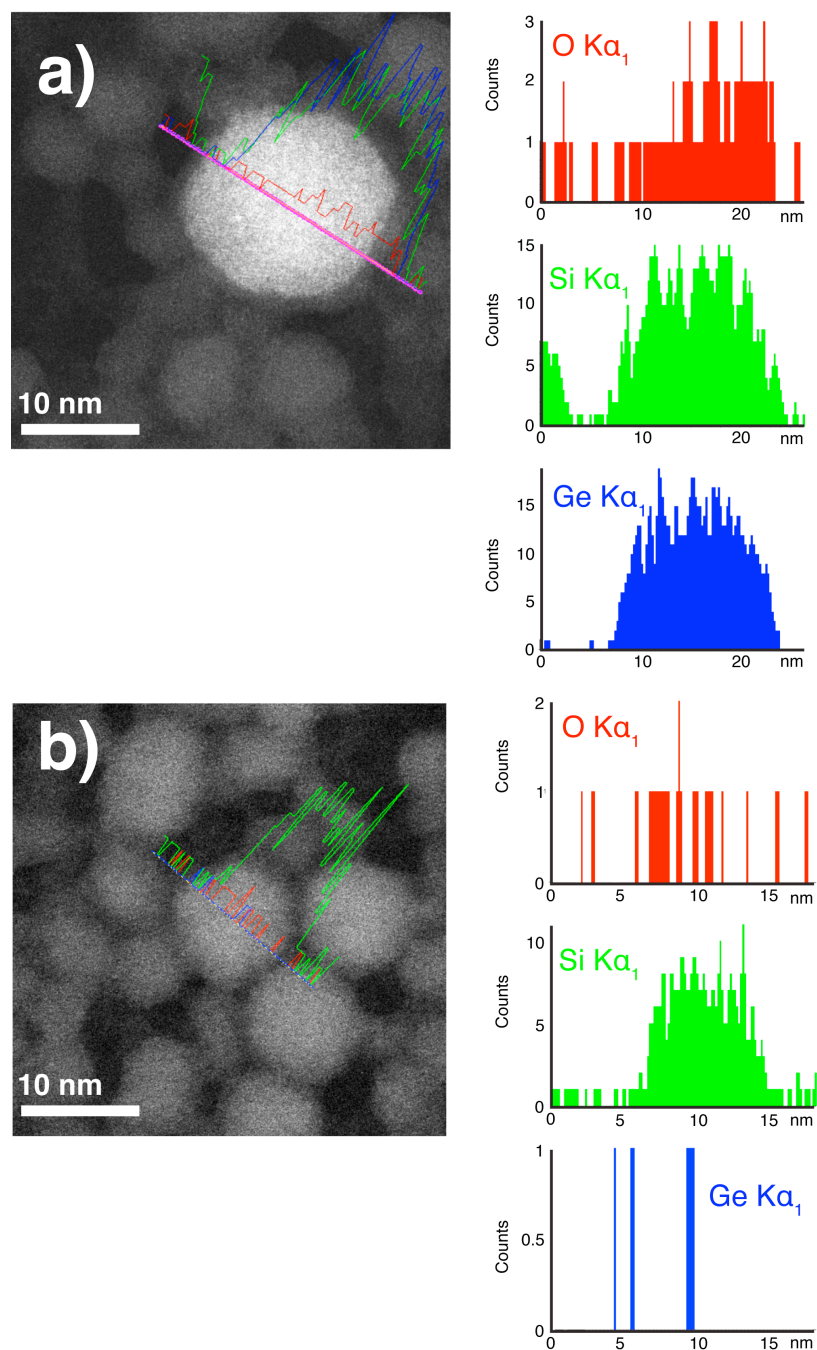
Figure 6-3: HAADF images with overlaid EDS line scans of a) a high Z-contrast particle indicating the homogeneous distribution of Si and Ge throughout the particle and b) a low Z-contrast particle indicating the presence of Si and minimal amounts of Ge.

6.3.2 Photoluminescence

It is interesting to note the hydride-terminated particles immediately after HF etching do not exhibit any observable PL, but after hydrosilylation both samples exhibit intense near-IR PL. TOP- and TBP-prepared particles exhibit PL centered at *ca.* 825 and 880 nm respectively, blue shifted from the corresponding oxide composite PL (Figure 6-4).[14] In comparison, pure HSQ annealed at 1100°C for 5 h, etched and functionalized under identical conditions exhibited a PL maximum of *ca.* 830 nm.
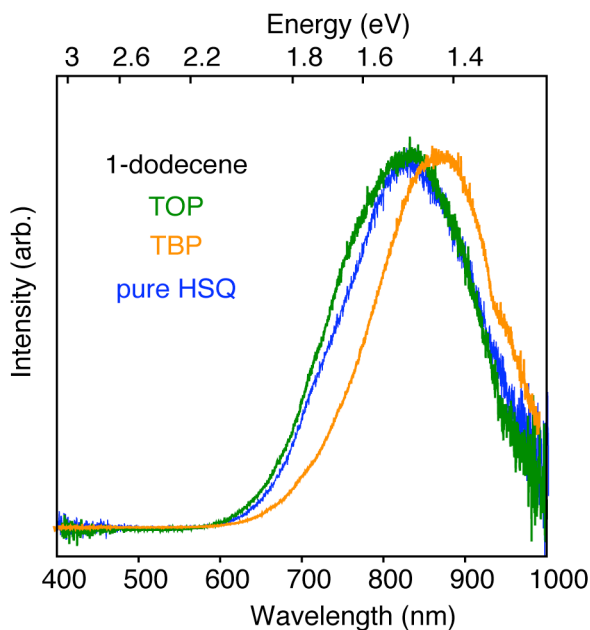
Figure 6-4: PL spectra of freestanding NCs functionalized by thermal hydrosilylation with 1-dodecene, prepared using a GeI_2/TOP adduct (green trace) and a GeI_2/TBP adduct (orange trace). PL from Si-NCs prepared from pure HSQ (blue trace) is shown for comparison.

The observed red shifted PL could arise from several factors related to the interdependent changes in NC size and composition as a function of processing

conditions previously studied described above. The possibility of PL from both Si- and Ge-rich populations is also a complicating factor. Thus, discussion of the impact of Ge alloying on the optoelectronic properties needs to be limited to a broad delineation.

Both functionalized Si_xGe_{1-x} samples had PL quantum yields of 16 ± 3 %, compared to 18 ± 3 % for similarly-functionalized 1100°C- processed Si-NCs from HSQ. Pi and Kortshagen studied 3 nm freestanding Si_xGe_{1-x}-NCs prepared by a non-thermal plasma, suggesting composition did not appreciably shift the bandgap and attributed this to a Si-like band structure.[11] Instead, they noted increased Ge incorporation was correlated with a loss of PL QY, attributed to the formation of Ge-related surface defects. The present observations of a HF-induced loss of PL response are consistent with $Ge-H_x$ related surface defects that are passivated upon thermal hydrogermylation. The relatively high quantum yields in comparison to Si-NCs of similar size and surface-chemistry indirectly suggests Ge plays an active role in the emission. If Ge-containing NCs were entirely non-luminescent, it would significantly reduce the quantum yield through competitive absorption.

6.3.3 X-ray Absorption Spectroscopy (XAS)

XAS is a complementary technique to Raman spectroscopy and XRD often used to characterize the structure and composition of Si_xGe_{1-x} nanomaterials. Near-edge X-ray absorption fine structure (NEXAFS) provides information on elemental-specific local chemical environments, does not require samples to be crystalline, and affords both bulk- and surface-sensitivity depending on the emission channel monitored (*e.g.*, total electron yield- TEY or X-ray fluorescence yield- FLY). It also offers the potential to correlate the local chemical environments present in a sample with any X-ray excited optical luminescence (XEOL, also referred to as photoluminescence yield, PLY). However, as discussed in Chapters 1 and 5, several factors can influence the selectivity of the XEOL experiment, chiefly "edge-inversion" effects arising from competition for X-ray absorption with nonluminescent samples.

6.3.3.1 Near-Edge X-ray Absorption Fine Structure (NEXAFS)

Figure 6-5A shows Si *K*-edge FLY NEXAFS of oxide-embedded Si_xGe_{1-x} samples prepared using HSQ and GeI_2: trialkylphosphine adducts (alkyl= octyl and butyl), as a function of processing temperature. Two features are evident in all samples at *ca.* 1841 and 1848 eV, corresponding to elemental Si and SiO_2, in keeping with previous NEXAFS characterization of similarly prepared oxide-embedded Si-NCs using HSQ.[20] FLY detection (with a sampling depth of *ca.* 200-300 nm[21]) was chosen as TEY detection of these materials can suffer from charging effects stemming from the insulating oxide matrix.

The ratio of the $Si^{(0)}$ and $Si^{(IV)}$ FLY NEXAFS intensities can be used to quantify the disproportionation and diffusion processes identified for the thermal decomposition of HSQ under reducing atmosphere.[22, 23] As a suboxide with $SiO_{1.5}$ stoichiometry, full disproportionation of HSQ yields a ratio of 3 SiO_2:1 Si (*i.e.*, 25% Si). However, previous studies have demonstrated Si-NC growth is still occurring from 1100-1400°C, implying full disproportionation into the thermodynamic products has not been reached. Figure 6-5B shows the $Si^{(0)}$:$Si^{(IV)}$ FLY ratio as a function of temperature for HSQ from 1100-1400°C in comparison to the HSQ: GeI_2 phosphine adducts from 1000-1100°C. Increasing the processing temperature from 1100-1300°C for HSQ composites increases the $Si^{(0)}$ ratio from 0.25 to 0.31, consistent with further disproportionation, although a decrease is noted for the 1400°C sample to 0.29. Deviation over the maximum expected ratio of 0.25 is likely related to self-absorption effects in FLY detection, which would suppress the SiO_2 feature intensity.[24] This could be avoided through the use of inverted partial fluorescence yield (IPFY) detection, recently demonstrated to be both bulk-sensitive and free of self-absorption effects.[25]

Interestingly, the $Si^{(0)}$ ratio of HSQ: GeI_2 phosphine adducts annealed at 1000-1100°C shifted substantially depending on the alkyl chain length of phosphine used. Samples prepared with trioctylphophine (TOP) increased in $Si^{(0)}$ ratio from 0.09 at 1000°C to 0.21 at 1100°C, slightly below HSQ samples. Conversely, samples prepared with tributylphosphine (TBP) exhibited very high $Si^{(0)}$ ratios of *ca.* 0.28, shifting slightly with temperature. For the TOP samples, the increase in $Si^{(0)}$ content with temperature is consistent with the trend observed for pure HSQ.

$R_3P:GeI_2$ adducts liberate GeI_2 and the corresponding phosphine at *ca.* 400°C;[26] decomposition of the phosphine into carbonaceous impurities (*e.g.*, silicon oxycarbides) would be expected to lower the $Si^{(0)}$ ratio compared to HSQ, as these species do not participate in the disproportionation process.[27] However, this hypothesis is not fully consistent with the high $Si^{(0)}$ ratio observed for the TBP sample, which is higher than pure HSQ annealed at the same temperature.

Previous XRD characterization of oxide-embedded Si-NC composites prepared from $HSiO_{1.5}$ sol-gel polymers has shown incorporation of network-modifying methyl groups can influence NC growth processes by "opening up" the matrix to lower the activation barrier for $Si^{(0)}$ diffusion, leading to larger Si-NCs.[27] However, in the present system the TBP samples exhibited broader, weaker XRD peaks than similarly-prepared TOP samples, consistent with smaller NCs (not shown). Instead, the GeI_2:TBP adduct could provide additional heterogeneous nucleation sites for Si-NC formation, decreasing the effective diffusion length of $Si^{(0)}$ species through the oxide matrix while also lowering the average NC size. Heterogeneous nucleation is a well-known consideration for the synthesis of other monodisperse nanocrystals;[28] however, the exact role of the GeI_2:phosphine adduct is still unclear as it could participate in both elemental Ge nucleation and Si_xGe_{1-x} growth processes. These Si *K*-edge FLY NEXAFS results suggest further study is warranted to determine the influence of the trialkylphosphine on Si_xGe_{1-x} formation.
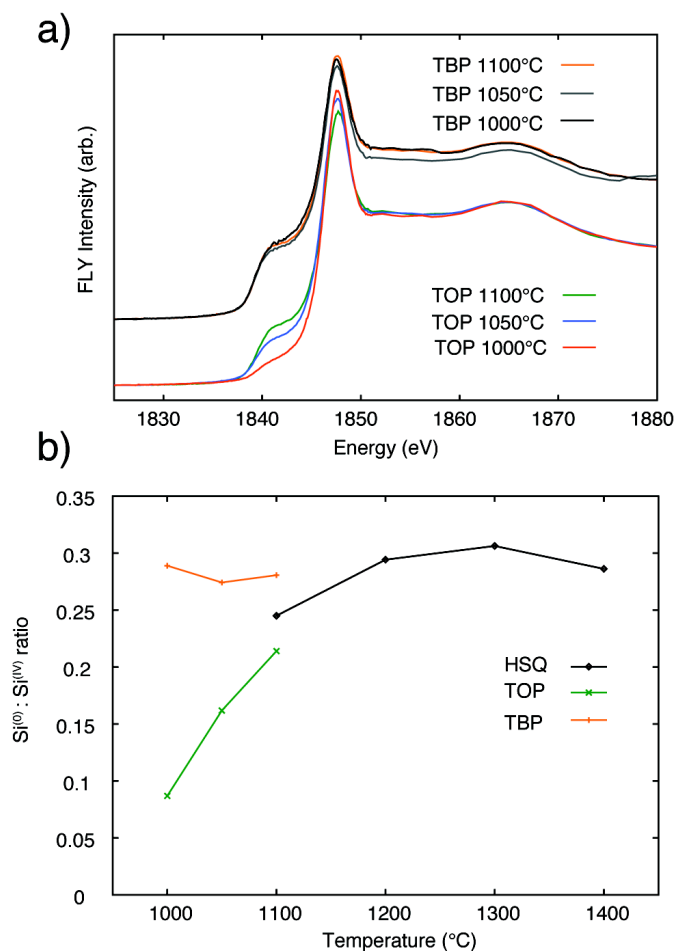
Figure 6-5: a) Si *K*-edge FLY NEXAFS of HSQ and GeI_2/alkyl phosphine adducts annealed from 1000-1100°C. b) Ratio of Si *K*-edge $Si^{(0)}$ and $Si^{(IV)}$ FLY intensities (at 1841 and 1848 eV respectively) for tributylphosphine (TBP), trioctylphosphine (TOP) and pure HSQ composites as a function of temperature.

Despite the significant changes observed by Si *K*-edge NEXAFS for the Si_xGe_{1-x} samples, the Ge L_3-edge XAS data for these oxide composites exhibited extremely poor signal-to-noise ratios (data not shown). These ratios are attributed to evaporative losses of Ge over extended annealing because of its higher vapor pressure.[29] Although the detection limit of FLY NEXAFS has been estimated to be as

low as 100 μM for some metal edges,[30] dilute samples are challenging to evaluate because of the influences of self-absorption and edge-inversion effects, particularly in the soft X-ray regime where many elements absorb indiscriminately, increasing background absorption.[24]

To overcome this challenge and identify the chemical environment(s) of Ge in these materials, Si_xGe_{1-x} samples processed with TOP and TBP at 1100°C were selected for HF etching and thermal hydrosilylation and Si K- and Ge L_3-edge FLY NEXAFS analysis. Using full disproportionation as an upper limit (*i.e.*, 25% Si available for Si or Si_xGe_{1-x} formation), oxide-embedded samples are expected to contain *ca.* 85% SiO_2 by mass; etching is thus expected to improve the poor signal-to-noise issues associated with detection of diluted, low amounts of Ge. Si K- and Ge L_3-edge FLY NEXAFS are shown for hydride-terminated samples immediately after HF etching and functionalized samples after thermal hydrosilylation (Figure 6-7). A Si K-edge spectrum of a reference sample of functionalized Si-NCs prepared from 1100°C-processed HSQ is also shown for comparison.

HF-etched Si_xGe_{1-x} samples exhibit Si K-edge features very similar to previously studied hydride-terminated Si-NC samples (Figure 6-6A). A strong $Si^{(0)}$ feature at *ca.* 1841 eV is noted, with very little or no oxide noted at 1848 eV,[20] consistent with the complete removal of the encapsulating matrix. Ge L_3-edge spectra of Si_xGe_{1-x} samples are still hampered by low signal-to-noise, consistent with low, diluted amounts of Ge through evaporative losses, *vide supra* (Figure 6-6B). However, a feature at *ca.* 1218 eV is apparent in both samples, matching the $Ge^{(0)}$

signal for bulk Ge and consistent with previous Ge L_3-edge NEXAFS of thin film Si_xGe_{1-x} super lattices grown by molecular beam epitaxy.[31]

After thermal hydrosilylation, Si K-edge FLY NEXAFS of all samples showed a strong $Si^{(0)}$ feature at 1841 eV for all samples along with features at 1844 and 1848 eV consistent with the alkyl-grafting process and oxidation during functionalization and/or subsequent ambient exposure (Figure 6-6C).[32] The TOP-prepared Si_xGe_{1-x} sample exhibited a more intense feature at 1848 eV, suggesting a higher degree of surface oxidation. Ge L_3-edge FLY NEXAFS of functionalized Si_xGe_{1-x} samples showed a similar trend, with a $Ge^{(0)}$ signal at 1218 eV and an oxide related feature at 1220 eV (Figure 6-6D). Increased intensity of the oxide feature is observed for the TOP sample. As discussed in Chapter 5, it is challenging to pinpoint the exact source of oxidation in these samples, as purification and transport to the CLS unavoidably exposes them to ambient conditions. However, as XAS spectra of the hydride-terminated samples shows the NC surfaces are oxide-free immediately after etching, the correlated increase in Si and Ge oxide species for the TOP sample is qualitatively consistent with a homogeneous alloy rather than a Si-rich core.

Unfortunately, the heterogeneous nature of this system prevents unambiguous assignment of the Si and Ge species in either population. Bostedt *et al.* have demonstrated the utility of Ge L_3-edge XAS in measuring quantum confinement effects in small Ge-NCs through shifts in the conduction band (analogous to the use of Si $L_{3,2}$-edge XAS in Chapter 5).[33] These results show Ge-NCs experience stronger quantum confinement effects than Si-NCs; interestingly, this contrasts with theoretical predictions which suggest Ge-NCs might exhibit Si-

like behavior owing to a shift in the conduction band minimum in k-space from a *L*-derived to *X*-derived state.[34] In this regard, a Ge L_3- and Si $L_{3,2}$-edge XAS investigation into the electronic properties of homogeneous Si_xGe_{1-x}-NCs with well-defined size and composition could be useful in elucidating the differences between Si and Ge in nanoscale size effects. The energy resolution of the SGM beamline is approximately 0.1 and 0.24 eV at the Si $L_{3,2}$- and Ge L_3-edges, sufficient to discern small shifts as a result of gradual changes in NC size and composition.

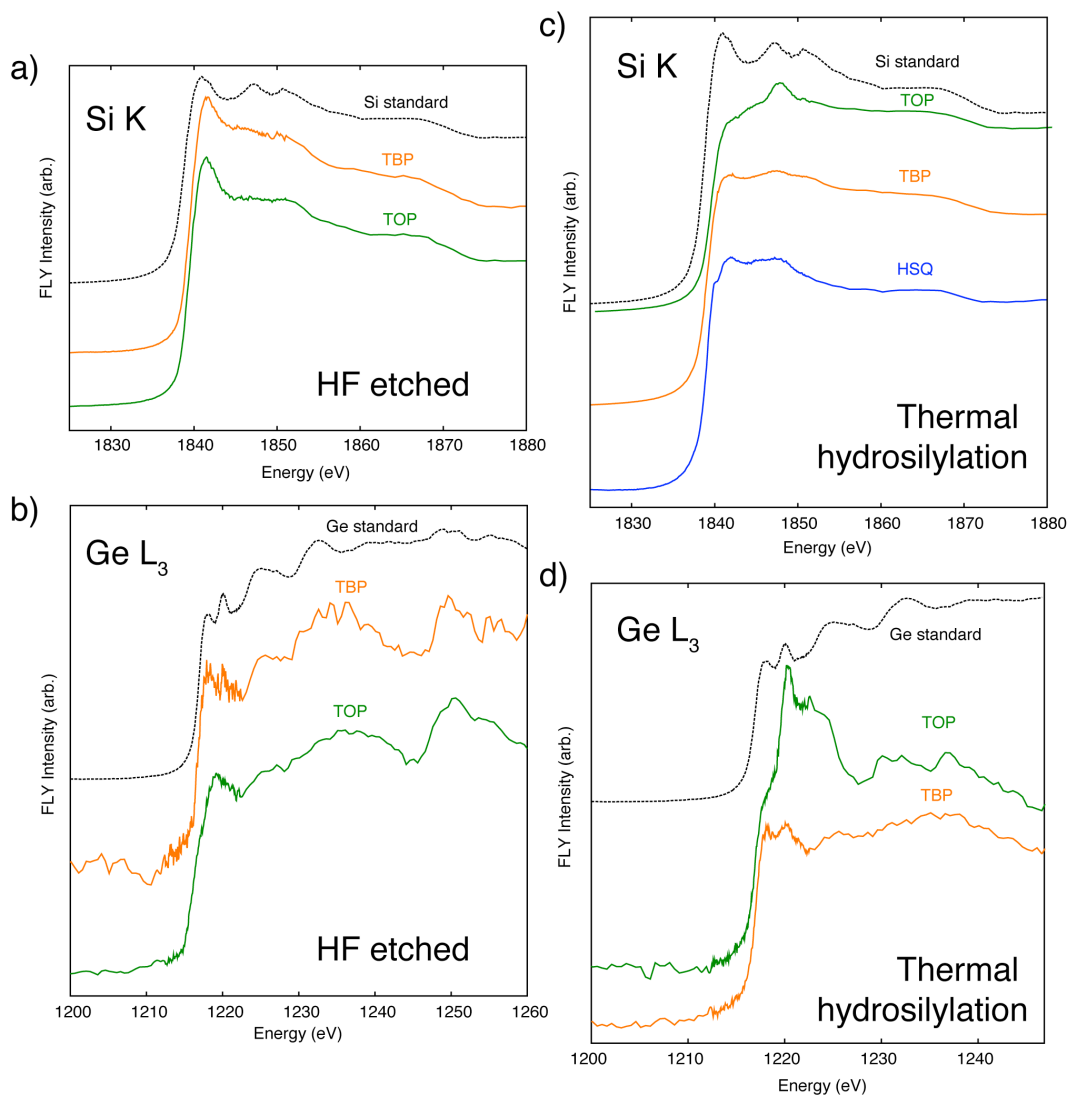**Figure 6-6:** FLY NEXAFS spectra of freestanding Si_xGe_{1-x} samples. Si *K*-edge spectra (a) and Ge L_3-edge spectra (b) of freshly etched hydride-terminated Si_xGe_{1-x} samples. Corresponding Si *K*-edge (c) and Ge L_3-edge spectra (d) after thermal hydrosilylation.

6.3.3.2 XEOL spectroscopy of oxide-embedded Si_xGe_{1-x} samples

The heterogeneity of these Si_xGe_{1-x} samples presents an interesting challenge for the use of XEOL in characterizing the origin of their near-IR luminescence. Ideally, the elemental selectivity inherent to XEOL might reveal the role of the observed elemental and oxide Si and Ge species in the emission process. However, this specificity can be erased through competing edge-inversion effects because of the shallow penetration depth of soft X-rays in comparison to visible photons, as well as X-ray-induced sample damage. Here, preliminary XEOL results of oxide-embedded Si_xGe_{1-x} samples are presented, illustrating how these effects merit consideration for the characterizing the emissive species.

Figure 6-7 shows XEOL spectra excited at 1841 eV (*i.e.*, the $Si^{(0)}$ absorption maximum). Samples prepared with TOP exhibit two spectral bands: one in the near-IR centered at *ca.* 850 nm, resembling the laser-excited PL in Figure 6-3 (*vide supra*) and a higher energy band that varies with processing temperature over the blue-green spectral regions. Representative composites processed at 1050 and 1100°C show a sharp band centered at *ca.* 400 nm and a broad band centered at *ca.* 600 nm respectively. All examined samples prepared with TBP exhibit a single XEOL band in the near IR; a representative spectra of 1100°C-processed TBP composite exhibited a band centered at *ca.* 850 nm.
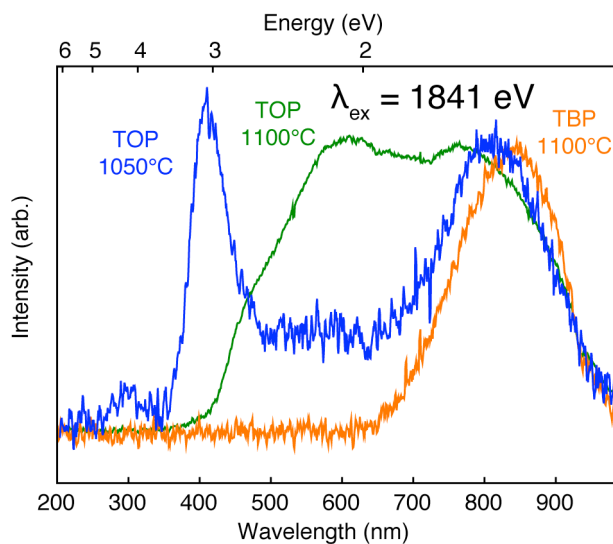
Figure 6-7: Representative normalized XEOL spectra (λ_{ex} = 1841 eV) of oxide-embedded Si_xGe_{1-x} samples.

In both samples, the observed near-IR XEOL signals decay irreversibly over the timescale of minutes during the PLY experiment (similar to the PLY decay observed for functionalized Si-NC samples in Chapter 5), whereas the visible bands persist. This sample damage prevented collection of PLY spectra for TBP-processed samples. Uncorrected Si *K*-edge PLY spectra of the TOP-processed samples are shown in Figure 6-8. No edge features were observed in Ge *L₃*-edge PLY in any samples examined (representative spectrum shown in Figure 6-9).

PLY of the green band from the 1100°C-processed TOP sample (integrated over 400-685 nm) showed an edge jump at the SiO_2 feature at 1848 eV. Conversely, the near-IR band (integrated over 685-1000 nm) does not exhibit a white line feature evident apart from the irreversible decay.

PLY of the blue band from the 1050°C-processed TOP sample (integrated over 330-515 nm) shows an inverted edge centered at the SiO_2 feature at 1848 eV. Recall, this occurs in samples where the decrease in X-ray penetration depth (resulting from the sharp increase in X-ray absorption cross-section) dominates over the enhancement in intensity owing to preferential excitation of the emissive species in producing the PLY signal. The near-IR PLY signal (integrated over 610-1000 nm) also exhibits an inverted edge dropping in intensity at the SiO_2 feature at 1848 eV.

Given the similarities in near-IR emissive bands between these Si_xGe_{1-x} samples and the previously studied HSQ-prepared materials,[20, 32] it is plausible (but not necessarily guaranteed) they share a common near-IR emissive species through the influence of quantum confinement effects. If so, the observed differences in PLY NEXAFS are likely related to edge-inversion and X-ray induced sample damage. Previous XEOL characterization of HSQ-prepared oxide composites relied upon the observation of multiple XEOL bands to assign the origin of luminescence;[20] the change in relative intensity of each band excited at X-ray energies corresponding to elemental and oxide species suggested the near-IR "slow" band was preferentially excited at the $Si^{(0)}$ edge whereas the blue "fast" band was preferentially excited at the $Si^{(IV)}$ edge. However, this ratiometric approach would erroneously implicate an oxide species for the presently observed near-IR band in the 1050°C-processed sample, as the inverted oxide edge for the blue band would lead to a relative enhancement of near-IR intensity.

As discussed in Chapter 5, oxide species have been implicated as the origin of X-ray excited blue-green emission bands in a variety of Si nanostructures,[35-40]

consistent with the present results for the green band from the 1100°C-processed sample. The lack of a high energy band in TBP-prepared samples might also suggest C-containing species play a role in the emission process as less C-contamination is expected than in TOP-prepared samples. In studying the optical properties of carboxylate-containing sol-gel materials, Green *et al.* suggested the observed PL originated from C substitutional defects in the oxide network.[41] In this regard, C *K*-edge XEOL of the present samples might be useful in identifying the role of O- and C-related emissive species.
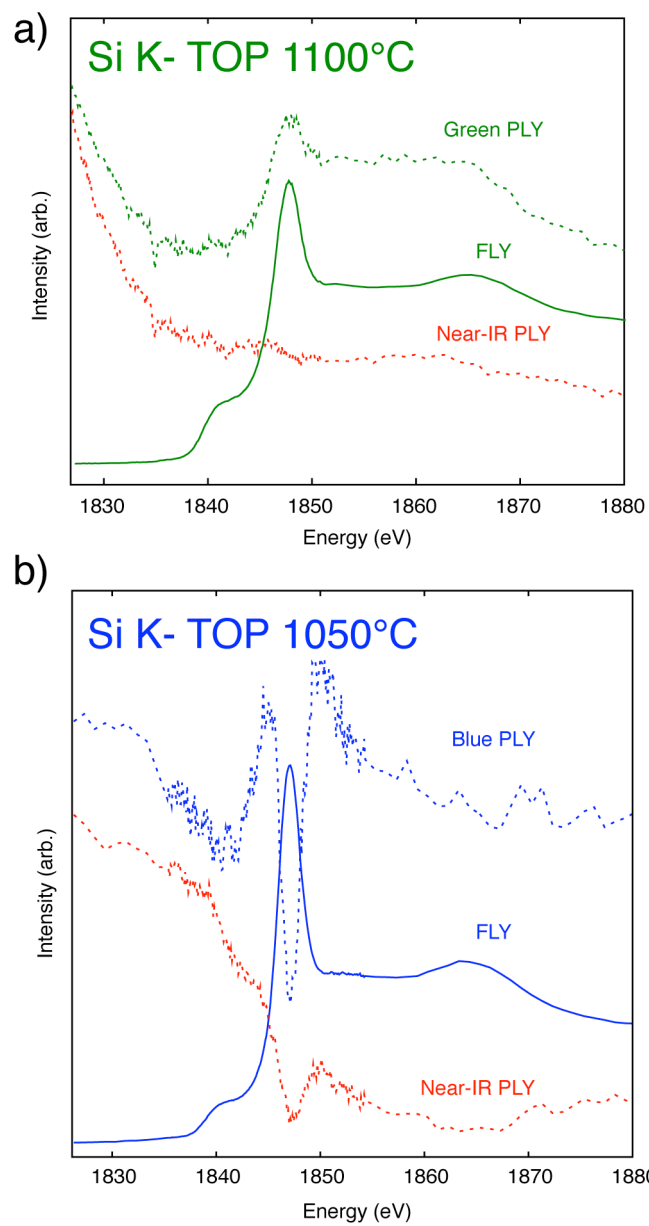
Figure 6-8: Si *K*-edge PLY (dashed traces) and FLY of TOP Si_xGe_{1-x} samples processed at 1100°C (a) and 1050°C (b).
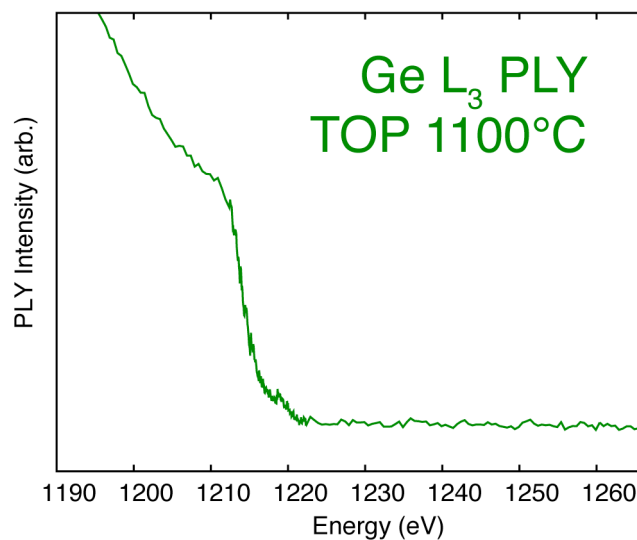
Figure 6-9: Representative Ge L_3-edge PLY spectrum of Si_xGe_{1-x} composite prepared with TOP at 1100°C showing no appreciable features near the edge.

6.4. Conclusions

The morphology and optical properties of Si_xGe_{1-x} NCs prepared from HSQ and GeI_2: trialkylphosphine adducts was studied using electron microscopy, PL and Si *K*- and Ge L_3-edge XAS characterization. The morphology of the NCs consisted of a heterogeneous mixture of Si- and Ge-rich NCs (*i.e.*, morphology C in Scheme 6-1). Indirect evidence for Ge participation in the emission process was presented through the observation of non-luminescent hydride-terminated NCs, and relatively high QYs for alkyl-functionalized samples. Si *K*-edge NEXAFS results suggested the trialkylphosphine used substantially influences Si_xGe_{1-x} NC nucleation and growth processes. Ge L_3-edge NEXAFS confirmed the presence of Ge within the Si_xGe_{1-x} alloy but was hampered by low signal-to-noise issues.

Preliminary Si K- and Ge L_3-edge XEOL results did not definitively confirm the role of elemental Si or Ge as expected for quantum confinement effects, likely related to the influence of edge inversion effects and beam-induced sample damage. A secondary blue-green XEOL band was observed for TOP-prepared samples, arising from a Si oxide related species. Although the heterogeneous nature samples studied prevented conclusive determination of the influence of quantum size effects on the near-IR PL, future XAS investigation on Si_xGe_{1-x} NCs with homogeneous size, composition, and morphology could be valuable in understanding the impact of Ge incorporation on the NC PL.

6.5 References

1. Norris, D. J.; Efros, A. L.; Erwin, S. C. *Science* **2008**, *319*, 1776-1779.

2. Regulacio, M. D.; Han, M. *Acc. Chem. Res.* **2010**, *43*, 621-630.

3. Wang, X.; Ren, X.; Kahen, K.; Hahn, M. A.; Rajeswaran, M.; MacCagnano-Zacher, S.; Silcox, J.; Cragg, G. E.; Efros, A. L.; Krauss, T. D. *Nature* **2009**, *459*, 686-689.

4. De Sousa, J. S.; Freire, V. N.; Leburton, J. *Appl. Phys. Lett.* **2007**, *90*.

5. Takashiri, M.; Borca-Tasciuc, T.; Jacquot, A.; Miyazaki, K.; Chen, G. *J. Appl. Phys.* **2006**, *100*.

6. Schäffler, F. *Semicond. Sci. Technol.* **1997**, *12*, 1515-1549.

7. Fujii, M.; Kovalev, D.; Diener, J.; Koch, F.; Takeoka, S.; Hayashi, S. *J. Appl. Phys.* **2000**, *88*, 5772-5776.

8. Takeoka, S.; Toshikiyo, K.; Fujii, M.; Hayashi, S.; Yamamoto, K. *Phys. Rev. B Condens. Matter* **2000**, *61*, 15988-15992.

9. Virgilio, M.; Grosso, G. *J. Phys Condens. Matter* **2006**, *18*, 1021-1031.

10. Mogaddam, N. A. P.; Alagoz, A. S.; Yerci, S.; Turan, R.; Foss, S.; Finstad, T. G. *J. Appl. Phys.* **2008**, *104*.

11. Pi, X. D.; Kortshagen, U. *Nanotechnology* **2009**, *20*.

12. Cai, K.; Li, C.; Zhang, Y.; Xu, J.; Lai, H.; Chen, S. *Appl. Surf. Sci.* **2008**, *254*, 5363-5366.

13. Henderson, E. J.; Veinot, J. G. C. *Chem. Mater.* **2007**, *19*, 1886-1888.

14. Henderson, E. J. Ph.D. Thesis. Group 14 Semiconductor Nanocrystals, University of Alberta, Canada, 2009.

15. Buriak, J. M. *Chem. Rev.* **2002**, *102*, 1271-1308.

16. Jackson, H. L.; McCormack, W. B.; Rondestvedt, C. S.; Smeltz, K. C.; Viele, I. E. *J. Chem. Educ.* **1970**, *47*, A175-A188.

17. Semonin, O. E.; Johnson, J. C.; Luther, J. M.; Midgett, A. G.; Nozik, A. J.; Beard, M. C. *J. Phys. Chem. Lett.* **2010**, *1*, 2445-2450.

18. Regier, T.; Krochak, J.; Sham, T. K.; Hu, Y. F.; Thompson, J.; Blyth, R. I. R. *Nucl. Instrum. Methods Phys. Res., Sect. A* **2007**, *582*, 93-95.

19. Ravel, B.; Newville, M. *J. Synchrotron Radiat.* **2005**, *12*, 537-541.

20. Hessel, C. M.; Henderson, E. J.; Kelly, J. A.; Cavell, R. G.; Sham, T. K.; Veinot, J. G. C. *J. Phys. Chem. C* **2008**, *112*, 14247-14254.

21. Kasrai, M.; Lennard, W. N.; Brunner, R. W.; Bancroft, G. M.; Bardwell, J. A.; Tan, K. H. *Appl. Surf. Sci.* **1996**, *99*, 303-312.

22. Stöhr, J. *NEXAFS Spectroscopy;* Springer-Verlag: Berlin, 1992; .

23. Hessel, C. M.; Henderson, E. J.; Veinot, J. G. C. *J. Phys. Chem. C* **2007**, *111*, 6956-6961.

24. Sham, T. K.; Coulthard, I.; Naftel, S. J. *Multicore, multichannel detection (MCMD) X-ray absorption fine structure studies of thin films;* Sham, T. K., Ed.; Chemical Applications of Synchrotron Radiation, Part II: X-ray Applications; World Scientific: Singapore, 2002; Vol. 1, pp 1154-1212.

25. Achkar, A. J.; Regier, T. Z.; Wadati, H.; Kim, Y.; Zhang, H.; Hawthorn, D. G. *Phys. Rev. B Condens. Matter.* **2011**, *83*, 081106.

26. King, R. B. *Inorg. Chem.* **1963**, *2*, 199-200.

27. Henderson, E. J.; Kelly, J. A.; Veinot, J. G. C. *Chem. Mater.* **2009**, *21*, 5426-5434.

28. Kudera, S.; Carbone, L.; Manna, L.; Parak, W. J. *Growth mechanism, shape and composition control of semiconductor nanocrystals;* Rogach, A. L., Ed.; Semiconductor Nanocrystal Quantum Dots; Springer Vienna: pp 1-34.

29. Searcy, A. W. *J. Am. Chem. Soc.* **1952**, *74*, 4789-4791.

30. Hasnain, S. S.; Quinn, P. D.; Diakun, G. P.; Wardell, E. M.; Garner, C. D. *J. Phys. E. Sci. Instrum.* **1984**, *17*, 40-43.

31. Castrucci, P.; Gunnella, R.; Pinto, N.; De Crescenzi, M.; Sacchi, M.; Dufour, G.; Rochet, F. *Surf. Sci.* **1998**, *416*, 466-471.

32. Kelly, J. A.; Henderson, E. J.; Clark, R. J.; Hessel, C. M.; Cavell, R. G.; Veinot, J. G. C. *J. Phys. Chem. C* **2010**, *114*, 22519-22525.

33. Bostedt, C.; Van Buuren, T.; Willey, T. M.; Franco, N.; Terminello, L. J.; Heske, C.; Möller, T. *Appl. Phys. Lett.* **2004**, *84*, 4056-4058.

34. Reboredo, F. A.; Zunger, A. *Phys. Rev. B Condens. Matter* **2000**, *62*, R2275-R2278.

35. Jiang, D. T.; Coulthard, I.; Sham, T. K.; Lorimer, J. W.; Frigo, S. P.; Feng, X. H.; Rosenberg, R. A. *J. Appl. Phys.* **1993**, *74*, 6335-6340.

36. Hua, F.; Erogbogbo, F.; Swihart, M. T.; Ruckenstein, E. *Langmuir* **2006**, *22*, 4363-4370.

37. Pi, X. D.; Liptak, R. W.; Deneen Nowak, J.; Wells, N. P.; Carter, C. B.; Campbell, S. A.; Kortshagen, U. *Nanotechnology* **2008**, *19*.

38. Chao, Y.; Houlton, A.; Horrocks, B. R.; Hunt, M. R. C.; Poolton, N. R. J.; Yang, J.; Šiller, L. *Appl. Phys. Lett.* **2006**, *88*.

39. Chao, Y.; Krishnamurthy, S.; Montalti, M.; Lie, L. H.; Houlton, A.; Horrocks, B. R.; Kjeldgaard, L.; Dhanak, V. R.; Hunt, M. R. C.; Šiller, L. *J. Appl. Phys.* **2005**, *98*, 1-8.

40. Siller, L.; Krishnamurthy, S.; Kjeldgaard, L.; Horrocks, B. R.; Chao, Y.; Houlton, A.; Chakraborty, A. K.; Hunt, M. R. C. *J. Phys. Condens. Matter* **2009**, *21*, 095005.

41. Green, W. H.; Le, K. P.; Grey, J.; Au, T. T.; Sailor, M. J. *Science* **1997**, *276*, 1826-1828.

Chapter 7:

Conclusions

and Future Directions

7.1 Conclusions

The development of luminescent group 14 nanostructures has progressed rapidly over the last twenty years, from Canham's initial discovery[1] to fundamental study of their size-dependent properties, and development toward market-ready technologies. Promising recent reports demonstrating the use of these materials in biological imaging,[2] light-emitting diodes[3, 4] and photovoltaics[5] along with a diversity of other applications have shown these materials as viable, biologically-compatible alternatives to the widely-studied II-VI family of NCs. As with any scientific field, this progress has not been linear nor straightforward, and can be generally classified along four main objectives:

1) Synthetic methods that yield scaleable quantities of size-controlled materials with narrow polydispersity, well-defined morphology, composition and crystallinity.

2) Methods to control the surface chemistry of these materials to effectively passivate the surface against the formation of electronically-active defects (namely from oxidation), to produce stable colloidal dispersions in a range of relevant solvents, and to provide a platform for subsequent derivatization (*e.g.*, bioconjugate coupling for biological imaging applications).

3) Detailed understanding of the relationship between quantum size effects and surface species as they affect the desired optoelectronic properties.

4) Incorporation of these materials into functional devices, and the identification and development of suitable counterparts in these devices.

Progress toward these objectives has occurred in parallel. For example, at the time of Canham's discovery of intense PL from porous Si, the origin of luminescence was fiercely debated with several competing hypotheses being proposed, including the involvement of molecular species, defects, surface states or hydrogenated amorphous Si.[6] Part of this controversy can be attributed to the wide variability of samples arising from their fabrication methods (*e.g.*, via anodic or stain etching, under illumination or in the dark, method of drying), inhomogeneity through inevitable gradients in porosity, and sample storage and handling conditions. Acceptance of the quantum confinement model grew through greater understanding into the synthetic conditions required to produce brightly-emitting samples, the importance of ageing on sample surface chemistry, and through detailed spectroscopic characterization.

In the present thesis, each chapter has utilized the synthetic advantages of thermal processing of HSQ in an attempt to address the above goals. A primary objective throughout has been control over reactions at the NC surface, particularly in hydrosilylation or HF etching.

In chapter two, the use of near-UV light to initiate hydrosilylation at the surface of Si-NCs with PL in the visible spectral region was investigated. A range of alkene and alkyne substrates was studied in the context of their utility for a range of applications as well as the exciton-mediated and free-radical mechanisms proposed for this reaction. The choice of 365 nm light corresponds to a region of Si-NC direct-gap light absorption, which enhances the rate of exciton formation and thus as the potential to drive the hydrosilylation process. As well, the PL emitted during

reaction was collected *in situ*, allowing direct observation of the changing surface chemistry impacting the emission process. A model invoking surface states formed by etching, hydrosilylation and concomitant oxidation was proposed to account for the size-dependent spectral shifts observed.

This investigation into near-UV hydrosilylation was extended in chapter three toward the functionalization of larger Si-NCs with PL in the near-IR spectral region. Using PL and SAXS, it was shown larger Si-NCs react at a slower rate, allowing a mixture of sizes to be partially separated based on their reactivity in near-UV hydrosilylation. This size-dependent reactivity was proposed to arise through an exciton-mediated mechanism, confirming previous theoretical predictions. Interestingly, size-dependent reactivity was also observed in reaction with phenylacetylene, previously suggested to be incompatible with an exciton-based mechanism. These results suggest other methods of initiation may be preferable for efficient hydrosilylation of larger nanostructures, although olefin compatibility may further limit choice of initiation (*e.g.*, thermal hydrosilylation requires temperatures above the boiling point of shorter chain olefins).

Chapter four explored the impact of pH and HF concentration in the etching of oxide-embedded Si-NCs. Using neat solutions of HF at pH 1, oxide dissolution was dramatically enhanced, facilitating the liberation of a wide range of Si-NC sizes. As well, under these conditions etching proceeded primarily through an exciton-mediated pathway, rather than an oxidize/etch pathway previously employed. Mechanistic considerations may be of interest for tailoring Si-NC size and polydispersity, as PL during photochemical etching experiments could be controlled

by the wavelength of irradiation. However, comparison of PL from hydride-terminated Si-NCs to PL and SAXS results of functionalized Si-NCs suggested a significant portion of Si-NCs are not active in the exciton-mediated pathway. Nonradiative defects which limit the availability of holes to participate in the etching process were proposed to slow the etching of dark Si-NCs. To circumvent this, a two-step etching process was studied using first the oxidize/etch pathway to reduce the number of defects within the Si-NCs and then switching to the exciton-mediated pathway to control and narrow the polydispersity.

In chapter five, the origin of luminescence from Si-NCs functionalized using near-UV hydrosilylation was demonstrated to be consistent with quantum confinement effects using XAS. These experiments confirm the formation of Si-C bonds through hydrosilylation does not substantially alter the emission mechanism. Differences between the XEOL spectra of Si-NCs functionalized with 1-hexene and styrene were rationalized in the context of surface oxidation related to ambient exposure, resulting in a reduction in white-line intensity through edge-inversion effects.

Chapter six pursued the formation of Si_xGe_{1-x} NCs using HSQ in combination with GeI_2 trialkylphosphine complexes. This synthesis yields a mixture of crystalline Si- and Ge-rich particles with intense near-IR PL. Etching and functionalizing these materials by thermal hydrosilylation allowed characterization by HAADF imaging and EDS linescanning, confirming a heterogeneous mixture of phases. The Ge-rich Si_xGe_{1-x} NCs were homogenously alloyed rather than a graded or core-shell morphology. Using XAS, the trialkylphosphine used to solubilize GeI_2

239

in HSQ-compatible solvents was demonstrated to significantly impact the redistribution processes occurring during thermal processing. Although indirect evidence for the participation of Ge in the emission was shown through relatively high PL quantum yields, XEOL characterization was inconclusive, likely stemming from the heterogeneous nature of this system.

7.2 Future directions

There are numerous avenues for new experiments building upon the present work. In general, these investigations have focused on the fundamental study of group 14 nanostructures and their unique properties, but stopped short of testing their potential in a functional device. Given the demonstration of near IR PL with relatively high quantum yields from alkyl-grafted Si- and Si_xGe_{1-x} NCs, a natural starting point for these studies could be the use of these materials as a biological imaging agent in tandem with a aqueous dispersing agent such as phospholipid micelles[2] or amphiphilic polymer,[7] previously studied for similar systems.

Chapter one highlighted the advantages of using *in situ* measurements during the hydrosilylation reaction to eliminate the impact of ambient exposure on the PL. Similarly, the use of electron paramagnetic resonance during functionalization might facilitate identification of electronically-active dangling bonds that could quench or shift the PL response as previously discussed.[8] This may be of particular interest for reaction with conjugated alkynes which quench Si-NC PL. The mechanism of this quenching is still unresolved, and could be of interest for charge separation in photovoltaic applications.

The improved control over the HF etching of oxide-embedded Si-NC composites described in chapter four presents an interesting opportunity for studying the impact of faceting on NC surface passivation. As the "acid" etch rapidly removes the oxide matrix within seconds, it is reasonable the observed mixture of Si-H$_x$ surface species arises from the thermodynamic balance between minimizing surface area and the formation of densely-packed surface planes during thermal processing of HSQ. After the rapid removal of the encapsulating oxide, hydride-terminated Si-NCs could be anisotropically etched with buffered NH$_4$:HF mixtures, which produce monohydride (111) planes with near-atomic flatness.[9] This might minimize the number of di- and trihydride species associated with (100), (110) planes or at edge steps, which cannot be as well passivated because of steric crowding.[10] The effectiveness of passivation using hydrosilylation could be evaluated as a function of the initial surface structure.

The heterogeneous mixture of Ge- and Si-rich NCs resulting from the thermal processing of HSQ and GeI$_2$ trialkylphosphine complexes is a limitation for this approach, as this significantly complicates characterization of the emissive species. Furthermore, separation of these phases is a daunting task given their similar size and surface chemistry. As Si *K*-edge NEXAFS of these materials suggest the GeI$_2$ complexes are influencing NC nucleation, it is possible there are two modes of NC formation through initial nucleation versus subsequent disproportionation and diffusion. However, as the trialkylphosphine ligands studied do not appear to otherwise majorly impede the disproportionation of HSQ, it may be interested to explore the use of phosphine-capped Ge-NCs as a precursor for Si$_x$Ge$_{1-x}$ NCs.[11]

241

These materials would provide a source of elemental Ge for co-precipitation with HSQ, but avoid their own disproportionation pathways, maximizing the potential for a homogeneous morphology. Given the widespread use of phosphine ligands as capping agents in wet-chemical NC syntheses (including both metallic and semiconductor nanostructures), this strategy might be an interesting starting point for the preparation of other Si-containing binary NC systems. Finally, if this approach proved successful in overcoming the current issues of heterogeneity, it might enable direct confirmation of Ge participation in the quantum-confined PL through the use of XEOL characterization.

7.3 References

1. Canham, L. T. *Appl. Phys. Lett.* **1990**, *57*, 1046-1048.

2. Erogbogbo, F.; Yong, K. -T.; Roy, I.; Hu, R.; Law, W.; Zhao, W.; Ding, H.; Wu, F.; Kumar, R.; Swihart, M. T.; Prasad, P. N. *ACS Nano* **2011**, *5*, 413-423.

3. Puzzo, D. P.; Henderson, E. J.; Helander, M. G.; Wang, Z.; Ozin, G. A.; Lu, Z. *Nano Lett.* **2011**, *11*, 1585-1590.

4. Cheng, K.; Anthony, R.; Kortshagen, U. R.; Holmes, R. J. *Nano Lett.* **2011**, *11*, 1952-1956.

5. Liu, C.; Holman, Z. C.; Kortshagen, U. R. *Adv. Funct. Mater.* **2010**, *20*, 2157-2164.

6. Cullis, A. G.; Canham, L. T.; Calcott, P. D. J. *J. Appl. Phys.* **1997**, *82*, 909-965.

7. Hessel, C. M.; Rasch, M. R.; Hueso, J. L.; Goodfellow, B. W.; Akhavan, V. A.; Puvanakrishnan, P.; Tunnel, J. W.; Korgel, B. A. *Small* **2010**, *6*, 2026-2034.

8. Pereira, R. N.; Rowe, D. J.; Anthony, R. J.; Kortshagen, U. *Phys. Rev. B* **2011**, *83*, 155327.

9. Higashi, G. S.; Chabal, Y. J.; Trucks, G. W.; Raghavachari, K. *Appl. Phys. Lett.* **1990**, *56*, 656-658.

10. Nemanick, E. J.; Hurley, P. T.; Webb, L. J.; Knapp, D. W.; Michalak, D. J.; Brunschwig, B. S.; Lewis, N. S. *J. Phys. Chem. B* **2006**, *110*, 14770-14778.

11. Lu, X.; Korgel, B. A.; Johnston, K. P. *Chem. Mater.* **2005**, *17*, 6479-6485.